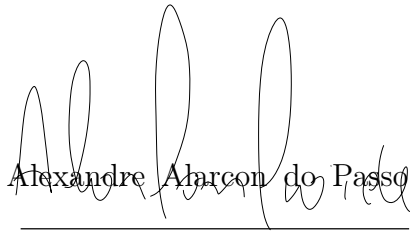


Universidade de São Paulo  
Instituto de Física

Estudo da produção de quarks pesados no  
experimento ALICE através de medidas de dieletron

Hermann Franz Degenhardt

Orientador: Prof. Dr. Alexandre Alarcon do Passo  
Suaide



Tese de doutorado apresentada ao Instituto de Física da  
Universidade de São Paulo, como requisito parcial para  
a obtenção do título de Doutor em Ciências.

Banca Examinadora:

Prof. Dr. Alexandre Alarcon do Passo Suaide (Orientador) - IFUSP

Prof. Dr. Fernando Silveira Navarra - IFUSP

Prof. Dr. Ignácio Alfonso de Bediaga e Hickman - CBPF

Prof. Dr. Mauro Rogério Cosentino - UFABC

Profa. Dra. Maria Beatriz de Leone Gay Ducati - UFRGS

São Paulo  
2021

**FICHA CATALOGRÁFICA**  
**Preparada pelo Serviço de Biblioteca e Informação**  
**do Instituto de Física da Universidade de São Paulo**

Degenhardt, Hermann Franz

Estudo da produção de quarks pesados no experimento ALICE através de medidas de dieletron. São Paulo, 2021.

Tese (Doutorado) – Universidade de São Paulo. Instituto de Física. Depto. de Física Nuclear

Orientador(a): Prof. Dr. Alexandre Alarcon do Passo Suaide

Área de Concentração: Física Nuclear e de Partículas

Unitermos: 1. Dieletron; 2. Quarks pesados; 3. Seção de choque; 4. Mecanismos de produção

USP/IF/SBI-085/2021

University of São Paulo  
Physics Institute

Study of the heavy-flavour production with the  
ALICE experiment through dielectron measurements

Hermann Franz Degenhardt

Supervisor: Prof. Dr. Alexandre Alarcon do Passo  
Suaide

---

Thesis submitted to the Physics Institute of the University of São Paulo in partial fulfillment of the requirements for the degree of Doctor of Science.

Examining Committee:

Prof. Dr. Alexandre Alarcon do Passo Suaide (Supervisor) - IFUSP

Prof. Dr. Fernando Silveira Navarra - IFUSP

Prof. Dr. Ignácio Alfonso de Bediaga e Hickman - CBPF

Prof. Dr. Mauro Rogério Cosentino - UFABC

Prof. Dr. Maria Beatriz de Leone Gay Ducati - UFRGS

São Paulo  
2021





# Resumo

Quarks pesados, como *charm* e *beauty*, são produzidos quase que exclusivamente através de processos de espalhamento duro iniciais, uma vez que suas massas são significativamente maiores do que o parâmetro de escala da Cromodinâmica Quântica (QCD). Isso os faz ferramentas singulares na caracterização de diferentes sistemas de colisões, já que experimentam toda a evolução dos produtos da colisão.

Esse trabalho sumariza o estudo da produção de quarks pesados a partir de medidas de dieletrons em colisões proton-proton (pp) com energia de centro de massa de  $\sqrt{s} = 13$  TeV utilizando dados dos anos de 2016, 2017 e 2018 do experimento ALICE. A produção de quarks pesados foi estudada na rapidez intermediária ( $|\eta| < 0.8$ ) como função da massa invariante, parâmetro de impacto, correlação angular e momento transversal no intervalo de massa intermediário (1.1 - 2.7 GeV/ $c^2$ - IMR). As seções de choque de quarks pesados foram extraídas através de ajustes bidimensionais de dados de  $(m_{ee}, p_{T,ee})$  e  $(DCA_{xy}^{ee}, p_{T,ee})$ , utilizando simulações de Monte Carlo gerados a partir dos geradores de evento PYTHIA e POWHEG. As seções de choque extraídas são:  $d\sigma_{c\bar{c}}/dy|_{y=0} = 1746 \pm 116$  (stat)  $\pm 249$  (sys)  $\pm 134$  (B.R.)  $\mu\text{b}$  e  $d\sigma_{b\bar{b}}/dy|_{y=0} = 74.9 \pm 5.7$  (stat)  $\pm 7.4$  (sys)  $\pm 4.5$  (B.R.)  $\mu\text{b}$  para o PYTHIA e  $d\sigma_{c\bar{c}}/dy|_{y=0} = 2378 \pm 160$  (stat)  $\pm 376$  (sys)  $\pm 190$  (B.R.)  $\mu\text{b}$  e  $d\sigma_{b\bar{b}}/dy|_{y=0} = 55.2 \pm 6.3$  (stat)  $\pm 3.6$  (sys)  $\pm 3.3$  (B.R.)  $\mu\text{b}$  para o POWHEG. Os resultados obtidos neste trabalho são consistentes com resultados anteriores e apresentam uma maior precisão devido ao aumento da estatística dos dados analisados ( $\approx 4x$ ). As diferenças de resultados entre os geradores estão relacionados à diferenças cinemáticas na produção dos pares de elétrons entre os geradores.

Neste trabalho também foram investigados os mecanismos de produção de quarks charm através de medidas de correlações angulares e momento transversal de dieletrons no IMR. As correlações angulares entre quarks pesados se mostraram profundamente correlacionadas com a distribuição de momento transversal do par, e um poder de discriminação similar entre os dois parâmetros foi encontrado. A análise sobre  $\Delta\varphi_{ee}$  e  $p_{T,ee}$  observou frações similares para *flavour creation*, *flavour excitation* e *gluon splitting* daqueles esperados pelo PYTHIA, considerando-se as incertezas.

**Palavras-chaves:** dieletron; quarks pesados; seção de choque; mecanismos de produção

---

# Abstract

Heavy-quarks, i.e. charm and beauty, are produced almost exclusively via initial hard scattering processes since their (bare) mass are significantly larger than the Quantum ChromoDynamics (QCD) scale parameter. This makes them unique probes for the characterization of collision systems, since they experience the whole evolution of the product of the collision. The study of the heavy-flavour production in inelastic proton-proton (pp) collisions is crucial to provide vacuum reference when studying heavy-ion collisions and its effects.

This work summarises the study of the heavy-flavour production from the measurements of dielectron pairs in pp collisions at  $\sqrt{s} = 13$  TeV using 2016 + 2017 + 2018 ALICE data. The heavy-flavour production is studied at midrapidity ( $|\eta| < 0.8$ ) as a function of the invariant mass, impact parameter, angular correlation and transverse momentum in the intermediate mass region (1.1 - 2.7 GeV/ $c^2$ - IMR). The heavy-flavour cross sections are extracted using 2D fits of the  $(m_{ee}, p_{T,ee})$  and  $(DCA_{xy}^{ee}, p_{T,ee})$  data, using Monte Carlo templates generated by PYTHIA and POWHEG generators. The extracted cross sections are:  $d\sigma_{c\bar{c}}/dy|_{y=0} = 1746 \pm 116$  (stat)  $\pm 249$  (sys)  $\pm 134$  (B.R.)  $\mu\text{b}$  and  $d\sigma_{b\bar{b}}/dy|_{y=0} = 74.9 \pm 5.7$  (stat)  $\pm 7.4$  (sys)  $\pm 4.5$  (B.R.)  $\mu\text{b}$  for PYTHIA generator and  $d\sigma_{c\bar{c}}/dy|_{y=0} = 2378 \pm 160$  (stat)  $\pm 376$  (sys)  $\pm 190$  (B.R.)  $\mu\text{b}$  and  $d\sigma_{b\bar{b}}/dy|_{y=0} = 55.2 \pm 6.3$  (stat)  $\pm 3.6$  (sys)  $\pm 3.3$  (B.R.)  $\mu\text{b}$  for POWHEG generator. The results obtained in this work are consistent with previous published results but present a higher precision due to the improved statistics ( $\approx 4x$ ) of the analysis. The difference between the generators are related to differences in the dielectron acceptances between the generators.

This work also investigated the production mechanisms of charm quarks by the measurements of the angular correlations and transverse momentum of dielectron pairs in the IMR. The angular correlations between heavy-flavour pairs are found to have a deep correlation with the pair transversal momentum, and a similar discrimination power between the two measurements are found. The analysis over  $\Delta\varphi_{ee}$  and  $p_{T,ee}$  observed similar fractions of flavour creation, flavour excitation and gluon splitting as predicted by PYTHIA, within uncertainties.

**Keywords:** dielectron, heavy quarks; cross section; production mechanisms;

---

# Acknowledgments

First of all, I thank God for the gift of life, for the opportunity and persistence given to carrying out this work, surrounding me with outstanding people.

I would like to express my deepest gratitude to my supervisor Alexandre Suaide for his endless support and mentoring to this PhD study. He always supported my initiatives and was always ready to give extraordinary ideas to solve analysis obstacles. He has always been an accessible person ready to help with any problem, from academic to personal, from technical to bureaucratic, at any time.

I would like to thank all of my colleagues from HEPIC, in special: Marcel Figueiredo, Cristiane Jahnke, Henrique Zanolli, Diógenes Domenicis, Antônio da Silva, Camila de Conti, Geovane Grossi, Milton Nogueira Júnior, Lucas Teixeira, Lucas de Arruda, Arthur Lopes, and Caio Prado, for all of the useful discussions and the fun. Special thanks to the professors Marcelo Munhoz, Marco Bregant, Hugo Luz and Tiago Fiorini. Thanks in special also to Marcel who helped me during the first research steps of my PhD.

I express my deepest thankfulness to my co-supervisor in Germany, Torsten Dahms, who helped to all of these studies happen. He always found time to look at the codes together and to discuss new ideas to solve problems - thanks for challenging me with the development of the  $DCA_{xy}^{ee}$  method! - and was always ready to help in anything he could. I would like to thank also Prof. Laura Fabbietti for receiving me in her group with a great welcome and help. I extend my gratitude to all of my colleagues at the research group of the Technische Universität München, in special to Ivan Vorobyev, Oton Vazquez Doce, Anisa Dashi and Lucas Cordova. Special thanks to Ivan Vorobyev who contributed in an invaluable way to the deepest parts of this study. Thanks also to Oton Vazquez Doce for helping to configure the production of the PYTHIA and POWHEG simulations.

I express my acknowledgments also to all of my colleagues from the Physics Analysis Group of the ALICE, in special to Michael Weber, Sebastian Scheidt, Raphaele Bailhache, Elisa Meninno and Daiki Sekihata, for the fruitful discussions and incalculable suggestions to improve this work. Special thanks to Michael Weber, for the deep involvement and analysis review of this work, as well as Sebastian Scheidt specially regarding the  $DCA_{xy}^{ee}$  analysis.

I thank my friends from São Paulo, Flávio, Renato, Heloise and Marina, for countless days and nights of chat and laughs, and for their friendship. A special thanks goes to

---

Marli, who became our "hearted-grandma" in São Paulo.

My deepest gratitude to my parents, Marcos Degenhardt and Erminia Schneider Degenhardt, for the unconditional love, patience and support during this time and all of my life. In the good and in the bad times, you always had my back. Thank you for the caring and cuddle, for the countless trips and concerns, for teaching that the greatest treasure is knowledge, and for allowed me to learn to fight while watching you never giving up, no matter what. All of this was only possible because of you. To my sister, Ämilie Degenhardt, for the friendship and laughs, and for always being supportive and caring, far way before the beginning of this PhD. I extend my acknowledgments to all of my family.

I can not find words to thank my wife Maximilia de Souza Degenhardt and what she means to me. Thank you for the love and affection, for the companionship and understanding, and for the continuous incentive and encouragement to life and to this work - I would not have gone this far without you. Thanks for making me to discover a new type of quark in you: a light and a beauty at the same time, making everything lighter and beauty. Thanks for the laughs, funny trips and for all of the time spent together, in charming cities, throughout nights awake or in a simple cup of coffe - I love you! I extend my gratitude to her parents, Maria de Lourdes Frazão and Ornélio de Souza, for all of their support, caring, understanding and love. I also thank Luciele de Souza and Diego Gheller for all of the good time spent together, the chats and growth, and for our precious nephews: Naiara, Theo and Helena.

This study was financed in part by the Coordenação de Aperfeiçoamento de Pessoal de Nível Superior - Brasil (CAPES) - Finance Code 001.

# Contents

<b>1</b>	<b>Introduction</b>	<b>1</b>
<b>2</b>	<b>Heavy-Flavour Production in Hadronic Collisions</b>	<b>5</b>
2.1	Introduction to the Quantum Chromodynamics . . . . .	5
2.2	Deconfined State of the Matter: the QGP . . . . .	7
2.3	Heavy-Flavour Production . . . . .	10
2.4	Heavy-Flavour Decays . . . . .	13
2.5	Dielectron Pairs . . . . .	16
2.6	Previous Experimental Measurements . . . . .	17
<b>3</b>	<b>Experimental Setup</b>	<b>23</b>
3.1	The Large Hadron Collider . . . . .	23
3.2	The ALICE Experiment . . . . .	24
3.3	Inner Tracking System . . . . .	25
3.4	Time Projection Chamber . . . . .	26
3.5	Time of Flight . . . . .	28
3.6	V0 . . . . .	30
<b>4</b>	<b>Data Analysis</b>	<b>33</b>
4.1	Data samples . . . . .	33
4.2	Event Selection . . . . .	34
4.3	Track Selection . . . . .	35
4.4	Electron Identification . . . . .	36
4.5	TPC and TOF post-calibration . . . . .	39
4.6	Pairing and Signal Extraction . . . . .	43
4.6.1	Invariant Mass Yield . . . . .	43
4.6.2	Signal Extraction . . . . .	43
4.6.3	$\Delta\eta$ $\Delta\varphi$ signal . . . . .	45
4.6.4	Dielectron Cross Section . . . . .	46
4.7	Systematic Uncertainties . . . . .	48

<b>5</b>	<b>Monte Carlo Analysis</b>	<b>51</b>
5.1	Pure Monte Carlo . . . . .	51
5.1.1	Produced samples . . . . .	51
5.1.2	Event and Track Selection . . . . .	52
5.1.3	Heavy-Flavour Electron Identification . . . . .	53
5.1.4	Pairing . . . . .	53
5.2	Reconstructed Monte Carlo . . . . .	54
5.2.1	Monte Carlo samples . . . . .	54
5.2.2	Event and Track Selection . . . . .	55
5.2.3	TPC and TOF post-calibration . . . . .	56
5.2.4	Smearing Procedure . . . . .	56
5.2.5	Single Electron Efficiency . . . . .	60
5.2.6	Pair Efficiency . . . . .	60
<b>6</b>	<b>Heavy-Flavour Cross Sections</b>	<b>63</b>
6.1	Invariant Mass Analysis . . . . .	63
6.1.1	Mass Efficiency . . . . .	64
6.1.2	Signal Extraction . . . . .	67
6.1.3	Systematic Uncertainties . . . . .	67
6.1.4	Monte Carlo Templates . . . . .	75
6.1.5	Results . . . . .	76
6.2	Impact Parameter Analysis . . . . .	80
6.2.1	DCA Efficiency . . . . .	80
6.2.2	Signal Extraction . . . . .	81
6.2.3	Systematic Uncertainties . . . . .	82
6.2.4	Monte Carlo Templates . . . . .	86
6.2.5	Results . . . . .	92
6.3	Chapter Summary . . . . .	97
<b>7</b>	<b>Heavy-Flavour Production Mechanisms</b>	<b>99</b>
7.1	$\Delta\varphi$ Analysis . . . . .	99
7.1.1	$\Delta\varphi$ Efficiency . . . . .	99
7.1.2	Signal Extraction . . . . .	101
7.1.3	Systematic Uncertainties . . . . .	101
7.1.4	Monte Carlo Templates . . . . .	103
7.1.5	Results . . . . .	111
7.2	$p_T$ Analysis . . . . .	116
7.2.1	$p_T$ Efficiency . . . . .	116
7.2.2	Signal Extraction . . . . .	117
7.2.3	Systematic Uncertainties . . . . .	119



7.2.4	Monte Carlo Templates . . . . .	120
7.2.5	Results . . . . .	120
7.3	Chapter Summary . . . . .	124
<b>8</b>	<b>Summary and Outlook</b>	<b>127</b>
<b>A</b>	<b>Kinematic Variables</b>	<b>129</b>
A.1	Kinematics . . . . .	129
A.2	ALICE Coordinates . . . . .	131
<b>B</b>	<b>Data Sets</b>	<b>133</b>
B.1	2016 Data . . . . .	133
B.2	2017 Data . . . . .	135
B.3	2018 Data . . . . .	137
<b>C</b>	<b>TPC and TOF Post-Calibration</b>	<b>141</b>
C.1	Data . . . . .	141
C.2	Monte Carlo . . . . .	142
<b>D</b>	<b><math>m_{ee}</math> Additional Fits</b>	<b>161</b>
<b>E</b>	<b><math>DCA_{xy}^{ee}</math> Additional Fits</b>	<b>169</b>
<b>F</b>	<b><math>\Delta\varphi_{ee}</math> Additional Fits</b>	<b>173</b>
	<b>Bibliography</b>	<b>177</b>



# List of Figures

1.1	Expected contributions to the dielectron mass spectrum . . . . .	3
1.2	Angular correlation between high- $p_T$ hadrons . . . . .	4
2.1	Standard Model for elementary particles . . . . .	6
2.2	Phase diagram of the nuclear matter . . . . .	8
2.3	Schematic figure of the system created in heavy-ion collisions . . . . .	9
2.4	Feynman diagrams of the heavy-flavour production . . . . .	11
2.5	Exploratory properties of heavy-flavour production mechanisms . . . . .	12
2.6	Discovery of the $J/\psi$ and $\Upsilon$ . . . . .	13
2.7	Invariant mass distributions of D mesons candidates . . . . .	14
2.8	Transversal momentum distributions of D mesons . . . . .	15
2.9	Semi-leptonic decay of heavy quarks . . . . .	15
2.10	Dielectron invariant mass yield compared to MC cocktail . . . . .	16
2.11	$c\bar{c}$ and $b\bar{b}$ cross sections extracted from dielectron mass and $p_T$ . . . . .	18
2.12	$c\bar{c}$ and $b\bar{b}$ cross sections as a function of $\sqrt{s}$ compared to FONLL . . . . .	19
2.13	Dielectron invariant mass yield in Pb–Pb collisions compared to cocktail . . . . .	20
2.14	Charm production mechanisms fitted to invariant mass data . . . . .	21
3.1	Schematic diagram of the ALICE experiment . . . . .	25
3.2	Schematic diagram of the ITS detector . . . . .	26
3.3	Energy loss distribution signal in the ITS as a function of the momentum . . . . .	26
3.4	Schematic example of the TPC detector . . . . .	27
3.5	Specific energy loss in the TPC as a function of the momentum . . . . .	28
3.6	Energy loss distribution in the TPC in pp and Pb–Pb collisions . . . . .	29
3.7	Schematic diagram of the TOF detector . . . . .	29
3.8	Time-of-flight particle distribution as a function of the momentum . . . . .	30
3.9	Front views of V0A and V0C scintillators . . . . .	31
3.10	Schematic view of the V0A and V0C positions . . . . .	31
4.1	$n\sigma_{TPC}^{ele}$ distribution of the PID cut schemes . . . . .	38
4.2	TPC electron distribution fit example . . . . .	40

4.3	Re-calibration maps of the TPC for 2016 . . . . .	41
4.4	Re-calibration maps of the TOF for 2016 . . . . .	42
4.5	Heavy-flavour $\Delta\eta$ $\Delta\varphi_{ee}$ signal subtraction and background estimation . . .	46
4.6	Heavy-flavour $\Delta\eta$ $\Delta\varphi_{ee}$ signal as a function of $p_{T,ee}$ . . . . .	47
5.1	Re-calibration maps of the TPC for 2016 MC . . . . .	57
5.2	Re-calibration maps of the TOF for 2016 MC . . . . .	58
5.3	Smearing resolution maps for MC generated parameters . . . . .	59
5.4	Smearing resolution maps for MC in different $p_T$ projections . . . . .	59
5.5	Number of reconstructed electrons and single efficiencies . . . . .	61
5.6	Single electron efficiency of $\eta$ and $\varphi$ . . . . .	61
6.1	Heavy-flavour $m_{ee}$ efficiencies for $p_{T,e} > 0.2$ GeV/ $c$ . . . . .	65
6.2	Heavy-flavour $m_{ee}$ efficiencies for $p_{T,e} > 0.4$ GeV/ $c$ . . . . .	66
6.3	$m_{ee}$ R-factor for $p_{T,e} > 0.2$ GeV/ $c$ . . . . .	68
6.4	$m_{ee}$ R-factor for $p_{T,e} > 0.4$ GeV/ $c$ . . . . .	68
6.5	$m_{ee}$ signal and background estimation for $p_{T,e} > 0.2$ GeV/ $c$ . . . . .	69
6.6	$m_{ee}$ signal and background estimation for $p_{T,e} > 0.4$ GeV/ $c$ . . . . .	69
6.7	$m_{ee}$ signal over background ratio for $p_{T,e} > 0.2$ GeV/ $c$ . . . . .	70
6.8	$m_{ee}$ signal over background ratio for $p_{T,e} > 0.4$ GeV/ $c$ . . . . .	70
6.9	Extracted $m_{ee}$ signals for systematic uncertainties for $p_{T,e} > 0.2$ GeV/ $c$ . .	71
6.10	Extracted $m_{ee}$ signals for systematic uncertainties for $p_{T,e} > 0.4$ GeV/ $c$ . .	71
6.11	Systematic uncertainties of $m_{ee}$ for $p_{T,e} > 0.2$ GeV/ $c$ . . . . .	72
6.12	Systematic uncertainties of $m_{ee}$ for $p_{T,e} > 0.4$ GeV/ $c$ . . . . .	72
6.13	Comparison of dielectron cross sections over the years as a function of the $m_{ee}$ for $p_{T,e} > 0.2$ GeV/ $c$ . . . . .	73
6.14	Comparison of dielectron cross sections over the years as a function of the $m_{ee}$ for $p_{T,e} > 0.4$ GeV/ $c$ . . . . .	74
6.15	Simulated $m_{ee}$ templates - PYTHIA . . . . .	75
6.16	Simulated $m_{ee}$ templates - POWHEG . . . . .	75
6.17	The dielectron cross section in pp collisions at 13 TeV as a function of $m_{ee}$ for $p_{T,e} > 0.2$ GeV/ $c$ compared to PYTHIA templates . . . . .	77
6.18	The dielectron cross section in pp collisions at 13 TeV as a function of $m_{ee}$ for $p_{T,e} > 0.4$ GeV/ $c$ compared to PYTHIA templates . . . . .	77
6.19	The dielectron cross section in pp collisions at 13 TeV as a function of $m_{ee}$ for $p_{T,e} > 0.2$ GeV/ $c$ compared to POWHEG templates . . . . .	78
6.20	The dielectron cross section in pp collisions at 13 TeV as a function of $m_{ee}$ for $p_{T,e} > 0.4$ GeV/ $c$ compared to POWHEG templates . . . . .	78
6.21	Heavy-flavour production cross sections from $m_{ee}$ fits using PYTHIA . . . .	79
6.22	Heavy-flavour production cross sections from $m_{ee}$ fits using POWHEG . . . .	79

6.23	DCA <sub>xy</sub> <sup>ee</sup> R-factor for $p_{T,e} > 0.4$ GeV/ $c$ . . . . .	81
6.24	DCA <sub>xy</sub> <sup>ee</sup> signal and background estimation for $p_{T,e} > 0.4$ GeV/ $c$ . . . . .	83
6.25	DCA <sub>xy</sub> <sup>ee</sup> signal over background ratio for $p_{T,e} > 0.4$ GeV/ $c$ . . . . .	83
6.26	Extracted DCA <sub>xy</sub> <sup>ee</sup> signals for systematic uncertainties for $p_{T,e} > 0.4$ GeV/ $c$ . . . . .	84
6.27	Systematic uncertainties of DCA <sub>xy</sub> <sup>ee</sup> for $p_{T,e} > 0.4$ GeV/ $c$ . . . . .	84
6.28	Comparison of dielectron cross sections over the years as a function of the DCA <sub>xy</sub> <sup>ee</sup> . . . . .	85
6.29	Distance of closest approach scheme . . . . .	87
6.30	Distance of closest approach calculation . . . . .	88
6.31	DCA <sub>xy</sub> <sup>e</sup> smearing resolutions . . . . .	89
6.32	Simulated DCA <sub>xy</sub> <sup>ee</sup> templates - PYTHIA . . . . .	90
6.33	Simulated DCA <sub>xy</sub> <sup>ee</sup> templates - POWHEG . . . . .	90
6.34	Charm DCA <sub>xy</sub> <sup>ee</sup> templates correction . . . . .	92
6.35	Simulated DCA <sub>xy</sub> <sup>ee</sup> templates QA . . . . .	93
6.36	The dielectron cross section in pp collisions at 13 TeV as a function of DCA <sub>xy</sub> <sup>ee</sup> for $p_{T,e} > 0.4$ GeV/ $c$ compared to PYTHIA templates . . . . .	94
6.37	The dielectron cross section in pp collisions at 13 TeV as a function of DCA <sub>xy</sub> <sup>ee</sup> for $p_{T,e} > 0.4$ GeV/ $c$ compared to POWHEG templates . . . . .	94
6.38	Heavy-flavour production cross sections from $m_{ee}$ and DCA <sub>xy</sub> <sup>ee</sup> fits using PYTHIA . . . . .	96
6.39	Heavy-flavour production cross sections from $m_{ee}$ and DCA <sub>xy</sub> <sup>ee</sup> fits using POWHEG . . . . .	96
7.1	Heavy-flavour $\Delta\varphi_{ee}$ efficiencies . . . . .	100
7.2	$\Delta\varphi_{ee}$ R-factor . . . . .	101
7.3	$\Delta\varphi_{ee}$ signal and background estimation . . . . .	102
7.4	$\Delta\varphi_{ee}$ signal over background ratio . . . . .	102
7.5	Extracted $\Delta\varphi_{ee}$ signals for systematic uncertainties . . . . .	104
7.6	Systematic uncertainties of $\Delta\varphi_{ee}$ . . . . .	104
7.7	Comparison of dielectron cross sections over the years as a function of the $\Delta\varphi_{ee}$ . . . . .	105
7.8	Heavy-flavour $\Delta\varphi_{ee}$ inheritance . . . . .	105
7.9	$\Delta\varphi_{ee}$ of different production mechanisms of heavy flavour . . . . .	106
7.10	$\Delta\varphi_{ee}$ and $p_{T,ee}$ of different production mechanisms of heavy flavour . . . . .	107
7.11	$\Delta\varphi_{ee}$ and $p_{T,ee}$ of different production mechanisms of heavy flavour - no cuts	108
7.12	$\Delta\varphi_{D\bar{D}}$ and $p_{T,D\bar{D}}$ of different production mechanisms of heavy flavour . . . . .	109
7.13	$\Delta\varphi_{c\bar{c}}$ and $p_{T,c\bar{c}}$ of different production mechanisms of heavy flavour . . . . .	109
7.14	Simulated $\Delta\varphi_{ee}$ templates - PYTHIA . . . . .	110
7.15	Simulated $\Delta\varphi_{ee}$ templates - POWHEG . . . . .	110

7.16	The dielectron cross section in pp collisions at 13 TeV as a function of $\Delta\varphi_{ee}$ compared to heavy-flavour PYTHIA templates . . . . .	112
7.17	The dielectron cross section in pp collisions at 13 TeV as a function of $\Delta\varphi_{ee}$ compared to heavy-flavour POWHEG templates . . . . .	112
7.18	The dielectron cross section in pp collisions at 13 TeV as a function of $\Delta\varphi_{ee}$ compared to heavy-flavour + $J/\psi$ PYTHIA templates . . . . .	113
7.19	The dielectron cross section in pp collisions at 13 TeV as a function of $\Delta\varphi_{ee}$ compared to heavy-flavour + $J/\psi$ POWHEG templates . . . . .	113
7.20	The dielectron cross section in pp collisions at 13 TeV as a function of $\Delta\varphi_{ee}$ compared to heavy-flavour processes + $J/\psi$ PYTHIA templates . . . . .	114
7.21	The dielectron cross section in pp collisions at 13 TeV as a function of $\Delta\varphi_{ee}$ compared to charm processes + $J/\psi$ (beauty fixed) PYTHIA templates . . . . .	115
7.22	The dielectron cross section in pp collisions at 13 TeV as a function of $\Delta\varphi_{ee}$ (1D) compared to PYTHIA templates . . . . .	116
7.23	The dielectron cross section in pp collisions at 13 TeV as a function of $\Delta\varphi_{ee}$ (1D) compared to PYTHIA templates (beauty fixed) . . . . .	117
7.24	Heavy-flavour $p_{T,ee}$ efficiencies . . . . .	118
7.25	$p_{T,ee}$ R-factor . . . . .	118
7.26	$p_{T,ee}$ signal and background estimation and their ratio . . . . .	119
7.27	Extracted $p_{T,ee}$ signals and the calculated systematic uncertainties . . . . .	119
7.28	Comparison of dielectron cross sections over the years as a function of the $p_{T,ee}$ . . . . .	120
7.29	Simulated $p_{T,ee}$ templates - PYTHIA . . . . .	121
7.30	Simulated $p_{T,ee}$ templates - POWHEG . . . . .	121
7.31	The dielectron cross section in pp collisions at 13 TeV as a function of $p_{T,ee}$ compared to PYTHIA templates . . . . .	122
7.32	The dielectron cross section in pp collisions at 13 TeV as a function of $p_{T,ee}$ compared to POWHEG templates . . . . .	122
7.33	The dielectron cross section in pp collisions at 13 TeV as a function of $p_{T,ee}$ compared to PYTHIA templates - processes fit . . . . .	123
A.1	Schematic view of the coordinate system within ALICE experiment . . . . .	131
C.1	TPC mean re-calibration maps for 2016 . . . . .	142
C.2	TPC mean re-calibration maps for 2017 . . . . .	143
C.3	TPC mean re-calibration maps for 2018 . . . . .	144
C.4	TPC width re-calibration maps for 2016 . . . . .	145
C.5	TPC width re-calibration maps for 2017 . . . . .	146
C.6	TPC width re-calibration maps for 2018 . . . . .	147
C.7	TOF mean re-calibration maps for 2016 . . . . .	148

C.8	TOF mean re-calibration maps for 2017 . . . . .	149
C.9	TOF mean re-calibration maps for 2018 . . . . .	150
C.10	TOF width re-calibration maps for 2016 . . . . .	151
C.11	TOF width re-calibration maps for 2017 . . . . .	152
C.12	TOF width re-calibration maps for 2018 . . . . .	153
C.13	Re-calibrated TPC and TOF for 2016 . . . . .	154
C.14	Re-calibrated TPC and TOF for 2017 . . . . .	155
C.15	Re-calibrated TPC and TOF for 2018 . . . . .	156
C.16	TPC and TOF re-calibration MC maps for 2016 . . . . .	157
C.17	TPC and TOF re-calibration MC maps for 2017 . . . . .	157
C.18	TPC and TOF re-calibration MC maps for 2018 . . . . .	158
C.19	Re-calibrated MC TPC and TOF for 2016 . . . . .	158
C.20	Re-calibrated MC TPC and TOF for 2017 . . . . .	159
C.21	Re-calibrated MC TPC and TOF for 2018 . . . . .	159
D.1	The dielectron cross section in pp collisions at 13 TeV as a function of $m_{ee}$ for $p_{T,e} > 0.2$ GeV/ $c$ compared to PYTHIA templates using 2016 data . . .	162
D.2	The dielectron cross section in pp collisions at 13 TeV as a function of $m_{ee}$ for $p_{T,e} > 0.4$ GeV/ $c$ compared to PYTHIA templates using 2016 data . . .	162
D.3	The dielectron cross section in pp collisions at 13 TeV as a function of $m_{ee}$ for $p_{T,e} > 0.2$ GeV/ $c$ compared to POWHEG templates using 2016 data . .	163
D.4	The dielectron cross section in pp collisions at 13 TeV as a function of $m_{ee}$ for $p_{T,e} > 0.4$ GeV/ $c$ compared to POWHEG templates using 2016 data . .	163
D.5	The dielectron cross section in pp collisions at 13 TeV as a function of $m_{ee}$ for $p_{T,e} > 0.2$ GeV/ $c$ compared to PYTHIA templates using 2017 data . . .	164
D.6	The dielectron cross section in pp collisions at 13 TeV as a function of $m_{ee}$ for $p_{T,e} > 0.4$ GeV/ $c$ compared to PYTHIA templates using 2017 data . . .	164
D.7	The dielectron cross section in pp collisions at 13 TeV as a function of $m_{ee}$ for $p_{T,e} > 0.2$ GeV/ $c$ compared to POWHEG templates using 2017 data . .	165
D.8	The dielectron cross section in pp collisions at 13 TeV as a function of $m_{ee}$ for $p_{T,e} > 0.4$ GeV/ $c$ compared to POWHEG templates using 2017 data . .	165
D.9	The dielectron cross section in pp collisions at 13 TeV as a function of $m_{ee}$ for $p_{T,e} > 0.2$ GeV/ $c$ compared to PYTHIA templates using 2018 data . . .	166
D.10	The dielectron cross section in pp collisions at 13 TeV as a function of $m_{ee}$ for $p_{T,e} > 0.4$ GeV/ $c$ compared to PYTHIA templates using 2018 data . . .	166
D.11	The dielectron cross section in pp collisions at 13 TeV as a function of $m_{ee}$ for $p_{T,e} > 0.2$ GeV/ $c$ compared to POWHEG templates using 2018 data . .	167
D.12	The dielectron cross section in pp collisions at 13 TeV as a function of $m_{ee}$ for $p_{T,e} > 0.4$ GeV/ $c$ compared to POWHEG templates using 2018 data . .	167

E.1	The dielectron cross section in pp collisions at 13 TeV as a function of $DCA_{xy}^{ee}$ compared to PYTHIA templates using 2016 data . . . . .	170
E.2	The dielectron cross section in pp collisions at 13 TeV as a function of $DCA_{xy}^{ee}$ compared to POWHEG templates using 2016 data . . . . .	170
E.3	The dielectron cross section in pp collisions at 13 TeV as a function of $DCA_{xy}^{ee}$ compared to PYTHIA templates using 2017 data . . . . .	171
E.4	The dielectron cross section in pp collisions at 13 TeV as a function of $DCA_{xy}^{ee}$ compared to POWHEG templates using 2017 data . . . . .	171
E.5	The dielectron cross section in pp collisions at 13 TeV as a function of $DCA_{xy}^{ee}$ compared to PYTHIA templates using 2018 data . . . . .	172
E.6	The dielectron cross section in pp collisions at 13 TeV as a function of $DCA_{xy}^{ee}$ compared to POWHEG templates using 2018 data . . . . .	172
F.1	The dielectron cross section in pp collisions at 13 TeV as a function of $\Delta\varphi_{ee}$ compared to heavy-flavour processes + $J/\psi$ PYTHIA templates using 2016 data . . . . .	174
F.2	The dielectron cross section in pp collisions at 13 TeV as a function of $\Delta\varphi_{ee}$ compared to heavy-flavour processes + $J/\psi$ PYTHIA templates using 2017 data . . . . .	174
F.3	The dielectron cross section in pp collisions at 13 TeV as a function of $\Delta\varphi_{ee}$ compared to heavy-flavour processes + $J/\psi$ PYTHIA templates using 2018 data . . . . .	175



# List of Tables

4.1	Data-taking years and periods used in the analyses . . . . .	34
4.2	Track requirements . . . . .	35
4.3	Electron identification scheme . . . . .	37
4.4	Purity of the PID scheme used . . . . .	39
4.5	Electron identification variations applied for systematic uncertainty study .	49
4.6	Track cut variations applied for systematic uncertainty study . . . . .	49
5.1	Number of MC produced events . . . . .	52
5.2	Monte Carlo samples used in the analyses . . . . .	55
6.1	Charmed hadron fractions and decay length . . . . .	91
6.2	Heavy-flavour production cross sections extracted in this thesis . . . . .	95



# 1 Introduction

The main purpose of relativistic heavy-ion collisions is to study and characterize the properties of the Quark Gluon Plasma (QGP). According to the Quantum Chromodynamics theory (QCD) [1, 2, 3], the field theory that describes the strong interaction, it would be expected to happen a phase transition between the hadronic matter (confined state) to a deconfined state of matter, the QGP [4, 5, 6, 7], at sufficiently high temperatures or baryon densities.

During the last decades, several measurements from different heavy-ion experiments provided indications that the QGP is produced in heavy-ion collisions at sufficiently high energies. On this matter, accelerators such as the Relativistic Heavy-Ion Collider (RHIC)[8] built at the Brookhaven Nacional Laboratory (BNL) in New York and starting to operate in 2000, and the Large Hadron Collisor (LHC)[9], located at the French/Swiss border and in operation since 2008, stand out. At the STAR experiment (Solenoidal Tracker at RHIC)[10], it is possible to study collisions of Au nuclei up to 200 GeV per nucleon pair in the center of mass reference frame. On the other hand, in the ALICE experiment (A Large Ion Collider Experiment) [11, 12, 13, 14], at the LHC, it is possible to study the production of collisions up to 13 TeV per nucleon pairs, making the LHC to explore regions of particle energies and densities significantly beyond those achievable at RHIC.

One between the vast interests in the understanding and characterization of the QGP lays in the fact that the Universe in its first fractions of seconds after the Big Bang would be in a similar state of the QGP. For this reason, the comprehension of the QGP and its evolution is also of interest to the cosmology, as this knowledge would also help to describe the primordial universe and its evolution.

It is also interesting to study not only heavy-ion collisions but also proton-proton (pp) and proton-lead (p-Pb) collisions, since these systems can be used as reference systems where it should not occur the formation of the QGP, in contrast to the Pb-Pb collisions. In pp collisions we can extract a vaccum reference to both p-Pb and Pb-Pb collisions, while in p-Pb, for example, the Cold Nuclear Matter effects (CNM) can also be studied. The CNM effects modify the particle production and even the proper dynamic of the initial state of the system and could be misinterpreted as properties of the created medium. Several similar behaviors found in heavy-ion collisions have been also observed in pp

collisions, attracting even more interest to this collision system, such as collective effects [15, 16, 17].

To the characterization of the QGP, heavy quarks, such as charm and beauty, are extremely convenient since they are particles predominantly produced through initial hard scattering processes between partons, which happen in the initial moments of the collision. This makes heavy quarks excellent and unique probes of the system created in the collision, since they experience the whole evolution of the system.

In face of all of the possible measurements, this work is deeply focused in the heavy-flavour production, which can also be well used to probe perturbative QCD calculations, to study the CNM and QGP, and also to provide useful information to event generators. On this matter, distinct tools to study these properties are the electromagnetic probes, such as photons or dilepton pairs ( $l^+l^- = e^+e^-$  or  $\mu^+\mu^-$ ). The reason behind the usage of electromagnetic probes in this kind of study is the fact that once they are created they carry all of their information to the detectors without being affected by strong final-state interactions with the medium. Dilepton pairs are a rich source of physical information since they are produced during all stages of the collisions by a great number of different sources, and the invariant mass of the pair is greater the earlier they were produced. The expected contributions to the dielectron mass spectrum in pp collisions at  $\sqrt{s} = 13$  TeV is shown in Figure 1.1. The intermediate mass region of the dielectron invariant mass can be used to extract the heavy-flavour production cross section, since it provides a clear window with predominant heavy-flavour contribution. This process has already been used before [18, 19, 20] to extract charm and beauty cross sections. However, the ALICE published results regarding pp collisions at  $\sqrt{s} = 13$  TeV used only 2016 data-taken year, and a more precise measurement could be achieved by using the full Run-2 available data. More than this, a better separation between the heavy-flavour sources (charm and beauty) can be achieved by an analysis of the impact parameter, since it presents a better discrimination power.

The first part of this work will be focused on the extraction of more precise measurements of the heavy-flavour production cross sections in pp collisions at  $\sqrt{s} = 13$  TeV using the invariant mass method using 2016, 2017 and 2018 ALICE data-taking years followed by the development of a new method to study the impact parameter, both to extract and validate the obtained results. The impact parameter in this case is related to the distance to the primary vertex that a particle was created. A complementary analysis between the two techniques had already been carried out using pp collisions at  $\sqrt{s} = 7$  TeV [18] and they were found to be complementary. The new approach developed in this work focuses in the calculation of the impact parameter directly from the generated simulations, instead of using the reconstructed simulations by using softwares such as GEANT. This would allow us to perform faster and more effective simulations to compare to data than what is available nowadays.

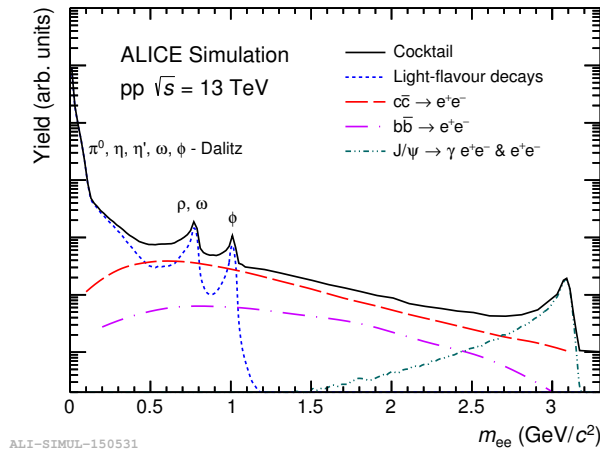


Figure 1.1: Expected contributions to the dielectron mass spectrum from hadron decays in pp collisions at  $\sqrt{s} = 13$  TeV.

The second part of this work is focused in the study of the different heavy-flavour production mechanisms through the the angular correlations measurements between heavy-flavour electrons (HFe) and by the transverse momentum distribution compared to predictions from PYTHIA and POWHEG, also in pp collisions at  $\sqrt{s} = 13$  TeV. The 2-particle angular correlation function is defined as the difference distribution in the azimuthal angle and pseudorapidity between a reference (trigger) particle and its associate and this kind of measurement has been vastly used to study a large number of different properties [21, 22, 23, 24, 25, 26, 27, 28, 29].

One of the highlighted examples of angular correlation analyses with a huge impact was obtained and published by the STAR collaboration [21, 22, 23]. The angular distribution between hadrons is showed in Figure 1.2, where the distribution along  $\Delta\varphi = 0$  is dominated by the near-side jet, which is related to the correlation between particles produced in the fragmentation of the same parton (which is one of the partons created in the initial hard scattering). The structure around  $\Delta\varphi = \pi$  can be understood as a back-to-back pair production and correlated to the away-side jet, being strongly sensitive to the parton-medium interaction. One of the first evidences of the QGP was the suppression of the away-side jet in relativistic heavy-ion collisions (Au–Au) [21]. A suppression in the away-side correlation was not observed in pp and d–Au collisions, and the jet suppression is explained as happening due to the medium created specifically in Au–Au collisions. The explanation is that one of the partons created in the initial hard scattering (and that creates the away-side jet) suffers enough scattering by the medium created in the collision to be extinguished [21].

More studies have been also carried out using the angular correlations between electron and charged particles [30, 31, 32, 33, 34], focusing mainly in the usage of heavy-flavour electrons as triggers. The particle production and production mechanisms of particles have also been studied using the angular correlation between same particles and the par-

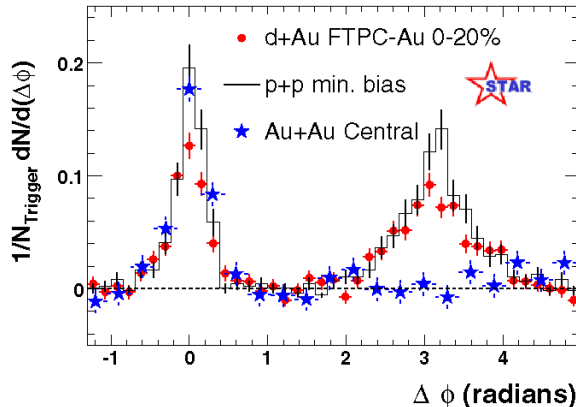


Figure 1.2: Angular correlation between high- $p_T$  hadrons in pp, d–Au e Au–Au collisions at 200 GeV. [21, 22, 23]

ticle production is expected to present different angular distributions depending on the production mechanism that generated that particle, and has already been used for a variety of particles [35, 36, 37, 38, 39, 40, 41]. This points that the angular correlations between heavy-flavour electrons would allow us to disentangle the production mechanism that generated the heavy-flavour pair [42, 43, 44, 45, 46, 47, 48]. These studies predict that Gluon Splitting processes would produce pairs with a small angle between them. On the other hand, Gluon Fusion and Flavour Creation processes would produce more back-to-back pairs while Flavour Excitation processes would present less azimuthal preferences. All of these make this a very interesting subject, to study the possibility to disentangle the heavy-flavour production mechanisms through the measurements of the angular correlation distribution between heavy-flavour electrons, extracting their fractions and comparing to the predictions from simulations. This work presents the first measurement of the angular correlation between heavy-flavour electrons in pp collisions at  $\sqrt{s} = 13$  TeV to study the heavy-flavour production mechanisms.

Moreover, in the future, these measurements may allow us to study differences in the heavy-flavour production in each of the colliding systems (pp, p–Pb and Pb–Pb), as well as how the medium presented in each colliding system modify the production mechanisms fractions.

This thesis is organized as the following: Chapter 2 presents a short theoretical description of the heavy-flavour production and the physics involved, such as the QCD theory and QGP formation. In Chapter 3 the ALICE apparatus is shortly discussed together with the detectors used in the analyses. The data analysis details are discussed in Chapter 4 while the MC analysis are presented in Chapter 5. Chapter 6 presents the results obtained through the invariant mass and impact parameter analyses: the charm and beauty production cross sections, while Chapter 7 shows the results of the study of the charm production mechanisms obtained through the analyses of the angular correlations and transverse momentum. The conclusions of this thesis are summarized in Chapter 8.

# 2 Heavy-Flavour Production in Hadronic Collisions

It is well established that in the most elementary level the matter is constituted by fundamental particles, organized within some groups, being them the quarks, leptons and bosons. [49, 50]. Within all of these elementary particles there are four fundamental interaction forces: gravitational, electromagnetic, weak and strong. The interaction itself, in the point of view of particle physics, is understood as the exchange between a third particle, known as the quantum of the field involved in the interaction. Each of the interactions are related to a gauge symmetry mediated by the gauge bosons. A scheme of the particles and their mediators following the Standard Model (SM) for elementary particles is shown in Figure 2.1. Photons, for example, are the quantum of the electromagnetic interaction, so this interaction is understood as the photon exchange between charged particles. In the weak interaction there are the  $W^\pm$  and the  $Z$  bosons as mediators. In the strong interaction, analogous to the photon, there are the gluons, which are the exchange particles between coloured charged particles. Each fundamental interaction has a Quantum Field Theory (QFT) that describes the dynamics of the elementary particles. The QFT of the electromagnetic force is the Quantum ElectroDynamics (QED), while the strong interaction is described by the Quantum ChromoDynamics (QCD).

This chapter will briefly describe the QCD theory (Section 2.1), what is expected to happen to the matter at sufficiently high temperatures (Section 2.2) and effects that may modify the production of particles. Afterwards, the Heavy-Flavour production (Section 2.3) will be presented, as well as possible measurements through them (Section 2.4). Finally, the dielectron production spectrum will be discussed for the understanding of the measurements (Section 2.5) with previous experimental results (Section 2.6).

## 2.1 Introduction to the Quantum Chromodynamics

The QCD describes the interaction between particles containing color charge, i.e., quarks and gluons, and their possible colors are represented by the red, green and blue. As gluons also carry a color charge (differently than photons in the QED that does not

Three Generations of Matter (Fermions)					
	I	II	III		
mass →	2.4 MeV/c <sup>2</sup>	1.27 GeV/c <sup>2</sup>	171.2 GeV/c <sup>2</sup>	0	±125 GeV/c <sup>2</sup>
charge →	2/3	2/3	2/3	0	0
spin →	1/2	1/2	1/2	1	0
name →	<b>u</b> up	<b>c</b> charm	<b>t</b> top	<b>γ</b> photon	<b>H</b> Higgs-boson
Quarks	4.8 MeV/c <sup>2</sup>	104 MeV/c <sup>2</sup>	4.2 GeV/c <sup>2</sup>	0	
	-1/3	-1/3	-1/3	0	
	1/2	1/2	1/2	1	
	<b>d</b> down	<b>s</b> strange	<b>b</b> bottom	<b>g</b> gluon	
Leptons	<2.2 eV/c <sup>2</sup>	<0.17 MeV/c <sup>2</sup>	<15.5 MeV/c <sup>2</sup>	91.2 GeV/c <sup>2</sup>	
	0	0	0	0	
	1/2	1/2	1/2	1	
	<b>ν<sub>e</sub></b> electron neutrino	<b>ν<sub>μ</sub></b> muon neutrino	<b>ν<sub>τ</sub></b> tau neutrino	<b>Z<sup>0</sup></b> weak force	Bosons (Forces)
0.511 MeV/c <sup>2</sup>	105.7 MeV/c <sup>2</sup>	1.777 GeV/c <sup>2</sup>	80.4 GeV/c <sup>2</sup>		
	-1	-1	-1	±1	
	1/2	1/2	1/2	1	
	<b>e</b> electron	<b>μ</b> muon	<b>τ</b> tau	<b>W<sup>±</sup></b> weak force	

Figure 2.1: Standard Model for elementary particles: quarks, leptons and bosons.

carry electric charge), they can interact between themselves, leading to more complicated Feynman diagrams containing not only quark-gluon vertices but also gluon-gluon.

Another fundamental difference between QCD and QED is the dimension of the coupling constant. Each vertex in the Feynman diagram in the QED introduces a  $\alpha \approx \frac{1}{137}$  factor, and as small as this value is it indicates that it is only necessary to consider diagrams with a small number of vertices [50]. In the case of the QED, for high energies (or small distances), the coupling constant is higher, i.e., the interaction is stronger for smaller distances. It can be said, equivalently, that for shorter distances the electric charge is greater, and the reason to this effect is that for short distances the screening effect of the polarized vacuum is smaller. In the QCD, on the other hand, and in sufficiently high energies (or short distances),  $\alpha_S$  asymptotically decreases to nil. This means that for sufficiently short distances  $\alpha_S$  becomes so small that it can be treated perturbatively, as it is the case of QED. This QCD aspect is known as Asymptotic Freedom [5, 6], and can be understood as consequence of an anti-screening effect due to the gluon interaction. This way, gluons virtually created in the vacuum around a color charge increase the intensity of the color of this charge. The coupling constant in the QCD is [50]:

$$\alpha_S(Q^2) \approx \frac{12\pi}{(11n - 2f)\ln(Q^2/\Lambda_{QCD}^2)} \quad (2.1)$$

Where  $\Lambda_{QCD} \approx 200$  MeV is known as QCD scale and defines a intensity reference for the strong interaction,  $n$  is the number of color charges (3 at the Standard Model) and



$f$  is the number of quark flavours (6 at the Standard Model). Other interesting aspect of the strong interaction is that particles with color charge can not be observed alone. In other words, they must always be confined in hadrons producing a colorless state, or "white" (sum of the colors), and this property is known as confinement [50].

It becomes perceptible in Equation 2.1 the separation of two regimes that are characterized by the transferred momentum in the interactions. Hard processes are characterized by high transferred momentum, i.e.,  $Q \gg \Lambda_{QCD}$ . In these cases, the coupling constant becomes  $\alpha_s < 1$  and only the simpler Feynman diagrams (with smaller number of vertices) need to be considered in the calculations, depending on the necessary precision [49, 50]. This regime is also known as perturbative QCD (pQCD). On the other hand, the soft regime is characterized by processes with small energy scales ( $Q \leq \Lambda_{QCD}$ ). In these cases, analytical calculations of the QCD are not possible anymore, since more complicated Feynman diagrams strongly contribute to the production cross section. Presently, the only way to provide prediction of the soft regime is through a technique known as Lattice QCD, in which the calculations are done numerically in a space-time discrete lattice using Monte Carlo methods.

## 2.2 Deconfined State of the Matter: the QGP

The QCD theory normally describe the matter in which the quarks are strongly bounded within themselves via strong force. However, the asymptotic freedom predicts that at sufficiently high temperatures the quarks may exist in a deconfined state. The study of the matter in extreme conditions has increased rapidly as a research field. The phase diagram of the QCD is still precisely unknown, but a schematic estimate is shown in Figure 2.2. In sufficiently high temperatures/densities the system has a transition to a deconfined state, the QGP. A simplified model to the explanation of the QGP is the bag model [51, 52], where the hadrons are treated as bags of massless quarks that do not interact between themselves. The confinement would be the consequence between the internal and external pressures of the bag. The condition to a deconfined phase is characterized by a temperature in which the internal and external pressures are not balanced anymore, and there is an abrupt change in the density of the system, transitioning to an ideal gas of quarks and gluons.

A precise description of the thermodynamic properties of the QGP is provided by lattice QCD. From the Stefan-Boltzmann law, the ratio between the energy density by the fourth power of the temperature is a constant proportional to the degrees of freedom (d.o.f) of the system ( $\epsilon/T^4 \propto N_{d.o.f}$ ). This way, after a transition to a deconfined state the degrees of freedom of the system should increase including the color and the flavour. From the calculations, for a null baryonic density it is not observed an abrupt transition but a soft transition between the phases [53]. One of the main aspects that is currently

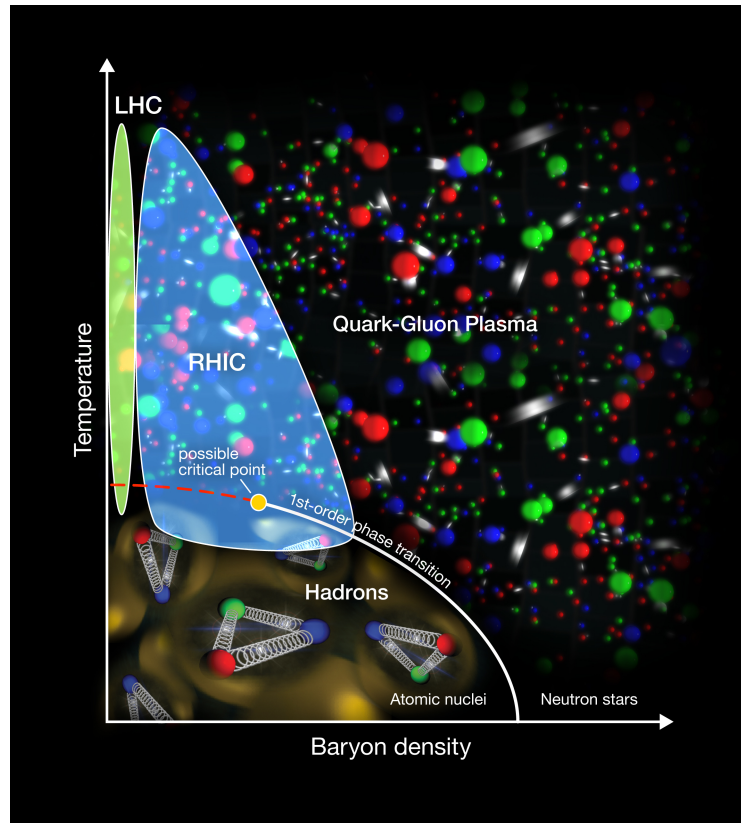


Figure 2.2: Phase diagram of the nuclear matter - Courtesy of Brookhaven National Laboratory.

been discussed is in the nature of the phase transition and the existence of a critical point that separates the transition of a first/second order from a cross-over transition. This can be visualized in Figure 2.2, where the dashed red line represents the cross-over phase transition, the continuous white line represents the first/second order transition and the yellow circle the critical point that separates the nature of the transitions.

Inside the lab, the QGP properties are investigated through the heavy-ion collisions. The space-time evolution of the system, after a relativistic collision between heavy-ion is shown in Figure 2.3. Soon after the collision there is a pre-equilibrium state with the production of particles, where the system has not achieved the thermal equilibrium yet. After a given time, the medium reaches the thermal equilibrium and, at sufficiently high energy densities, it is expected this medium to be in a QGP phase. At this point, global properties (state equations) can be estimated by lattice QCD and by phenomenological models (using characteristics such as volume, temperature, viscosity, within others). Moreover, the evolution of this medium can be described by hydrodynamical models that treat the medium as an expanding fluid [54]. As the system expands and consequently cools, there is a transition from the deconfined state to a hadronic gas. Afterwards, the hadronic system reaches a chemical freeze-out, where the inelastic collisions stop and the production of hadrons is already performed. At this time, the medium can be described

by thermal-statistical models [54].

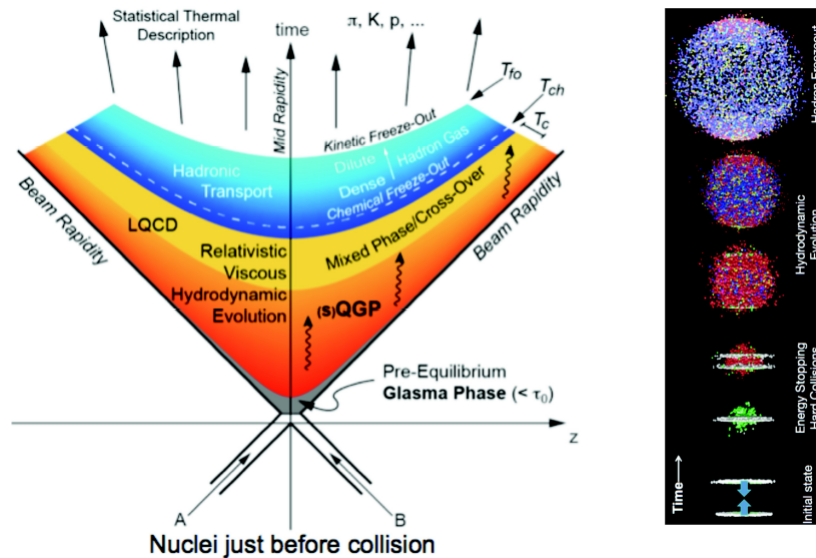


Figure 2.3: Schematic figure of the evolution of the system created in heavy-ion collisions. The different stages of the collision are specified at the right side while theoretical tools to study such stages are described at the left side. [55]

In the last stage, called as thermal-kinetic freeze-out the elastic collisions are also extinguished, happening when the typical mean free path of the system is higher than the inverse rate of interactions and the system behaves as an ideal hadronic gas that does not interact. These hadrons can be measured by detectors positioned around the interaction point.

However, it is also well known that Pb–Pb collisions present not only modifications related to the QGP but also from effects of the Cold Nuclear Matter (CNM), related to the nuclear medium. These effects will be present any time that a heavy-ion participate of the collision, such as in p–A (proton–nucleus), d–A (deuteron–nucleus) and A–A (nucleus–nucleus) collisions. To perform a good characterization of the QGP it is firstly important to separate the CNM effects of the initial state from those which are really due to the QGP created in the final state of A–A collisions. These effects can be studied in p–A and d–A collisions, where it should not be observed QGP effects but CNM only. Within many factors, these effects can modify the particle production.

One of these effects, for example, is known as Cronin Enhancement and consists in the increasing of the hadron production in p–A collisions when compared to pp, scaled by the number of binary collisions. This, in parts, can happen because of the energy loss in the initial state when there is an atomic nucleus involved in the collision. Before the partonic hard scattering processes, some partons may lose a fraction of their energy as a result of multiple scattering within the nucleus. Another known effect is the Shadowing, where the partonic density in the bounded nucleons is small when compared to free nucleons, and this "shadowing" can be explained by the fact that the nucleons in the surface of the

ion obfuscate the internal nucleons. Moreover, there are also the gluon saturation and the color glass condensate (CGC)[56], that occur at high energies and small transferred momentum.

## 2.3 Heavy-Flavour Production

The choice in the usage of heavy quarks, i.e., charm and beauty quarks, to the study of the medium lays in the fact that the heavy quarks are produced in the early stages of the collisions, in the initial hard scattering processes. Hence, they experience all of the formation created in the collision, since the pre-equilibrium phase up to the final stages. In comparison, for example, the light-flavours can be created by many different sources, as valence quarks from the nuclei in the collision, from the initial hard scattering, thermal production in the medium and other ways. This way, the information carried by light quarks may become ambiguous, since they can also be produced in different times after the initial process of the collision.

The heavy-flavour production can be calculated through pQCD calculations. The differential cross section can be described as an expansion in powers of the  $\alpha_S$ , as shown in Equation 2.2 [57, 58, 59], where  $\mu_{F,R}$  are the typical scales of the fundamental processes and are typically taken as  $\mu_F = \mu_R = m_Q = \sqrt{m_q^2 + p_T^2}$ , the transversal mass of the heavy quark [58, 59].

$$\frac{d\sigma}{dp_T^2} = \alpha_S^2(\mu_F) \sum_{k=0}^{\infty} C_k(m_Q) \alpha_S^k(\mu_F) \sum_{l=0}^k c_{kl} \log^l \left( \frac{\mu_R}{m_Q} \right) \quad (2.2)$$

As  $\alpha_S < 1$  for heavy quarks, the first reliable approximation for the cross section can be obtained through the Leading Order (LO), i.e., up to order  $k = 0$  ( $\mathcal{O}(\alpha_S^2)$ ), and *Next-to-Leading Order* (NLO,  $k = 1 - \mathcal{O}(\alpha_S^3)$ ), which bring us to:

$$NLO : A(m_Q) \alpha_S^2 + B(m_Q) \alpha_S^3 \quad (2.3)$$

The NLO leads to reliable results to low and intermediate momentum, for  $p_T$  in the order of the quark mass or less. In the regimes where  $p_T \gg m_Q$  the factor  $\log(\mu_R/m_Q)$  becomes significant in the expansion and the Leading-Log (LL) and Next-to-Leading Log (NLL) corrections are necessary [58, 59]:

$$NLL : \alpha_S^2 \sum_{i=0}^{\infty} a_i \left( \alpha_S \log \left( \frac{\mu_R}{m_Q} \right) \right)^i + \alpha_S^3 \sum_{i=0}^{\infty} b_i \left( \alpha_S \log \left( \frac{\mu_R}{m_Q} \right) \right)^i \quad (2.4)$$

The two schemes that are used the most to calculate the QCD cross sections are the NLO and the fixed-order-next-to-leading logarithm (FONLL). The FONLL cross sections are evaluated by NLO calculations also taking into account the large terms related to NLL

accuracy. Calculations show that the total NLO and FONLL calculated cross sections are consistent with each other, since each one of them is more accurate than the other in a given  $p_T$  region.

The Figure 2.4[45] illustrates the main production mechanisms of heavy quarks using the LO e NLO. In LO the contributions come from the pair creation through the gluon fusion and light-flavour annihilation. In NLO the processes can be classified by the number of heavy quarks present in the interaction of the initial hard scattering. These processes are the flavour excitation, which happens when a heavy quark suffers a scattering by a parton, and Gluon Splitting, when there is no heavy quark involved in the interaction.

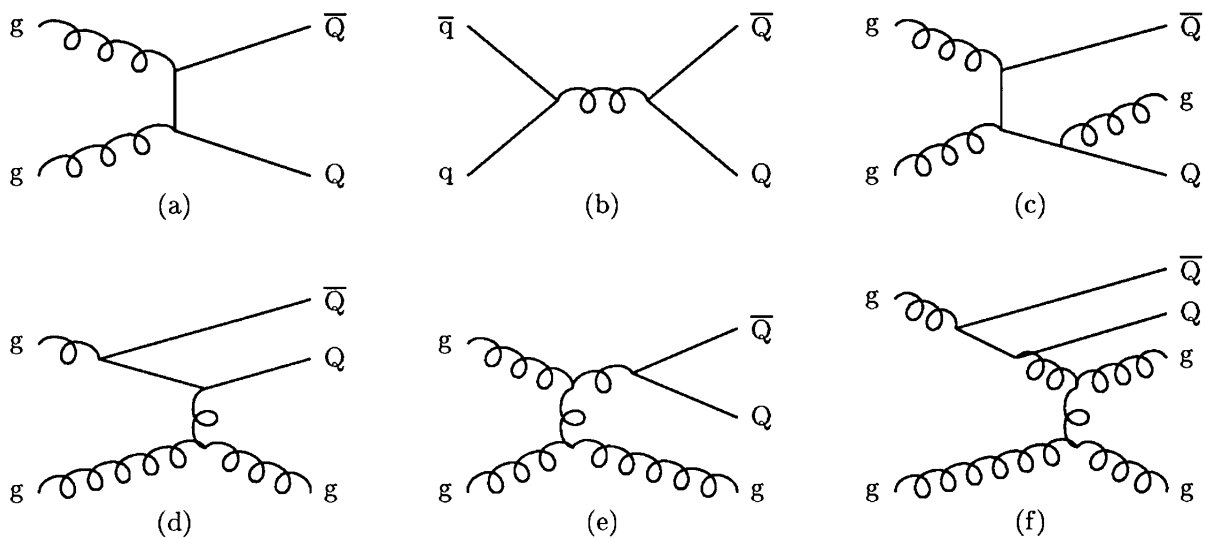


Figure 2.4: Feynman diagrams of the main production mechanisms of heavy-flavour production through pQCD, LO and NLO: (a,b) pair production; (c) pair production with gluon emission; (d) flavour excitation; (e) gluon splitting; (f) gluon splitting process but with flavour excitation behavior.

In summary, there are three main ways of heavy-flavour production (check [45] for a well descriptive paper regarding these mechanisms):

- Pair Creation: leading order processes ( $\mathcal{O}(\alpha_s^2)$ ) of  $gg \rightarrow Q\bar{Q}$  and  $q\bar{q} \rightarrow Q\bar{Q}$ . In LO contribution, the heavy-flavour pair should be created towards the back-to-back directions in azimuth for momentum conservation.
- Flavour Excitation: When taking the NLO processes into consideration, when a heavy flavour from the parton distribution of one of the beam particles is put on a mass shell by scattering against a parton on the other beam. It normally happens in a gluon splitting process ( $g \rightarrow Q\bar{Q}$ ), and the total effective interaction is  $gq \rightarrow Q\bar{Q}q$  or  $gg \rightarrow Q\bar{Q}g$ .
- Gluon Splitting: Process that involves  $g \rightarrow Q\bar{Q}$  in the initial or final state. There is no heavy quark involved in the initial hard scattering. Except at high energies, most of the gluons splitting processes in the initial state ends up in flavor excitation.

Some properties of such different mechanisms are explored in Figure 2.5, by [45]. There, the three production mechanisms for a  $b\bar{b}$  pair are shown as a function of the differences in rapidity,  $p_T$  and  $\Delta\varphi$ , and also as a function of the mass. Flavour excitations and gluon splitting present similar behaviors in some of these properties, and the flavour creation (pair production) is the one that presents more differences than the others. Flavour creation has a preference for smaller regions of the  $\Delta p_T$  and also for the creation of pairs back-to-back in azimuth. Gluon splitting presents the higher contribution for highest transversal momentum and also a greater contribution for pairs created with small angles than the other processes, although it creates pairs in all of the regions of  $\Delta\varphi$ , creating both small angle pairs and also back-to-back (almost flat distribution).

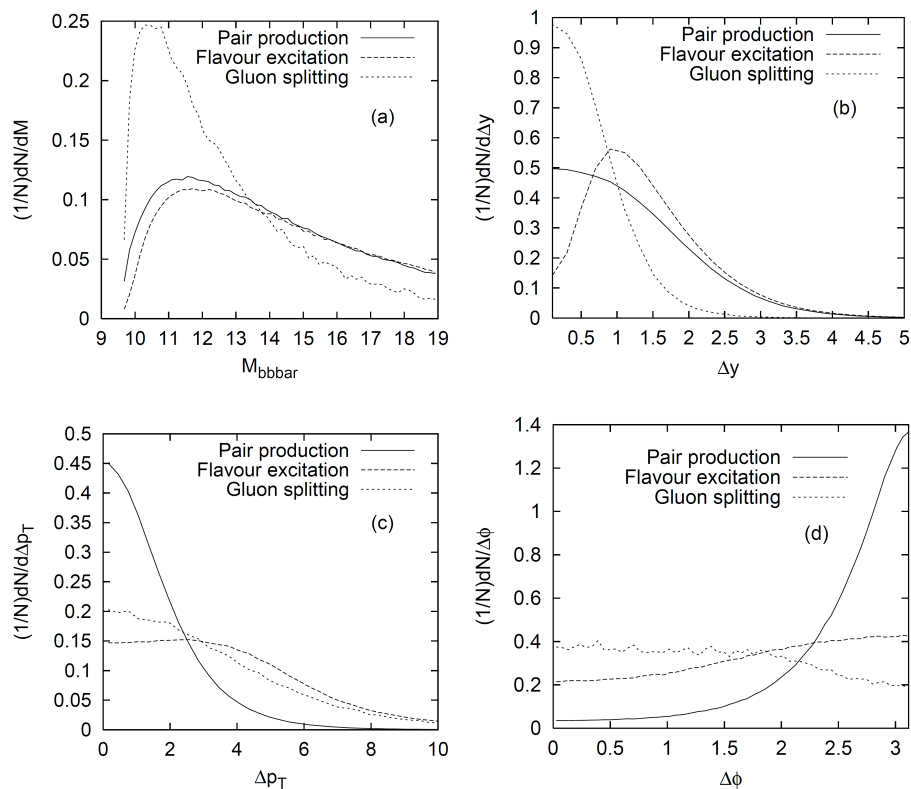


Figure 2.5: Correlations between  $b\bar{b}$  pairs at 2 TeV  $p\bar{p}$  collider. For simplification, each mechanism are normalized to unity for better comparisons. [45]

The difference in the rapidity of the  $b\bar{b}$  pair presents also very different distributions for each production mechanisms. Flavour excitation is depleted at small rapidity differences, and this could be explained by the evolution of a gluon in the parton distribution splitting into a  $b\bar{b}$  pair, giving them a small initial rapidity separation, as it happens in the gluon splitting process. However, one of the heavy quarks enters in the hard scattering process and it is back-scattered by a parton from the other beam [45], as explained in the summarization of the three processes. This is what makes the depletion observed for small rapidity.

## 2.4 Heavy-Flavour Decays

The  $J/\psi$  was the first particle containing charmed quarks discovered, composed of a resonant state of a  $c\bar{c}$  pair. Two different experiments had the papers submitted with a difference of 1 day in November of 1974, through dilepton analyses. It was found a narrow peak in the  $e^+e^-$  spectrum at 3.1 GeV. The so-called J particle was found in the BNL AGS facility [60] while the  $\psi$  particle was found by the SPEAR experiment at SLAC-LBL [61]. Since their measurements (Figure 2.6a,b) were surprisingly close in time both of the names given by the two experiments to the particle got shared, and the  $J/\psi$  had been found. Soon after the  $J/\psi$  discovery, another charm bound state was found, the  $\psi'$  [62].

Three years after the discovery of the charm quark from the  $J/\psi$  measurements in the dielectron spectrum, a resonant state of beauty quarks was also found in the dimuon spectrum, the  $\Upsilon$  [63] (Figure 2.6c), followed by the discovery of two another beauty bound states, the  $\Upsilon'$  and  $\Upsilon''$ .

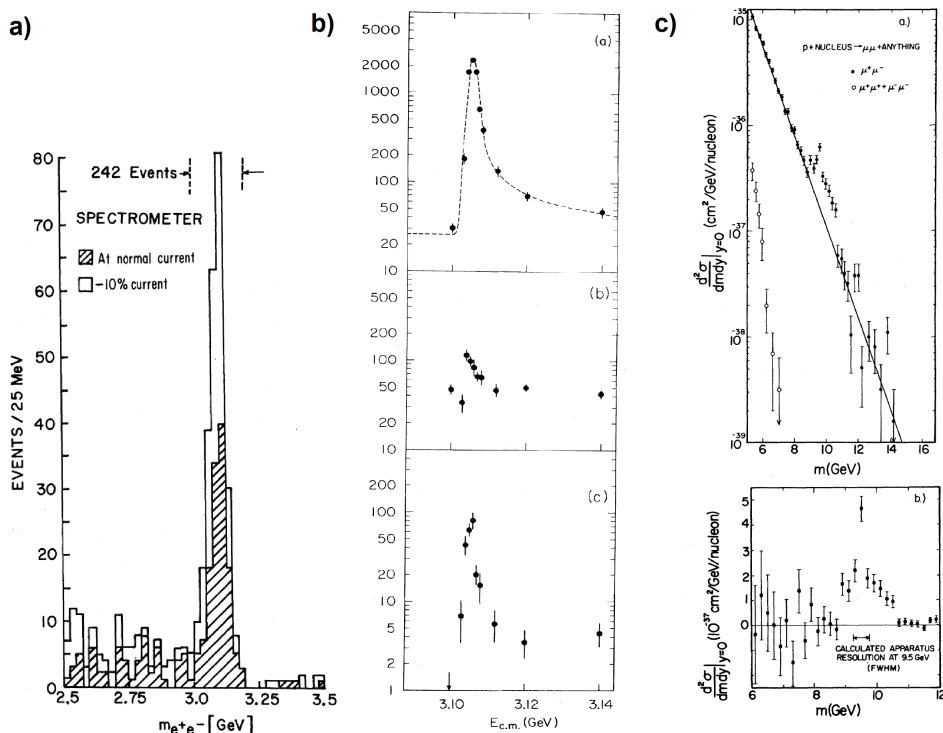


Figure 2.6: a) Mass spectrum showing the existence of J. Results from two spectrometer settings are plotted showing that the peak is independent of spectrometer currents[61]. b) Cross section versus energy for (top-a) multi-hadron final states, (middle-b)  $e^+e^-$  final states, and (bottom-c)  $\mu^+\mu^-$ ,  $\pi^+\pi^-$ , and  $K^+K^-$  final states[60]. c) Measured dimuon production cross sections as a function of the invariant mass of the muon pair, with the solid line as the continuum baseline fit. On top are shown both the peak and the continuum spectrum while in bottom it is shown the cross sections with the smooth exponential continuum fit subtracted[63].

With the heavy quarks discovery, the searching for open heavy flavours also started.

Particles composed by charm quarks ( $c$  or  $\bar{c}$ ) with a charm quantum number different than zero are called as an open charm, while if the charm quantum number is equal to zero (such as  $J/\psi$ ) they are known as hidden charm particles. The same happens to particles that contain beauty quarks ( $b$  or  $\bar{b}$ ). Such open heavy flavour particles were also found soon, starting with the discovery of the D mesons [64]. D mesons are particles that are constituted of an open charm quark and another light quark, such as up, down or strange quark. B mesons, on the other hand, are particles constituted by an open beauty quark and a light quark such as up, down, strange or even another charm quark. D or B baryons, however, are composed of 3 quarks, and only one of them is a charm or beauty quark. Recent invariant mass and production measurements [65] of the  $K\pi\pi$  decay channel of mesons D are shown in Figure 2.7.

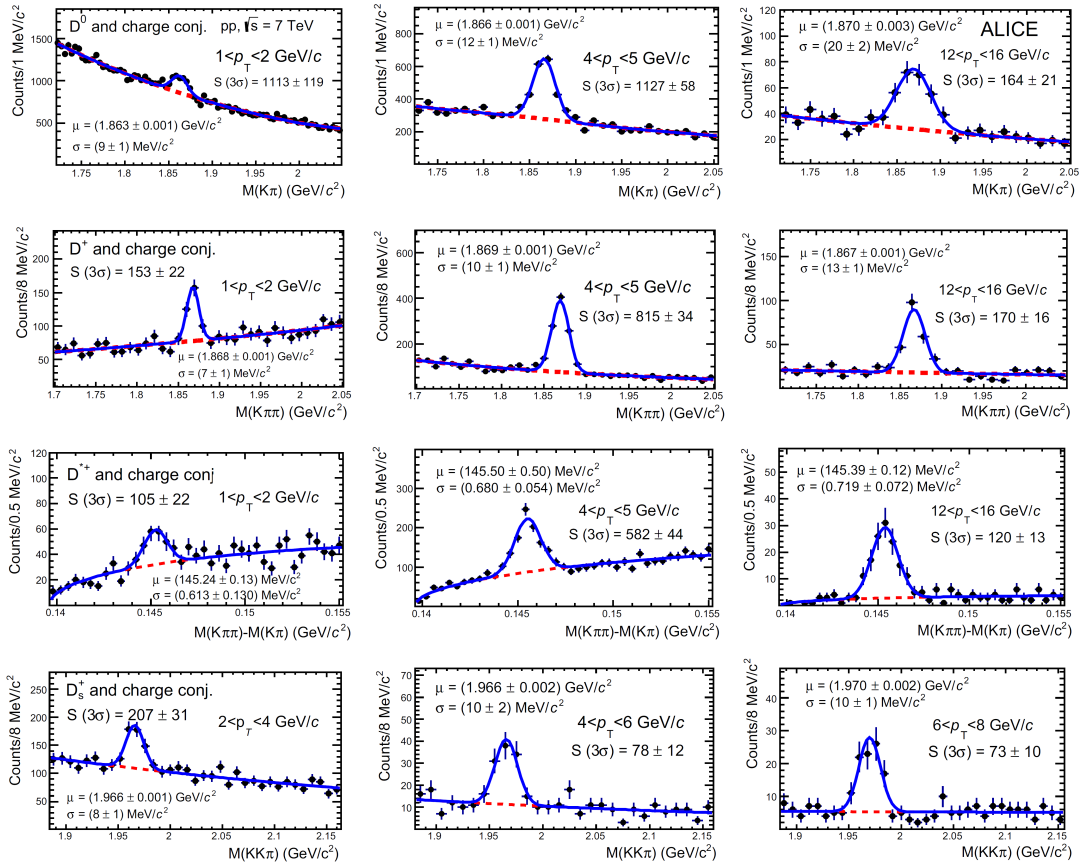


Figure 2.7: Invariant mass (mass-difference) distributions of  $D^0$ ,  $D^+$ , ( $D^{*+}$ ) and  $D_s^+$  candidates and charge conjugates in three  $p_T$  intervals for a sample of pp collisions at  $\sqrt{s} = 7 \text{ TeV}$ . [65]

A comparison of the recent D meson production measurements as a function of the transversal momentum  $M(K\pi)$  is shown in Figure 2.8 compared to FONLL predictions. The high-order pQCD calculations such as NLO and FONLL are in agreement with the D meson production measurements, although the experimental data is systematically in the upper edge of the calculations.



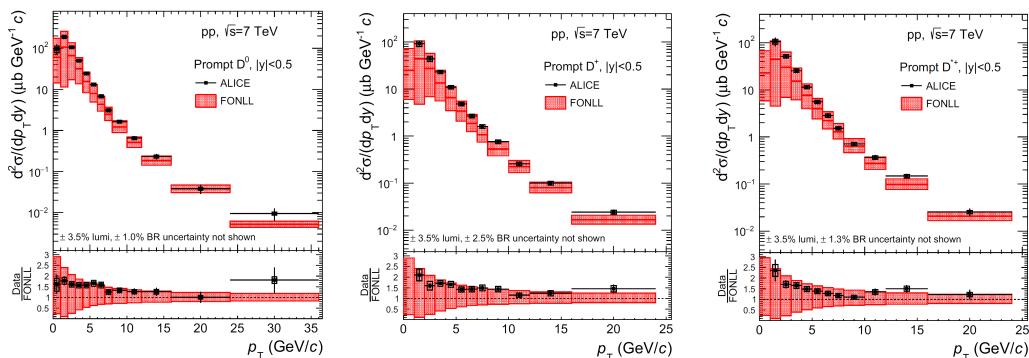


Figure 2.8: Transversal momentum distributions of  $D^0$ ,  $D^+$  and  $D^{*+}$  candidates from a sample of pp collisions at  $\sqrt{s} = 7$  TeV compared to FONLL predictions. [65]

Heavy quarks can decay semi-leptonically into electrons, after the creation of these heavy-flavour hadrons in the quark hadronisation. Since the heavy quarks can not be measured directly by the detectors, they can only be studied by the signals of their decays. As the ALICE detector have excellent particle identification and vertexing, it is perfectly-suited to study the reconstructed charmed and beauty hadrons and specially electrons from heavy-flavour decays.

A good description of what happens would be: the heavy quarks are produced only in the initial stages of the collisions due to their increased mass; in sequence, they interact with the medium and hadronize forming D or B mesons or baryons; after that, they can decay into leptons such as electrons or muons. This brings us a way to identify the presence of these hadrons: through electrons. More than that, we can study the production properties and kinematics of the heavy-flavour pair created by identifying and pairing two heavy-flavour electrons. The decay channels into electrons have been updated recently and are in the order of  $\approx 7\%$ [66] (instead of  $\approx 10\%$  of the older measurements[67]) for charm and  $\approx 22\%$  for beauty. In Figure 2.9[20] it is shown a schematic example of the semi-leptonic decay of charm quarks into leptons.

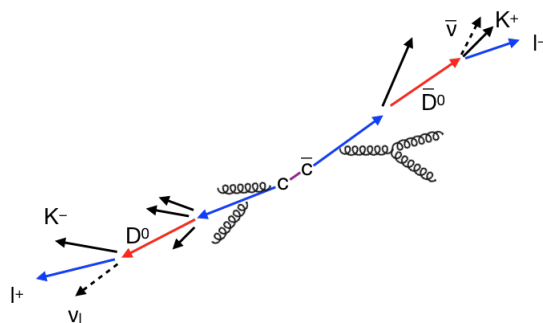


Figure 2.9: Semi-leptonic decay of heavy quarks.

The heavy-flavour production can be studied via single heavy-flavour hadrons or heavy-flavour electrons measurements. However, the advantage of the measurements of the

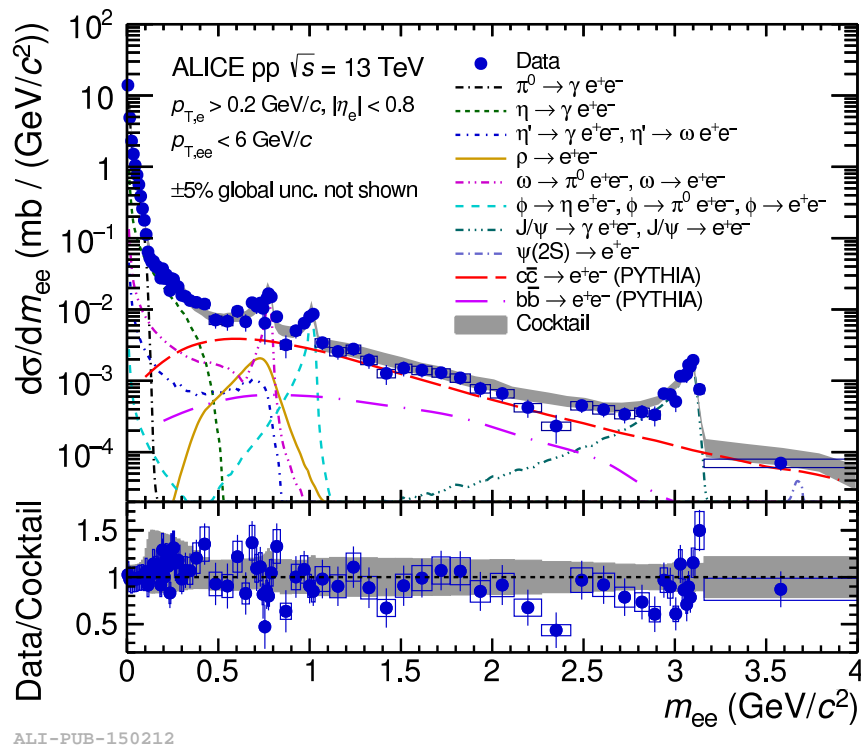


Figure 2.10: Dielectron invariant mass yield obtained from 2016 data-taking year and the comparison to the MC cocktail.

heavy-flavour production through dielectrons is that they are sensitive to the initial correlations of the produced quark pair, such as their kinematic properties, that single heavy-flavour measurements are not. They can also probe the full  $p_T$  range of the heavy-quark pairs, looking directly at possible production mechanisms that generate pairs with those kinematic properties.

## 2.5 Dielectron Pairs

The proposed strategy to study the heavy-flavour production is through a dielectron analysis. The dielectron analysis consist in the finding of the electrons in a given event and in the subsequent pairing of all of them. Electrons that came from the same mother are called correlated electrons and have physical meaning. Uncorrelated electrons, on the other hand, are paired electrons which have different mother particles, leading to uncorrelated signals. In a dielectron analysis the correlated signal can be separated from the uncorrelated signal, as it will be discussed later in Section 4.6. The correlated signal will carry information from the decaying sources, and for this purpose it is first important to understand and clarify all of the possible sources to the dielectron production, to be able to extract only the dielectron correlated signal related to heavy-flavour electrons.

The dielectron invariant mass yield is shown in Figure 2.10[19] compared to predictions from MC simulations. The dielectron invariant mass yield in these limits can be separated

into 3 parts. The first one is the low invariant mass region ( $0 < m_{ee} < 1.1 \text{ GeV}/c^2$ ), dominated by the contribution from light flavour (LF -  $\pi^0$ ,  $\eta$ ,  $\eta'$ ,  $\rho$ ,  $\omega$ ,  $\phi$ ) and direct photons (produced in the inelastic scattering between partons) to electrons sources, some of them being through Dalitz decays. In cases of Pb–Pb collisions the medium created will also contribute with thermal radiation. The second region, between  $1.1 < m_{ee} < 2.7$  is known as the intermediate invariant mass region (IMR) and it is dominantly composed by heavy-flavour sources, i.e., charm and beauty. The last one is the  $J/\psi$  mass region that includes the  $J/\psi$  peak, and it is composed by contributions from both  $J/\psi$  and open heavy flavour sources.

The LF production happens mainly at the latter stages of the collision, dominating the dielectron production at this time. Since  $\rho$ ,  $\omega$  and  $\phi$  mesons present the same quantum number as photons they can decay directly into leptons, after pion scattering or annihilation, such as  $\pi^+\pi^- \rightarrow \rho \rightarrow \gamma^* \rightarrow l^+l^-$ . The other dominance of the dielectron production happens through the resonances and Dalitz decays ( $\pi^0 \rightarrow \gamma e^+e^-$ ) from the light-flavour sources.

The dielectron spectrum is known to have also contributions from the Drell-Yan process [68], however, this process is expected to have a very small contribution in the invariant mass region considered [69, 70], specially in pp collisions. This production mechanism happens at the initial stages of the collision, when a quark in one of the incoming nucleus annihilate with a sea antiquark from the other incoming nucleus, creating a virtual photon which will be converted into a dilepton pair afterwards.

To analyze signals and extract the heavy-flavour contribution one can use the full invariant mass yield and simulate all of the cocktail contributions, such as all of the LF contribution and  $J/\psi$ . So each of the contributions can be identified in a given signal. The other procedure that can be used is to consider only the signal in the IMR, where it will be predominantly dominated by dielectrons from heavy flavour sources and a small contribution from  $J/\psi$ . The decision of the method to be used to identify and extract the heavy-flavour contribution depends on needs and precision requirements of each analysis.

The dielectron signals analysed in this thesis are the invariant mass ( $m_{ee}$ ), impact parameter (distance of closest approach -  $\text{DCA}_{xy}^{ee}$ ), angular correlations ( $\Delta\varphi_{ee}$ ) and pair transverse momentum ( $p_{T,ee}$ ). The kinematic and mathematical definitions of these variables can be found in Appendix A.1.

## 2.6 Previous Experimental Measurements

The previous measurements of the dielectron analyses for studies of the heavy-flavour production are discussed in the following. ALICE has already measured the heavy-flavour production cross sections in pp collisions at  $\sqrt{s} = 5.02$  [71], 7 [18], and 13 [19] TeV energies through dielectron analyses. These are important results since they allow one to test

pQCD calculations and also to perform comparative studies between different collisions systems when investigating CNM and QGP properties.

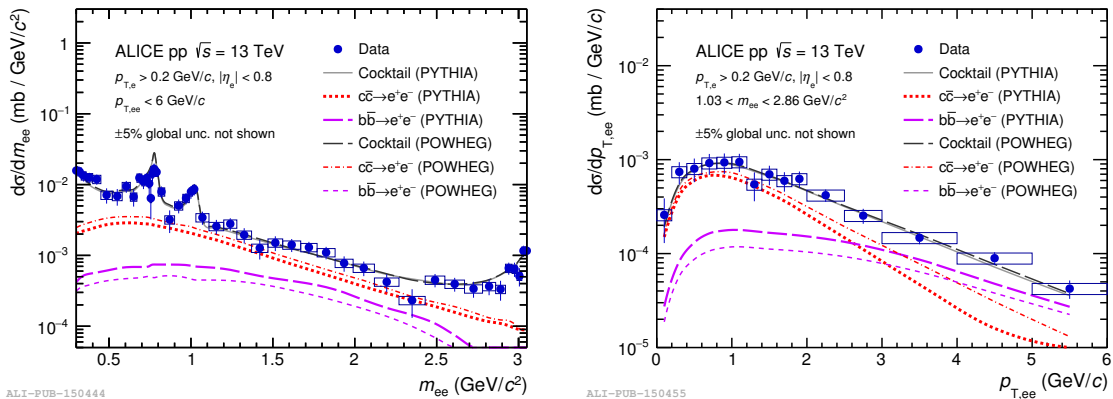


Figure 2.11: Projection of the heavy-flavour dielectron fit (grey line) in inelastic pp collisions onto the dielectron mass (left) and pair transverse momentum (right) using the PYTHIA and POWHEG event generators. The lines show the charm (red) and beauty (magenta) contributions after the fit. The global scale uncertainty on the pp luminosity (5%) is not shown. The statistical and systematic uncertainties of the data are shown as vertical bars and boxes, respectively. [19]

To extract the cross sections the dielectron invariant mass and pair  $p_T$  were fitted in the intermediate mass region, and the other contributions such as  $J/\psi$  were fixed as additional contributions from own measurements. One exemplary fit is shown in Figure 2.11 in the same collision energy studied in this thesis, 13 TeV. This procedure was used for the three collision energies described above, and summarized in comparison to FONLL predictions (Figure 2.12). There is an agreement, within large uncertainties, between the extracted cross sections for both PYTHIA and POWHEG generator for charm and beauty in comparison to FONLL predictions. However, brand new charm fragmentation fraction measurements obtained by ALICE [66] showed a higher baryon fraction than previous measurements, and this observation modified the total calculated branching ratio (BR) used to normalize the charm templates from  $\approx 10\%$  to  $\approx 7\%$ , increasing the charm measured cross section by  $\approx 92\%$ , extrapolating the upper limit of the FONLL uncertainty predictions.

When comparing pp to p–Pb collisions [71], the contribution from open heavy flavour electrons to the total hadronic cocktail did not include any modification beyond the scaling with binary nucleon-nucleon collisions. Hence, it was not found significant modifications of the heavy-flavour contribution from the vacuum expectation, suggesting that within the current uncertainties of the measurements the CNM effects plays a small role [71]. Preliminary results from ALICE in central Pb–Pb collisions at  $\sqrt{s_{NN}} = 5.02$  TeV, on the other hand, showed a suppression in the IMR of the dielectron invariant mass when compared to vacuum cocktails (Figure 2.13). This points that something in the medium created in Pb–Pb collisions is suppressing the heavy-flavour production as it is the domi-

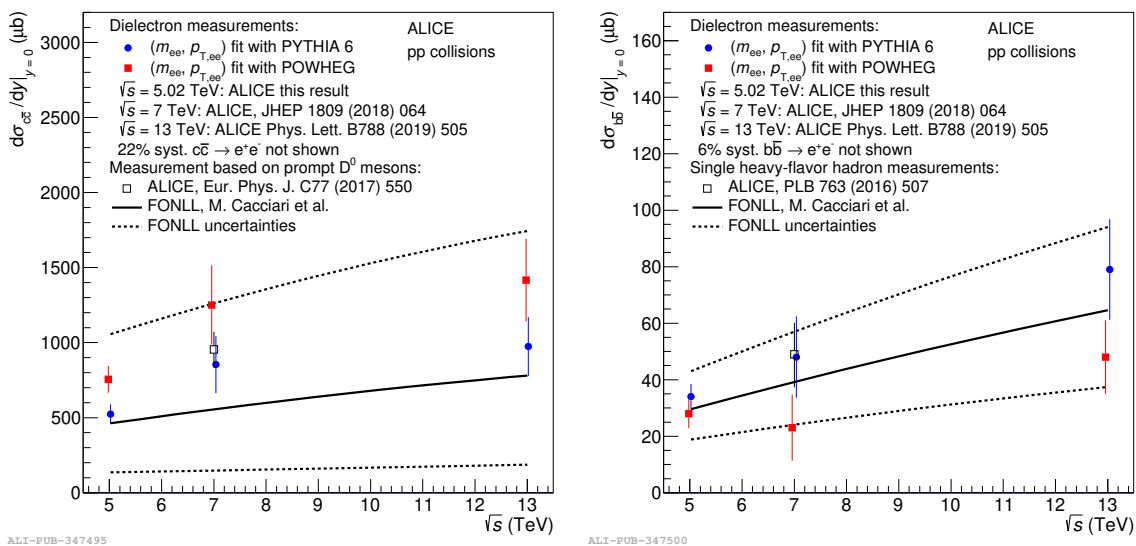


Figure 2.12: Cross sections at midrapidity for  $c\bar{c}$  (left) and  $b\bar{b}$  (right) as a function of  $\sqrt{s}$  in pp collisions. The colored markers represent the measured midrapidity cross sections at  $\sqrt{s}$  5.02, 7 and 13 TeV which are derived using either PYTHIA 6 (blue circles) or POWHEG (red squares) simulations. The systematic and statistical uncertainty of the data points are summed in quadrature and represented by vertical bars. The measurements are compared with FONLL calculations (black solid line), with model uncertainties (dashed lines), and to single heavy-flavour hadron measurements (open markers). The referenced  $c\bar{c}$  cross section at  $\sqrt{s} = 7$  TeV was obtained from a measurement of prompt  $D^0$  meson production with  $p_T > 0$  GeV/c and  $|y| < 0.5$  using the fragmentation fraction  $f(c \rightarrow D^0) = 0.542 \pm 0.024$  from  $e^+e^-$  LEP data. [71]

nant contributor to the IMR, which can be an indication of the QGP. An updated analysis in central Pb–Pb collisions at  $\sqrt{s_{NN}} = 5.02$  TeV with a larger dataset is ongoing and a new comparison should be released soon, with better statistics. These examples also help to understand why such measurements are important and why they need to be updated when better precision can be achieved.

The production mechanisms of charm have also already been studied before in two master’s thesis [47, 48], although they did not have  $\Delta\varphi_{HF e-HF e}$  experimental data to compare their results from simulations. In a very interesting analysis [47], the production mechanisms of charm were studied specially as a function of the invariant mass, and they were used to fit the ALICE dielectron invariant mass data in pp collisions at 13 TeV, in the intermediate mass region - see Figure 2.14. They found that the production mechanisms were too similar in shape and also that the current statistics of data back then was not enough. They pointed out that the best way to separate them would be to use the  $\Delta\varphi$  measurements, but there was no experimental  $\Delta\varphi$  data measurement available for the comparison of the templates at that time.

Other interesting result was obtained in [48]. The analysis followed a bit different path, where the simulations were carried out by the 2-particle angular correlations as it is done in h-h (hadron-hadron) and e-h (electron-hadron) angular correlation analyses. In

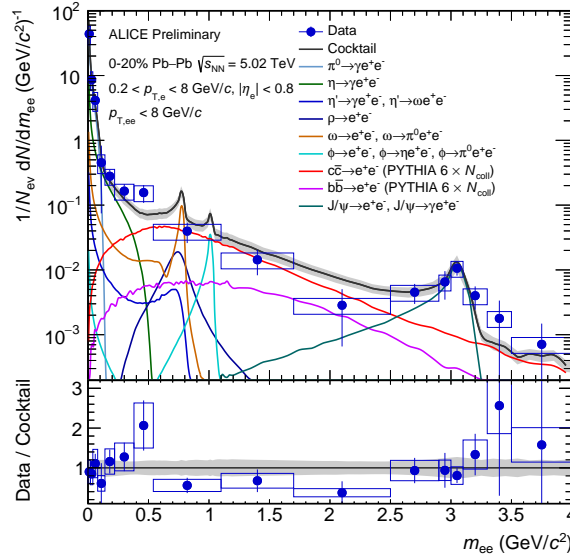


Figure 2.13: The dielectron invariant mass yield in 0 - 20 % central Pb–Pb collisions at  $\sqrt{s_{NN}} = 5.02$  TeV compared to vacuum cocktail from PYTHIA generator.

these kind of analyses, the measurements are separated into different trigger  $p_T$  ranges and associated particles  $p_T$ , instead of looking directly to the pair  $p_T$ . They compared their simulations to the data available back then, which was angular correlations between e-h and they found out that the e-h correlations were not conclusively enough to separate the production mechanisms when looking at the correlations involving only a single HFe, but, again, there was no experimental  $\Delta\varphi_{HFe-HFe}$  measurement available to compare the results from their simulations.

These studies showed the importance of having such experimental measurement available ( $\Delta\varphi_{HFe-HFe}$ ) for further tests and comparisons with predictions from generators. These measurements involving HFe-HFe correlations are performed in this thesis, not only for  $\Delta\varphi_{ee}$  but also for  $m_{ee}$ ,  $DCA_{xy}^{ee}$  and  $p_{T,ee}$ .

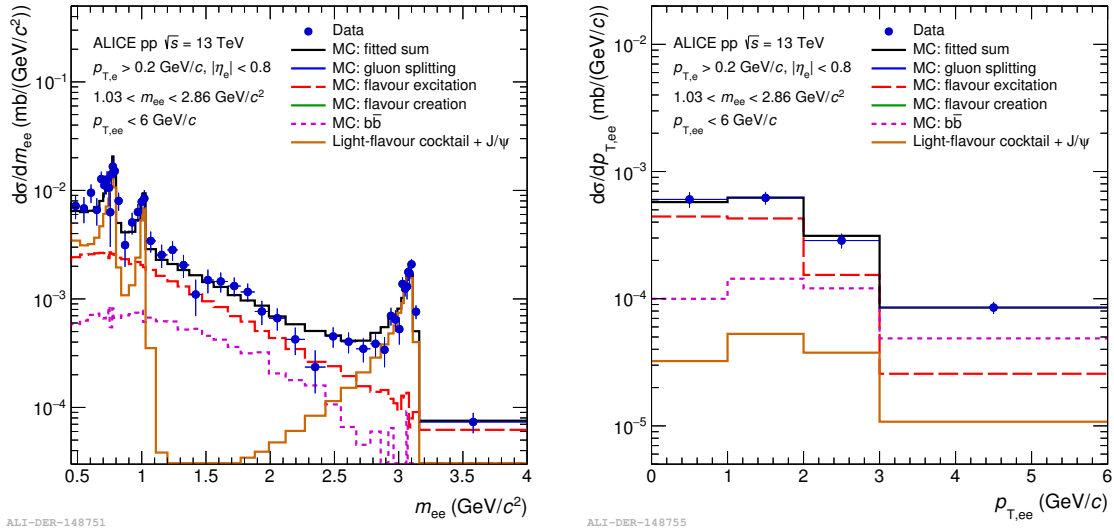


Figure 2.14: Two-dimensional non-extended fit of the data. The fit result suppresses the FCR and GSP contributions, describing the IMR of the data with only the FEX and  $b\bar{b}$  contributions. [47]





# 3 Experimental Setup

In this Chapter the experimental apparatus will be briefly described to understand how the data-taking is performed and how some of the detectors used in the analysis work. First the Large Hadron Collider (LHC) will be introduced in Section 3.1 along with the ALICE apparatus (A Large Ion Collider Experiment) - Section 3.2, followed by the detectors used in the analysis, such as the Inner Tracking System (ITS) - Section 3.3, the Time Projection Chamber (TPC) - Section 3.4, the Time Of Flight (TOF) - Section 3.5 and V0 - Section 3.6.

## 3.1 The Large Hadron Collider

The Large Hadron Collider, built at the France-Switzerland border, is the largest and most powerful particle accelerator of the world, operated by the European Organization for Nuclear Research (CERN). The LHC is a 27-kilometer-long ring composed of superconducting magnets, with structures capable of accelerate and to boost the energy of the particles until it reaches almost the speed of the light. It has been projected to increase the energy of particles reaching 14 TeV at the center of mass for proton-proton collisions (pp), 8.8 TeV in proton-lead collisions (p-Pb) and 5.5 TeV in lead-lead collisions (Pb-Pb).

The proton beams are firstly accelerated through the linear accelerator (Linac) reaching 50 MeV. This beam is then injected into the Proton Synchrotron Booster where the energy of the beam is increased to 1.4 GeV, followed to the Proton Synchrotron to reach 25 GeV. After this stage the beam is inserted into the Super Proton Synchrotron pushing the energy to 450 GeV. Finally, two beams are guided to enter in the LHC in opposite directions, clockwise and anti-clockwise, and both of the beams are able to reach 7 TeV. A similar process happen to lead nuclei beams. The LHC has 4 interaction points, where the beams cross each other and can interact. In each of these interaction points we have huge detectors waiting to record the collisions: ALICE[72], ATLAS[72], CMS[73] and LHCb[73]. We also have 2 minor detectors, the LHCf[73] and the TOTEM[73].

The ATLAS (A Torroidal LHC Apparatus) and CMS (Compact Muon Solenoid) experiments are multi-purpose experiments, with a large range of studies such as the search for the Higgs Boson or Beyond Standard Model (BSM) physics. On the other hand, the LHCb (Large Hadron Collider beauty) has its main focus on the matter and anti-matter

through the study of beauty quarks. The ALICE experiment (A Large Ion Collider Experiment) was built with the purpose of studying the physics of the strong interaction of the matter in extreme conditions of density and energy. The TOTEM (Total Elastic and diffractive cross section Measurement), which share the same interaction point of the CMS, and the LHCf (The Large Hadron Collider forward), that share the same interaction point of ATLAS, are minor experiments with specific purposes. The LHCf uses the particles created in the LHC collisions to simulate cosmic rays in lab conditions, while the TOTEM measure cross sections, elastic scattering and diffractive processes.

## 3.2 The ALICE Experiment

The ALICE detector was specifically projected to study the product of heavy-ion collisions, being optimized to identify thousands of simultaneously produced particles and to reconstruct tracks in a wide range of the phase-space. It can reconstruct particles with both very low and high momentum ( $\approx 150$  MeV/c,  $\approx 100$  GeV/c) with a very short lifetime. An schematic overview of the ALICE and its detectors is shown in Figure 3.1. Some of the answers that the Experiment is searching are related to fundamental questions, such as why protons and neutrons have masses 100 times higher than the particles that compose them, the quarks. Or, is it possible these quarks to be free? Deconfined of the particles that they form? What happens to the matter if we submit it to extremely high temperatures? Some of these answers could be found through the studies of heavy-ion collisions.

The detection and identification of hadrons, electrons and photons happen in the midrapidity region ( $|\eta| < 0.9$ ) where many detectors are immersed in a strong magnetic field generated by a magnetic solenoid. The intensity of the magnetic field generated by the solenoid aims to enable maximum performance of the detectors, harmonizing characteristics such as momentum resolution, accessibility to low momentum and tracking reconstruction. The detection and track reconstruction are performed through the ITS, which consists of a 6 layers of silicon detector, the TPC which is a temporal projection chamber with total volume of  $88\text{ m}^3$  and the TRD (Transition Radiation Detector) that capture transition radiations.

The particle is identified through the energy loss of each of the particles while they cross the ITS and TPC, by their time-of-flight with the TOF detector, by the transition radiation in the TRD and also by the Cherenkov radiation in the HMPID (High-Momentum Particle Identifier Detector). The photons can be identified by both the PHOS (Photon Spectrometer) and EMCal (Electromagnetic Calorimeter). Beside these detectors, there are other located in less central regions, with different purposes, as the FMD (Forward Multiplicity Detector), the V0 and T0, which are responsible to identify charged particles and trigger the record of the event. In less central regions there are still the

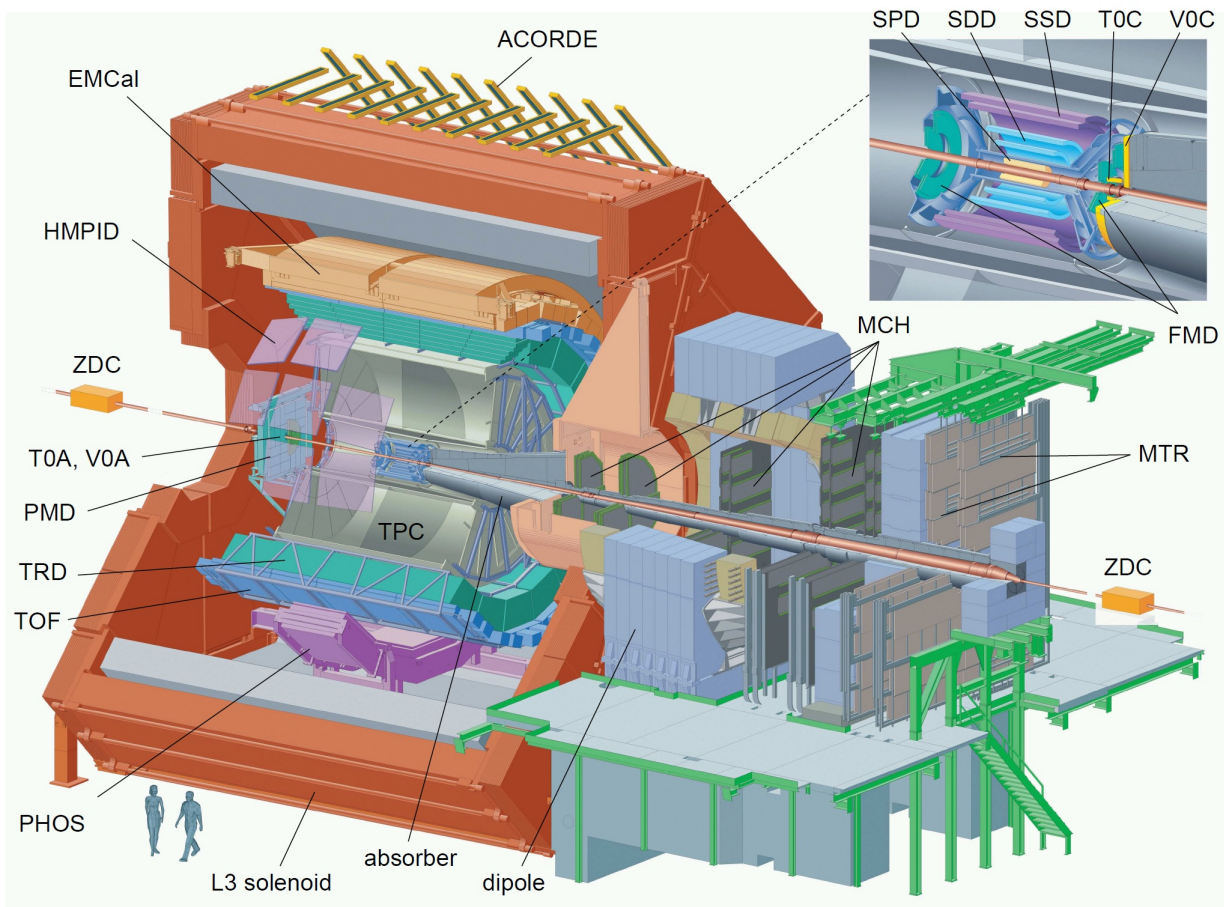


Figure 3.1: Schematic diagram of the ALICE detector. [12]

PMD (Photon Multiplicity Detector), which measures the multiplicity of photons while the ZDC (Zero-Degree Calorimeters) is used to estimate the multiplicity of the events through the measurement of the spectator nucleons in the event in heavy-ion collisions. Other detector that can be used to estimate the centrality of the events is the V0, that consists in two detectors asymmetric-located that measure the relative arrival time and the charge of particles, being also used as an event trigger. For muon detection there is a dedicated spectrometer, between  $-4.0 < \eta < -2.5$ .

### 3.3 Inner Tracking System

The ITS is the closest detector to the interaction point, so, the innermost detector of the whole experiment. It is composed by 6 cylindrical layers of silicon detectors. The first two layers are the SPD (Silicon Pixel Detector), followed by two layers of the SDD (Silicon Drift Detector) and the last 2 external layers are the SSD (Silicon Strip Detector), as shown in Figure 3.2. The number, position and segmentation of the layers are optimized to locate the tracks efficiently, with high resolution of the impact parameter and to best perform the correspondence of tracks between the ITS and the TPC.

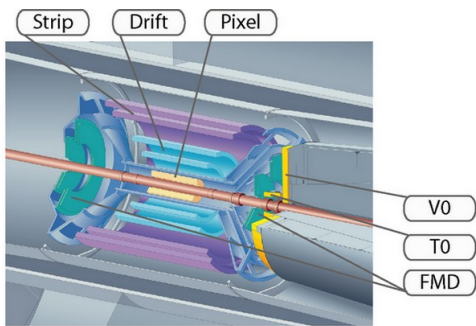


Figure 3.2: Schematic diagram of the ITS detector. [74]

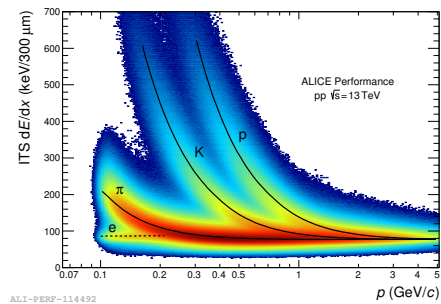


Figure 3.3: Energy loss distribution signal in the ITS as a function of the momentum in pp collisions.

Due to the high density of particles produced in heavy-ion collisions (around 80 particles per  $cm^2$ ), the SPD detectors are chosen to be the first layers, so a higher impact parameter resolution is achieved. The following layers, SDD and SSD, are used to identify the particles through the energy loss by ionization in the non-relativistic region.

The main purpose of the ITS is the identification of the primary vertex, which can be determined with relatively high precision, in the order of  $100 \mu m$ . It also provides the reconstruction of the particles until the extrapolation to the primary vertex, as the reconstruction of secondary vertexes from the hyperon decays and B and D mesons. The primary particles, have, in general, a hit in one of the ITS layers, while non-primary particles do not. It also allow the detection and identification of particles with low transversal momentum ( $p_T < 700 \text{ MeV}/c$ ). The granularity of the ITS is optimized to a maximum density of 8000 tracks per unity of rapidity and a spatial resolution in the order of some dozens of  $\mu m$ .

The measured charge of each cluster in the detector is normalized by the length of the path, which is calculated from the parameters of the reconstructed track to obtain the energy loss ( $dE/dx$ ) for each layer. To each layer, the  $dE/dx$  is calculated using a truncated mean. If four hits were identified, it is used the mean of the two innermost hits, or, if only 3 points were identified, it is used a weighted sum of the innermost hit with weight 1 and the most external with weight  $1/2$  [12]. An example of the measured energy loss distribution as a function of the momentum in the ITS is shown in the Figure 3.3.

### 3.4 Time Projection Chamber

The Time Projection Chamber is the main detector of the ALICE. It provides information to the identification of particles in a wide range of momentum, and the particles are identified in a simultaneous measurement of the specific energy loss ( $dE/dx$ ), the charge, and the momentum of each particle that cross the detector's gas. The TPC is composed by a large cylindrical cage with an electric field generated in its interior in the direction

of the beam axis. Its design is based in one central electrode with high voltage and two opposing axial potentials that creates an intense and uniform field in all of the gas volume. The charged particle interact with the gas while crossing the detector, losing energy and ionizing it [75, 76, 77], in a way that the produced ions (and electrons) are displaced to the TPC plates due to the electrical field, where the total produced charge is collected. Operated with high voltage gradients, with around 400 V/cm, and with a voltage of -100 kV in the central electrode, results in a maximum drift time of  $\approx 90 \mu\text{s}$  [11]. The TPC is filled with a gas mixture of Ne,  $\text{CO}_2$  e  $\text{N}_2$  (85.7%/9.5%/4.8%). A schematic overview of the TPC detector is shown in Figure 3.4.

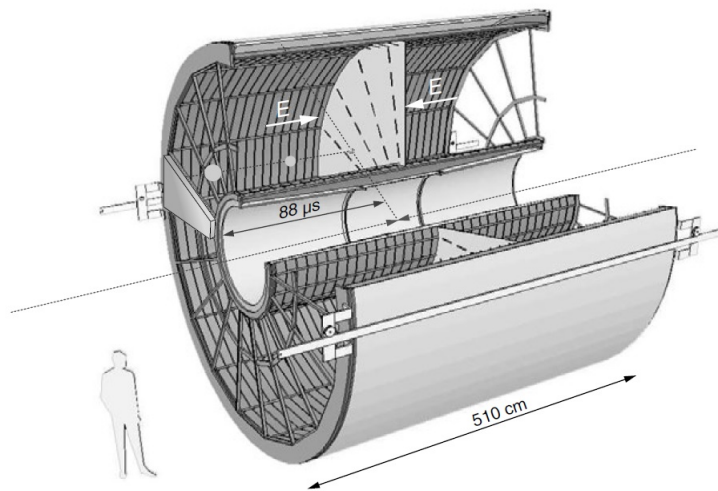


Figure 3.4: Schematic example of the TPC detector. [13]

The position where the charge is collected in the TPC plates, together with the drift time, are used to find the spatial position of the particle. Each information like this is called cluster, as it happens in the ITS. Normally a particle produces between 60 - 120 clusters at the TPC, and these clusters, together with the ones measured by the ITS and TOF are used to identify and reconstruct the trajectory of the particle. The energy loss by ionization, which is described by the Bethe-Bloch equation [77], is parameterized by a function proposed by the ALEPH Collaboration [78],

$$f(\beta\gamma) = \frac{P_1}{\beta^{P_4}} \left( P_2 - \beta^{P_4} - \ln \left( P_3 + \frac{1}{(\beta\gamma)^{P_5}} \right) \right) \quad (3.1)$$

where  $\beta$  is the velocity of the particle,  $\gamma$  is the Lorentz factor and  $P_{1-5}$  are fitting parameters that depend on the detector properties. In Figure 3.5 it is shown the energy loss ( $dE/dx$ ) as a function of the momentum of detected particles in the TPC, showing the separation between different species of particles.

While for low momentum ( $p \lesssim 1 \text{ GeV}/c$ ) the tracks can be easily identified one by one, in higher momentum the particles could still be identified with statistical basis through multiple Gaussian fitting [12, 79], as shown in Figure 3.6 (or include additional detectors



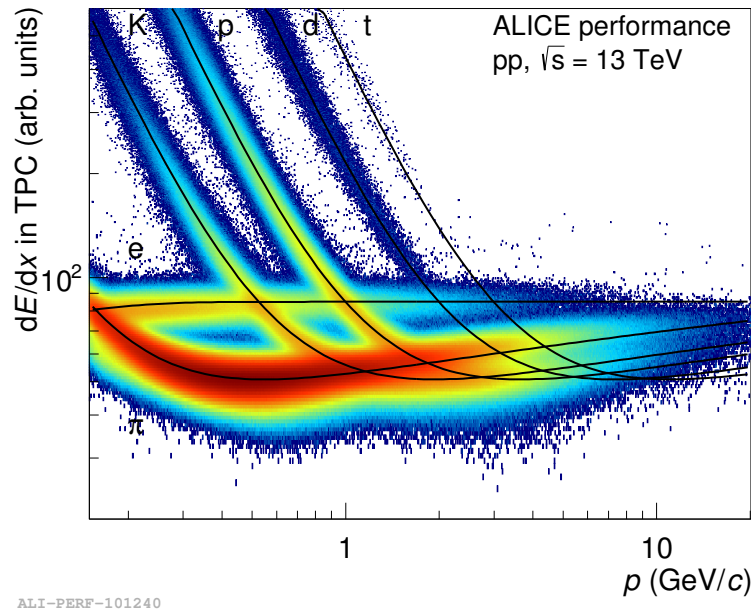


Figure 3.5: Specific energy loss ( $dE/dx$ ) in the TPC as a function of the momentum of detected particles in pp collisions. The lines represent the parameterizations of the mean energy loss for each kind of particle.

to help in this task, such as TOF). For this, the histogram is firstly projected in a given momentum interval and afterwards the energy loss is subtracted with the expected energy loss for a given particle, e.g., a pion. With this graph it is possible to fit different species of particles, as shown in Figure 3.6. In the study of this thesis, the energy loss of tracks will always be compared to the expected energy loss of electrons, since they are the particles of interest in the analysis.

In addition to the particle identification, the TPC also allows the determination of the transversal momentum, the momentum along the z-axis, the total momentum, and the charge. This happens because the detectors are immersed in a longitudinal magnetic field of 0.5 T and the particles passing through the field end up describing orbits, which are totally related to their momentum and charge. Having the spatial and temporal positions of the particles, the tracks can be parameterized by a helix function [75, 80], which enables to extract the charge and momentum of the particle. Given all of the identification and kinematic description capabilities of the TPC, it becomes one of the main detectors of the ALICE.

### 3.5 Time of Flight

The Time of Flight detector is a particle detector capable of discriminate lighter from heavier particles, with both having the same momentum, by the time that these particles take to travel a given distance in a medium. In its geometry, the TOF is very similar to the other detectors described earlier. Its elementary unit is based on MRPC (Multi-gap

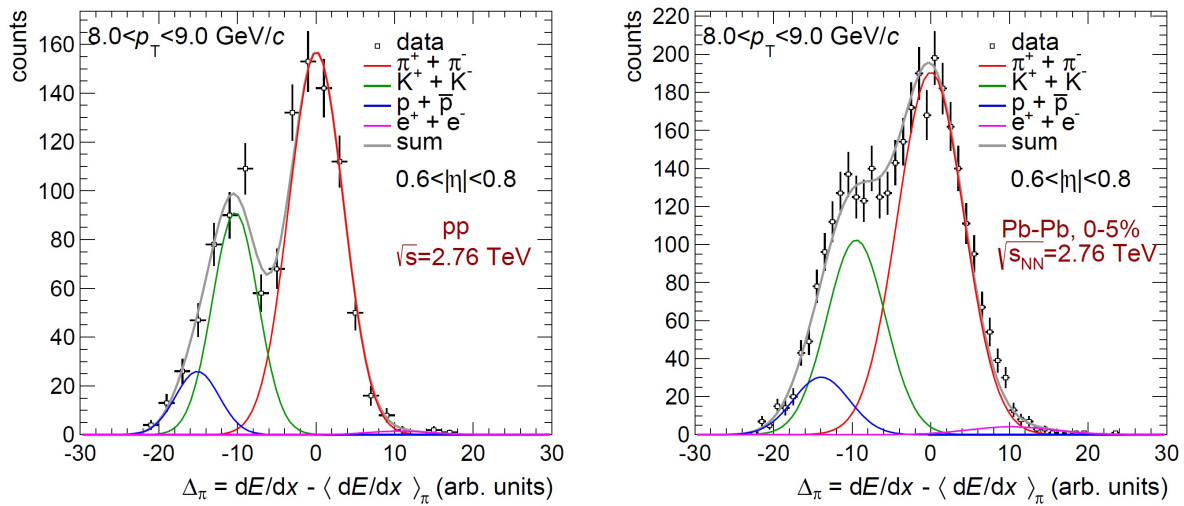


Figure 3.6: Energy loss distribution ( $dE/dx$ ) in the TPC in pp (left) and Pb–Pb (right) collisions. The lines represent the result of Multi-Gaussian fit. [12]

Resistive-Plate Chamber) chamber strips, which are subdivided into 96 reading blocks and installed within the gas volume. A group of 5 modules composes a super-module covering the entire range of the detector in pseudo-rapidity. This arrangement is shown in Figure 3.7.

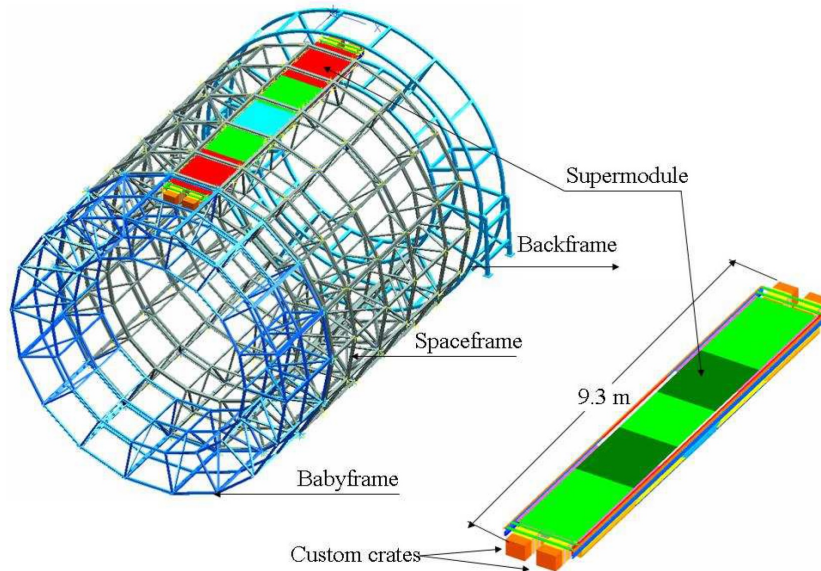


Figure 3.7: Schematic diagram of the TOF detector. [11]

In total, the TOF is composed of about  $10^5$  channels and, therefore, it is well suited for studies of high multiplicity events, which is the case of collisions with heavy ions at the energies of the LHC. The key aspect of these chambers is that the electric field is high and uniform all over the total sensitive gaseous volume of the detector. Any ionization produced by a transversely charged particle immediately initiates an avalanche process in

the gas that generates the signals observed in the pickup electrodes. Unlike other types of gas detectors, there is no drift time associated with moving electrons into a region of high electric field.

The main objective of the TOF is identifying particles with low and intermediate momentum, allowing a good identification up to about 2.5 GeV/c for pions and kaons and up to about 4 GeV/c for protons, with a separation between the pion distributions and kaons and between kaons and protons better than  $3\sigma$ . Figure 3.8 shows a distribution of time-of-flight measurements for tracks as a function of momentum in pp collisions.

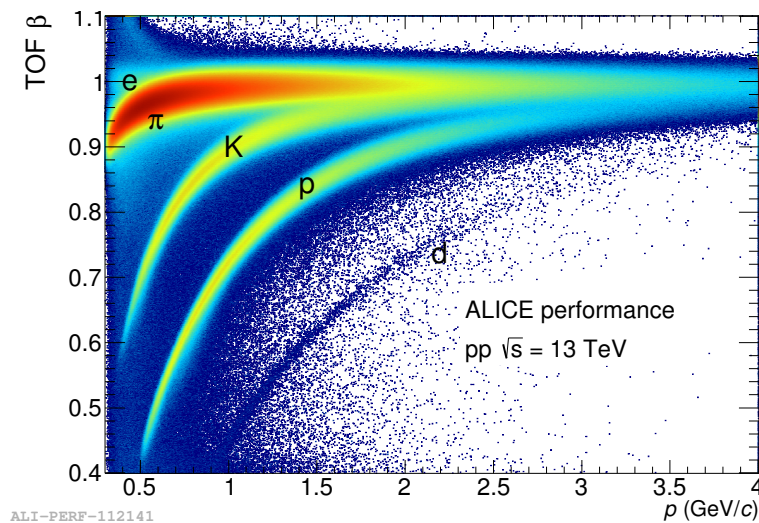


Figure 3.8: Time-of-flight particle distribution,  $\beta$ , measured by the TOF as a function of the momentum in pp collisions.

### 3.6 V0

The V0 detector is composed of two sets of plastic scintillators, V0A and V0C (see Figure 3.9), asymmetrically placed on both sides of the interaction point. The V0A is located 340 cm from the interaction point while the V0C is attached to the front face of the absorber, 90 cm from the vertex, as shown in Figure 3.10. Each of these detectors is segmented into 32 cells where each one is associated with optical reading fibers. When a charged particle passes through the plastic, light is produced by flickering.

It has several functions, such as providing triggering: the minimum bias trigger (MB) in the cases of pp and p-Pb collisions, and the multiplicity trigger (MT), semi Central Trigger (CT1) and Central Trigger (CT2) in Pb-Pb collisions. The minimum bias trigger aims to detect the largest possible fraction of inelastic events without inserting significant selection bias. On the other hand, the multiplicity triggering is possible because of the dependence between the number of particles registered in the scintillators of the V0 and the number of primary particles emitted, that is repetitive, and, therefore, the V0 serves



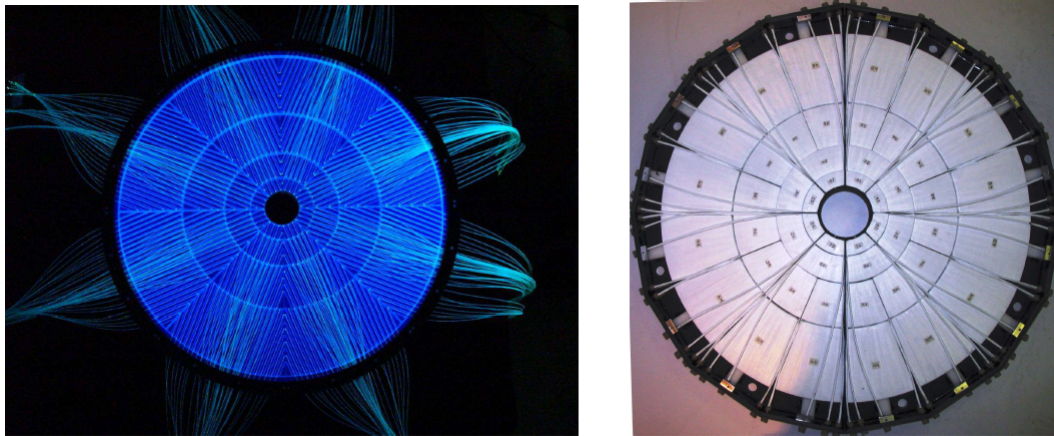


Figure 3.9: Front views of V0A and V0C scintillators are shown on the left and right, respectively. [11]

as an indicator of the centrality of the collision, as it measures the total charge of the particles and the relative time difference between detection at V0A and V0C. The V0 is placed asymmetrically in order to reject bunch-residual gas interaction, generating a signal in both V0 detectors any time that one of the bunches of the beam cross the detectors. Because of the asymmetry, both detectors must measure an activity inside a time window that takes this distance into account.

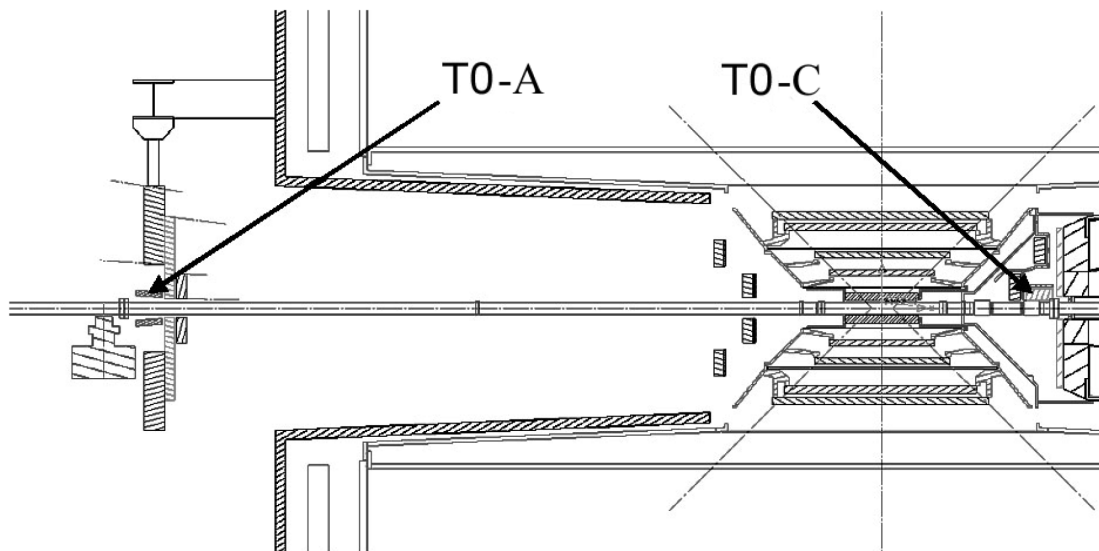


Figure 3.10: Schematic view of the positions around the interaction point. [11]



# 4 Data Analysis

In this chapter the general procedure of the data analysis and signal extraction is described. Four dielectron signals were obtained for the study of the production mechanisms of heavy-flavour electrons:  $m_{ee}$  (Section 6.1),  $DCA_{xy}^{ee}$  (Section 6.2),  $\Delta\varphi_{ee}$  (Section 7.1) and  $p_{T,ee}$  (Section 7.2), hence, this chapter will focus on the common aspects of these analyses and the general dielectron signal extraction, whereas the detailed signal extraction of each of these parameters will be followed in each of their respective analysis chapters. The data samples used for these analyses were 2016, 2017 and 2018 data available for pp collisions at  $\sqrt{s} = 13$  TeV, as described in Section 4.1. The whole analysis starts by a selection of good quality events that are triggered by the Minimum Bias trigger (Section 4.2), followed by a quality selection of tracks within the selected events (Section 4.3). The next step is to look at the tracks that match at least the minimum quality of the selection to identify electron candidates through the TPC and TOF detectors (Section 4.4), and also to recalibrate these PID signals (Section 4.5). The pairing of these electron candidates, together with the signal extraction method, is discussed in (Section 4.6). The final checks and determination of the systematic uncertainties in the signals conclude this Chapter in Section 4.7.

## 4.1 Data samples

Proton-proton collisions at  $\sqrt{s} = 13$  TeV from 2016, 2017 and 2018 ALICE data-taking years (with the nominal B-field strength of 0.5 T in the ALICE central barrel) are used for this analysis. The detailed periods and lists of runs can be found in the Appendix B. The selection of the good runs to be analyzed is done through the global quality status of the detectors used in this analysis in the Run Condition Table (RCT)<sup>1</sup>. A "run" is defined as the shortest period of data-taking with stable conditions, and the ALICE Collaboration, through the ALICE Quality Assurance group, performs several tests of calibrations, stability, detector performance and other checks for all of the available runs. This information is accessible through the RCT, where one can check which runs of each data-taking period matches the needs to carry out an analysis. A summary of the number

---

<sup>1</sup><https://alimonitor.cern.ch/configuration/> - CERN Certificate needed

2016	MB events	2017	MB events	2018	MB events
16d	39 m	17c	22 m	18b	205 m
16e	78 m	17e	12 m	18d	46 m
16g	33 m	17f	12 m	18e	60 m
16h	111 m	17h	122 m	18f	62 m
16i	38 m	17i	58 m	18g	9 m
16j	80 m	17j	42 m	18h	4 m
16k	193 m	17k	115 m	18i	56 m
16l	52 m	17l	84 m	18j	< 1 m
16o	62 m	17m	111 m	18k	11 m
16p	22 m	17o	120 m	18l	72 m
		17r	28 m	18m	230 m
				18n	4 m
				18o	32 m
				18p	74 m
Total	708 m	Total	726 m	Total	865 m
		<b>Analysed</b>	<b><math>\approx 2.3</math> b</b>		

Table 4.1: Data-taking years and periods used in the analyses.

of events analyzed in each period is shown in Table 4.1.

## 4.2 Event Selection

The minimum-bias trigger (see Section 3.6) kINT7 and an offline pile up rejection are required (through a Physics Selection task with pile up rejection). Several pp collisions can happen close in time producing a pile-up of events, sometimes being wrongly considered in slow detectors as a single event. This pile up event can be originated from collisions of protons from different bunch crossings (when the separation between proton bunches circulating in the LHC is small) or from multiple collisions within the same bunch. To reject these events we use the information from fast detectors such V0 and SPD, ensuring that only the favorable events are selected.

There is a correlation between the number of SPD clusters and tracklets (track segments of two hits extrapolated back to the beam line) in minimum-bias events. The number of SPD clusters is sensitive to pile-up events and beam-gas interactions, since more tracks are generated, while the SPD tracklets are not, since they need to point back to the primary vertex. The correlation is then unbalanced by the pile-up effect in the number of SPD clusters, generating outliers from the diagonal correlation. This makes it possible to reject pile-up events by looking at this correlation. Events are also rejected when SPD tracklets points to a secondary interaction vertex, which also points to a pile-up event.

The Primary Vertex is also required to be in the geometric center of the Central Barrel

Detectors, with its position along the z-axis as  $|\text{Vertex } Z| < 10$  cm. This requirement ensures that all detectors used in the analysis cover the pseudorapidity range commonly used. The primary vertex should also not differ its position in more than 0.5 cm when comparing to the vertex position determined by using the extrapolation of tracks. Also, we need to have at least 1 track or tracklet contributing to the vertex reconstruction. Events in which the vertex is determined with poor resolution and only in the z coordinate are rejected.

### 4.3 Track Selection

After selecting good quality events, we proceed to the selection of tracks within each event. To assure a selection of good tracks the reduction of fake and/or background tracks are necessary, as well as the requirement of some minimum quality. A list of the requirements used for the track selection is shown in Table 4.2. There are two different  $p_{T,e}$  cuts shown in the table that depend on the analysis type. The  $\text{DCA}_{xy}$  analysis requires a higher minimum  $p_{T,e}$  cut because of the poor resolution of the impact parameter for  $p_{T,e}$  below than  $0.4 \text{ GeV}/c$ , that will be discussed later. For all of the other analyses, the minimum  $p_{T,e}$  cut is defined as  $0.2 \text{ GeV}/c$  because below this value the particles deflected in the magnetic field of ALICE may not produce enough information on the TPC. The smallest possible  $p_T$  cut leads to a higher number of particle considered in the analysis, which is preferable.

Variable	Requirement
$p_T$	$> 0.2 \text{ GeV}/c$
$p_T$ ( $\text{DCA}_{xy}$ )	$> 0.4 \text{ GeV}/c$
$ \eta $	$< 0.8$
TPC refit	Required
Number of TPC crossed rows	$\geq 100$
Number of TPC clusters	$\geq 80$
Ratio of TPC crossed rows / findable clusters	$> 0.8$
$\chi^2$ per TPC cluster	$< 4$
Fraction of shared TPC clusters	$< 0.4$
ITS refit	Required
Hit in first SPD layer	Required
Number of ITS clusters	$\geq 3$
$\chi^2$ per ITS cluster	$< 4.5$
Number of shared ITS clusters	0
Reject kink daughters	Required
$\text{DCA}_{xy}$	$< 1.0 \text{ cm}$
$\text{DCA}_z$	$< 3.0 \text{ cm}$

Table 4.2: Track requirements.

Starting from TPC, it is required at least 80 clusters at the detector and  $\chi^2$  smaller

than 4 per cluster in order to assure reliable parameters in the description of the track. Moreover, the fraction of shared TPC clusters is required to be smaller than 40 %, and the fraction between the number of crossed rows and the number of findable clusters to be greater than 80 %. Shared TPC clusters are clusters that share more than one track trajectory, which means that a cluster may be from one of the trajectories or even from both, while a findable cluster is a cluster with another cluster within some pad rows. Crossed rows are defined as the number of clusters designated to a track plus some missing clusters, but that are findable. The selected track will also need to have at least 3 clusters at the ITS and not to share any of its clusters with other possible tracks. A hit in the first SPD layer is required to reduce background effects and reject non-primary particles. This cut has a great effect restraining the selection of photon conversions that happen in the detector material behind this layer. Cuts on the Distance of Closest Approach (DCA) of the primary vertex is also requested to avoid non-primary tracks and to reject background. The cuts on DCA cannot be too tight in order to keep electrons from the decays of charm and beauty mesons (decay lengths in the order of hundred micrometers).

Sometimes tracks can show some deviations in their trajectories due to undetected decays, such as a neutral decay, and these trajectories are not continuous. Part of the energy of the initial particle is lost because of these decays (e.g.  $K^+ \rightarrow \pi^+\pi^0$ , or Bremsstrahlung) and the remaining decay particle, which is charged, presents a different orbit in the magnetic field than the mother particle. These tracks are called kinks, and all of the parts of the trajectory that deviates from the original trajectory are called kink-daughters, which are discarded from the analysis.

## 4.4 Electron Identification

The electrons<sup>2</sup> are identified and selected using the information of the energy loss from the TPC and the time-of-flight from TOF. In this context we define a variable which is the difference in the energy loss on the TPC (and time-of-flight for TOF) between a given particle and what would be expected by an electron, in number of  $\sigma$  (resolution).

$$n\sigma_{TPC}^{electrons} = \frac{[\frac{dE}{dX}]_{track} - [\frac{dE}{dX}]_{electron}}{\sigma_{TPC}^{electron}} \quad (4.1)$$

$$n\sigma_{TOF}^{electrons} = \frac{TOF_{track} - TOF_{electron}}{\sigma_{TOF}^{electron}} \quad (4.2)$$

These detectors are used together in order to reduce the hadron contamination. To identify correctly the electrons without losing too many tracks because of the matching of these detectors, two schemes are used on which the track can be considered as an electron.

---

<sup>2</sup>The term electron will be used for both electrons and positrons along this text, unless explicitly stated.

The track is considered as an electron candidate if it is accepted in one **or** another scheme of PID (particle identification) cuts (Table 4.3).

Scheme	Detector	Particle	Reject	$n(\sigma)$ cut	$p$ range [GeV/c]
A	TPC ( $dE/dx$ )	electron	No	[-3.0, 3.0]	[0.2, $\infty$ )
	TPC ( $dE/dx$ )	pion	Yes	$(-\infty, 4.0]$	[0.2, $\infty$ )
	TOF ( $\beta$ )	electron	No	[-3.0, 3.0]	[0.4, $\infty$ )
B	TPC ( $dE/dx$ )	electron	No	[-3.0, 3.0]	[0.2, $\infty$ )
	TPC ( $dE/dx$ )	pion	Yes	$(-\infty, 4.0]$	[0.2, $\infty$ )
	TPC ( $dE/dx$ )	kaon	Yes	[-4.0, 4.0]	[0.2, $\infty$ )
	TPC ( $dE/dx$ )	proton	Yes	[-4.0, 4.0]	[0.2, $\infty$ )

Table 4.3: Scheme used for the electron identification.

Essentially, by the scheme A, the track is rejected if the  $|n\sigma_{TPC}^{electrons}|$  is greater than  $3\sigma_{TPC}^{electrons}$ , if the  $n\sigma_{TPC}^{pions} < 4\sigma_{TPC}^{pions}$ , or if the  $|n\sigma_{TOF}^{electrons}|$  is greater than  $3\sigma_{TOF}^{electrons}$ . These cuts in essence select electrons within  $3\sigma$  of the measurements and reject particles that could be hadrons within  $-\infty$  to  $4\sigma_{TPC}^{pions}$ . On the other hand, the scheme B takes a good place when a particle is mismatched or it cannot be found in TOF even though it was detected by TPC, so the TOF information is not mandatory. The Scheme B uses the rejections of particles with signals in the TPC similar to those from pions, kaons and protons, instead of the TOF cut, requiring that the accepted electron candidate track should have  $|n\sigma_{TPC}^{kaon}| < 4\sigma_{TPC}^{kaon}$  and  $|n\sigma_{TPC}^{proton}| < 4\sigma_{TPC}^{proton}$  and the same pion rejection from scheme A. The difference on the final  $n\sigma_{TPC}^{ele}$  spectra for each of these PID schemes can be found in Figure 4.1.

In Figure 4.1 the differences on the electron identification by schemes A or B become clear. In the top plot, the full  $p_T$  and TPC signals are filled by electron candidates while in the middle plot there are empty slices in the signal due to the hadron rejections. These empty spaces in the PID of the middle plot are in agreement to the expected rejection of signals from kaons (intercepting the energy loss of electrons around  $p_T \approx 0.5$  GeV/c) and protons (around  $p_T \approx 1$  GeV/c), as already discussed in Figure 3.5. In the bottom plot of Figure 4.1 the TOF distribution of selected electrons is shown (when the TOF is available). Since the TOF cut is required only for particles with momentum above 0.4 GeV/c, there is a band below 0.4 GeV/c containing the full TOF distribution without cuts of the selected electrons.

A deep study regarding hadron contamination using this eID (electron identification) scheme has already been carried out [20]. For this purpose the same cuts were used in MC simulations to check if there was any misidentified electron after the eID. The purity of the eID sample for HFe using these schemes are found to be  $> 99.9\%$  and no systematical uncertainty and hadron contamination subtraction are needed, as seen Table 4.4. An initial event cut was made to have a controlled and clear environment with only one  $c\bar{c}$  or  $b\bar{b}$  pair, and in the beauty case it was investigated also if there were differences in events

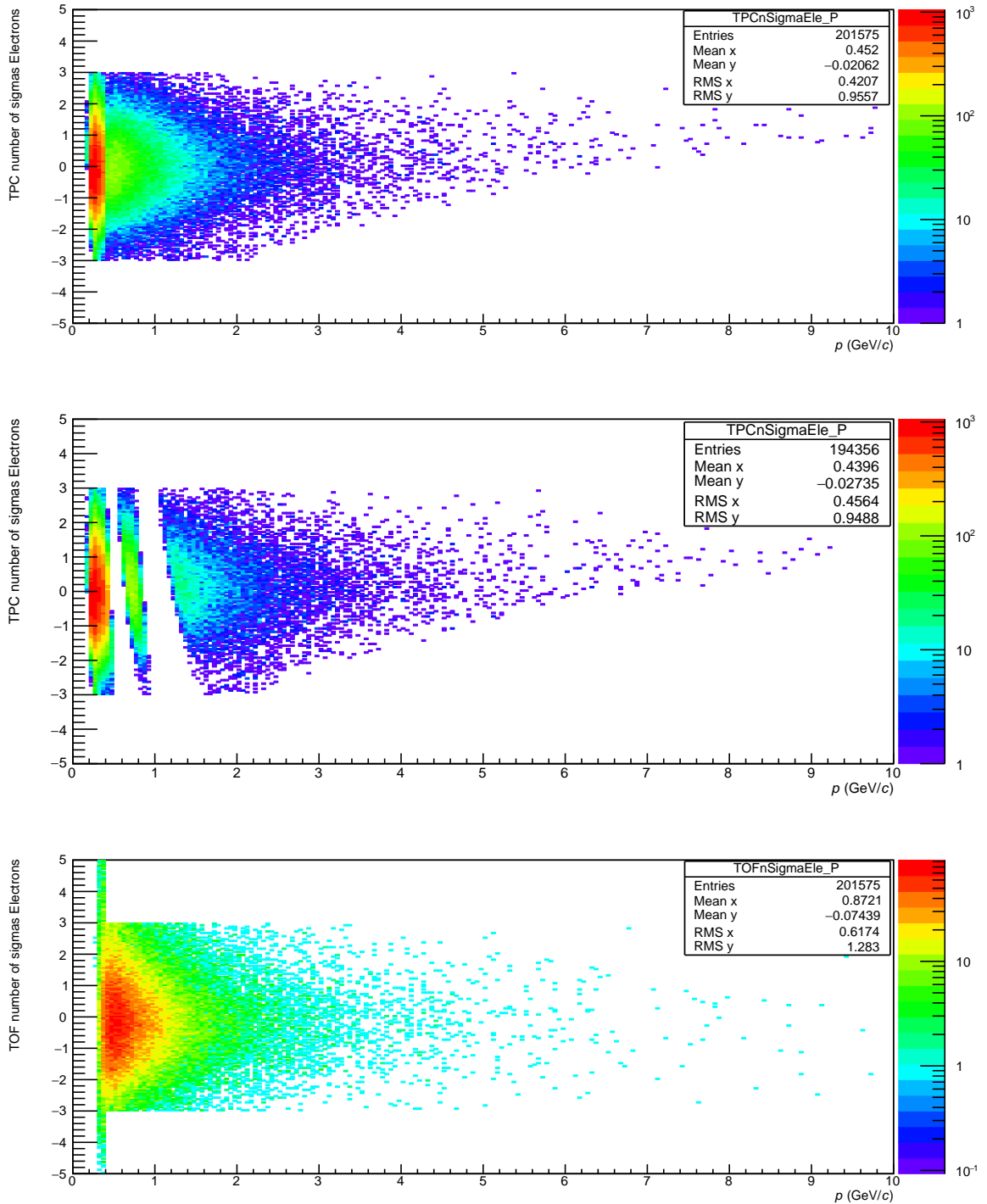


Figure 4.1: Examples of the  $n\sigma_{TPC}^{ele}$  for each of the PID cut schemes described in Table 4.3, scheme A on top and B in the middle. The bottom plot is the  $n\sigma_{TOF}^{ele}$  distribution of the PID cut when the TOF information is available. These results were obtained using the LHC16d period alone from 2016 data and show the selected electrons using scheme A on top, scheme B on the middle, and TOF signal for scheme A on the bottom.



where beauty oscillation happens.

PID Scheme	Event Type	ULS pairs (contamination)	LS pairs (contamination)
A	$c\bar{c}$	14314 (1)	0 (0)
	$b\bar{b}$ no osc	19124 (9)	7925 (1)
	$b\bar{b}$ with osc	9546 (4)	5778 (3)
B	$c\bar{c}$	3958 (1)	0 (0)
	$b\bar{b}$ no osc	6380 (3)	2310 (1)
	$b\bar{b}$ with osc	2826 (2)	1831 (1)

Table 4.4: Number of ULS and LS pairs found in MC simulations using the eID described in this Section and in parenthesis the number of misidentified electrons found. Extracted from [20].

## 4.5 TPC and TOF post-calibration

In some phase-space regions the PID calibration of the TPC and TOF show some deviations on the accepted electron candidate distributions, where the mean and  $\sigma$  of these distributions are different from the expected for a Gaussian with mean = 0 and  $\sigma = 1$ . In order to correct this effect, a re-calibration to the PID response for TPC and TOF is applied. The mean and width values of the initial distribution are extracted by fitting the distributions with two Gaussian functions, one for the electron signal and other for a possible background, as shown in Figure 4.2, always taking into account the  $\chi^2$  of the fitting. This procedure is applied for different  $\eta$  and  $p$  interval projections and in the end the re-calibration maps are built for both TPC and TOF, for both parameters mean and width, for each of the data-taking periods used in the analysis. It is important to mention that, for this purpose, only the electrons selected by scheme A are used for these fits, since it is symmetric with respect to  $n\sigma_{TPC}^{ele}$  and  $n\sigma_{TOF}^{ele}$ . Otherwise, the asymmetry of the scheme B, due to rejections, would mess up the distributions and consequently the recalibration informations obtained.

After this procedure these maps are included as corrections and the analysis over data is repeated, correcting the distributions by applying the following transformation to the  $n\sigma_{TPC,TOF}^{ele}$  for each track:

$$\begin{aligned}
 n\sigma_{TPC}^{ele,rec.} &\rightarrow \frac{n\sigma_{TPC}^{ele} - \text{mean}_{TPC}^{ele}(p, \eta)}{\text{width}_{TPC}^{ele}(p, \eta)} \\
 n\sigma_{TOF}^{ele,rec.} &\rightarrow \frac{n\sigma_{TOF}^{ele} - \text{mean}_{TOF}^{ele}(p, \eta)}{\text{width}_{TOF}^{ele}(p, \eta)}
 \end{aligned}
 \tag{4.3}$$

All of the calibration maps for TPC and TOF, for all of the periods studied in each of the 2016, 2017 and 2018 data-taking years can be found in the Appendix C.1, with much more details. All of the corrections for each period of a given data-taking year is

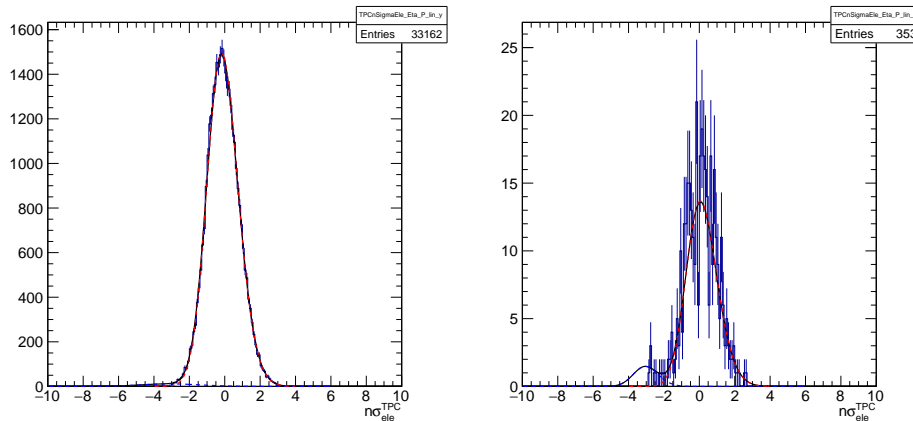


Figure 4.2: Examples of: TPC electron distribution fit for  $0.4 < \eta < 0.5$  and  $0.2 < p < 0.3$  GeV/ $c$  (left); TOF electron distribution fit for  $-0.1 < \eta < 0.0$  and  $1.4 < p < 1.5$  GeV/ $c$  (right).

compared to all of the other periods in the same year, to check if there are any anomalies or different behaviors between periods. In general the re-calibration maps are completely similar within the periods of the same year. If there are no differences, such as in 2016 and 2017, the fit is performed again over the full sample (all periods) and this map is taken as correction for all of the periods in the same year. The 2018 is the only year where some periods present differences between themselves. These differences are due to the availability<sup>3</sup>, or not, of the TPC Splines. To take care of these differences, two different maps were created for 2018, the maps using all of the periods containing TPC splines and the maps for periods that do not have the splines available. For simplicity, only an example of the re-calibration results using 2016 data is shown on this Section - Figure 4.3 for the TPC and 4.4 for TOF, remembering that the full description with all of the periods and years can be found in in the Appendix C.1.

These corrections are extremely useful to avoid selecting wrong hadrons by shifting the PID signals or even losing electrons. If the width of this uncalibrated distribution is greater than the expected for a Gaussian signal ( $1\sigma$ ), we will be losing electrons when applying our cuts of, e.g.  $3\sigma$ . If the width is smaller, on the other hand, our  $3\sigma$  will select electrons more far from the real  $3\sigma$  cut, allowing to select hadrons. If the PID is shifted in relation to the distribution center, electrons will be lost in the selection and we will also have a higher probability of selecting hadrons instead of electrons. This is important since electrons will be paired with other electrons, and the purity of the samples should be maxed out at the same time that the rejection of real electrons should be diminished.

<sup>3</sup><https://twiki.cern.ch/twiki/bin/view/ALICE/TPCSplines> - CERN Certificate needed

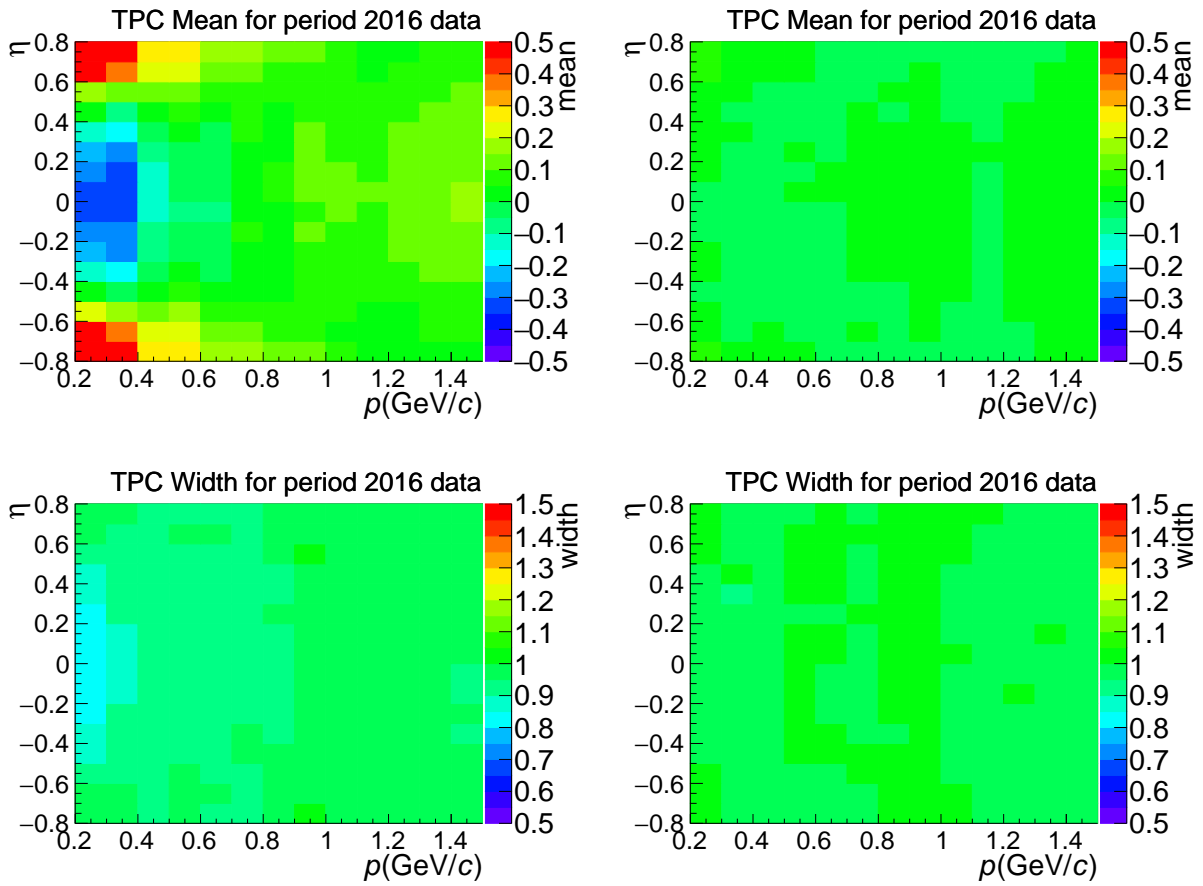


Figure 4.3: TPC electron spectra for 2016 data before (left) and after (right) the recalibration of the PID.

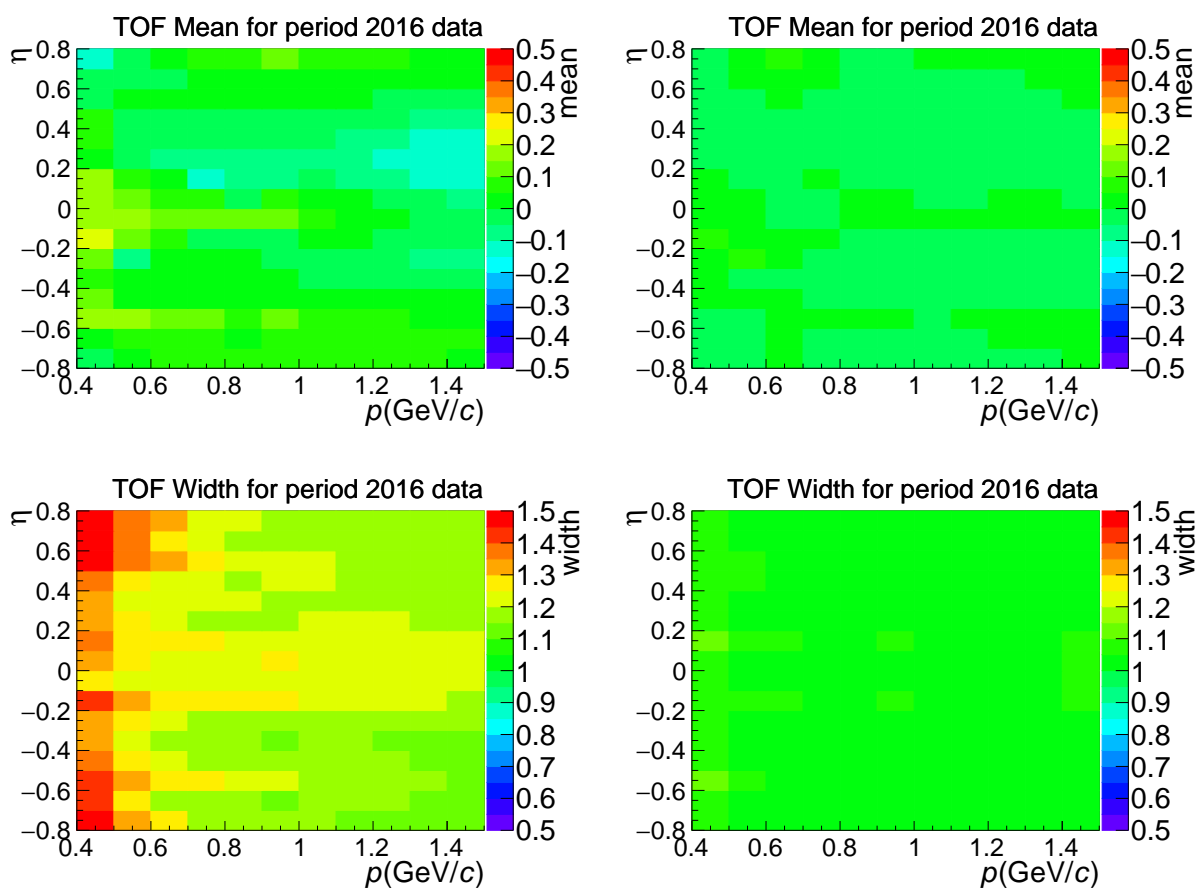


Figure 4.4: TOF electron spectra for 2016 data before (left) and after (right) the recalibration of the PID.

## 4.6 Pairing and Signal Extraction

Once a track is accepted and it is selected as an electron candidate in a selected event, this track is paired with all other electron candidates selected by the same procedure in the same event. All of the important parameters, such as  $p_{T,ee}$ ,  $m_{ee}$ ,  $DCA_{xy}^{ee}$ ,  $\Delta\varphi_{ee}$  and  $\Delta\eta_{ee}$  will be saved to further offline analysis during this pairing process. It is also important to differentiate whether it is an unlike-sign (charged) pair (ULS) or a like-sign (LS). The same analysis is also carried out for electrons in different selected events (mixed events), in order to subtract non-physical signals and also to identify differences in the acceptance of ULS and LS pairs.

### 4.6.1 Invariant Mass Yield

There are essentially two ways to follow the analysis in order to study the heavy-flavour production. The first one is to consider the full dielectron invariant mass yield, which provides us more statistics and also the investigation over this full yield. The problem arises because of the high contributions of electrons from another decaying sources, as it is shown in published 2016 data (Figure 2.10 [19]). The second way is to consider only a small range of the invariant mass spectrum where we have a predominant and clear contribution of heavy-flavour electrons, between 1.1 and 2.7 GeV/ $c^2$ . The statistics is reduced, but we have also a very clear environment, which is preferable for the analysis. The following data analysis description and also all MC analysis will use the same invariant mass cut to perform the selection of paired heavy-flavour electrons.

### 4.6.2 Signal Extraction

The pairing of all electrons in an event with each other is done because experimentally it is not possible to identify directly the origin of each electron created. This pairing method will bring both cases of correlated and uncorrelated electrons. Correlated electrons are electrons that were created together and hence they have physical properties to be investigated. Uncorrelated electrons are electrons that were paired only because of the combinatorial method but not because they carry physical information. We will denote correlated electrons as our physical signal ( $S$ ) to be obtained, and the uncorrelated electrons as our background ( $B$ ). The identification of these two contributions can be done since the physical signal come dominantly from unlike-sign (ULS) pairs, which means that these paired electrons have opposite charges. The like-sign (LS) pairs carry essentially, but not only, unphysical signal. There is a chance to produce correlated LS pairs as a final state of a  $\pi_0$  decay ( $\pi_0 \rightarrow \gamma^{(*)}\gamma^{(*)} \rightarrow e^+e^-e^+e^-$ ) and also, for higher invariant mass, correlated LS pairs can come from electrons produced in away side jets. LS pairs can be also correlated when produced by beauty pairs, either via oscillation of one of the B

mesons or via  $B \rightarrow e^+$  while  $\bar{B} \rightarrow D \rightarrow e^+$ . The background is then described as the geometric mean of the two different LS pairs:

$$B_{geo} = 2\sqrt{N_{++} \cdot N_{--}} \quad (4.4)$$

Where  $N_{++}$  are the paired positrons and  $N_{--}$  are the paired electrons. It is important to mention that sometimes, in regions with low statistics, it may happen that one of the LS pairs ( $N_{++}$  or  $N_{--}$ ) have empty bins. If that is the case, the geometric mean is not used and we use the arithmetic approach only in these regions, otherwise this empty bin would zero the total background. The arithmetic approach is the sum between the  $N_{++}$  and  $N_{--}$  pairs:

$$B_{arith} = N_{++} + N_{--} \quad (4.5)$$

This background still needs to be corrected by the different acceptances of the detector for ULS and LS pairs. In order to find these acceptances, the same analysis is carried out for electrons in different events, and so they do not carry any physical signal. To quantify this effect the correction factor  $R$  is defined as:

$$R = \frac{N_{+-}^{mix}}{2\sqrt{N_{++}^{mix} \cdot N_{--}^{mix}}} \quad (4.6)$$

Where  $N_{+-}^{mix}$  is the number of ULS pairs found in mixed events and  $N_{++}^{mix}$  and  $N_{--}^{mix}$  the number of LS pairs found in mixed events. If the acceptance for ULS and LS is the same, then this  $R$  factor is unitary. The real signal is then calculated as:

$$S = N_{+-} - RB = N_{+-} - 2R\sqrt{N_{++} \cdot N_{--}} \quad (4.7)$$

When it is necessary to group the results from many years together (e.g. 2016 + 2017 + 2018), one could try to add the separated signals (ULS-LS) from each of these years with the number of events in each year as a weight. However, this does not help us to solve problematic areas with low statistics. At this point of the analysis it was not necessary to include the efficiency correction discussion to the signal since it can be done afterwards by only normalizing the extracted signal  $S$  by the efficiency  $\epsilon$  of a given measurement. However, when dealing with the sum of different data-taking years it will be necessary to use the already efficiency-corrected ULS and LS contributions, that will be better described later in Section 5.2.6. To increase the background statistics in problematic regions and to minimize the number of LS empty bins, what is actually done is the sum of all of the efficiency-corrected  $N_{+-}$  pairs from all years together, followed by a sum of all of the  $N_{++}$  and  $N_{--}$  separately:

$$N_{+-}^{tot} = \frac{N_{+-}^{2016}}{\epsilon_{2016}} + \frac{N_{+-}^{2017}}{\epsilon_{2017}} + \frac{N_{+-}^{2018}}{\epsilon_{2018}} \quad (4.8)$$

$$N_{++}^{tot} = \frac{N_{++}^{2016}}{\epsilon_{2016}} + \frac{N_{++}^{2017}}{\epsilon_{2017}} + \frac{N_{++}^{2018}}{\epsilon_{2018}} \quad (4.9)$$

$$N_{--}^{tot} = \frac{N_{--}^{2016}}{\epsilon_{2016}} + \frac{N_{--}^{2017}}{\epsilon_{2017}} + \frac{N_{--}^{2018}}{\epsilon_{2018}} \quad (4.10)$$

After this, it is calculated the final background with these summed  $N_{++}^{tot}$  and  $N_{--}^{tot}$  by using the Equations 4.44.5, which we then subtract from the summed  $N_{+-}^{tot}$  pairs of all of the years together. All of the signal extraction starts with a rebinning of all of the  $N_{+-}$ ,  $N_{++}$  and  $N_{--}$ , in order to have a better signal to background ratio. This way we take into account different efficiencies due to different data-taking years and reduce the statistical uncertainties of the subtraction. This procedure was used in all of the analyzed signals, so the efficiencies for each signal was obtained for the three years separately. Additionally, the signal extraction was performed not only for all of the years together, but also separately for further studies of the measurements as a function of the data-taking year.

### 4.6.3 $\Delta\eta$ $\Delta\varphi$ signal

The  $\Delta\eta_{ee}$   $\Delta\varphi_{ee}$  for all ULS and LS pair cases and also for mixed events for 2016 data were analyzed in the invariant mass range of 1.1 to 2.7 GeV/ $c^2$  to build the background contribution by using the process described in Equation 4.7, shown in Figure 4.5. All the presented results here are normalized by the number of analyzed events. In Figure 4.6 it is also shown the  $\Delta\eta\Delta\varphi$  signal as a function of momentum intervals. It becomes evident that increasing the momentum, the opening angle of the pairs decreases. This behaviour is in agreement with the expected for a constant range of invariant mass analysis, where as the momentum of a given particle increases, the opening angle of its decays must decrease. This physical decay constrain by a given mother and its decay products follow the kinematic relation:

$$M^2 = m_1^2 + m_2^2 + 2p_{T1}p_{T2}(\cosh(\Delta\eta_{12}) - \cos(\Delta\varphi_{12})) \quad (4.11)$$

where  $M$  is the invariant mass of the mother particle,  $m_{1,2}$  are the masses of the decay products (electrons in our case),  $p_{T1,2}$  is the momentum of the decays, and  $\Delta\eta_{12}$  and  $\Delta\varphi_{12}$  are the difference in  $\eta$  and  $\varphi$ . In a common invariant mass analysis, the mass interval considered is constant in all of the momentum intervals, so as  $M$ ,  $m_1$  and  $m_2$  are constant, if the momentum of the pair increases, the opening angle must decrease to balance the equation. Since beauty and charm electrons are uncorrelated within each other ( $b \rightarrow \dots \rightarrow e$ ,  $c \rightarrow \dots \rightarrow e$ ), this signal will be composed of the beauty and charm

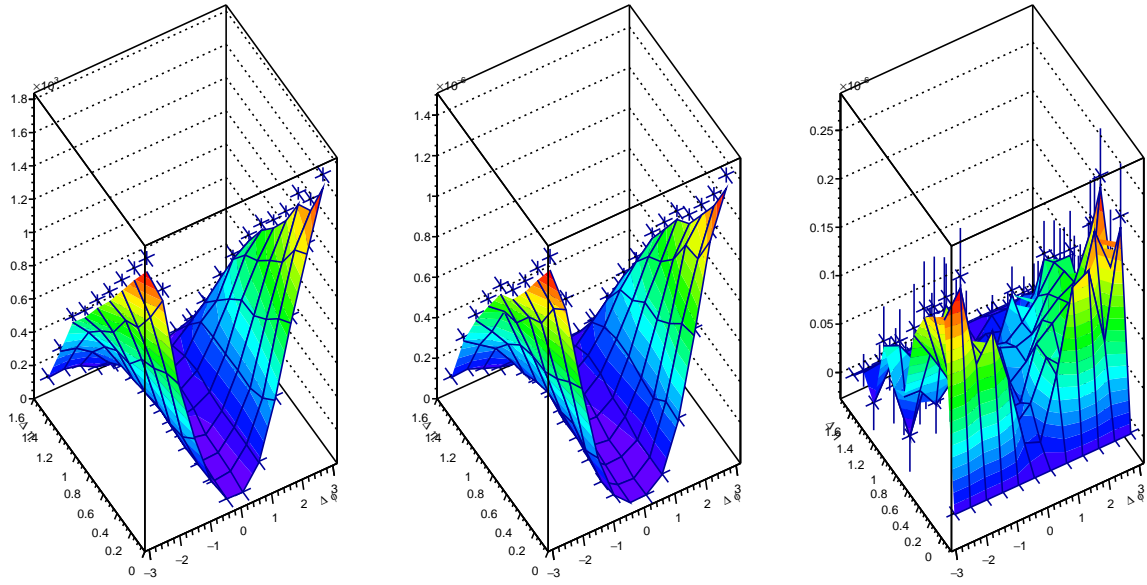


Figure 4.5: The ULS  $\Delta\eta$   $\Delta\varphi_{ee}$  signal is shown on the left plot and the final background B\*R in the center. In the right panel is shown the result of the subtraction of the background to the physical signal of correlated ULS electrons for integrated pair transversal momentum -  $0 < p_{T,ee} < 6$  GeV/c.

dielectron contributions separately.

The  $\Delta\eta_{ee}$   $\Delta\varphi_{ee}$  signal was included here as a matter of example and for completeness of the  $\Delta\varphi_{ee}$  analysis. The results shown in this section are not efficiency-corrected, so only the raw signals are shown. The full differential dielectron cross section of a given parameter is described in the next section.

#### 4.6.4 Dielectron Cross Section

The differential dielectron cross section is reported as:

$$\frac{d\sigma_{ee}}{dy_{ee}} = \frac{1}{L_{int}} \frac{S}{y_{ee} \varepsilon_{ee}^{trig} \varepsilon_{ee}^{vtx} \varepsilon_{ee}^{rec}}, \quad (4.12)$$

where:

- S is the measured dielectron signal with respect to  $y_{ee}$ , such as  $\Delta\varphi_{ee}$ ,  $DCA_{xy}^{ee}$ ,  $p_{T,ee}$ ,  $m_{ee}$  or mixed;
- $L_{int}$  is the integrated luminosity, which is calculated as the ratio between the number of events triggered by V0AND and the V0AND cross section ( $\sigma_{pp}^{V0AND} = 57.8 \pm 2.9$  mb). The number of V0AND triggered events is the number of events analyzed corrected by the vertex reconstruction efficiency ( $\varepsilon_{evt}^{vtx} = 0.973 \pm 0.001$ );



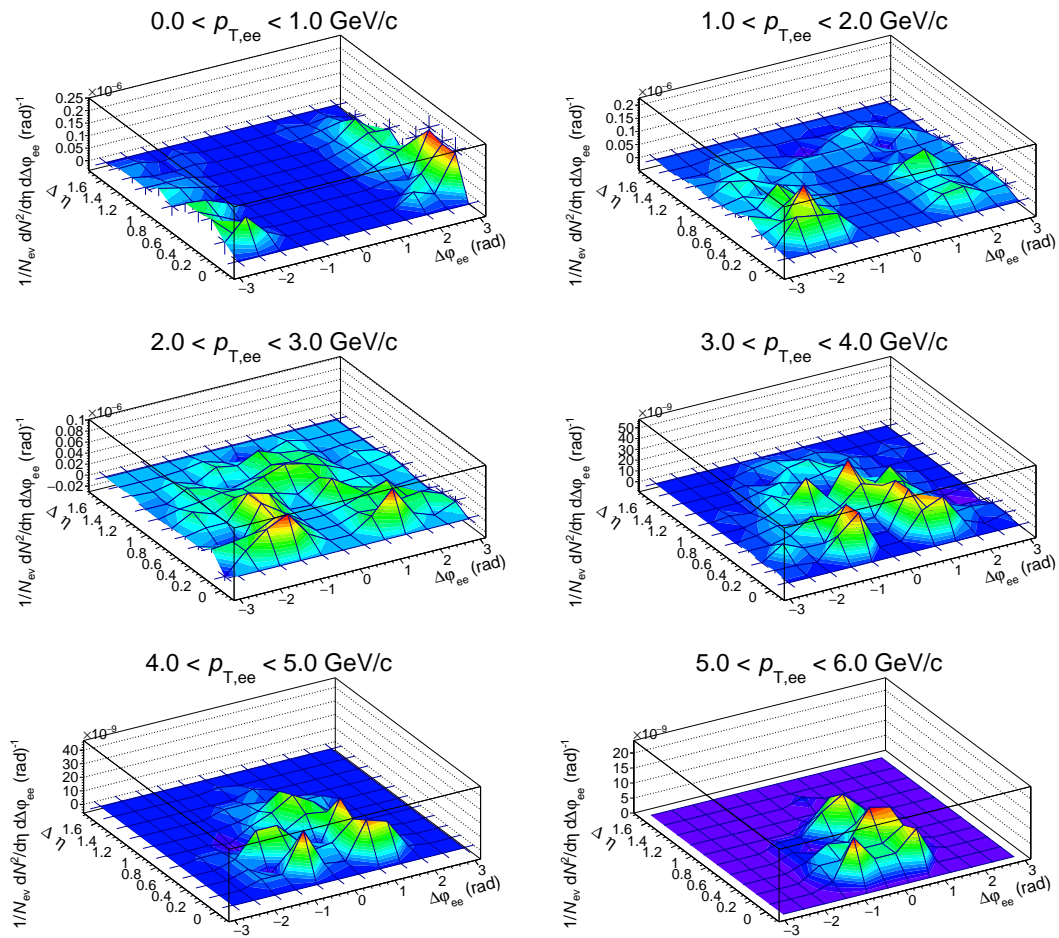


Figure 4.6:  $\Delta\eta\Delta\phi$  distributions of heavy-flavour electrons. The  $p_{T,ee}$  intervals are shown in the titles and all the plots are from dielectrons in the interval of  $1.1 < m_{ee} < 2.7$  GeV/ $c^2$ .

- $\varepsilon_{ee}^{trig}$  is the V0AND efficiency to trigger on a pp collisions containing an  $e^+e^-$  in the acceptance of the kinematic track cuts and it is found to be  $0.99 \pm 0.01$ ;
- $\varepsilon_{ee}^{vtx}$  is the vertex reconstruction efficiency for events that contain an electron pair in the acceptance and fired the V0AND trigger, found to be 1;
- $\varepsilon_{ee}^{rec}$  is the efficiency to reconstruct an dielectron pair in the acceptance (described in Section 5.2.6) in events with a reconstructed vertex that fired the V0AND trigger.

The complete signal extraction and differential dielectron cross sections for  $p_{T,ee}$ ,  $m_{ee}$ ,  $\Delta\varphi_{ee}$  and  $DCA_{xy}^{ee}$  will be detailed later in each of their respective analysis chapters.

## 4.7 Systematic Uncertainties

This section describes how the systematic uncertainties of the data were evaluated. For this purpose, several different sets of cut variations were created by varying the electron selection criteria [18], from the track selection to the identification. These configurations can be separated into 3 main groups that should not to be correlated with each other, so the variations can be done separately between these groups. The first group are a set of 2 different cut variations of the electron identification in the TPC, using a tighter and a looser cut. The second group have again 2 different cut variations of the electron identification in the TOF detector, using a tighter and a looser cut. The last group are 20 different track cuts picked randomly between normal, tight or loose cuts, and all of the possible cuts are varied at the same time to check possible correlations between these cuts.

The eID and track cut variations can be found in Tables 4.5 (eID) and 4.6, respectively. Each of the different track cuts were selected randomly (normal, tight or loose) to create a new configuration of track cuts. The exact same cut variations were also run in MC to obtain the efficiencies of each configuration. These systematic uncertainties evaluated contain systematic effects from signal efficiency and background estimation, which may vary depending on the set of cuts.

The root mean square (RMS) of the differences between the data signal of different configurations and the original data in larger binning is then calculated for all bins and the value found in each bin is inserted as the systematic uncertainty of the respective bin. Each of the systematic uncertainties of the studied signals ( $m_{ee}$ ,  $DCA_{xy}^{ee}$ ,  $\Delta\varphi_{ee}$  and  $p_{T,ee}$ ) will be shown in their own analysis chapters.

Configuration	Variable	Variation	Normal Requirement 4.3
TPC Loose	$n\sigma_{TPC}^{ele}$	[-3.5, 3.5]	[-3.0, 3.0]
	$\sigma_{TPC}^{pio}$ rej.	[-inf, 3.5]	[-inf, 4.0]
	$\sigma_{TPC}^{kao}$ rej.	[-3.5, 3.5]	[-4.0, 4.0]
	$\sigma_{TPC}^{pro}$ rej.	[-3.5, 3.5]	[-4.0, 4.0]
TPC Tight	$n\sigma_{TPC}^{ele}$	[-2.5, 2.5]	[-3.0, 3.0]
	$\sigma_{TPC}^{pio}$ rej.	[-inf, 4.5]	[-inf, 4.0]
	$\sigma_{TPC}^{kao}$ rej.	[-4.5, 4.5]	[-4.0, 4.0]
	$\sigma_{TPC}^{pro}$ rej.	[-4.5, 4.5]	[-4.0, 4.0]
TOF Loose	$n\sigma_{TOF}^{ele}$	[-3.5, 3.5]	[-3.0, 3.0]
TOF Tight	$n\sigma_{TOF}^{ele}$	[-2.5, 2.5]	[-3.0, 3.0]

Table 4.5: Electron identification variations applied for systematic uncertainty study.

Configuration	Loose	Common Cut 4.2	Tight
DCAxy	2.0 cm	1.0 cm	0.7 cm
DCAz	5.0 cm	3.0 cm	2.0 cm
Min. N. of Clus. TPC	100	80	60
Min. N. of Cross Rows TPC	120	100	80
Min. Ratio Cros./Find. TPC	0.9	0.8	0.6
Max. Fraction of Shared TPC Clus.	1.0	0.4	0.2
Maximum $\chi^2$ TPC	6.0	4.0	3.0
Min. N. of Clus. ITS	2	3	4
Maximum $\chi^2$ ITS	6.0	4.5	3.5
SPD hit	kAny	kFirst	kBoth

Table 4.6: Track cut variations applied for systematic uncertainty study.



# 5 Monte Carlo Analysis

The purpose of this chapter is to present the strategy used to analyze the Monte Carlo samples, how the pure Monte Carlo studies are carried out to produce the cocktail templates used for fitting the data signals (Section 5.1) and how the reconstructed samples are analyzed to obtain the efficiencies of the studied signals (Section 5.2).

## 5.1 Pure Monte Carlo

### 5.1.1 Produced samples

PYTHIA (6.4 Perugia 2011 tune)[81] and POWHEG [82] simulations of pp collisions at  $\sqrt{s} = 13$  TeV were produced in order to obtain predictions of the analyzed distribution functions between heavy-flavour electrons generated by different production mechanisms. These simulations were not propagate through GEANT, so they are only a pure generated MC - not reconstructed. The PYTHIA samples were produced directly using the SAMPA<sup>1</sup> grid at São Paulo - Brazil (also part of the ALICE grid), while the POWHEG samples were produced in the ALICE grid. POWHEG cannot identify a particular production mechanism, since it employs exact NLO matrix elements in the calculations of the hard scattering processes, but it still can provide us predictions of the distribution functions of dielectrons from  $c\bar{c}$  and  $b\bar{b}$  pairs.

For this purpose, the charmed heavy hadrons were forced to decay into electrons (but not the beauty), in both PYTHIA and POWHEG. In both charm and beauty simulations it was not requested any spatial preference to the created electrons. The total number of generated events for each simulation is shown in the Table 5.1. The reason of the difference in the number of generated events for PYTHIA and POWHEG is the large size of the simulations. Moreover, since in PYTHIA it is possible to discriminate over the production mechanisms, it was created more charm events in order to have enough statistics to separate the processes. In PYTHIA simulations the creation of the heavy-flavour pair was done through the choice of some specific production processes (ISUB) [83]: 11 ( $f_i f_j \rightarrow f_i f_j$ ), 28 ( $f_i g \rightarrow f_i g$ ), 53 ( $gg \rightarrow f_k \bar{f}_k$ ), 68 ( $gg \rightarrow gg$ ). The contributions from 11 and 53

---

<sup>1</sup>Advanced Multi-Processing Analysis System - <http://hepic.if.usp.br/>

corresponds to flavour creation processes, while 28 to flavour excitation and 68 to gluon splitting.

Generator	HF pair	Number of Events
PYTHIA	$c\bar{c}$	250 M
	$b\bar{b}$	100 M
POWHEG	$c\bar{c}$	30 M
	$b\bar{b}$	30 M

Table 5.1: Number of generated events.

### 5.1.2 Event and Track Selection

PYTHIA and POWHEG simulations were produced in order to investigate the distribution of  $p_T$ ,  $m_{ee}$ ,  $DCA_{xy}$  and  $\Delta\varphi$  between heavy-flavour electrons as a function of the mechanism that generated the heavy-flavour pair. As already mentioned, in POWHEG we cannot differentiate the mechanism that generated the pair, but we can check how these distributions behave for the  $c\bar{c}$  and  $b\bar{b}$  pairs.

The analysis described in this section is done for both charm and beauty files separately, since these simulations were also created separately. In order to have a clear environment for the analysis, we only analyze events with the following characteristics:

- For  $c\bar{c}$  analysis: It is only analyzed events where there are no beauty or anti-beauty quarks present, and when they have only one charm and one anti-charm quark. PYTHIA only provide us the information of one production mechanism, so if there are more heavy-quarks pairs produced it may be tricky to determine which one is the right heavy-quark produced by that mechanism reported by PYTHIA. Moreover, we may not have access to the information of the exact parents of the  $c\bar{c}$ , so it is impossible to pair one of the charm quarks,  $c$ , with its respective partner  $\bar{c}$  if there are more than one  $c\bar{c}$  pair - see [47] for a deeper discussion on this topic.
- For  $b\bar{b}$  analysis: In this case, since we are not looking to disentangle also the production mechanism of the beauty pair, only to obtain the total contribution, there is no limitation to the number of beauty and anti-beauty number of quarks or if there are charm quarks present. All events containing beauty quarks are analyzed. A test was performed using a cut of only 1  $b\bar{b}$  per event, or no  $c\bar{c}$  present but that did not modify the results, only reduced the statistics.

After the selection of the event, a track will be only considered if it satisfies the same kinematics cuts applied to data tracks (Section 4.2), which are the  $p_T$  and  $\eta$  cuts. The  $p_{T,e}$ ,  $\eta_e$  and  $\varphi_e$  smearing process that will be described later in Section 5.2.4 is also applied to these PYTHIA and POWHEG simulations in order to improve the comparison between reconstructed data and these generated simulations.

### 5.1.3 Heavy-Flavour Electron Identification

After the event and track selection, the next step is to identify if the track is a heavy-flavour electron. For  $c\bar{c}$  analysis we only select electrons from charm and for  $b\bar{b}$  analysis electrons from beauty. To do that, it is required:

- Charmed electron:
  - The pdg of the particle should be  $\pm 11$  (positron/electron);
  - The mother must exist and its pdg must be one of the pdg numbers of D mesons or baryons ( $|\text{pdg}|$  between 411 - 435, 4113 - 4445);
  - It can not be a beauty electron. This happens because for charm we only look at the immediate mother, but a beauty hadron can also decay into a D meson. A beauty electron is identified as described in the following.
- Beauty electron:
  - The pdg of the particle should be  $\pm 11$ ;
  - The pdg of the its mother<sub>i</sub> must be one of the pdg numbers of B mesons or baryons ( $|\text{pdg}|$  between 500 - 600, 5000 - 6000), or its mother could also be a D meson;
  - If the first mother pdg is already a beauty hadron, that is a beauty electron. If the pdg of the first mother is a D meson, on the other hand, we check recursively until we find if the ascendant mothers that generated these D mesons were a beauty hadron, which in a positive case, are also considered as a beauty electron.

### 5.1.4 Pairing

Essentially, the pairing of the heavy-flavour electrons are done under the finding of 2 or more different HFe in the same event. To do that we make a loop over all particles in the selected event and try to find one heavy-flavour electron which satisfies the track cuts. If it exists, we make a second loop trying to find its partner. For charm analysis we only look for ULS dielectrons, but for beauty analysis we also save both ULS and LS contributions. For charm we only look at ULS pairs since we only analyze events with only one charm and one anti-charm, so we should only find correlated signals from charm. Once we find them, we just save all important information, such as  $p_{T,ee}$ ,  $m_{ee}$ ,  $\Delta\varphi_{ee}$ ,  $\Delta\eta_{ee}$ ,  $\text{DCA}_{xy}^{ee}$ , and also which production mechanism generated the heavy quark. In the beauty case the process is a little bit more complicated since we can have more than one electron per heavy quark because beauty hadrons can also decay into a D meson plus one

electron, or it can oscillate. To take this into account the beauty templates are built by the subtraction of the LS pairs from the ULS; the same way it is done in data.

To compare pure MC templates, i.e., the expected distributions of  $p_{T,ee}$ ,  $m_{ee}$ ,  $\Delta\varphi_{ee}$  and  $DCA_{xy}^{ee}$  from the pure MC analysis, to the extracted data signals, it is necessary to normalize the entries of the distributions to obtain them in cross section units. This can be done through a scaling factor:

$$F_{c\bar{c}} = \frac{\sigma_{c\bar{c}}}{N_{c\bar{c}}|_{|y|<0.5}} B.R._{c \rightarrow e}^2 \quad (5.1)$$

for charm analysis, and:

$$F_{b\bar{b}} = \frac{\sigma_{b\bar{b}}}{N_{b\bar{b}}|_{|y|<0.5}} \quad (5.2)$$

for beauty analysis.  $\sigma_{c\bar{c}}$  and  $\sigma_{b\bar{b}}$  are charm and beauty cross sections,  $B.R._{c \rightarrow e}$  is the probability of the charm quark to decay into an electron and it is  $6.93_{-0.28}^{+0.24}$  %, and  $N_{c\bar{c}}|_{|y|<0.5}$  and  $N_{b\bar{b}}|_{|y|<0.5}$  are the number of  $c\bar{c}$  and  $b\bar{b}$  pairs, respectively, at midrapidity ( $|y| < 0.5$ ), which are parameters that are analogous to the luminosity parameter in the analysis over data. The branching ratio is only used to normalize charm samples because there is the only simulation where the hadrons were forced to decay into electrons. Since both of the correlated electrons from charm came from a forced decay, the BR must be taken to the square. The cross sections used in this normalization normally are a known cross section from measurement or from calculations, such as from FONLL ( $\sigma_{c\bar{c}}^{FONLL}$  and  $\sigma_{b\bar{b}}^{FONLL}$ ), so the final signal is already ready to be compared to data or to be used in some simulations. However, since we want to use these templates for fitting, we can just set this cross section as 1  $b$  (or 1  $mb$ , or 1  $\mu b$ ) and the signal then will be in the common cross section units of  $b$  ( $mb$ ,  $\mu b$ ), which is easier for the future fits.

## 5.2 Reconstructed Monte Carlo

### 5.2.1 Monte Carlo samples

All of the same event cuts (Section 4.2), track cuts (Section 4.3) and PID (Section 4.4) cuts are carried out exactly as it is done in data. To have nearly perfect  $n\sigma_{TPC}^{ele}$  signal in MC data the "TuneOnData" option is turned on (more details in Sections 4.5 and 5.2.3). The 2016, 2017 and 2018 MC data were considered in this analysis. The detection efficiencies are calculated using Monte Carlo (MC) simulated data anchored to the corresponding data-taking period. These simulations are attempts to reproduce the same detector configurations by using all the known details, calibrations, and effects of the detectors. To have enough statistics it is used the heavy-flavour enriched MC simulation,



produced with PYTHIA 6 (Perugia tune). The MC simulated data used in the analysis can be found in Table 5.2 containing the ALICE production names.

Year	Data Period	Heavy-flavour enriched MC (productions)
2016	d	LHC16j4h
	e	LHC16j4i
	g	LHC16j4j
	h	LHC16j4k
	i	LHC16j4b
	j	LHC16j4c
	k	LHC16j4f
	l	LHC16j4g
	o	LHC16j4d
	p	LHC16j4e
2017	c, e, f, h	LHC18k9a
	i, j, k, l	
	m, o, r	
2018	b, d, e, f	LHC18k9b
	h, i, k, l	
	m, n, o, p	

Table 5.2: Monte Carlo samples used in the analyses.

In each of these MC samples we have the following processes:

- $c\bar{c} \rightarrow e^+e^-$  ( $\approx 8\%$ ) or  $b\bar{b} \rightarrow e^+e^-$  (8%): the charmed (beauty) hadrons produced by the  $c\bar{c}$  ( $b\bar{b}$ ) pairs generated are forced to decay semileptonically, and their products, the electrons, are constrained to be within  $|y| < 1.2$ ;
- $b \rightarrow e$  ( $\approx 66\%$ ): a  $b\bar{b}$  pair is generated but only one electron is required to be produced in  $|y| < 1.2$ . Other charmed or beauty hadrons (if present) are not forced to decay into electrons or to be within  $|y| < 1.2$ ;
- $J/\psi \rightarrow e^+e^-$  ( $\approx 12\%$ ) and  $B \rightarrow J/\psi \rightarrow e^+e^-$  (6%):  $J/\psi$  production forced to decay into a dielectron pair.

### 5.2.2 Event and Track Selection

The same event cuts that are applied to data (Section 4.2) are also applied to the MC samples to have the same description of the data. However, for MC samples there are some cuts applied regarding the generator level. In MC samples we can identify the generated tracks and correlate them to their respective reconstructed track, in the case of that track was successfully reconstructed. The analysis described in this section is done for both charm and beauty files separately, since these simulations were created separately. In order to have a clear environment for the analysis, we only analyze events with one  $c\bar{c}$  pair in the case of charm and one  $b\bar{b}$  pair in the case of beauty, for efficiency studies.

After the selection of the event, we run over all of the generated tracks, identifying the true HF electrons generated by the simulation in the process already described in Section 5.1.3. After identifying the true HF generated electrons that fits the kinematic cuts of  $p_T$  and  $\eta$ , we find the reconstructed MC track related to this HF electron generated. If it exists, the track must fulfill the same kinematics and track cuts applied to data tracks (Table 4.2), and also de eID scheme (Table 4.3) to be considered in the analysis.

### 5.2.3 TPC and TOF post-calibration

The same procedure of electron identification (Section 4.4) and re-calibration of TPC and TOF PID response (Section 4.5) is also applied for Monte Carlo reconstructed tracks. The only difference is that the correction of the  $n\sigma_{TPC}^{ele}$  as a function of ( $p_T$ ,  $\eta$ , data-taking period) is already implemented in the analysis framework of ALICE when the option "TuneOnData" in PID response task is turned on and the AliMCEventHandler is used. When this procedure is applied, the parameterizations of expected signals of the anchored period are extracted directly from experimental data, resulting in a better description of the re-calibrated signal. All of the MC calibration maps for TPC and TOF can be found in the Appendix C.2, with some more details. For simplicity, here it is only shown the re-calibration results for TPC (Figure 5.1) and TOF (Figure 5.2) for the 2016 anchored MC. The MC samples already present a very good signal response for TPC due to the usage of the "TuneOnData" option (note the z-scale of the plot), but we still can obtain a small improvement by using the maps for correction, specially for low momentum. On the other hand, for the TOF response the improvement achieved is similar to what happens in data.

### 5.2.4 Smearing Procedure

Charged particles are scattered when moving in an external electric or magnetic field, losing part of its energy by radiation emission. Electrons, in special, strongly suffer this effect due to their small mass, possibly reducing the difference between the generated momentum and the reconstructed. This effect can modify the momentum distribution of the tracks and also shift the pair mass. This has a great impact into the efficiency study since the efficiency is taken as the ratio between the generated and the reconstructed tracks in a given interval of the parameters. If the generated parameters do not take these effects into account this would lead to wrong efficiencies and will greatly affect the whole data analysis. To take such effects into account and perform a better comparison between data and simulations, a smearing procedure is applied to the generated particles using the detector response matrices (see Figure 5.3), which are basically 2D histograms containing values of  $p_{T,e}^{rec}/p_{T,e}^{gen}$ ,  $\eta_e^{rec} - \eta_e^{gen}$  and  $\varphi_e^{rec} - \varphi_e^{gen}$  as a function of the  $p_{T,e}^{gen}$ . These histograms are built by selecting true generated electrons and comparing them to their reconstructed

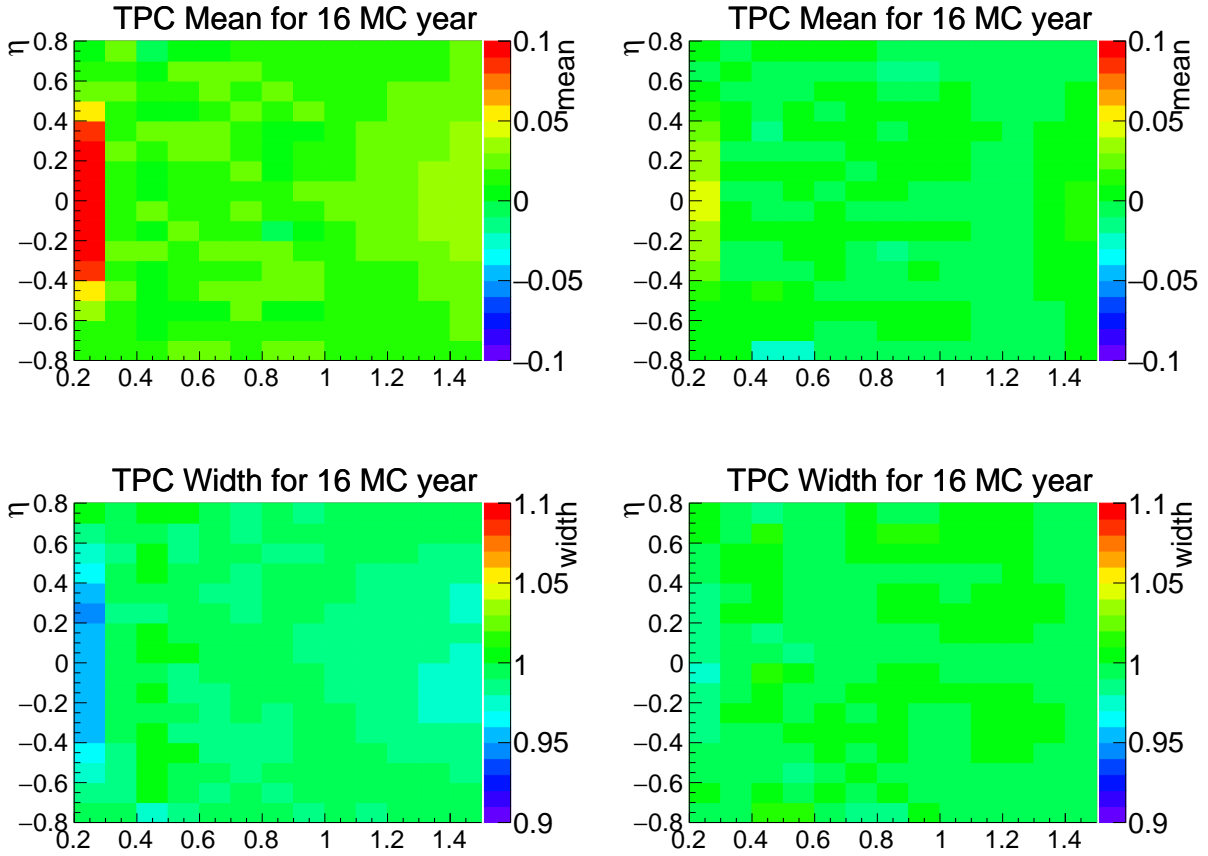


Figure 5.1: TPC electron spectra for 2016 MC year before (left) and after (right) the re-calibration of the PID.

tracks, correlating these distributions of generated and reconstructed parameters.

These response matrices are then used to smear the parameters of the generated particles. For each electron generated  $p_T$ , these response matrices are projected onto the  $p_T^{rec}/p_T^{gen}$ ,  $\Delta\eta$  and  $\Delta\varphi$  forming a probability distribution dependent of the electron generated  $p_T$ , as seen in Figure 5.4. When an electron is found, its generated  $p_T$  is used to get a random number weighted by the distribution probability of these response matrices, for  $p_T$ ,  $\eta$  and  $\varphi$ . The transformation from the generated value to the smeared one (analogous to the really measured) is given by the transformations:

$$p_{T,e}^{smr} = p_{T,e}^{gen} \times rand\left(\frac{p_T^{rec}}{p_T^{gen}}\right) \quad (5.3)$$

$$\eta_e^{smr} = \eta_e^{gen} + rand(\Delta\eta) \quad (5.4)$$

$$\varphi_e^{smr} = \varphi_e^{gen} + rand(\Delta\varphi) \quad (5.5)$$

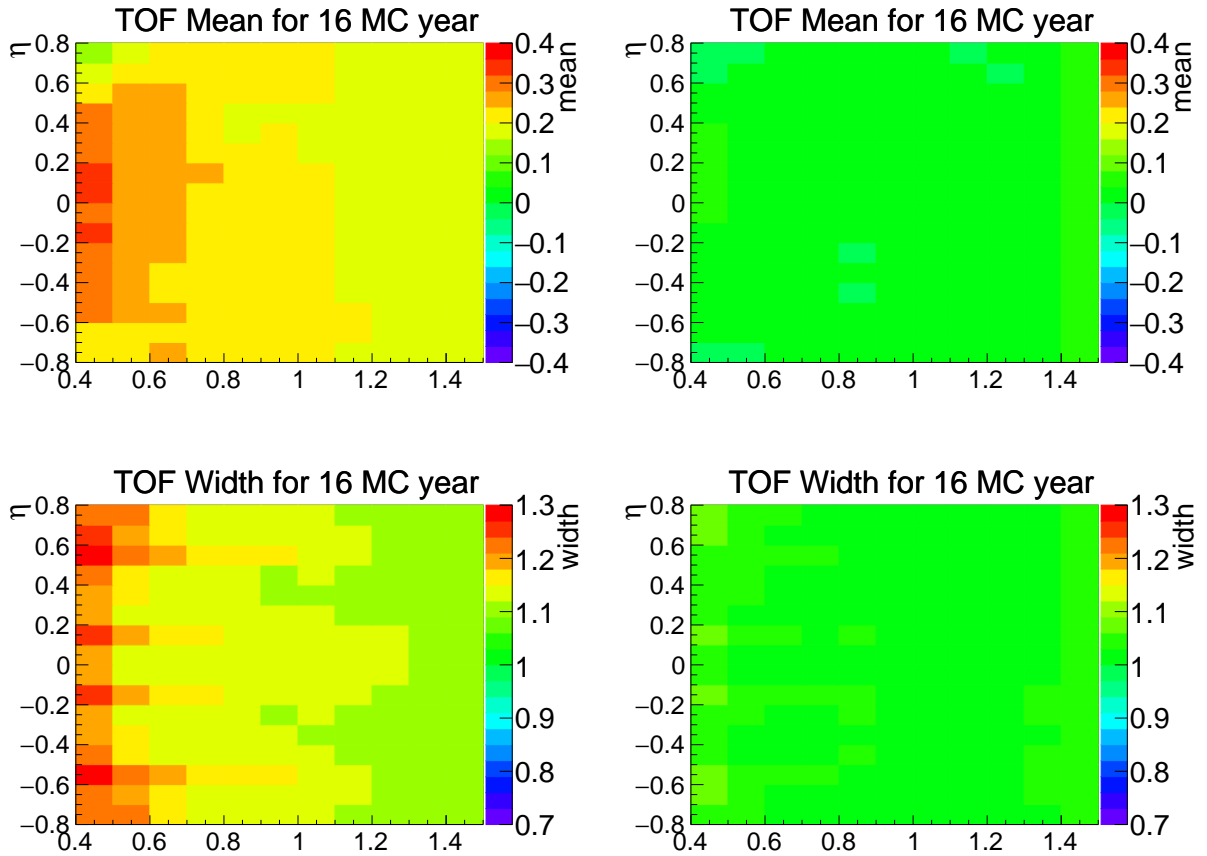


Figure 5.2: TOF electron spectra for 2016 MC year before (left) and after (right) the re-calibration of the PID.

From Figures 5.3 and 5.4 it is clear the great effect of the energy loss of electrons by looking at the  $p_T^{rec}/p_T^{gen}$  ratio. It is also evident that the  $\varphi$  of the electron and positrons are shifted to opposite directions due to the opposite bending in the magnetic field.

Since no dependence between the three parameters was found, the three are smeared independently. This smearing procedure is applied before the kinematic cuts applied to the generated electrons, in order to study the acceptance effects of the detectors with a better comparison between generated and reconstructed particles. Each MC sample use the smearing maps produced for each specific data year: 2016, 2017 or 2018, although here only the smearing for 2016 is shown for simplicity. Even though the smearing maps for different years are very similar in shape, they still present small differences and this procedure is also performed as a function of the year to simulate the right "anchored" templates for different signals from different years of data-taking comparison:  $m_{ee}$ ,  $DCA_{xy}^{ee}$ ,  $\Delta\varphi_{ee}$  and  $p_{T,ee}$ . When the templates are built for the analysis taking into account the three merged years, another smearing map is used, which is an event-weighted<sup>2</sup> sum of

<sup>2</sup>This event weight is extracted from data, taking into account the number of events to perform the sum of these smearing maps.

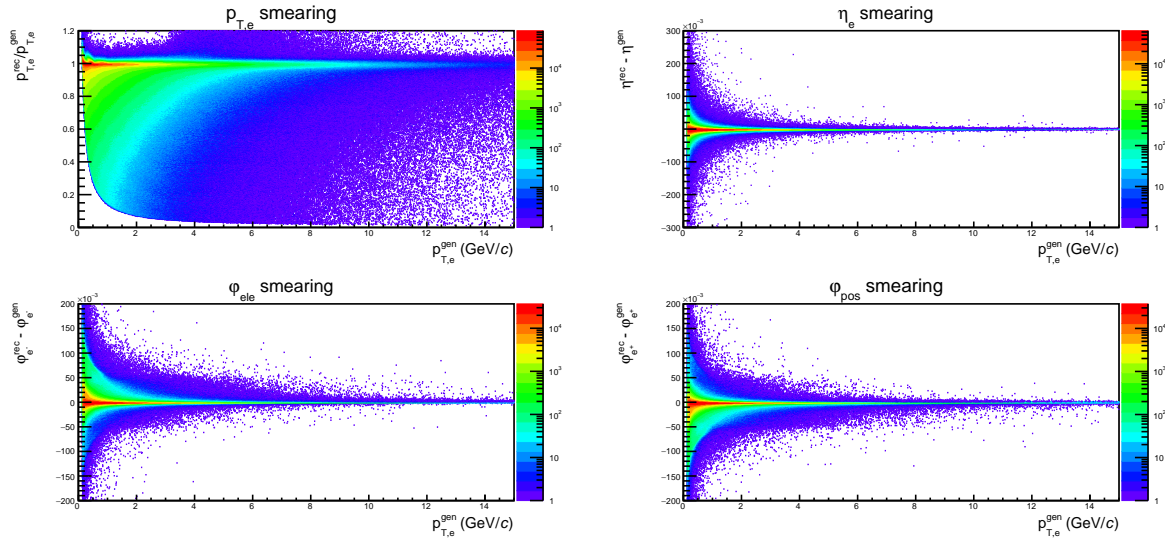


Figure 5.3: Resolution maps used for the smearing of MC generated parameters of 2016 MC anchored data. On top:  $p_T$  smearing on the left and  $\eta$  smearing on the right. On bottom:  $\varphi$  smearing for electrons (left) and positrons (right).

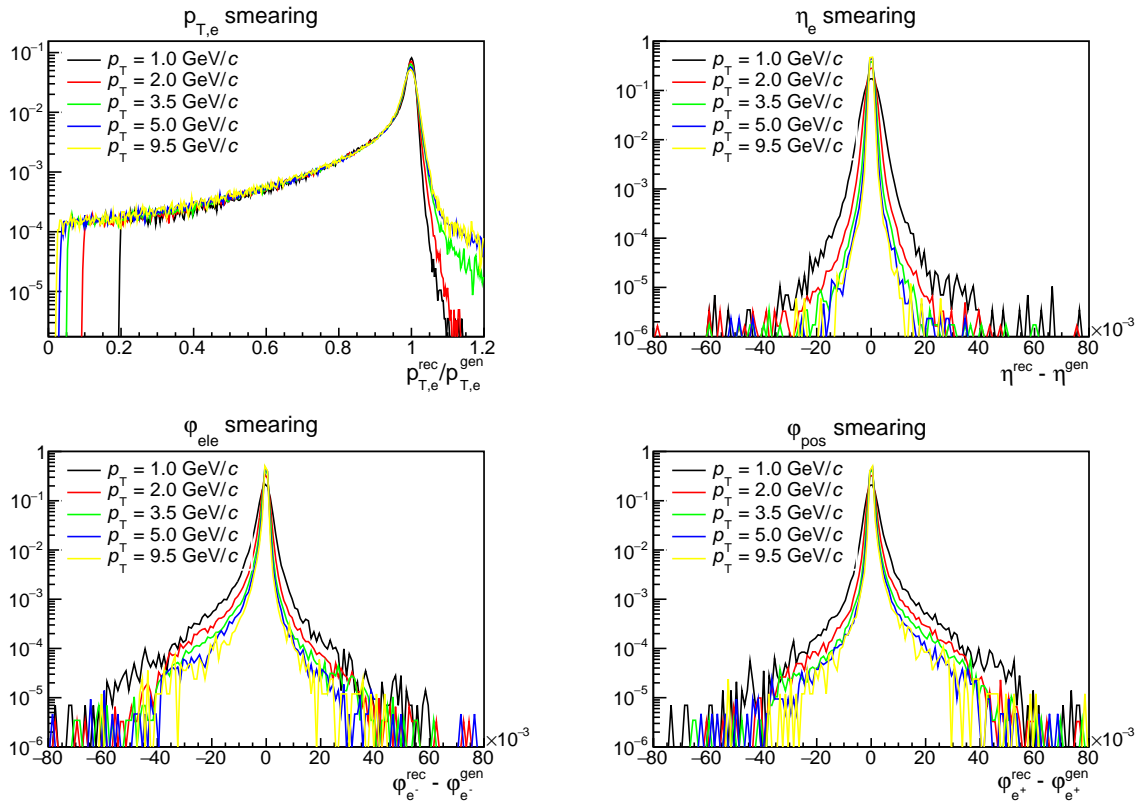


Figure 5.4: Smearing probability distribution of MC generated parameters of 2016 MC anchored data in different  $p_T$  projections. On top:  $p_T$  smearing on the left and  $\eta$  smearing on the right. On bottom:  $\varphi$  smearing for electrons (left) and positrons (right).

the smearing maps of 2016, 2017 and 2018 data.

### 5.2.5 Single Electron Efficiency

The single electron efficiency is calculated as the number of reconstructed electrons when compared to the number of generated electrons. For this case, no misidentified hadrons or electrons from real photon conversions are counted. This is done since we only consider a reconstructed track if that track was a true electron at the generated level. The single electron efficiency,  $\varepsilon_e$ , is calculated as a function of the studied signal  $x = p_T, \eta, \varphi$ :

$$\varepsilon_e(x) = \frac{\left(\frac{dN}{dx}\right)_{rec}}{\left(\frac{dN}{dx}\right)_{gen}} \quad (5.6)$$

The kinematics cuts, e.g.  $|\eta| < 0.8$  and  $p_T > 0.2$  GeV/ $c$ , are applied to both generated (after smearing - Section 5.2.4) and reconstructed electrons. The number of reconstructed electrons are reduced by detector acceptance effects, track cuts, TPC and TOF matching and also in the proper electron identification cuts (PID).

In the upper panel of Figure 5.5 the comparison between the number of reconstructed electrons and positrons as a function of  $p_T$  and  $\varphi$  is shown, as an example, for 2017 MC data. It is observed no preferential reconstruction of electrons or positrons, and the efficiencies are calculated considering no discrimination between electrons and positrons, as shown in the bottom panel of Figure 5.5. The drop of efficiency for low  $p_T$  is due to the hadron rejection cuts applied in eID, as already explained in Section 4.4, since those regions are the places where the kaons and protons had a similar response to the TPC detector as electrons, and were reject (electrons included) when there was no TOF available. A full map of the  $\eta$  and  $\varphi$  efficiencies can be found in Figure 5.6. It is clear that we have different acceptances for tracks in different regions of the phase space of the detector, which can be explained by some inactive areas in the ITS detector.

### 5.2.6 Pair Efficiency

The pair efficiency is calculated using the same idea of the single electron efficiency, but for paired electrons. It is defined as the ratio between the number of reconstructed paired electrons and the number of generated paired electrons as a function of the invariant mass, transverse momentum, and as a function of the  $\Delta\varphi_{ee}$ :

$$\varepsilon_{ee}(x) = \frac{\left(\frac{dN_{ee}}{dy}\right)_{rec}}{\left(\frac{dN_{ee}}{dy}\right)_{gen}} \quad (5.7)$$

for,

$$x = p_{T,ee}, m_{ee}, \Delta\varphi_{ee}. \quad (5.8)$$

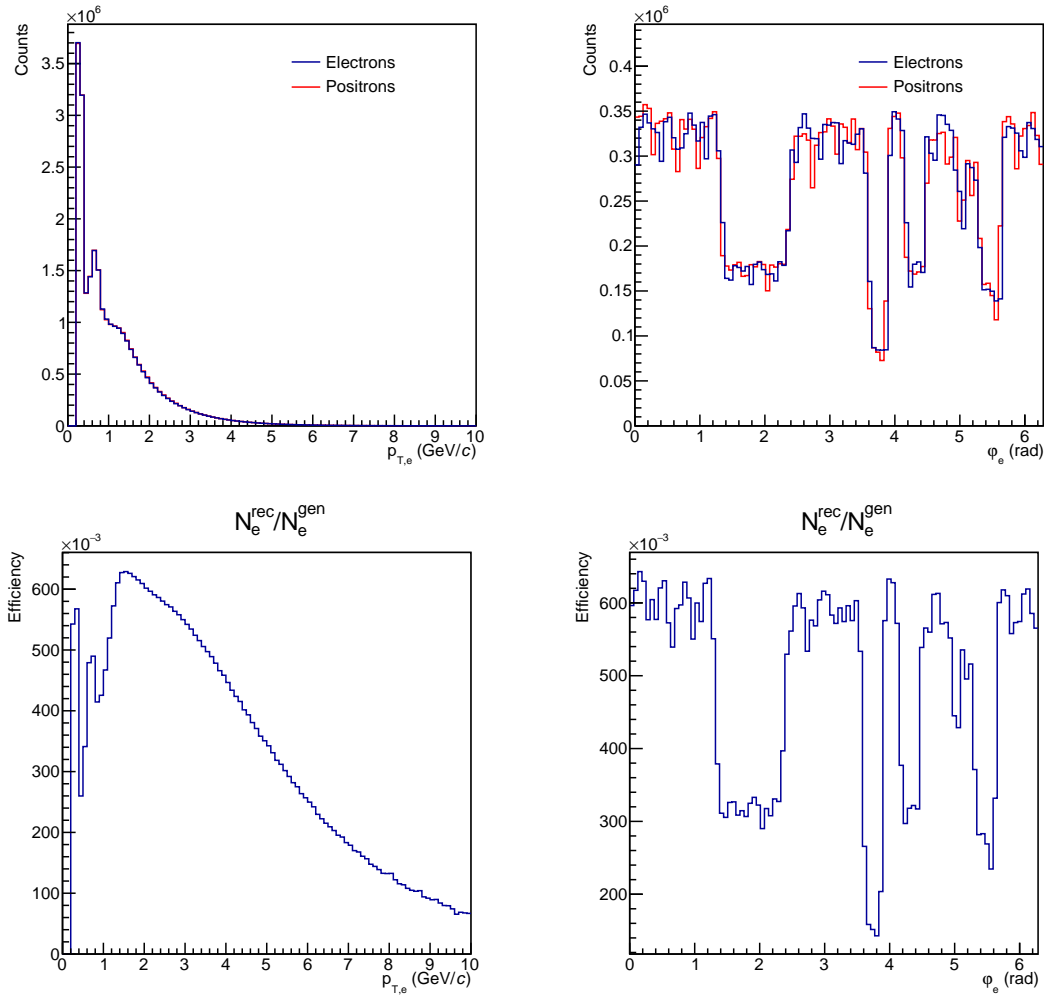


Figure 5.5: Comparison between the number of reconstructed electrons and positrons as a function of  $p_T$  and  $\varphi$  (top), and the calculated efficiencies (bottom).

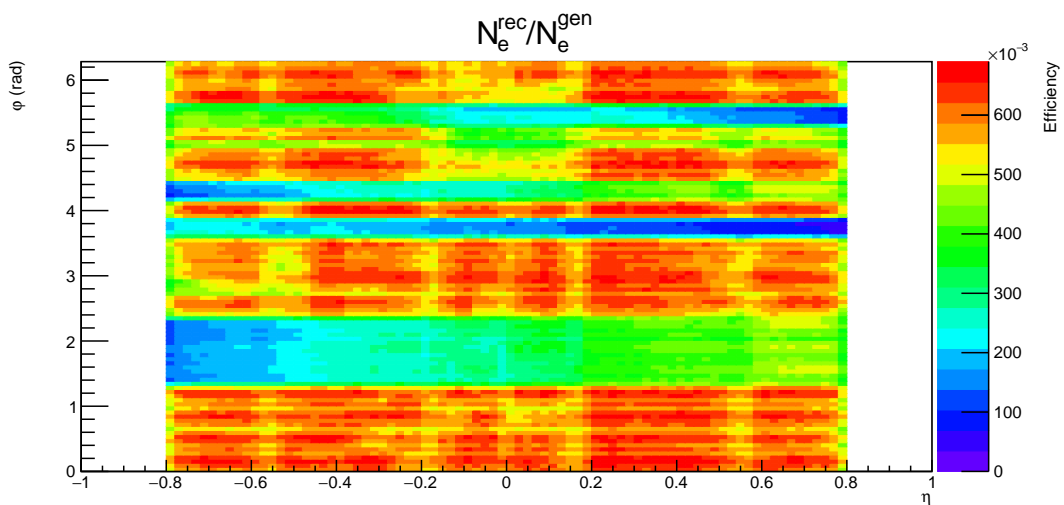


Figure 5.6: Calculated efficiency as a function of  $\eta$  and  $\varphi$ .

The heavy-flavour electron pair efficiency follows the same idea of general single pairs. The only difference is that the electrons are requested to come from heavy-flavour hadrons from the simulations. The heavy-flavour efficiency will then be:

$$\varepsilon_{c\bar{c}\rightarrow ee}(y) = \frac{\left(\frac{dN_{c\bar{c}\rightarrow ee}^{ULS}}{dy}\right)_{rec}}{\left(\frac{dN_{c\bar{c}\rightarrow ee}}{dy}\right)_{gen}} \quad (5.9)$$

for electrons from  $c\bar{c}$  and

$$\varepsilon_{b\bar{b}\rightarrow ee}(y) = \frac{\left(\frac{dN_{b\bar{b}\rightarrow ee}^{ULS} - dN_{b\bar{b}\rightarrow ee}^{LS}}{dy}\right)_{rec}}{\left(\frac{dN_{b\bar{b}\rightarrow ee}^{ULS} - dN_{b\bar{b}\rightarrow ee}^{LS}}{dy}\right)_{gen}} \quad (5.10)$$

for electrons from  $b\bar{b}$ .

The total efficiency is computed as the sum of the charm and beauty pair efficiencies taking into account their corresponding relative contributions to the total signal in each of the bins of the histograms, which is taken from cocktail calculations. The extracted efficiency is then used to correct the data, following the same binning used in data. The calculated efficiencies for each of the paired parameters will be detailed in each of the analysis chapters, respectively.



# 6 Heavy-Flavour Cross Sections

The heavy-flavour cross sections, i.e. charm and beauty, are fundamental information to the study of pQCD calculations and the medium created in Pb–Pb collisions. Not only this, but also to be able to disentangle the production mechanisms of heavy quarks, it is important to first understand and extract these measurements, which are done in this thesis using two different analyses:  $m_{ee}$  and  $DCA_{xy}^{ee}$ . This will allow us to fix contributions in more complex analysis, such as the  $\Delta\varphi_{ee}$  and  $p_{T,ee}$ . This chapter describes the extraction of the charm and beauty cross sections through an invariant mass ( $m_{ee}$ ) approach (Section 6.1) and a new method developed during this thesis of the generated impact parameter ( $DCA_{xy}^{ee}$ ) analysis (Section 6.2). The summary of heavy-flavour production from  $m_{ee}$  and  $DCA_{xy}^{ee}$  measurements closes this Chapter at Section 6.3.

The whole invariant mass analysis was carried out using two different minimum  $p_{T,e}$  cuts, one of 0.2 GeV/ $c$  and other of 0.4 GeV/ $c$ . This was done to be able to compare the cross sections extracted by the invariant mass analysis and by the  $DCA_{xy}$  analysis (which requires a minimum  $p_{T,e}$  cut of 0.4 GeV/ $c$ ). Since a new  $DCA_{xy}^{ee}$  analysis method is presented in this thesis, we need first to be sure that the results using the same measurement ( $m_{ee}$ ), although different cuts, leads to the same measured cross section values. This should be exactly the case, but to be sure that there are not any underlying effect by transitioning from one cut to another, except statistical, both minimum  $p_{T,e}$  cut analyses were carried out. The measurements were obtained in both  $m_{ee}$  and  $DCA_{xy}^{ee}$  analysis not only for the full dataset but also for each data-taking year separately (2016, 2017, 2018), which is important for a still better cross checking and comparison between the  $m_{ee}$  and  $DCA_{xy}^{ee}$  measurements, and a year-dependent analysis could also help other studies in the future.

## 6.1 Invariant Mass Analysis

The dielectron invariant mass yield was already discussed previously and the Figure 2.10 shows a complex number of particles that can originate a dielectron signal, mainly: Light Flavours ( $\pi^0$ ,  $\eta$ ,  $\eta'$ ,  $\rho$ ,  $\omega$ ,  $\phi$ ), Heavy Flavour (charm and beauty) and  $J/\psi$ . LF particles play an important role in low invariant mass range, HF contribute to the whole spectrum of  $m_{ee}$  and  $J/\psi$  to higher invariant mass values. As mentioned in Section 4.6.1,

to avoid complex subtractions from LF contributors and even  $J/\psi$  (when possible), all of the analyses will focus in the Intermediate Mass Range (IMR -  $1.1 - 2.7 \text{ GeV}/c^2$ ), where we should have mainly HF contribution. This cut also removes the uncertainties that would have been added due to the contributions from LF, since the LF would need to be fixed by their own parameterizations and uncertainties.

Sometimes, analyses such as this use a wider dielectron invariant mass range for the studies. However, we want to drastically reduce even the possible  $J/\psi$  contribution to obtain as clear spectrum as possible. That is why the considered region of the dielectron invariant mass for all of the fits and analyses showed in thesis is  $1.1 < m_{ee} < 2.7 \text{ GeV}/c^2$ .

The analysis is presented as the following: the determination of the heavy-flavour efficiencies is presented in Section 6.1.1, while the usage of these efficiencies to the extraction of the  $m_{ee}$  signal is described in Section 6.1.2, followed by the determination of the systematic uncertainties of the signal (Section 6.1.3). The  $m_{ee}$  templates obtained using the procedures described in Section 5.1 and that are used to fit the data are showed at Section 6.1.4. The comparison between the data and the cocktail is then performed and discussed at Section 6.1.5.

### 6.1.1 Mass Efficiency

The invariant mass efficiency is calculated using the process described in Section 5.2.6 for charm and beauty electron pairs. In this specific analysis, the efficiencies are investigated using 2 different minimum  $p_{T,e}$  cuts, which are  $0.2$  and  $0.4 \text{ GeV}/c$ . This was done to be able to compare the cross sections extracted by the invariant mass analysis and by the  $DCA_{xy}$  analysis (which requires a minimum  $p_{T,e}$  cut of  $0.4 \text{ GeV}/c$ ). The efficiencies for all of the 3 studied data-taking years are shown in Figures 6.1 and 6.2 in different  $p_{T,ee}$  intervals, for each of the minimum  $p_{T,e}$  cuts.

The efficiencies of charm and beauty electron pairs are similar but each one of them has its own behaviour. The efficiencies are calculated using Equations 5.9 and 5.10, respectively. Beauty electron pairs present an overall higher efficiency than charm, and it gets higher as we increase the  $p_{T,ee}$  intervals, specially at the higher invariant mass regions. The shapes of the efficiencies are completely consistent along the 3 different years, in all of the  $p_{T,ee}$  intervals. 2017 year presents the highest efficiency over the years, while 2018 presents the lowest. Differences in the efficiencies of different years happen depending on calibrations and fixes (which improve the efficiency) and ageing factors (which decrease the efficiency). However, in general these effects should not modify the overall shape of the pair efficiencies, only introduce an scaling factor behaviour, which is exactly what is observed within the years.

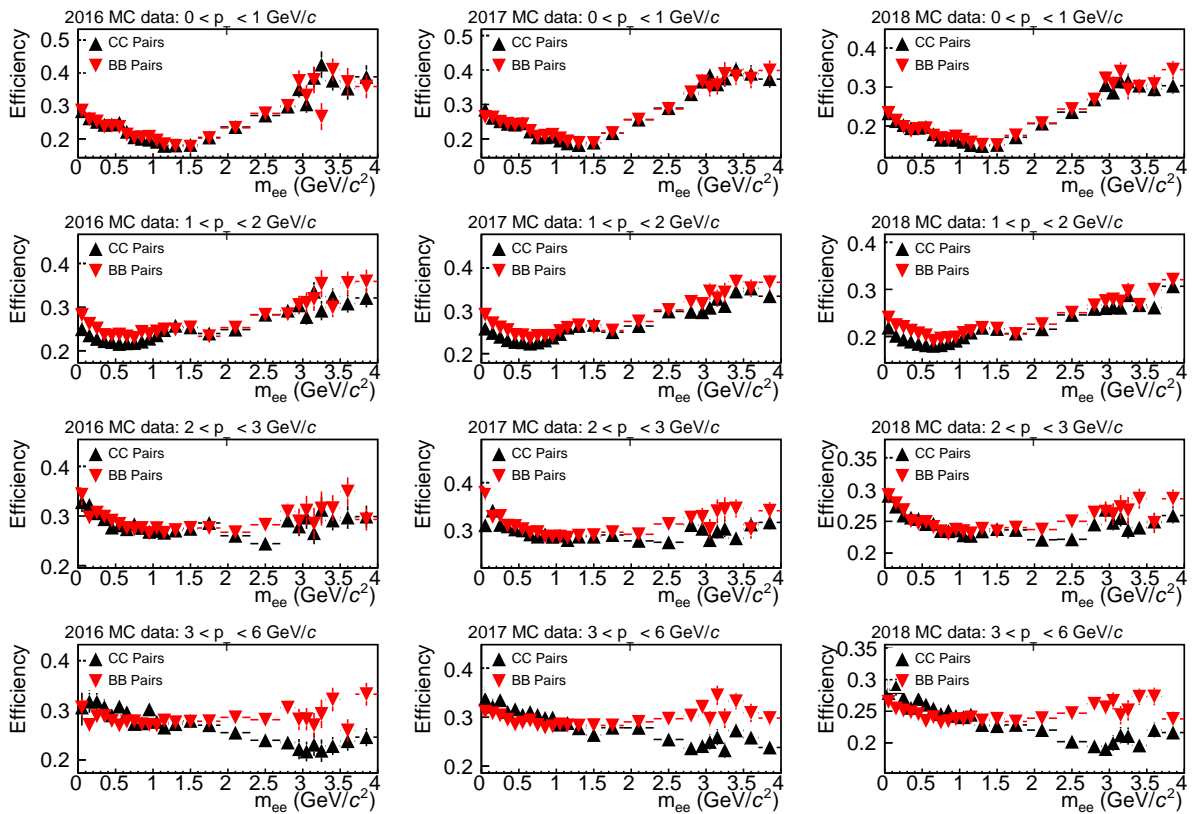


Figure 6.1: Invariant mass efficiencies of heavy-flavour electron pairs using a minimum  $p_{T,e}$  cut of  $0.2 \text{ GeV}/c$ . On the left column of plots it is shown the efficiencies for the 2016 year, in center for 2017 and on the right for 2018. In each line a different  $p_{T,ee}$  interval is presented, and can be directly compared with each of the neighbour columns.

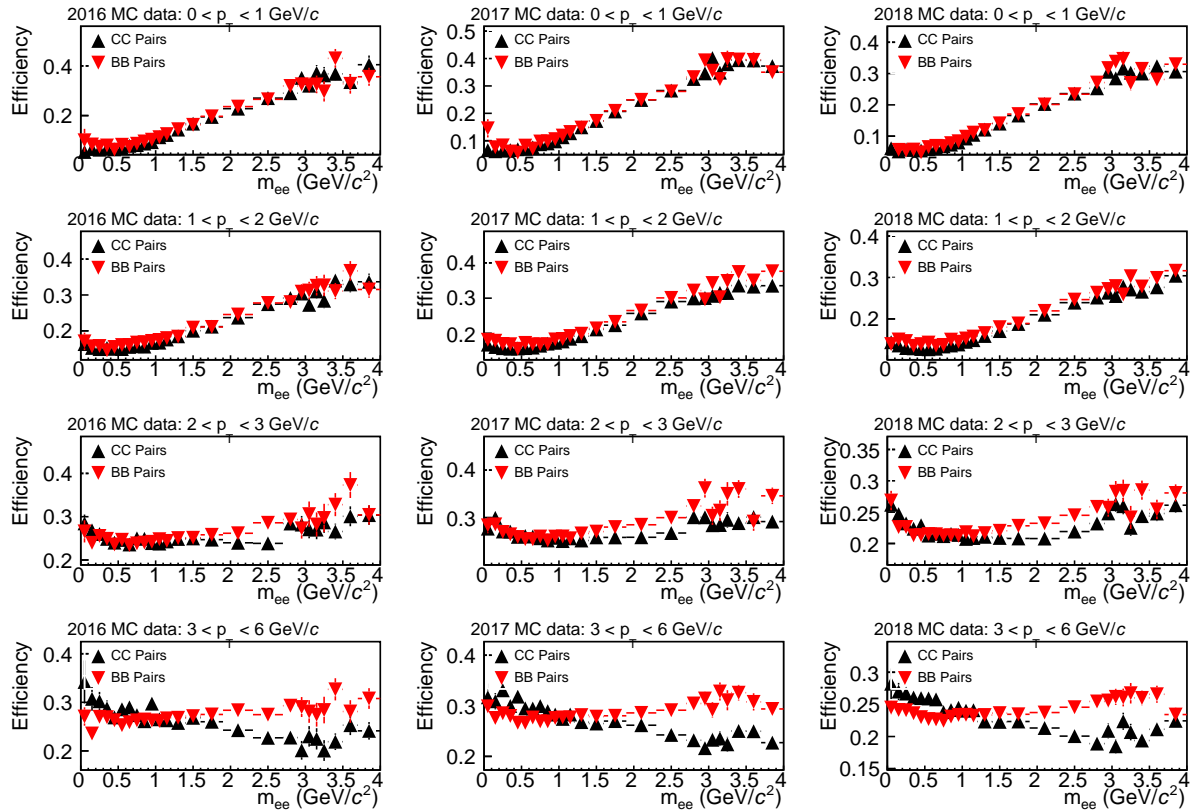


Figure 6.2: Invariant mass efficiencies of heavy-flavour electron pairs using a minimum  $p_{T,e}$  cut of  $0.4 \text{ GeV}/c$ . On the left column of plots it is shown the efficiencies for the 2016 year, in center for 2017 and on the right for 2018. In each line a different  $p_{T,ee}$  interval is presented, and can be directly compared with each of the neighbour columns.

### 6.1.2 Signal Extraction

The signal extraction of the  $m_{ee}$  follows the procedure already described in Section 4.6. The extraction of the  $m_{ee}$  signal starts with the 2D histogram of the  $p_{T,ee}$  and  $m_{ee}$ , which is then corrected by its 2D efficiency. The R-factor, calculated as a ratio between ULS and LS pairs from different events (completely uncorrelated), is shown as a function of the data year in Figures 6.3 and 6.4, for analyses with different minimum  $p_{T,e}$  cuts. As discussed, the R-factor allows us to check anomalies in the acceptance of ULS and LS pairs, and to be sure that we can correct and understand if such effects appear. The R-factors of the  $m_{ee}$  analyses show that there are no differences in acceptance of different signed charged pairs.

In Figures 6.5 and 6.6 the ULS and LS signals are shown for both analyses with different minimum  $p_{T,e}$  cut, and in Figures 6.7 and 6.8 the signal (ULS - LS) to background (LS) ratio of the merged 2016, 2017 and 2018 data. The whole idea is to use the maximum statistics available, and the contributions of each years separately will be only used as a matter of comparison and cross checking. As seen in the Figures below, the  $m_{ee}$  spectra in all of the  $p_{T,e}$  intervals present a good and stable signal to background ratio in the IMR - region of interest to this analysis.

### 6.1.3 Systematic Uncertainties

The systematic uncertainties of the  $m_{ee}$  was determined using the procedure of cut variations described in Section 4.7. The comparison of all of the variations are shown in the Figures 6.9 and 6.10, for the minimum  $p_{T,e}$  cut of 0.2 and 0.4, respectively. The Figures 6.11 and 6.12, on the other hand, are the final systematic uncertainties determined using the variations. The same procedure was used for all of the years separately, but they are not shown here for simplicity. The uncertainties are stable at around 10 % in the IMR, in both analyses with different minimum  $p_{T,e}$  cuts. The cut settings that presents the higher variation are the track cuts, and the different eID by TPC and TOF stay approximately stable at 5 % each.

The dielectron signal extracted using the procedure described in the last Sections as a function of the  $m_{ee}$  in different  $p_{T,ee}$  intervals for the different data-taking years and for the merged years are shown in Figures 6.13 and 6.14, for the analyses with minimum  $p_{T,e}$  cut of 0.2 and 0.4 GeV/ $c$ , respectively. The signal for each given year was corrected by its own anchored efficiency, and the systematical uncertainties were evaluated separately for each year and for the case of the merged years in the process described in this Section.

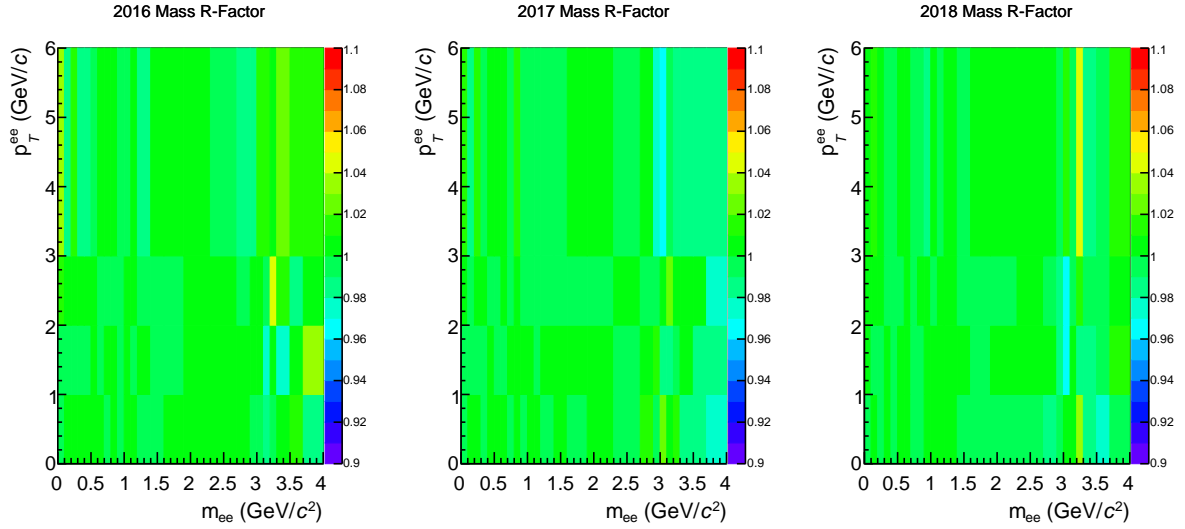


Figure 6.3: R-factor for each of the data taken years analysed with minimum  $p_{T,e}$  of 0.2 GeV/c. From left to right: 2016, 2017 and 2018 data years.

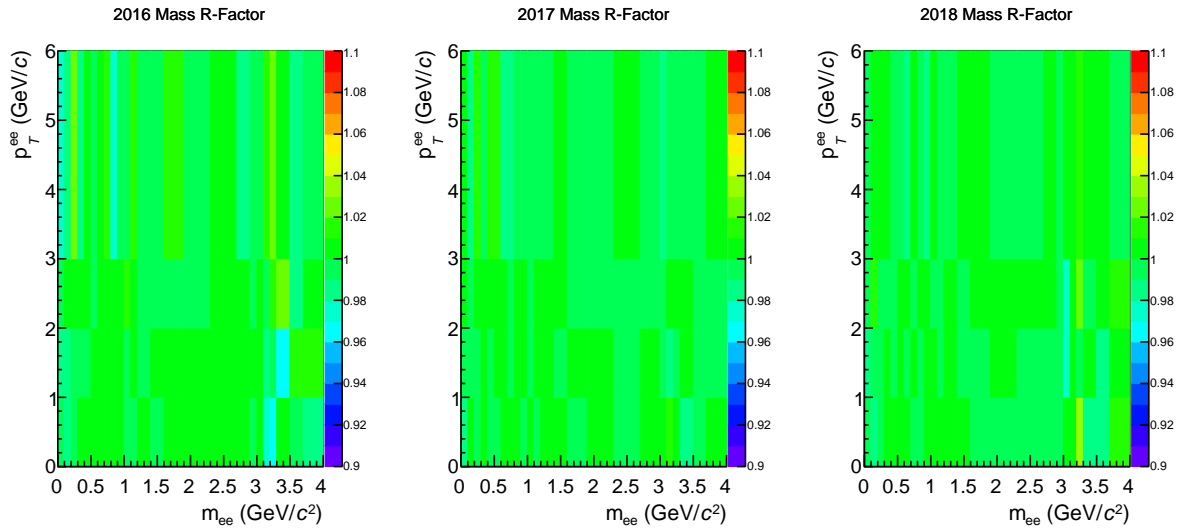


Figure 6.4: R-factor for each of the data taken years analysed with minimum  $p_{T,e}$  of 0.4 GeV/c. From left to right: 2016, 2017 and 2018 data years.

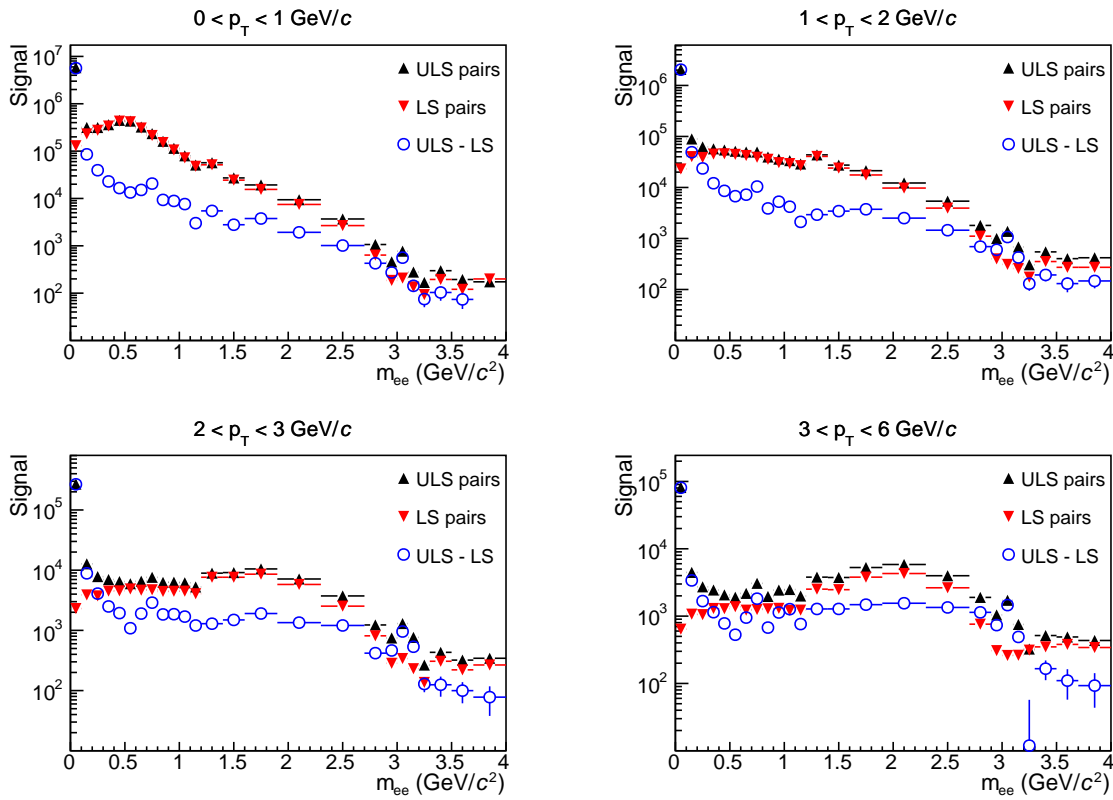


Figure 6.5: ULS and LS contributions for the analysis with minimum  $p_{T,e}$  of 0.2 GeV/ $c$  as a function of the  $p_{T,ee}$ , using all of the data years (2016 + 2017 + 2018). The ULS is shown in black, the LS contribution in red and the ULS - LS subtraction in blue.

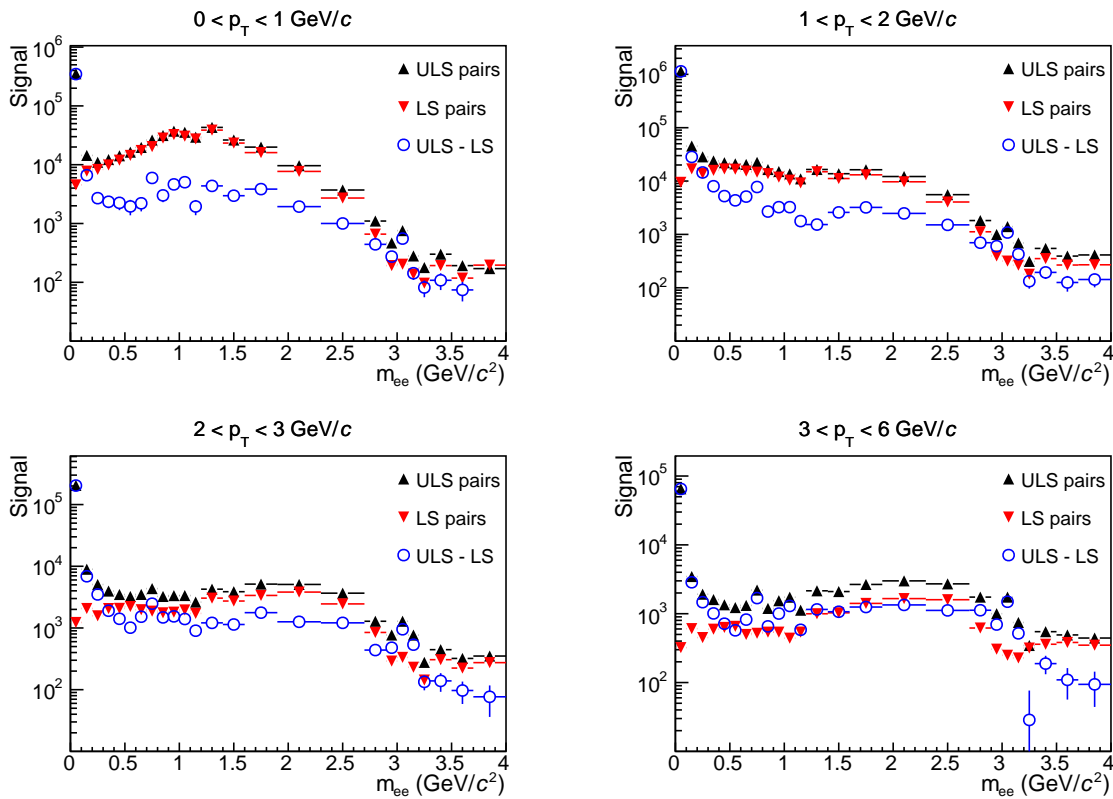


Figure 6.6: ULS and LS contributions for the analysis with minimum  $p_{T,e}$  of 0.4 GeV/ $c$  as a function of the  $p_{T,ee}$ , using all of the data years (2016 + 2017 + 2018). The ULS is shown in black, the LS contribution in red and the ULS - LS subtraction in blue. —69—

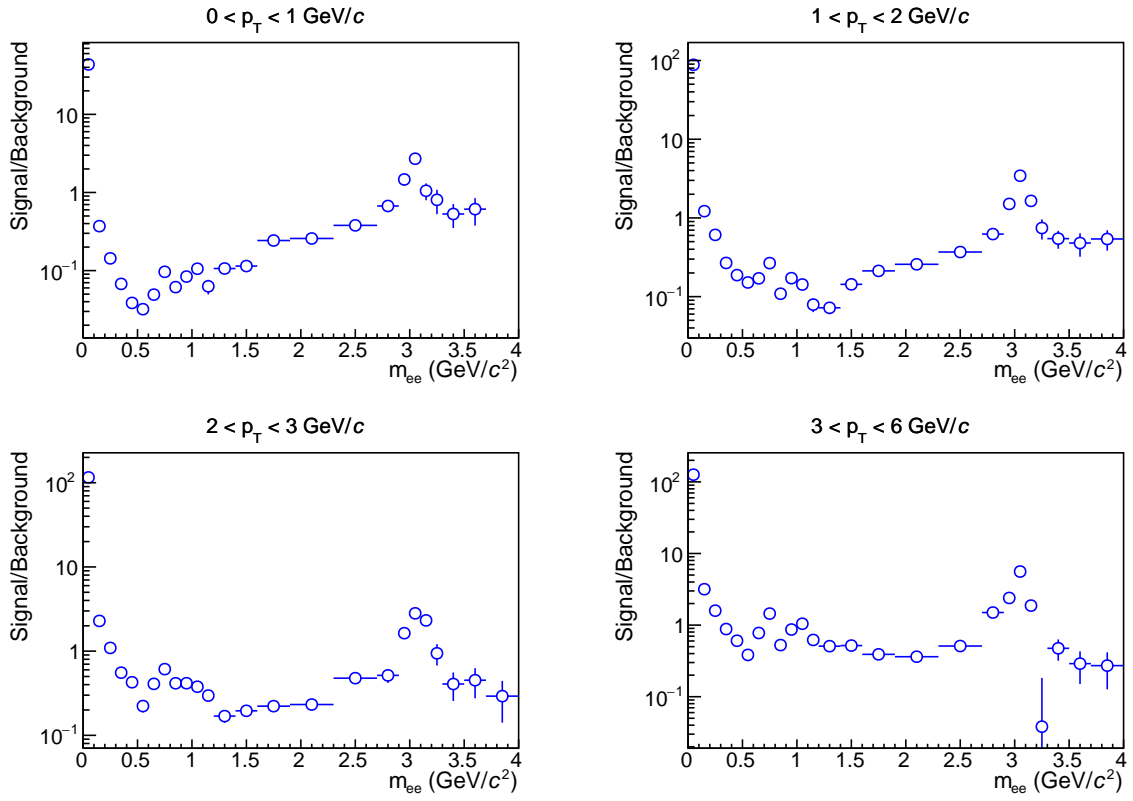


Figure 6.7: Signal over background ratio for the analysis with minimum  $p_{T,e}$  of  $0.2 \text{ GeV}/c$ , using all of the data years (2016 + 2017 + 2018).

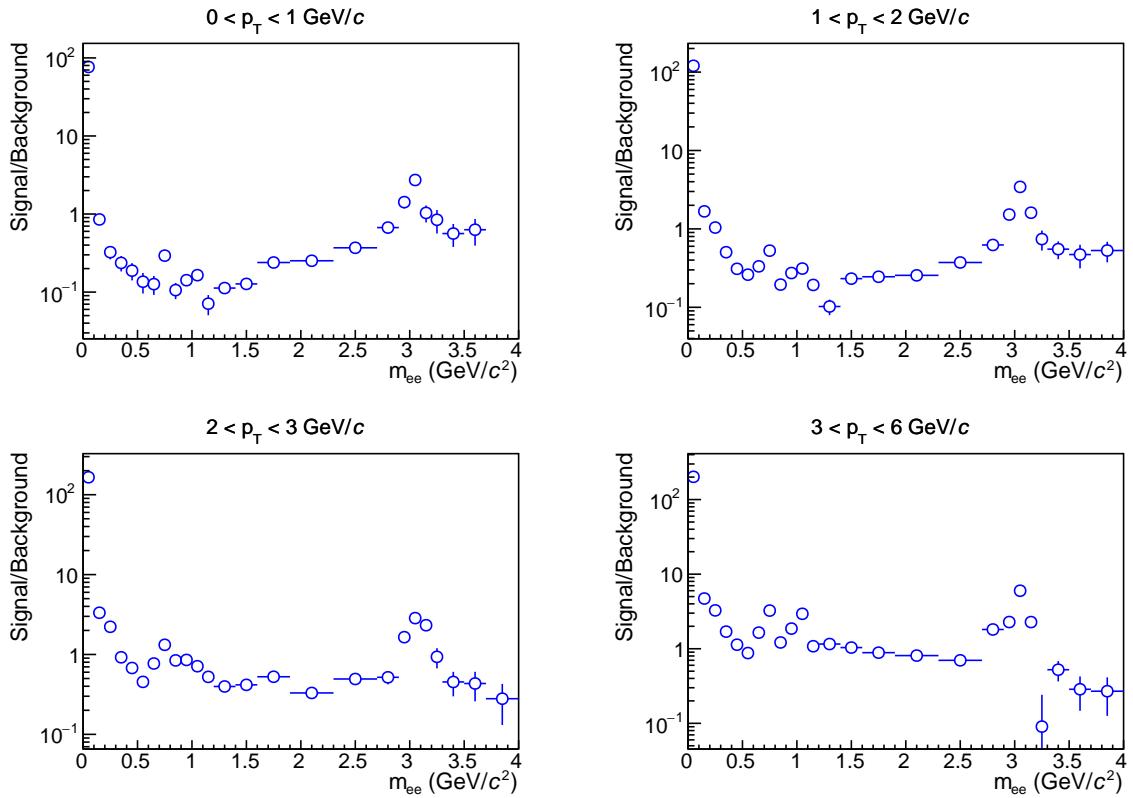


Figure 6.8: Signal over background ratio for the analysis with minimum  $p_{T,e}$  of  $0.4 \text{ GeV}/c$ , using all of the data years (2016 + 2017 + 2018).



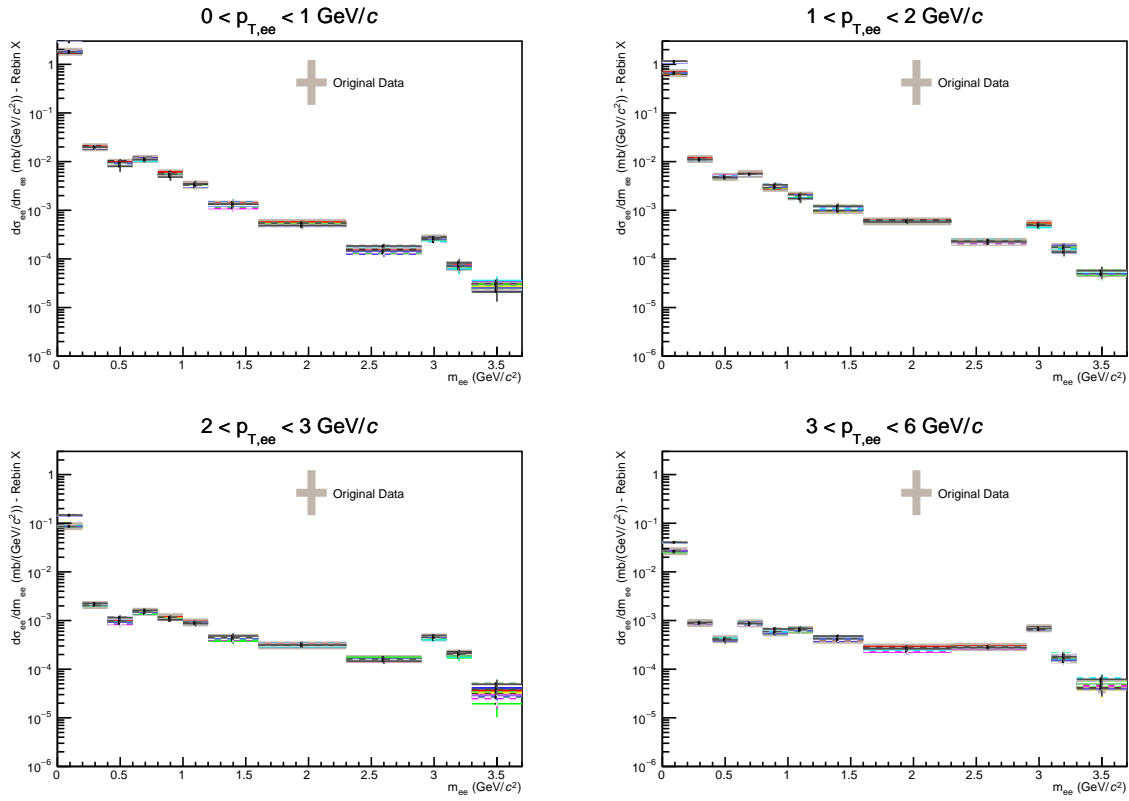


Figure 6.9: Comparison of the signal obtained using different sets of track and eID cuts for the  $m_{ee}$  analysis with minimum  $p_{T,e}$  of 0.2 GeV/ $c$  as a function of the  $p_{T,ee}$ , using all of the data years (2016 + 2017 + 2018).

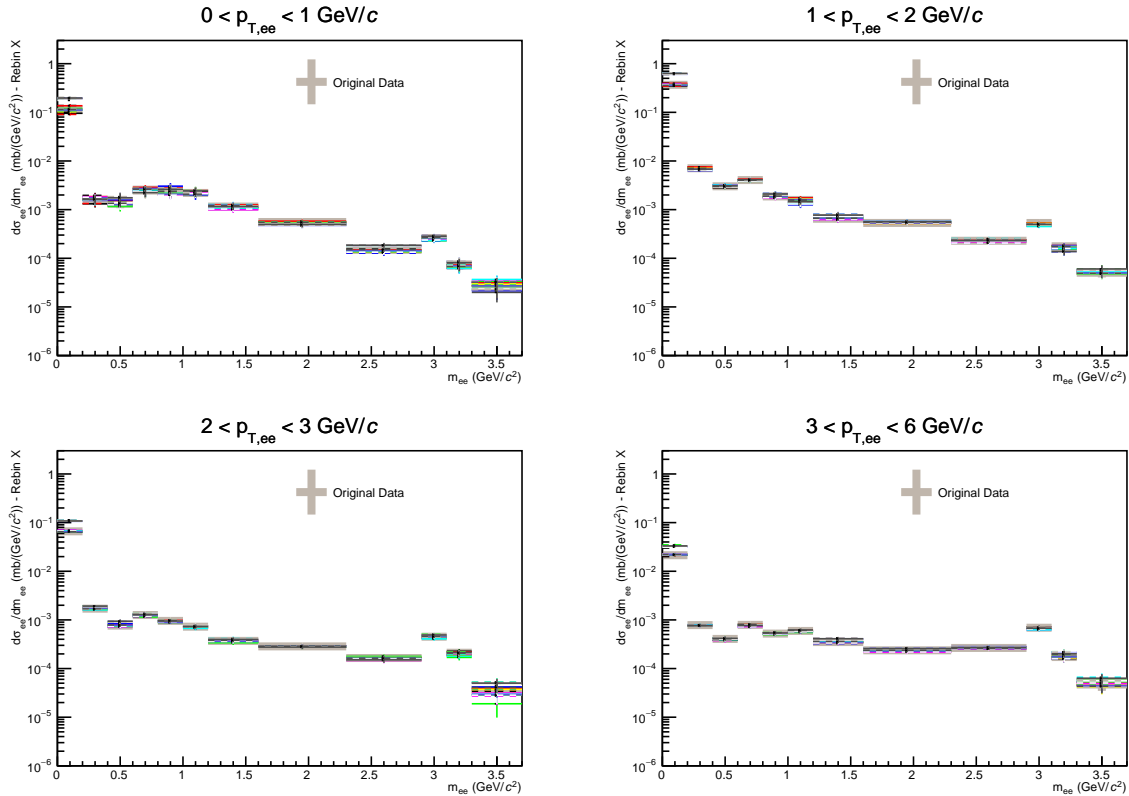


Figure 6.10: Comparison of the signal obtained using different sets of track and eID cuts for the  $m_{ee}$  analysis with minimum  $p_{T,e}$  of 0.4 GeV/ $c$  as a function of the  $p_{T,ee}$ , using all of the data years (2016 + 2017 + 2018).

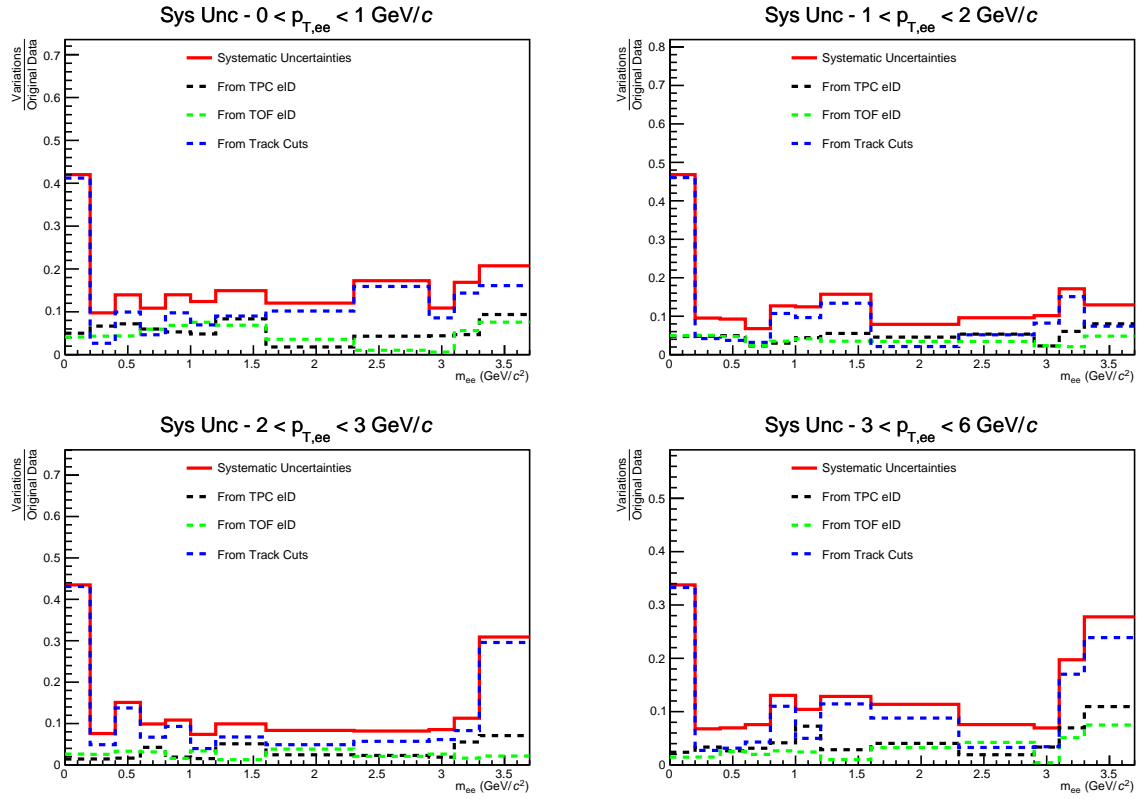


Figure 6.11: Systematic uncertainties of the  $m_{ee}$  analysis with minimum  $p_{T,e}$  of 0.2 GeV/c as a function of the  $p_{T,ee}$ , using all of the data years (2016 + 2017 + 2018).

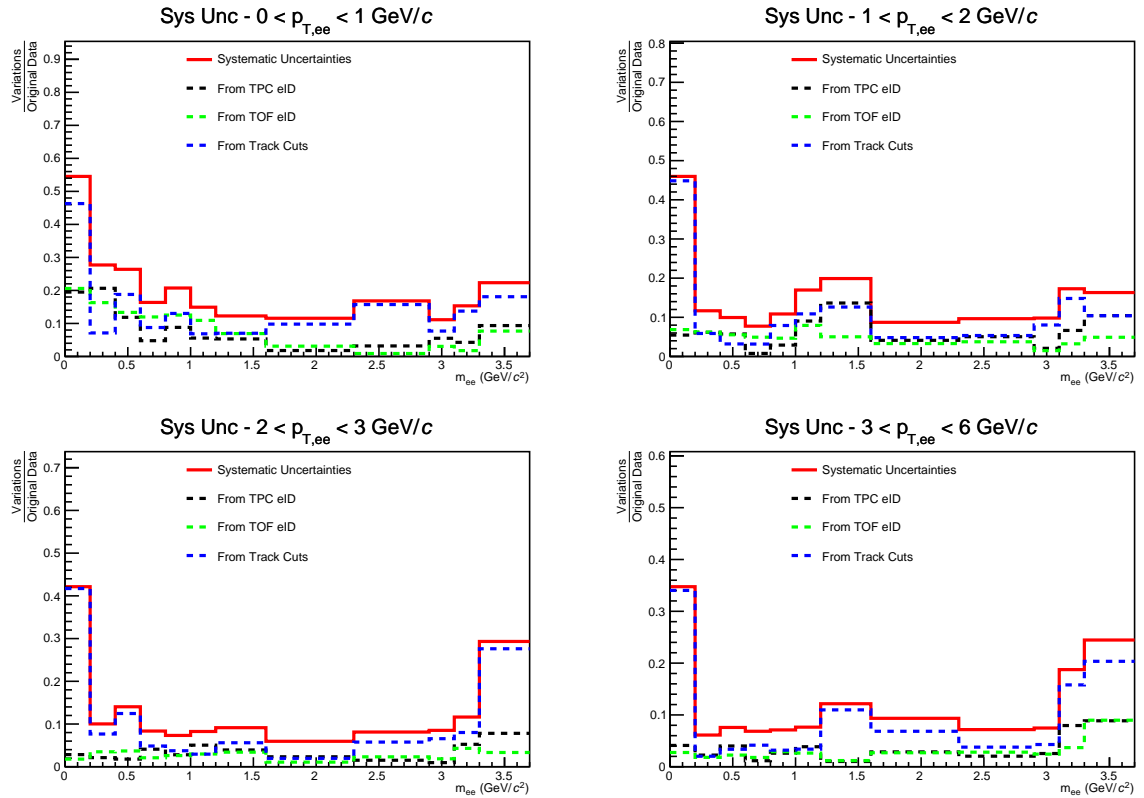


Figure 6.12: Systematic uncertainties of the  $m_{ee}$  analysis with minimum  $p_{T,e}$  of 0.4 GeV/c as a function of the  $p_{T,ee}$ , using all of the data years (2016 + 2017 + 2018).

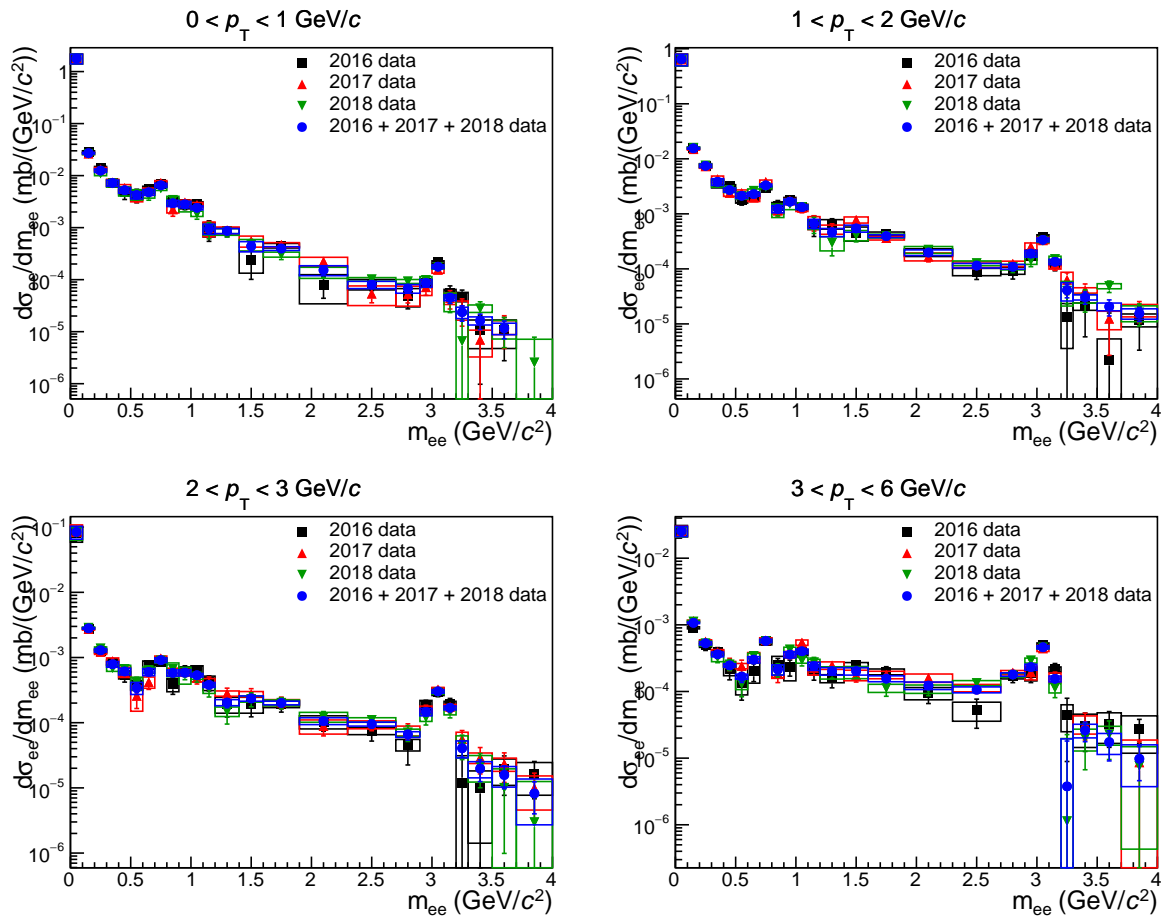


Figure 6.13: The dielectron cross section for the different data-taking years are shown as a function of the  $m_{ee}$  in different pair momentum intervals for the analysis with  $p_{T,e} > 0.2 \text{ GeV}/c$ . The signal obtained using 2016 data is shown in black, 2017 in red, 2018 in green and in blue for the merged years. The bar and boxes represent the statistical and systematic uncertainties of the data.

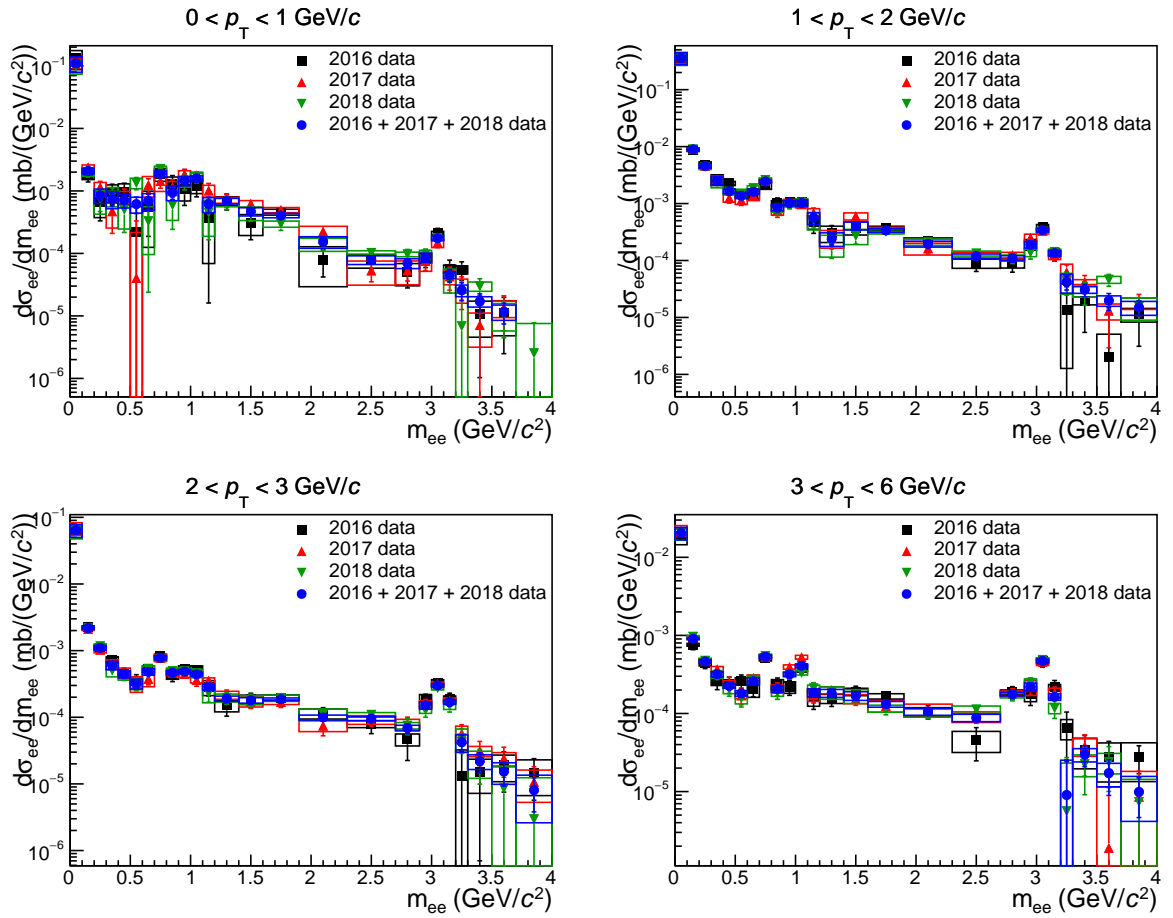


Figure 6.14: The dielectron cross section for the different data-taking years are shown as a function of the  $m_{ee}$  in different pair momentum intervals for the analysis with  $p_{T,e} > 0.4 \text{ GeV}/c$ . The signal obtained using 2016 data is shown in black, 2017 in red, 2018 in green and in blue for the merged years. The bar and boxes represent the statistical and systematic uncertainties of the data.

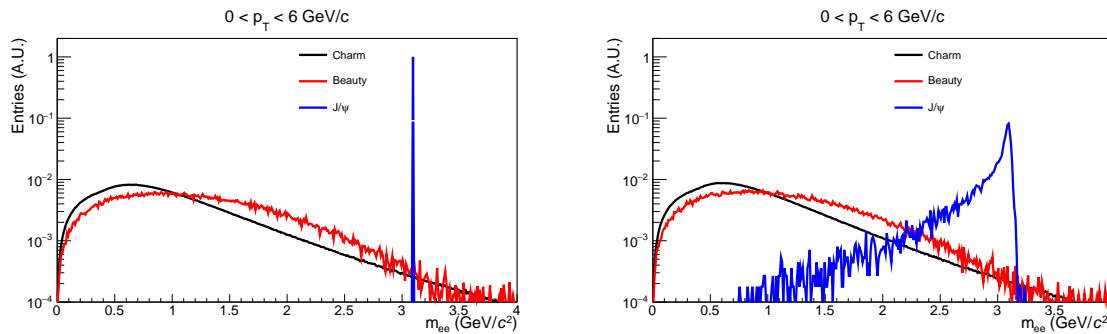


Figure 6.15: Comparison between charm, beauty and  $J/\psi$  templates using PYTHIA pure MC samples, without (left) and with  $p_T$ ,  $\eta$  and  $\varphi$  smearing (right). The templates were normalized by their integrals for a better comparison.

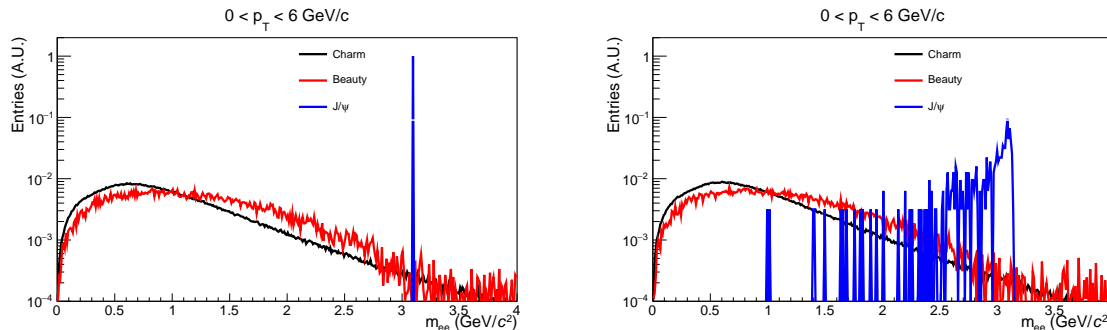


Figure 6.16: Comparison between charm, beauty and  $J/\psi$  templates using POWHEG pure MC samples, without (left) and with  $p_T$ ,  $\eta$  and  $\varphi$  smearing (right). The templates were normalized by their integrals for a better comparison.

### 6.1.4 Monte Carlo Templates

The templates obtained by PYTHIA and POWHEG simulations are shown in Figures 6.15 and 6.16, respectively. The templates obtained without the usage of the  $p_T$ ,  $\eta$  and  $\varphi$  smearing procedure are shown in the left plot of these Figures while on the right plots the smeared templates are shown. The templates are normalized by their own integrals for a better visualization, and a large  $J/\psi$  tail is obtained in the smearing procedure (see Section 5.2.4). Without the smearing procedure the  $m_{ee}$  peak for electrons from  $J/\psi$  is a simple bin entry centered in the  $J/\psi$  mass. The analyses over PYTHIA and POWHEG samples generate templates that are very similar in shape. The  $J/\psi$  template is obtained by pairing decaying electrons from  $J/\psi$  ( $|\text{pdg}| = 443$ ), and it is considered here because it can start to play an important role to higher  $p_{T,ee}$  and in the  $m_{ee}$  region of  $\approx 2.6 \text{ GeV}/c^2$  of the IMR. While in  $m_{ee}$  templates the  $J/\psi$  may be important only for a tiny part of the  $m_{ee}$  region studied, when analyzing the  $\text{DCA}_{xy}^{ee}$  signal the  $J/\psi$  will have an important effect for lower  $\text{DCA}_{xy}^{ee}$  values, as a prompt contribution.

### 6.1.5 Results

The charm and beauty MC templates were used to fit the data in the IMR region of the  $m_{ee}$  spectrum. In the first attempt, the fit was systematically smaller than data in the last fitting bin of the IMR when only charm and beauty templates were used. A better description of the data was achieved by extending the fit to part of the  $J/\psi$  region (up to  $3.0 \text{ GeV}/c^2$ ) and considering  $J/\psi$  templates to the fit. The fit was performed for each of the 3 years separately, but it will only be shown the fitting for the 3 merged years for simplicity, for PYTHIA and POWHEG simulations. The fit results of each of the years separately can be found in the Appendix D. The 3 years were fitted separately for three reasons: (i) to validate our measurements using previous published results with 2016 data, (ii) to compare the results within different years, and (iii) to provide validation results of each of the years to the  $\text{DCA}_{xy}^{ee}$  analysis. The invariant mass analysis was carried out using these two different minimum  $p_{T,e}$  cut to be able to check if the results are comparable and which effects could happen when transitioning from one cut to another. Both PYTHIA and POWHEG generators were able to describe the data reasonably well in both analyses with different minimum  $p_{T,e}$  cuts.

The dielectron spectrum is shown as a function of the  $p_{T,ee}$  and  $m_{ee}$  in Figures 6.17 and 6.18, for minimum  $p_{T,e}$  cut of 0.2 and 0.4  $\text{GeV}/c$ , using 2016, 2017 and 2018 data. The experimental data is compared to the expectation from the hadronic decay cocktail using PYTHIA simulations, while in Figures 6.19 and 6.20 the data is compared to a POWHEG-based cocktail. A summary of all of the parameters obtained can be found in Table 6.2 and in Figures 6.21 and 6.22 for PYTHIA and POWHEG, respectively. The systematic uncertainties of the extracted cross sections were obtained by fitting the data displaced by  $\pm\sigma$  of the systematic uncertainties of the data, accounting the differences of the parameters.

The cross sections extracted from the  $m_{ee}$  fits seen in Figures 6.21 and 6.22 show that the results are compatible within uncertainties within different years, different minimum  $p_{T,e}$  cuts, and compatible to the parameters extracted when using the data from the 3 years. The POWHEG simulations provided more fluctuating results, which may point out that the cocktail fit may fluctuate more depending on the available statistics. The cross sections are also compatible to the ones already published by ALICE using 2016 data [19]. Both analyses with different minimum  $p_{T,e}$  cuts follow the same behaviour within different years, except the beauty when looking at the 2017 data alone. It is also interesting to note that PYTHIA and POWHEG generators seem to observe the same behaviour within different years and minimum  $p_{T,e}$  cut, so if the PYTHIA analysis with minimum  $p_{T,e}$  cut of 0.4 saw a greater contribution from charm (e.g. 2017) when compared to the analysis with minimum  $p_{T,e}$  cut of 0.2, POWHEG also saw this behavior, and this also happened to the beauty cross sections. The systematic uncertainties are greater for charm than

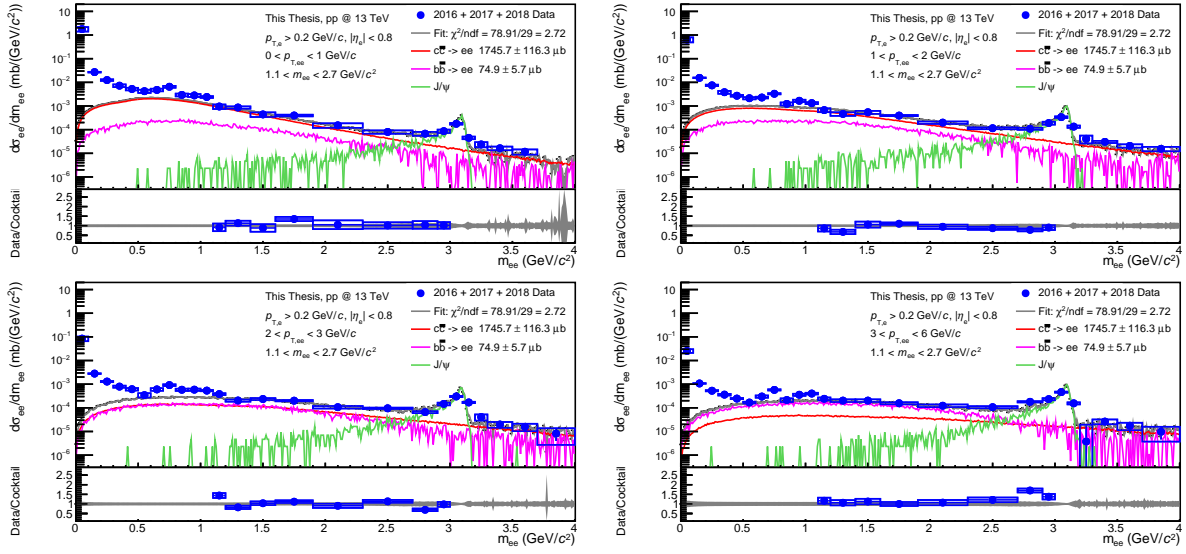


Figure 6.17: The dielectron cross section in pp collisions at 13 TeV as a function of invariant mass in different pair momentum intervals is shown in blue circles for the analysis using the minimum  $p_{T,e}$  cut of 0.2 GeV/c, and the PYTHIA cocktail is shown in red, purple and green for charm, beauty and  $J/\psi$  contributions, respectively. The bar and boxes represent the statistical and systematic uncertainties of the data, while the final cocktail is shown in a grey band. On the bottom of each pair momentum interval plot it is shown the data-to-cocktail ratio.

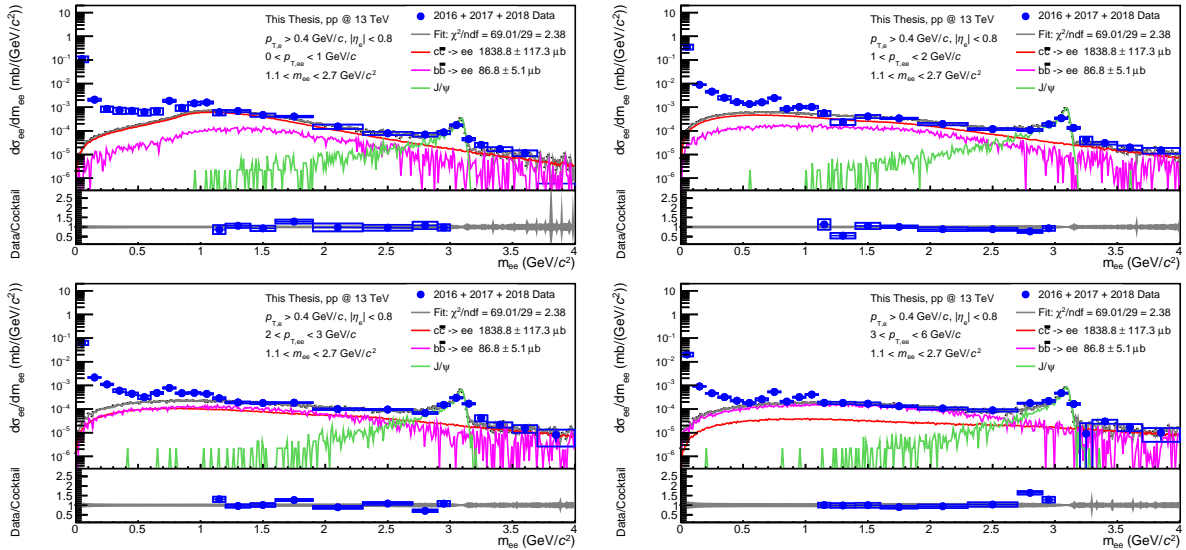


Figure 6.18: The dielectron cross section in pp collisions at 13 TeV as a function of invariant mass in different pair momentum intervals is shown in blue circles for the analysis using the minimum  $p_{T,e}$  cut of 0.4 GeV/c, and the PYTHIA cocktail is shown in red, purple and green for charm, beauty and  $J/\psi$  contributions, respectively. The bar and boxes represent the statistical and systematic uncertainties of the data, while the final cocktail is shown in a grey band. On the bottom of each pair momentum interval plot it is shown the data-to-cocktail ratio.

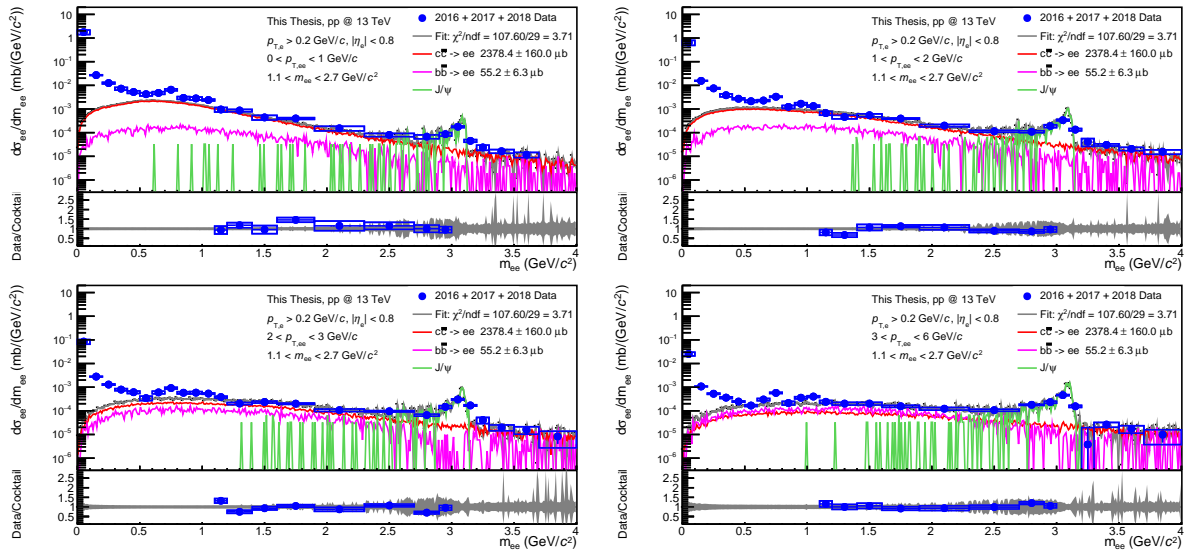


Figure 6.19: The dielectron cross section in pp collisions at 13 TeV as a function of invariant mass in different pair momentum intervals is shown in blue circles for the analysis using the minimum  $p_{T,e}$  cut of 0.2 GeV/c, and the POWHEG cocktail is shown in red, purple and green for charm, beauty and  $J/\psi$  contributions, respectively. The bar and boxes represent the statistical and systematic uncertainties of the data, while the final cocktail is shown in a grey band. On the bottom of each pair momentum interval plot it is shown the data-to-cocktail ratio.

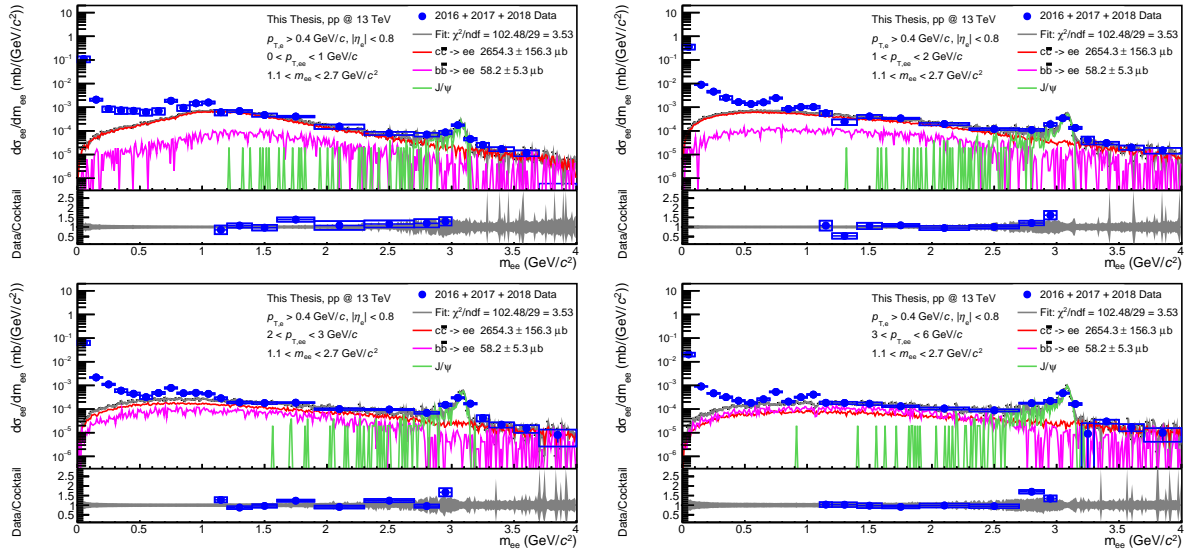


Figure 6.20: The dielectron cross section in pp collisions at 13 TeV as a function of invariant mass in different pair momentum intervals is shown in blue circles for the analysis using the minimum  $p_{T,e}$  cut of 0.4 GeV/c, and the POWHEG cocktail is shown in red, purple and green for charm, beauty and  $J/\psi$  contributions, respectively. The bar and boxes represent the statistical and systematic uncertainties of the data, while the final cocktail is shown in a grey band. On the bottom of each pair momentum interval plot it is shown the data-to-cocktail ratio.



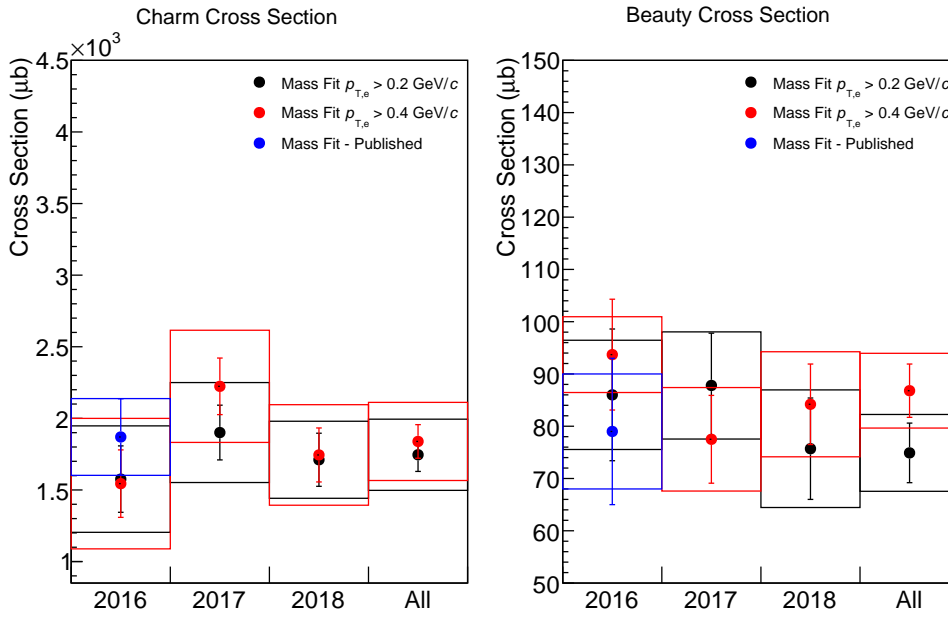


Figure 6.21: Heavy-flavour cross sections extracted through the mass fits as a function of the year and minimum  $p_{T,e}$  cut using PYTHIA cocktail. The results using a minimum  $p_{T,e}$  cut of 0.2 GeV/ $c$  are shown in black, while in red for minimum  $p_{T,e}$  cut of 0.4 GeV/ $c$ . The published cross section extracted by ALICE using 2016 data is shown in blue. The vertical bars and boxes are the statistical and systematic uncertainties.

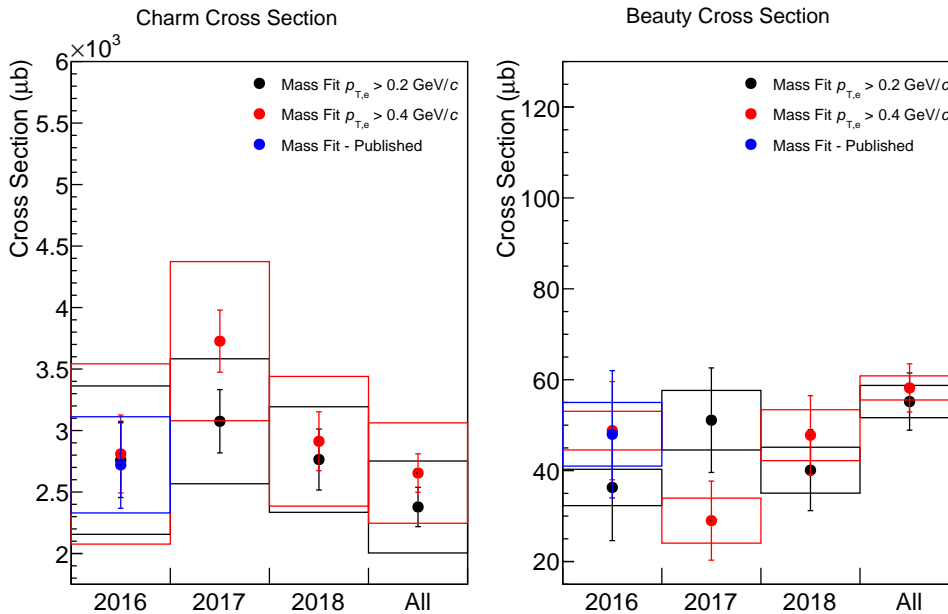


Figure 6.22: Heavy-flavour cross sections extracted through the mass fits as a function of the year and minimum  $p_{T,e}$  cut using POWHEG cocktail. The results using a minimum  $p_{T,e}$  cut of 0.2 GeV/ $c$  are shown in black, while in red for minimum  $p_{T,e}$  cut of 0.4 GeV/ $c$ . The published cross section extracted by ALICE using 2016 data is shown in blue. The vertical bars and boxes are the statistical and systematic uncertainties.

beauty, since when moving the data up and down by the systematic uncertainty the fit preferred to modify more the charm contribution than the beauty. The extracted cross section using the 3 years provided smaller uncertainties to the measurements, reducing the uncertainties by  $\approx 50\%$  for charm and  $\approx 40\%$  for beauty.

One of the most interesting result, already seen and reported before [19, 18], is that POWHEG finds a higher charm contribution and smaller beauty contribution than PYTHIA. This effect can be explained by a difference in the probabilities of a dielectron pair to enter in the detector acceptance (such as rapidity) by PYTHIA and POWHEG [18], and also by the fact that the  $p_{T,ee}$  distributions of a dielectron pair is harder in POWHEG than in PYTHIA generator. Dielectron measurements such as these can provide modeling constraints to MC event generators to be able to reproduce the heavy-flavour production cross sections, leading to consistent results between different generators.

## 6.2 Impact Parameter Analysis

The structure of this Section related to the  $DCA_{xy}^{ee}$  analysis follows the same structure used to describe the  $m_{ee}$  analysis, starting with the  $DCA_{xy}^{ee}$  signal extraction (Sections 6.2.1, 6.2.2 and 6.2.3). The Monte Carlo templates are deeply discussed and tested in Section 6.2.4 as the method of calculating the templates from pure MC samples was developed during this thesis. Finally, the data and the simulations are compared in Section 6.2.5 and the charm and beauty cross sections are extracted and compared to the ones extracted from  $m_{ee}$  analysis.

### 6.2.1 DCA Efficiency

The efficiency in a  $DCA_{xy}^{ee}$  analysis must be carefully carried out. This is simply due the fact that the  $DCA_{xy}^{ee}$  is a pure reconstructed parameter, and does not exist in the generator level. Just to remind, the PYTHIA and POWHEG simulations provide us the kinematics of a collision, starting with the particle production and shower, and all of these in a generator level. The simulation is not calculated as particles in a magnetic field, so the tracks follow straight lines. The reconstructed part of the simulations are obtained by using these generated simulations as input into GEANT, which takes care to simulate all of the detector effects and provide us the reconstructed track parameters, such as the  $DCA_{xy}$  of an electron, taking into account all of the detector calibrations and resolutions for each given particle, depending on its trajectory and kinematics.

Since there is no impact parameter in a generated level, the approach that will be used is that the efficiency does not depend on the  $DCA_{xy}^{ee}$ . This can also be understood by looking to parameters which are available for both generator and reconstructed level, such as the distance between the primary and the secondary vertex. The primary vertex

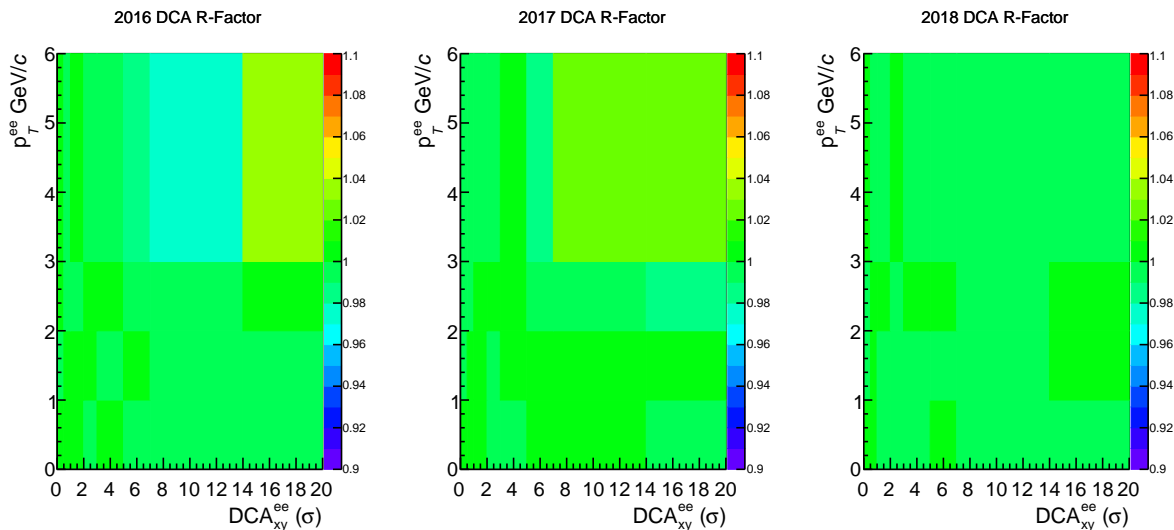


Figure 6.23: R-factor for each of the data taken years analyzed with minimum  $p_{T,e}$  of 0.2 GeV/ $c$ . From left to right: 2016, 2017 and 2018 data years.

is the event vertex and the secondary vertex is the vertex where we find from where the particles are coming from, and there is no  $DCA_{xy}^{ee}$  dependence in this parameter.

However, we know that there is a dependence on the  $p_{T,ee}$  and it should exist a correlation between  $DCA_{xy}^{ee}$  and  $p_{T,ee}$ . Different populations of particles will lead to different  $p_T$  distributions, which surely will affect the  $DCA_{xy}$ . To correct these effects, the  $DCA_{xy}^{ee}$  efficiency correction is built as a 3D-efficiency histogram where the 3rd dimension (related to  $DCA_{xy}^{ee}$ ) is a fixed contribution given by the specific  $p_{T,ee}, m_{ee}$  bin, so the value for all of the DCA bins follow the efficiency of that specific  $p_{T,ee}, m_{ee}$  bin. In summary, the same efficiencies shown in 6.1.1 were used, except that in order to increase the signal over background ratio, a single  $m_{ee}$  bin was used between 1.1 to 2.7 GeV/ $c^2$ .

### 6.2.2 Signal Extraction

The signal extraction of the  $DCA_{xy}^{ee}$  follows the procedure already described in Section 4.6 and already applied to  $m_{ee}$  analysis. The  $DCA_{xy}^{ee}$  analysis is more complicated than the simple  $m_{ee}$  analysis since there are here 3 pairing parameters:  $p_{T,ee}$ ,  $m_{ee}$  and  $DCA_{xy}^{ee}$ . Starting from this 3D histogram of the pairing parameters, the signal is corrected by its 3D efficiency histogram, being projected afterwards to a 2D histogram of  $p_{T,ee}$  and  $DCA_{xy}^{ee}$ , considering only the contributions that are in the IMR of the  $m_{ee}$ . The R-factor is shown in Figure 6.23 and there is no differences in acceptance of different signed charged pairs (ULS and LS). Fluctuations in low statistics bins are common and should be taken into account when analyzing such factor, and when more events are used (such in 2018 data) a better R-factor, around 1, is achieved.

In Figures 6.24 the ULS and LS signals for  $DCA_{xy}^{ee}$  are shown, while in Figure 6.25

the signal (ULS - LS) to background (LS) ratio is shown for the merged 2016, 2017 and 2018 data. This procedure was done to all of the single year analyses but they are not shown here for simplicity. As seen in the plots, the  $DCA_{xy}^{ee}$  distributions for  $p_{T,e} > 1$  GeV/ $c$  intervals present a good and stable signal to background ratio. In the first  $p_{T,e}$  interval (0 - 1 GeV/ $c$ ), the low resolution of the  $DCA_{xy}$  requests a minimum  $p_{T,e}$  higher than the usual - 0.4 GeV/ $c$ . This cut removes a great number of electrons from the analysis and has its strongest effect in the lowest  $p_{T,ee}$  intervals. It can be seen that the first  $p_{T,ee}$  interval has the smaller signal to background ratio and in one of the bins (7-14) it is really small, meaning that both ULS and LS contributions to that bin are very similar. The better signal to background ratio was found using the binning showed in the Figures, which gets wider as the  $DCA_{xy}$  value increases to balance the statistics reduction. It was also used a single  $m_{ee}$  bin in the IMR, and any other attempts of  $DCA_{xy}^{ee}$  binning lead to negative ULS - LS signals, which are physically uncorrect and would lead to huge systematic uncertainties. This can happen because using other set of track cuts the physically correct positive signal to background ratio can be achieved, leading to unreasonable systematic uncertainties.

### 6.2.3 Systematic Uncertainties

The systematic uncertainties of the  $DCA_{xy}^{ee}$  was determined using the procedure of cut variations described in Section 4.7. The comparison of all of the variations is shown in Figure 6.26, while in Figure 6.27 it is shown the final systematic uncertainties determined using the variations. As in the  $m_{ee}$  case, the same procedure was repeated for all of the years separately to obtain the systematic uncertainties for each year, but are not shown here for simplicity. The uncertainties increases for higher  $DCA_{xy}^{ee}$  values, and it gets better as the  $p_{T,ee}$  is increased. For smaller  $DCA_{xy}^{ee}$  values, the uncertainties starts at 20 % for low  $p_{T,ee}$  and it is reduced to around 10 % for higher  $p_{T,ee}$  intervals. The uncertainties for higher  $DCA_{xy}^{ee}$  values also reduces as we increase the  $p_{T,ee}$ . As in the  $m_{ee}$  case, the track cuts present the greatest variations, while the different eID by TPC and TOF stays approximately at 5 % each for low  $p_{T,ee}$  intervals and decreases to values around 3 % for higher  $p_{T,ee}$  intervals.

The dielectron signals extracted using the procedure described in the last Sections as a function of the  $DCA_{xy}^{ee}$  in different  $p_{T,ee}$  intervals for the different data-taking years and for the merged years are shown in Figure 6.28. The signal for each given year was corrected by its own anchored efficiency, and the systematical uncertainties were evaluated separately for each year and for the case of the merged years in the process described in this Section.

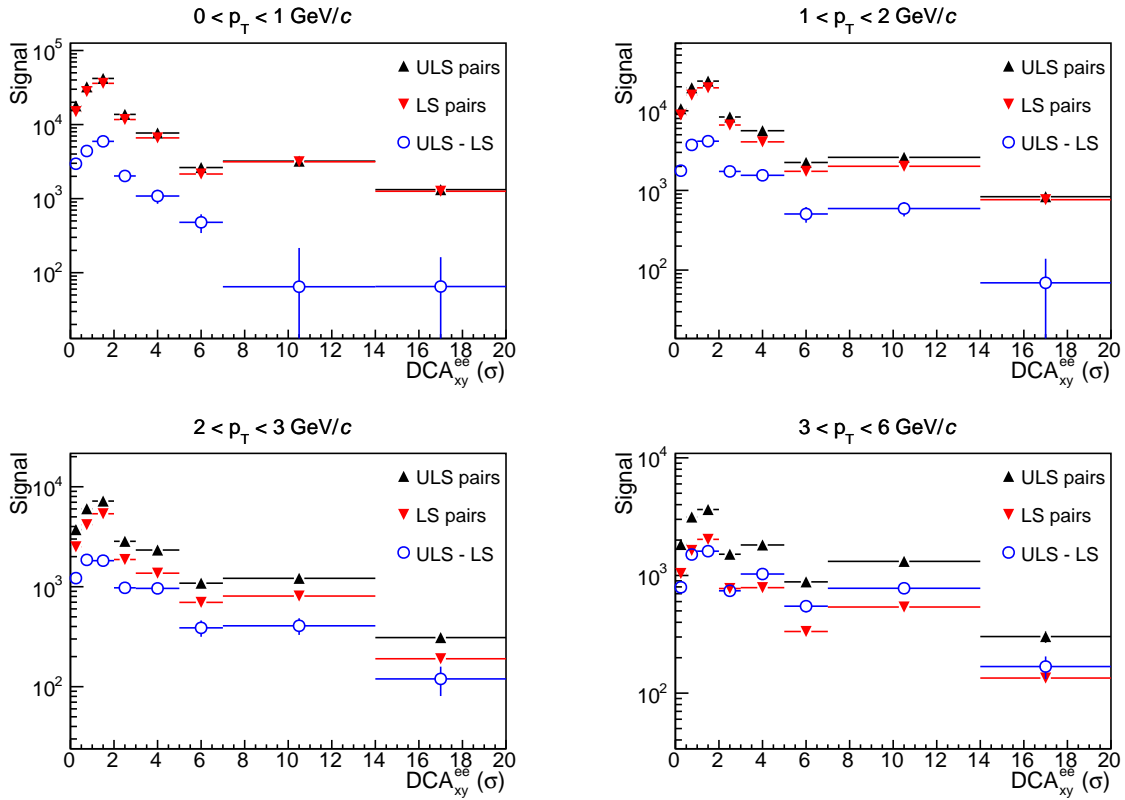


Figure 6.24: ULS and LS contributions for the  $DCA_{xy}^{ee}$  as a function of the  $p_{T,ee}$  using all of the data years (2016 + 2017 + 2018). The ULS is shown in black, the LS contribution in red and the ULS - LS subtraction in blue.

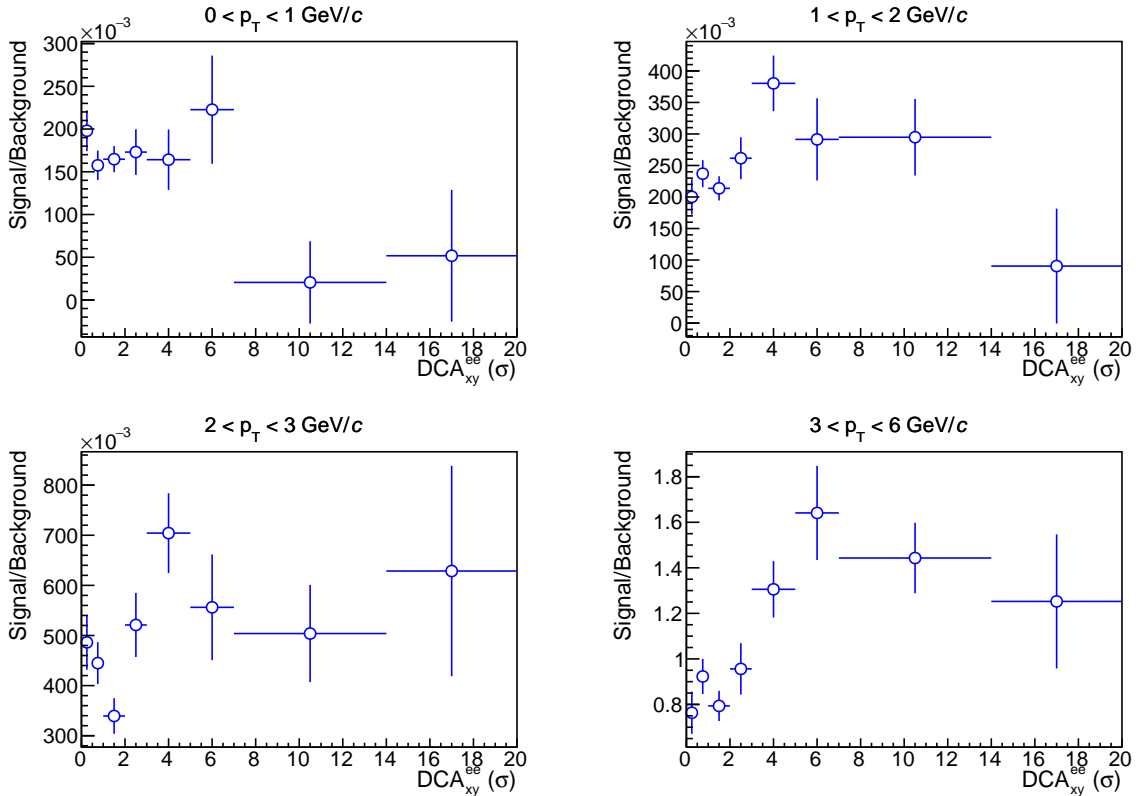


Figure 6.25: Signal over background ratio for the  $DCA_{xy}^{ee}$  analysis using all of the data years (2016 + 2017 + 2018).

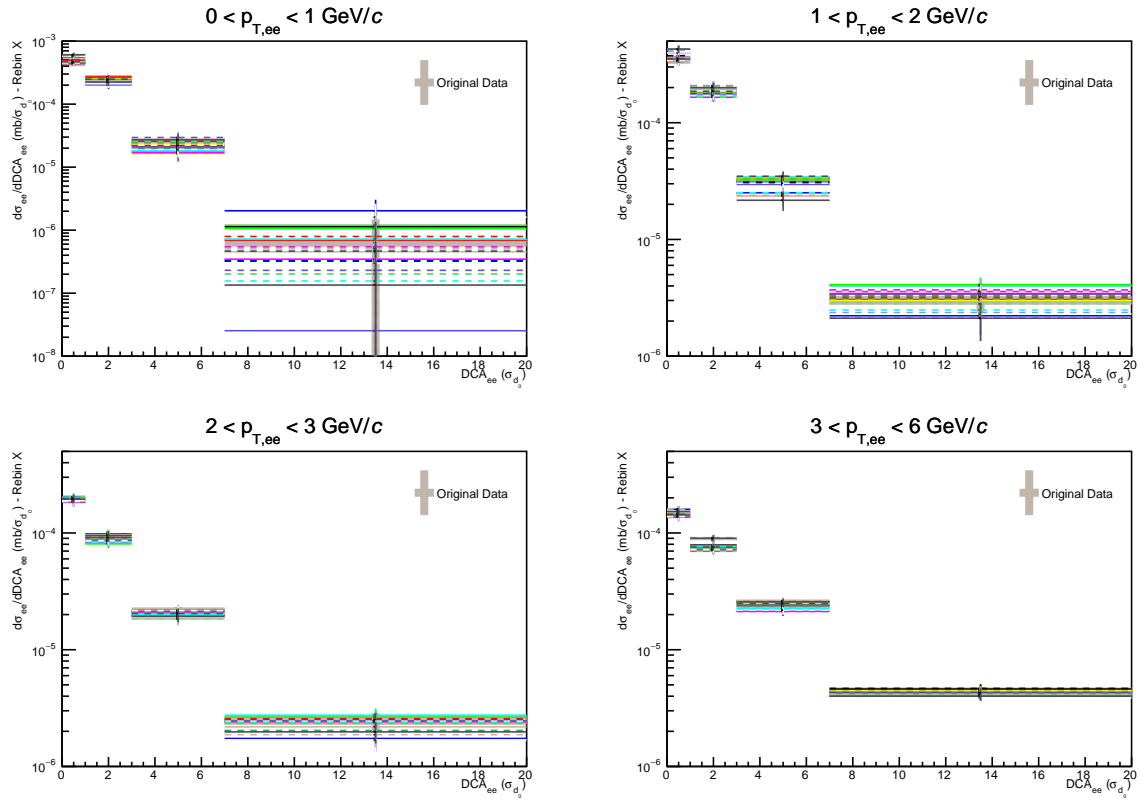


Figure 6.26: Comparison of the signal obtained using different sets of track and eID cuts for the  $DCA_{xy}^{ee}$  analysis as a function of the  $p_{T,ee}$ , using all of the data years (2016 + 2017 + 2018).

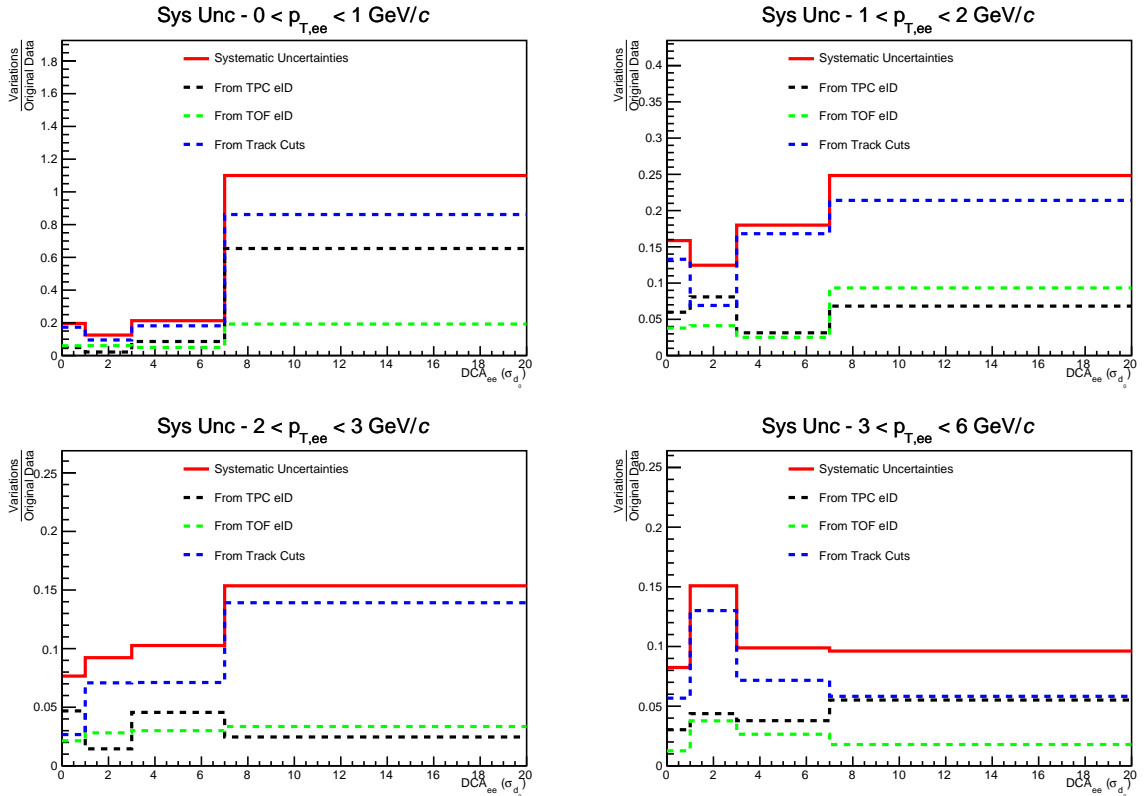


Figure 6.27: Systematic uncertainties of the  $DCA_{xy}^{ee}$  analysis as a function of the  $p_{T,ee}$ , using all of the data years (2016 + 2017 + 2018).

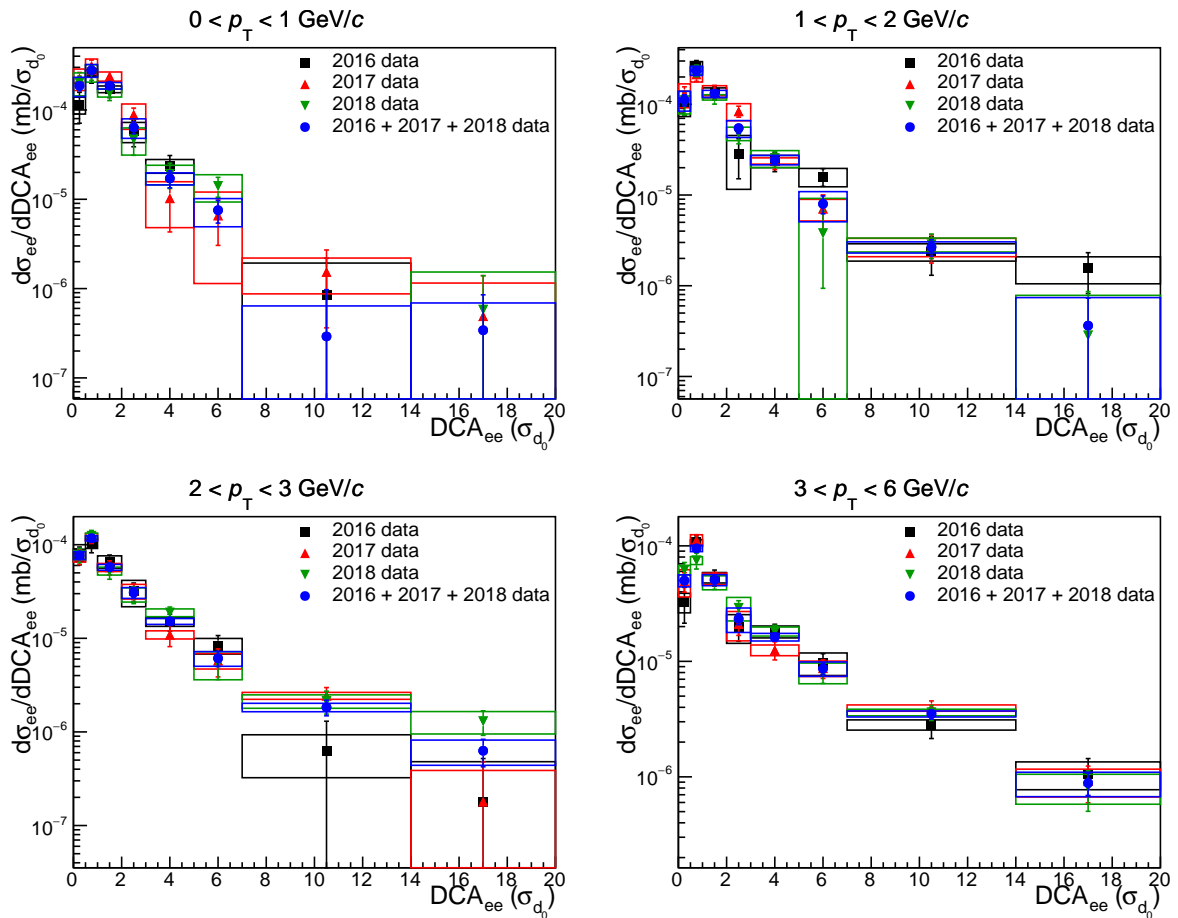


Figure 6.28: The dielectron cross section for the different data-taking years are shown as a function of the  $m_{ee}$  in different pair momentum intervals for the analysis with  $p_{T,e} > 0.4 \text{ GeV}/c$ . The signal obtained using 2016 data is shown in black, 2017 in red, 2018 in green and in blue for the merged years. The bar and boxes represent the statistical and systematic uncertainties of the data.

## 6.2.4 Monte Carlo Templates

The  $DCA_{xy}^{ee}$  contributions from charm and beauty is investigated because this is the analysis that provide us the best distinction between the two contributions. Charm hadrons have smaller decay lengths (50-300  $\mu\text{m}$ ) than beauty hadrons ( $\approx 500 \mu\text{m}$ ), which improves the identification of each fraction contribution.

The reconstructed MC  $DCA_{xy}^{ee}$  analysis can be a bit tricky. A direct comparison between the  $DCA_{xy}^{ee}$  from data and from reconstructed MC (from GEANT) is not easily done because the shapes present differences. This can happen because of the hard job to simulate all of the exact calibrations, resolutions and other parameters in GEANT. To solve this issue, what is done is obtaining a higher statistics  $DCA_{xy}$  shape from pions (which should present similar  $DCA_{xy}^{ee}$  signal to electrons) and then use this  $DCA_{xy}$  shape as input to normalize the entries of the MC dielectron  $DCA_{xy}$ . As already shown, in our  $m_{ee}$  templates we only used the generated simulations (not passed by GEANT) and only performed some smearing procedures to imitate some resolution effects, and this method was enough to describe the data and have already been used in other analyses. The same procedure of using only generated samples will also be used in the  $\Delta\varphi_{ee}$  and  $p_{T,ee}$  analyses. This increases the statistics and saves a lot of disk space, allowing us to produce bigger samples without the need to process them in GEANT, saving processing time and space. Since GEANT aims to reproduce the detector effects, we will also loose generated particles because of the reconstructed track cuts and PID. Using the generated samples instead, no particles are lost and the full production can be used.

However, as already explained, the  $DCA_{xy}^{ee}$  is a pure reconstructed parameter, so how can we try to obtain a  $DCA_{xy}^{ee}$  parameter from the generated level of simulations without using GEANT? The strategy method that was developed in this thesis and that answer this question is described below.

### Calculation

The  $DCA_{xy}$  is calculated using the orbit described by charged particles in the magnetic field. It is defined as the distance from the center of the helix (described by the particle) to the primary vertex (Figure 6.29), subtracted by the radius of its orbit [14, 84, 85]:

$$DCA_e = L - R \quad (6.1)$$

The orbit of a particle in the magnetic field of ALICE can be described as [14]:

$$p_T[\text{GeV}/c] = 0.3 \cdot qB[T]R[m] \quad (6.2)$$

So, the radius of the helix is:



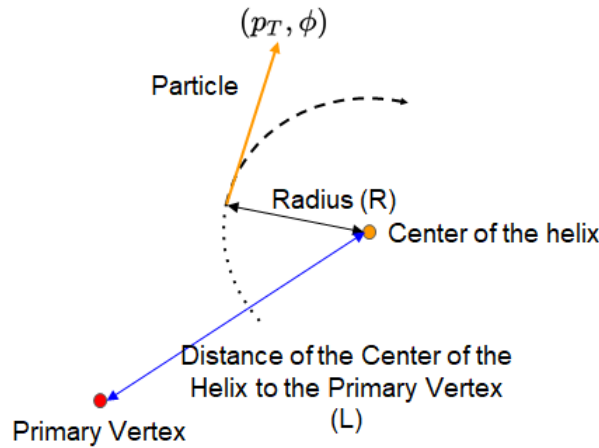


Figure 6.29: Scheme of the distance of closest approach of a particle. The yellow arrow represents a particle in the simulation and the dashed line its deviation inside an imaginary magnetic field. The center of this orbit is illustrated by an orange circle while the primary vertex is represented by the red one.

$$R[m] = p_T / (0.3 \cdot qB) \quad (6.3)$$

Hence, in the simulations the center of the helix can be determined by using the position where the particle was created,  $(x_0, y_0)$ , and its deviation kinematics. A scheme illustrating the equations can be found in Figure 6.30. The position of the center of the orbit then will be:

$$x_R[cm] = x_0[cm] + R[cm] \cdot \sin(\phi) \quad (6.4)$$

$$y_R[cm] = y_0[cm] - R[cm] \cdot \cos(\phi) \quad (6.5)$$

Since all of these variables are known by us from previous equations and from the simulations, we now have everything that we need to calculate the final  $DCA_{xy}$  parameter. The distance from the center of the orbit to the primary vertex will be:

$$L = \sqrt{(x_R - x_{PV})^2 + (y_R - y_{PV})^2} \quad (6.6)$$

Since the radius of the orbit  $R$  also carries information of the particle deviation to the left or to the right of the original direction (because of the charge  $q$  in the equation 6.3), the  $DCA_{xy}^e$  is now calculated as:

$$DCA_e = L - |R| \quad (6.7)$$

And the  $DCA_{xy}$  of a dielectron pair:

$$DCA_{ee}(cm) = \sqrt{\frac{DCA_{e_1}(cm)^2}{2} + \frac{DCA_{e_2}(cm)^2}{2}} \quad (6.8)$$

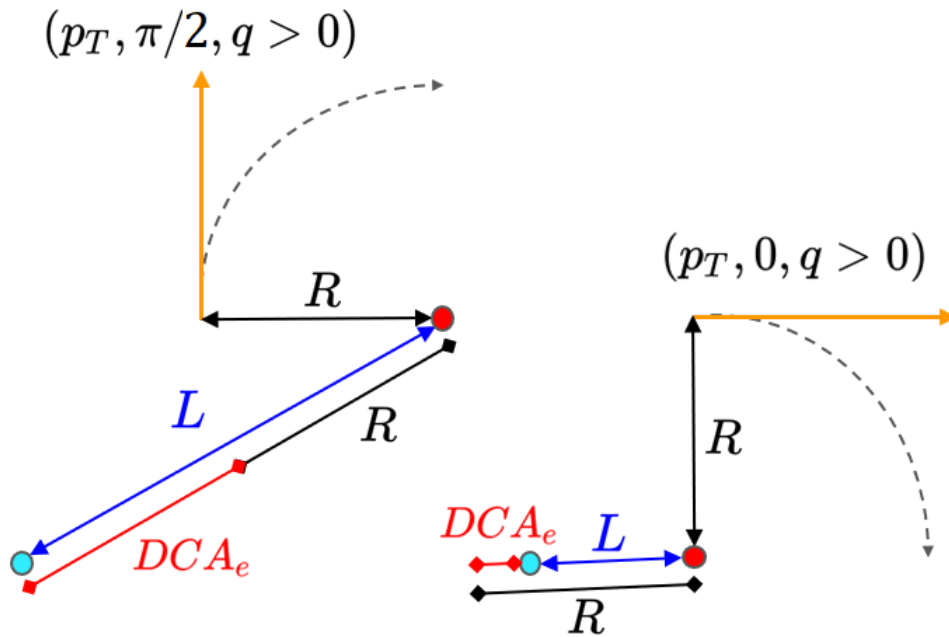


Figure 6.30: Illustration of the calculation of the distance of closest approach of a particle. The blue point represents the Primary Vertex while the blue line represents the distance (L) between the primary vertex and the center of the orbit. The  $DCA_{xy}^e$  is then calculated as the subtraction of this distance L by the radius of the orbit.

$$DCA_{ee}(\sigma_{d_0}) = \sqrt{\frac{DCA_{e_1}(cm)^2}{2\sigma_{d_0,1}} + \frac{DCA_{e_2}(cm)^2}{2\sigma_{d_0,2}}} \quad (6.9)$$

The  $DCA_{xy}^{ee}$  can be calculated as a function of distance unit or as a function of the detector resolution. The first one do not take into account the effects of the detector resolution and may present unreliable shape. That is the reason why in this kind of analysis it is preferable to use it as a function of  $\sigma_{d_0}$ . However, we should take into account that even our calculated  $DCA_{xy}^{ee}$  as a function of distance units is wrongly shaped. This happens because in our calculations we are not taking into account the resolution of the detector. The resolution of this measurement will shift the real value, and this effect is worst as poor as the resolution is. This is similar to what happened to the  $J/\psi$  mass templates, presenting a longer tail than a single narrow peak. To take care of these effects in our calculations we will need to perform a similar smearing procedure that is already applied to  $p_T$ ,  $\eta$  and  $\varphi$  (Section 5.2.4).

### Smearing

Figure 6.31 shows the resolution of the transverse distance to the primary vertex for identified ITS–TPC tracks extracted from the covariance matrix of data and MC. The resolution is better as we increase the momentum, but for low momentum the resolution worsens and become critical. This is the main reason for not using low- $p_T$  electrons.

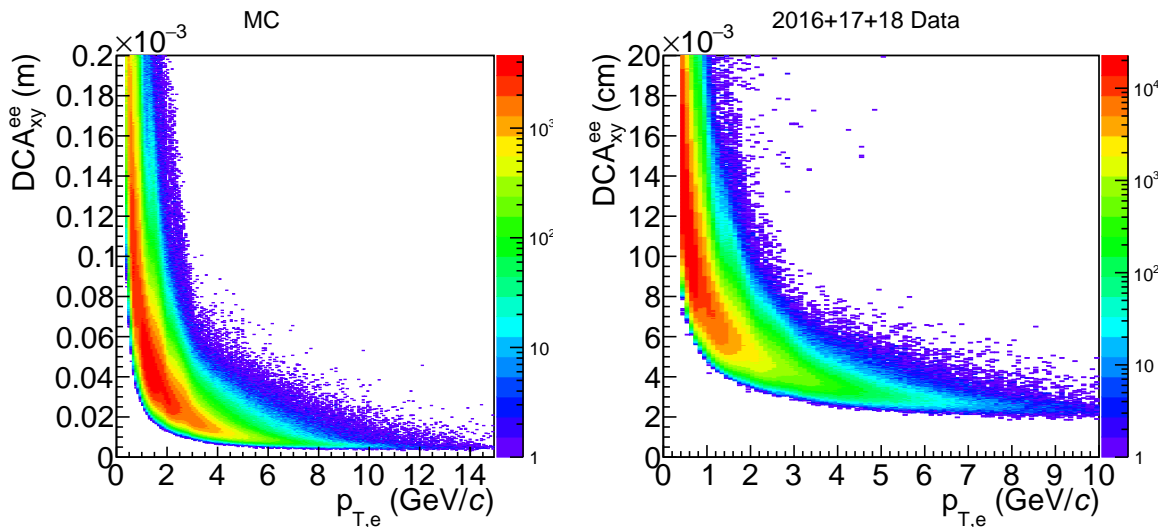


Figure 6.31: Impact parameter resolutions of electrons in pp collisions at 13 TeV as a function of the transverse momentum. On the left side it is shown the MC resolution of the tracks and on the right the resolution of the tracks extracted from data. **Note** that even that the Y-axis of them are not in same units, their axis were shown in the same physical window (0 - 20 cm).

The  $p_T$ -dependence shows what is expected from a momentum-independent contribution because of the spatial resolution of the detectors added to a momentum-dependent contribution due to multiple scattering. A more detailed explanation of these resolutions can be found at [14]. From what is observed, there are differences in resolution between data and MC. Since this resolution is used to normalize the  $DCA_{xy}^e$  it may explain some of other procedures that must be applied in reconstructed MC in order to make the data and MC  $DCA_{xy}^{ee}$  descriptions match. In this analysis we are not aiming to use reconstructed MC to perform the fits, but use the theory of the impact parameter to try to simulate detector effects on our pure MC simulations to calculate the  $DCA_{xy}^{ee}$  for pure MC samples.

The  $DCA_{xy}^e$  smearing procedure happens after finding a heavy-flavour electron. Its  $DCA_{xy}^e$  is calculated firstly by the procedure already described (Equations 6.3, 6.4, 6.5, 6.6 and 6.7), and then the smearing is applied as a random number within a Gaussian distribution centered at the calculated  $DCA_{xy}^e$  with its  $\sigma$  as the resolution for that particle's momentum. This resolution is extracted from the resolution maps from data (right plot of 6.31), as a random number weighted by the probability distribution of the resolution in the given  $p_{T,e}$  bin of that electron. The  $DCA_{xy}^{ee}$  templates obtained with and without this smearing procedure are shown in Figures 6.32 and 6.33, for PYTHIA and POWHEG samples, respectively. The templates of the left plot of these Figures were obtained without any smearing in  $p_T$ ,  $\eta$ ,  $\varphi$  and  $DCA_{xy}^e$ , and that is the reason that there are no  $J/\psi$  contribution since without  $p_T$ ,  $\eta$ ,  $\varphi$  there is no  $J/\psi$  in the IMR, as showed in the  $m_{ee}$  templates (Section 6.1.4). The  $DCA_{xy}^e$  smearing procedure has an effect of shifting the  $DCA_{xy}^e$  to greater values, and its strongest visible effect can be seen in the  $J/\psi$  templates,

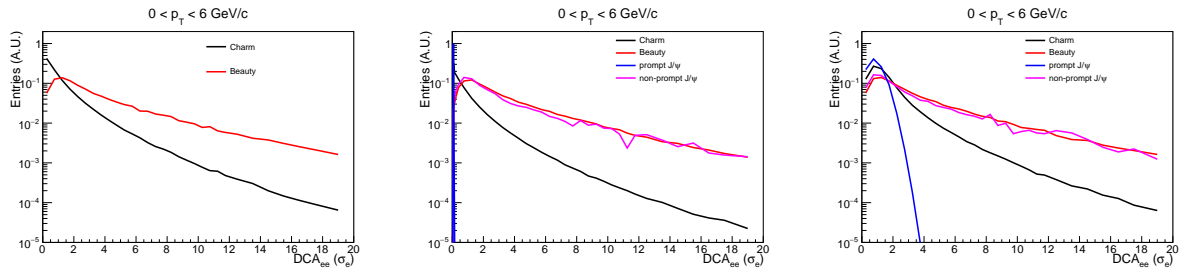


Figure 6.32: Comparison between charm, beauty and  $J/\psi$  templates using PYTHIA pure MC samples, without any smearing procedure (left), with  $p_T$ ,  $\eta$  and  $\varphi$  smearing (center), and with  $DCA_{xy}^{ee}$  smearing procedure (right). The templates were normalized by their integrals for a better comparison.

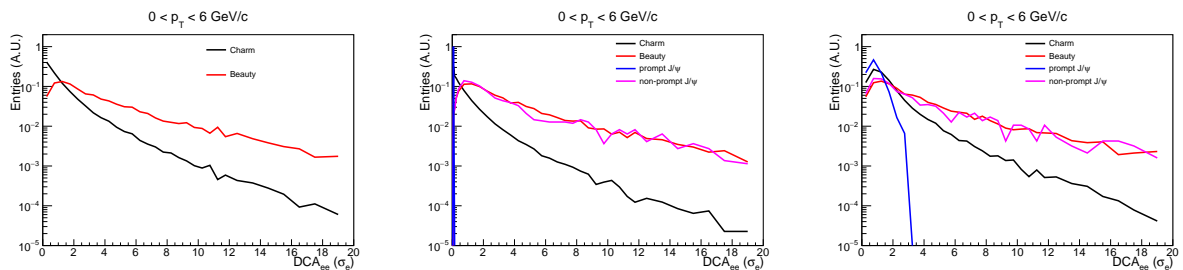


Figure 6.33: Comparison between charm, beauty and  $J/\psi$  templates using POWHEG pure MC samples, without any smearing procedure (left), with  $p_T$ ,  $\eta$  and  $\varphi$  smearing (center), and with  $DCA_{xy}^{ee}$  smearing procedure (right). The templates were normalized by their integrals for a better comparison.

followed by charm. The pseudo-root code of such calculation would be:

$$\sigma_{d_0}(p_{T,e}) \text{ (cm)} = \text{Resolution} \rightarrow \text{ProjectionY}(p_{T,e}) \rightarrow \text{GetRandom}() \quad (6.10)$$

$$DCA_e^{\text{smear}} \text{ (cm)} = \text{gRandom}() \rightarrow \text{Gaus}(DCA_e \text{ (cm)}, \sigma_{d_0}(p_{T,e}) \text{ (cm)}) \quad (6.11)$$

$$DCA_e^{\text{smear}}(\sigma_{d_0}) = DCA_e^{\text{smear}} \text{ (cm)} / \sigma_{d_0} \quad (6.12)$$

The  $J/\psi$  is an important contributor to the  $DCA_{xy}^{ee}$  as a prompt contribution. None of the other contributors, charm nor beauty, will contribute to the very small values of  $DCA_{xy}^{ee}$ , since that region is dominated by prompt sources. The non-prompt  $J/\psi$  has a similar behaviour than beauty templates, which is expected since non-prompt  $J/\psi$  are considered mainly as the decays from beauty hadrons.

It is important to mention that a decay probability fraction correction was applied to the charm templates. The reason for such correction is that in charm simulations, as already described, the charmed hadrons are forced to decay into electrons to increase the probability of finding a HFe in our simulations, creating more effective simulations

	B.R. $e^\pm$ semi-leptonic [66]	decay length $c\tau$ [86]
$D^0$	$(6.49 \pm 0.11) \%$	$122.9 \mu m$
$D^\pm$	$(16.07 \pm 0.30) \%$	$311.8 \mu m$
$D_s$	$(6.50 \pm 0.40) \%$	$151.2 \mu m$
$\Lambda_c$	$(3.95 \pm 0.35) \%$	$60.7 \mu m$
$\Xi_c^0$	$(1.8 \pm 1.2) \%$	$45.8 \mu m$
$\Xi_c^\pm$	$(2.3^{+0.7}_{-0.8}) \%$	$136.6 \mu m$

Table 6.1: Charmed hadron fractions and decay length. The latest measurements of fragmentation fractions were used.

regarding the size of the output files. When normalizing the charm contributions this is taken into account by normalizing our charm templates by the branching ratio,  $BR^2$ . This is perfectly fine to do in different studies but  $DCA_{xy}^{ee}$ . The problem in the  $DCA_{xy}^{ee}$  is that the BR is taken as the total probability of  $c \rightarrow e$ , but different mesons and baryons decays present different BR and also different decay lengths, which would lead to different  $DCA_{xy}^{ee}$  shapes. While this does not affect the  $m_{ee}$  or other parameters since the shape is similar for different decay channels, in  $DCA_{xy}^{ee}$  this correction is needed since the probability for different decays also present different decay length.

The probability of each of the possible decay channels are shown in Table 6.1. The issue lays on the enhancement of the heavy-flavour in our simulations that will not provide the correct fractions of decays since some of them were forced to get more statistics. What was done to correct and check such effects and different shapes was to obtain the probabilities of each of these decay channels by PYTHIA and POWHEG, and apply a correction factor to re-weight these probabilities by the right ones, using the recent measured charm fragmentation fractions [66].

For this correction it was used 3 contributions: (1)  $D^\pm$ , (2) a grouped contributions of  $D^0 + D_s + \Xi_c^\pm$ , and (3) a grouped contribution of  $\Lambda_c + \Xi_c^0$ . This was done since their decay lengths are similar, so they could be grouped together into a single template, instead of creating multiple templates that would need to be paired to all of the other contributors. For this purpose we built 3!  $DCA_{xy}^{ee}$  templates, containing all of the mixed possibilities of decaying channels of these paired groups, which is shown in the left plot of Figure 6.34. In this Figure we can clearly see the differences of shapes due to the differences in the decay length of each leg of the pairing.

What is done then is to compare the number of entries in each of these combined templates to the total number of entries, which is the output fraction by the PYTHIA or POWHEG generators. Knowing this generated fraction, we can multiply these obtained fractions by the mixed contribution probability of these 3 groups by their real probabilities of BR (the measured ones), so all of them are proportionally correct within each other. The total charm template using this correction is shown in the right plot of Figure 6.34. The corrected template has a greater tail to higher  $DCA_{xy}^{ee}$  values than the uncor-

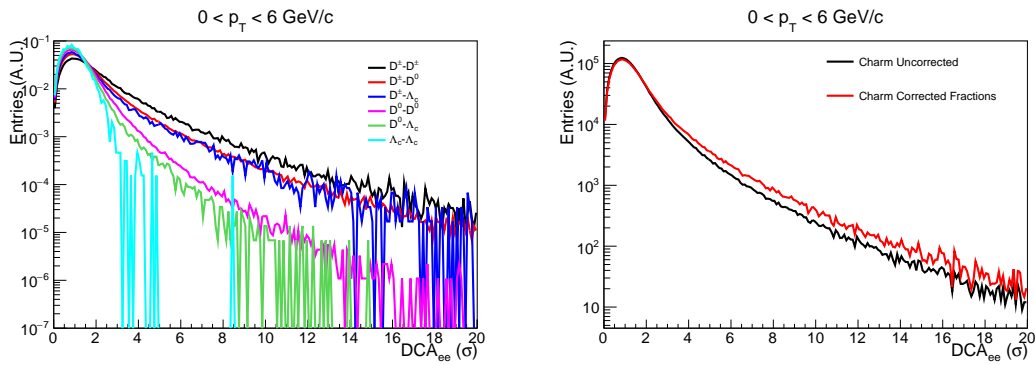


Figure 6.34: Left: contributions from different charm decay channels using the 3 grouped contributions described in text  $D^\pm$  stands for  $D^\pm$ ,  $D^0$  stands for  $D^0 + D_s + \Xi_c^\pm$  and  $\Lambda_c$  stands for  $\Lambda_c + \Xi_c^0$ . Right: final charm template before and after the re-weighting of the decaying fractions.

rected, meaning that the decay fractions of the larger charmed  $DCA_{xy}^{ee}$  contributors were underestimated by the generators compared to recent measurements.

## Templates QA

The templates from prompt (and non-prompt) sources such as  $J/\psi$  were used to compare the  $DCA_{xy}^{ee}$  data only using the  $m_{ee}$  region of  $J/\psi$  peak (3.0 - 3.1  $\text{GeV}/c^2$ ) to check if the templates can describe the  $J/\psi$   $DCA_{xy}^{ee}$  shape. This comparison aims to check if the calculations of such templates provide us realistic  $DCA_{xy}^{ee}$  shapes. The comparison in this  $m_{ee}$  region also has some contributions for charm and beauty sources but they should be small. To avoid using many templates and fit parameters the comparison was made just using the  $J/\psi$  templates. This comparison, Figure 6.35, has low statistics on data because of the hard  $m_{ee}$  cut (3.0 - 3.1) still divided in several  $p_{T,ee}$  bins. We can see a reasonably well description of the data by the templates, considering that charm and beauty were not considered to avoid a possible data over-fitting.

## 6.2.5 Results

The charm and beauty MC templates were used to fit the  $DCA_{xy}^{ee}$  data in the IMR  $m_{ee}$  region. For this purpose it was considered contributions from charm, beauty and  $J/\psi$  to the fit. The fit was performed for each of the 3 years separately, but it will be only shown the fitting for the 3 merged years here for simplicity, for PYTHIA and POWHEG simulations. The fit results of each of the years separately can be found in the Appendix E. The results from each of the years can be used now to compare with the results obtained using the invariant mass to validate the method.

The dielectron spectrum is shown as a function of the  $p_{T,ee}$  and  $DCA_{xy}^{ee}$  in Figures 6.36 and 6.37 compared to the expectation from the cocktail using PYTHIA and POWHEG simulations, respectively, with minimum  $p_{T,e}$  cut of 0.4  $\text{GeV}/c$ . A summary of all of the

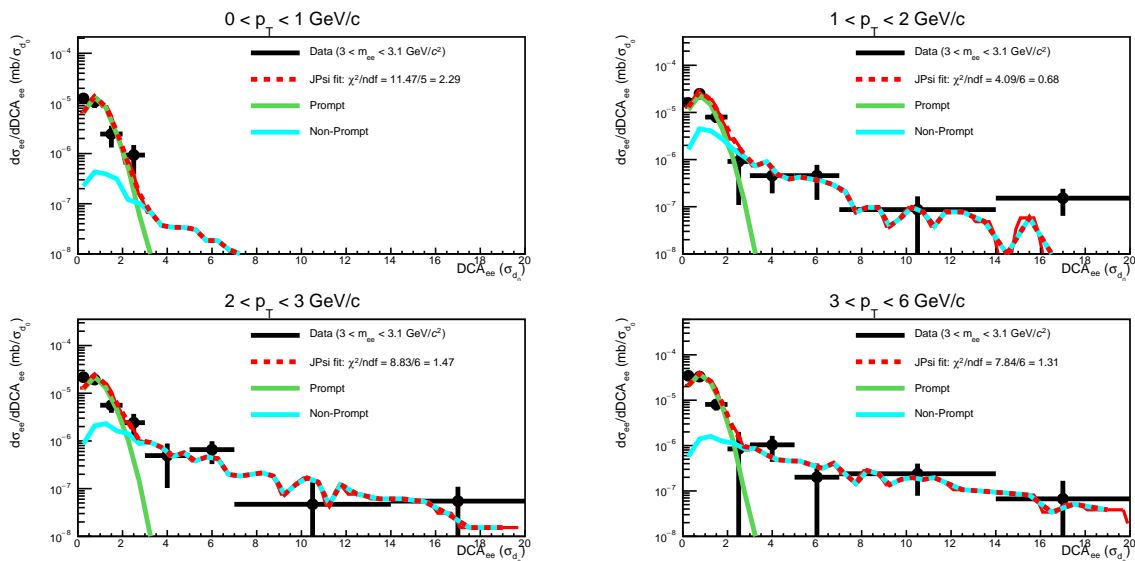


Figure 6.35:  $J/\psi$  PYTHIA templates fit to  $DCA_{xy}^{ee}$  data with  $m_{ee}$  within 3.0 - 3.1  $\text{GeV}/c^2$ .

parameters obtained can be found in Table 6.2. The data is well described using the contributions from charm, beauty and  $J/\psi$  by both PYTHIA and POWHEG generators. The cross sections found by the  $DCA_{xy}^{ee}$  fit using pure MC calculations seem to describe well the expected shapes and are in accordance to the ones obtained when using  $m_{ee}$  fits, for PYTHIA (Figure 6.38) and POWHEG (Figure 6.39).

As for further information, the corrections of the charm template shape by the measured decaying fractions modified the fitted cross sections by  $\approx 5\%$ . So if one tries to fit the data **without** this correction, it will be found a  $\approx 5\%$  **smaller charm** production cross section and a  $5\%$  **greater beauty** production cross section. This is consistent since the correction increased the charm contribution to higher  $DCA_{xy}^{ee}$  values, reducing the contribution of beauty to fit that region of the spectrum.

The cross sections extracted using  $DCA_{xy}^{ee}$  are completely compatible to the ones extracted by using the  $m_{ee}$  fits within uncertainties. However, the charm cross sections are systematically higher than the ones predicted by the  $m_{ee}$  fits when using the PYTHIA generator. On the other hand, when using the POWHEG generator it can be seen a systematically higher beauty cross sections by  $DCA_{xy}^{ee}$  than  $m_{ee}$ . These results are very promising and points out that it is really possible to use this method to estimate the  $DCA_{xy}^{ee}$  of pure MC pairs and that they present valid and consistent results. The  $DCA_{xy}^{ee}$  should have a greater discriminating power than the  $m_{ee}$  analysis because the charm, beauty and prompt templates are different in shape and each of them have higher contributions in different regions of the  $DCA_{xy}^{ee}$  spectrum. However, although most of the statistical uncertainties by the  $DCA_{xy}^{ee}$  and  $m_{ee}$  fits are comparable, the systematical uncertainties are greater for  $DCA_{xy}^{ee}$ , something that had already been observed in [18].

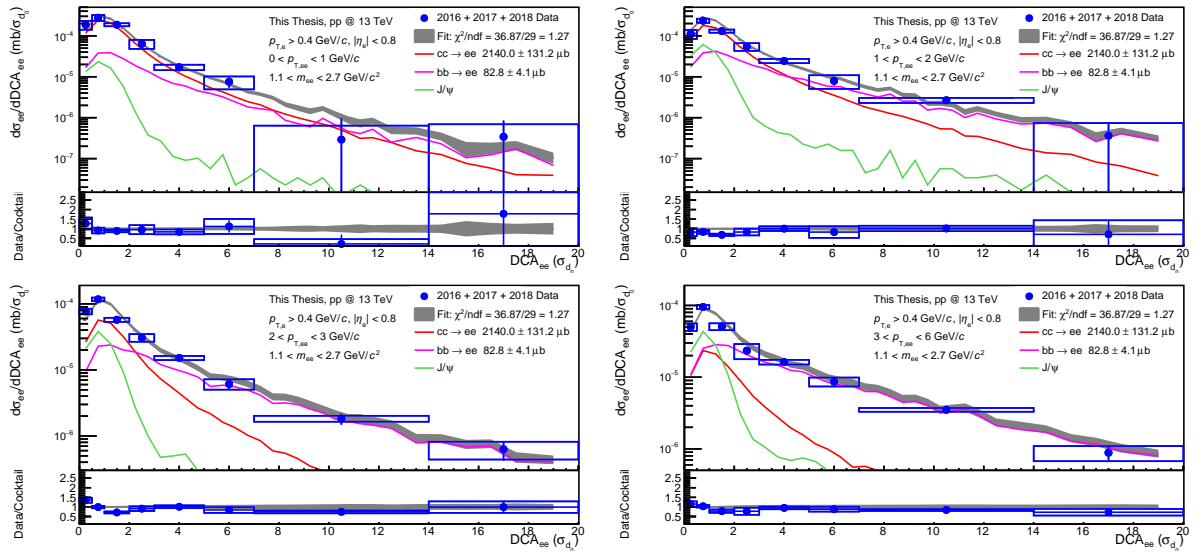


Figure 6.36: The dielectron cross section in pp collisions at 13 TeV as a function of the impact parameter in different pair momentum intervals is shown in blue circles for the analysis using the minimum  $p_{T,e}$  cut of 0.4 GeV/c, and the PYTHIA cocktail is shown in red, purple and green for charm, beauty and  $J/\psi$  contributions, respectively. The bar and boxes represent the statistical and systematic uncertainties of the data, while the final cocktail is shown in a grey band. On the bottom of each pair momentum interval plot it is shown the data-to-cocktail ratio.

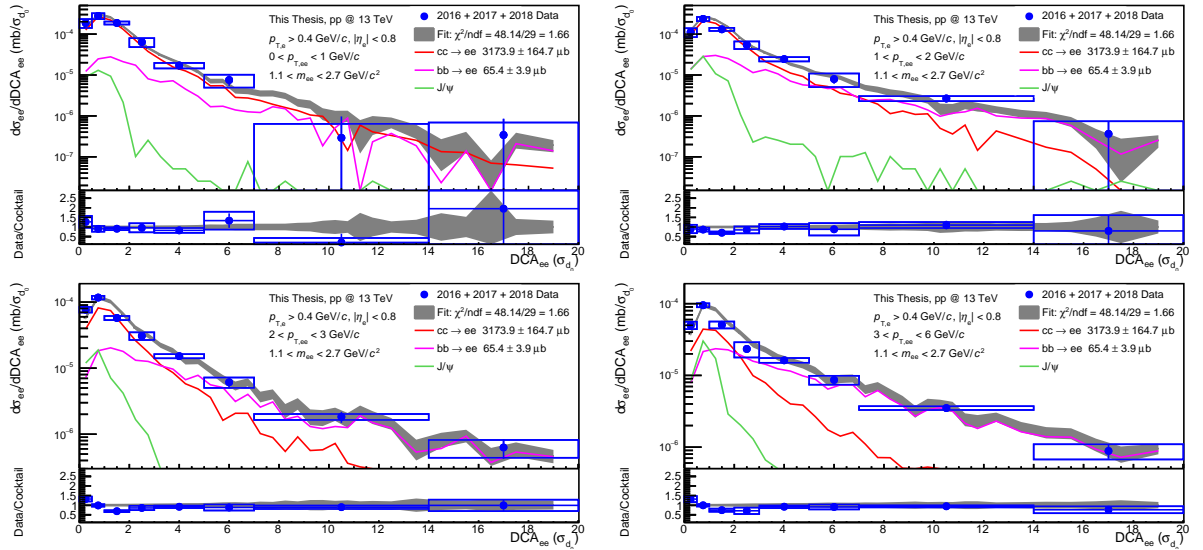


Figure 6.37: The dielectron cross section in pp collisions at 13 TeV as a function of the impact parameter in different pair momentum intervals is shown in blue circles for the analysis using the minimum  $p_{T,e}$  cut of 0.4 GeV/c, and the POWHEG cocktail is shown in red, purple and green for charm, beauty and  $J/\psi$  contributions, respectively. The bar and boxes represent the statistical and systematic uncertainties of the data, while the final cocktail is shown in a grey band. On the bottom of each pair momentum interval plot it is shown the data-to-cocktail ratio.



PYTHIA		2016 Data ( $\mu\text{b}$ )	2017 Data ( $\mu\text{b}$ )	2018 Data ( $\mu\text{b}$ )	All Data ( $\mu\text{b}$ )
$\frac{d\sigma_{c\bar{c}}}{dy}$	$(p_{T,e} < 0.2 \text{ GeV}/c)$	$1576 \pm 232 \text{ (stat)} \pm 372 \text{ (sys)}$	$1901 \pm 191 \text{ (stat)} \pm 349 \text{ (sys)}$	$1711 \pm 185 \text{ (stat)} \pm 269 \text{ (sys)}$	$1746 \pm 116 \text{ (stat)} \pm 249 \text{ (sys)}$
$\frac{d\sigma_{c\bar{c}}}{dy}$	$(p_{T,e} < 0.4 \text{ GeV}/c)$	$1544 \pm 236 \text{ (stat)} \pm 456 \text{ (sys)}$	$2224 \pm 198 \text{ (stat)} \pm 392 \text{ (sys)}$	$1744 \pm 189 \text{ (stat)} \pm 351 \text{ (sys)}$	$1839 \pm 117 \text{ (stat)} \pm 273 \text{ (sys)}$
$\frac{d\sigma_{c\bar{c}}}{dy}$	DCA $^{ec}_{xy}$	$2022 \pm 257 \text{ (stat)} \pm 397 \text{ (sys)}$	$2534 \pm 218 \text{ (stat)} \pm 541 \text{ (sys)}$	$2024 \pm 211 \text{ (stat)} \pm 422 \text{ (sys)}$	$2140 \pm 131 \text{ (stat)} \pm 376 \text{ (sys)}$
$\frac{d\sigma_{b\bar{b}}}{dy}$	$(p_{T,e} < 0.2 \text{ GeV}/c)$	$86.0 \pm 12.6 \text{ (stat)} \pm 10.5 \text{ (sys)}$	$87.8 \pm 10.0 \text{ (stat)} \pm 10.2 \text{ (sys)}$	$75.7 \pm 9.7 \text{ (stat)} \pm 11.2 \text{ (sys)}$	$74.9 \pm 5.7 \text{ (stat)} \pm 7.4 \text{ (sys)}$
$\frac{d\sigma_{b\bar{b}}}{dy}$	$(p_{T,e} < 0.4 \text{ GeV}/c)$	$93.7 \pm 10.6 \text{ (stat)} \pm 7.2 \text{ (sys)}$	$77.5 \pm 8.4 \text{ (stat)} \pm 9.9 \text{ (sys)}$	$84.2 \pm 7.7 \text{ (stat)} \pm 10.0 \text{ (sys)}$	$86.8 \pm 5.1 \text{ (stat)} \pm 7.1 \text{ (sys)}$
$\frac{d\sigma_{b\bar{b}}}{dy}$	DCA $^{ec}_{xy}$	$81.4 \pm 8.1 \text{ (stat)} \pm 17.4 \text{ (sys)}$	$74.5 \pm 6.7 \text{ (stat)} \pm 10.7 \text{ (sys)}$	$83.9 \pm 6.4 \text{ (stat)} \pm 15.4 \text{ (sys)}$	$82.8 \pm 4.1 \text{ (stat)} \pm 10.9 \text{ (sys)}$
POWHEG		2016 Data ( $\mu\text{b}$ )	2017 Data ( $\mu\text{b}$ )	2018 Data ( $\mu\text{b}$ )	All Data ( $\mu\text{b}$ )
$\frac{d\sigma_{c\bar{c}}}{dy}$	$(p_{T,e} < 0.2 \text{ GeV}/c)$	$2759 \pm 304 \text{ (stat)} \pm 603 \text{ (sys)}$	$3075 \pm 257 \text{ (stat)} \pm 508 \text{ (sys)}$	$2764 \pm 248 \text{ (stat)} \pm 429 \text{ (sys)}$	$2378 \pm 160 \text{ (stat)} \pm 374 \text{ (sys)}$
$\frac{d\sigma_{c\bar{c}}}{dy}$	$(p_{T,e} < 0.4 \text{ GeV}/c)$	$2810 \pm 317 \text{ (stat)} \pm 733 \text{ (sys)}$	$3727 \pm 253 \text{ (stat)} \pm 647 \text{ (sys)}$	$2913 \pm 239 \text{ (stat)} \pm 527 \text{ (sys)}$	$2654 \pm 156 \text{ (stat)} \pm 408 \text{ (sys)}$
$\frac{d\sigma_{c\bar{c}}}{dy}$	DCA $^{ec}_{xy}$	$3153 \pm 324 \text{ (stat)} \pm 548 \text{ (sys)}$	$3487 \pm 278 \text{ (stat)} \pm 719 \text{ (sys)}$	$2854 \pm 276 \text{ (stat)} \pm 536 \text{ (sys)}$	$3174 \pm 165 \text{ (stat)} \pm 502 \text{ (sys)}$
$\frac{d\sigma_{b\bar{b}}}{dy}$	$(p_{T,e} < 0.2 \text{ GeV}/c)$	$36.3 \pm 11.7 \text{ (stat)} \pm 4.0 \text{ (sys)}$	$51.1 \pm 11.5 \text{ (stat)} \pm 6.6 \text{ (sys)}$	$40.1 \pm 8.9 \text{ (stat)} \pm 5.1 \text{ (sys)}$	$55.2 \pm 6.3 \text{ (stat)} \pm 3.6 \text{ (sys)}$
$\frac{d\sigma_{b\bar{b}}}{dy}$	$(p_{T,e} < 0.4 \text{ GeV}/c)$	$48.8 \pm 10.8 \text{ (stat)} \pm 4.2 \text{ (sys)}$	$29.0 \pm 8.7 \text{ (stat)} \pm 4.9 \text{ (sys)}$	$47.8 \pm 8.7 \text{ (stat)} \pm 5.6 \text{ (sys)}$	$58.2 \pm 5.3 \text{ (stat)} \pm 2.6 \text{ (sys)}$
$\frac{d\sigma_{b\bar{b}}}{dy}$	DCA $^{ec}_{xy}$	$61.1 \pm 7.7 \text{ (stat)} \pm 13.4 \text{ (sys)}$	$58.0 \pm 7.1 \text{ (stat)} \pm 7.2 \text{ (sys)}$	$72.4 \pm 6.6 \text{ (stat)} \pm 12.7 \text{ (sys)}$	$65.4 \pm 3.9 \text{ (stat)} \pm 8.2 \text{ (sys)}$

Table 6.2: Heavy-flavour production cross sections extracted through  $m_{ee}$  and DCA $^{ec}_{xy}$  fits as a function of the year, minimum  $p_{T,e}$  cut and generator. An additional accountable cocktail uncertainty due to the branching ratios for charm (beauty) of 8 % (6 %) is not listed.

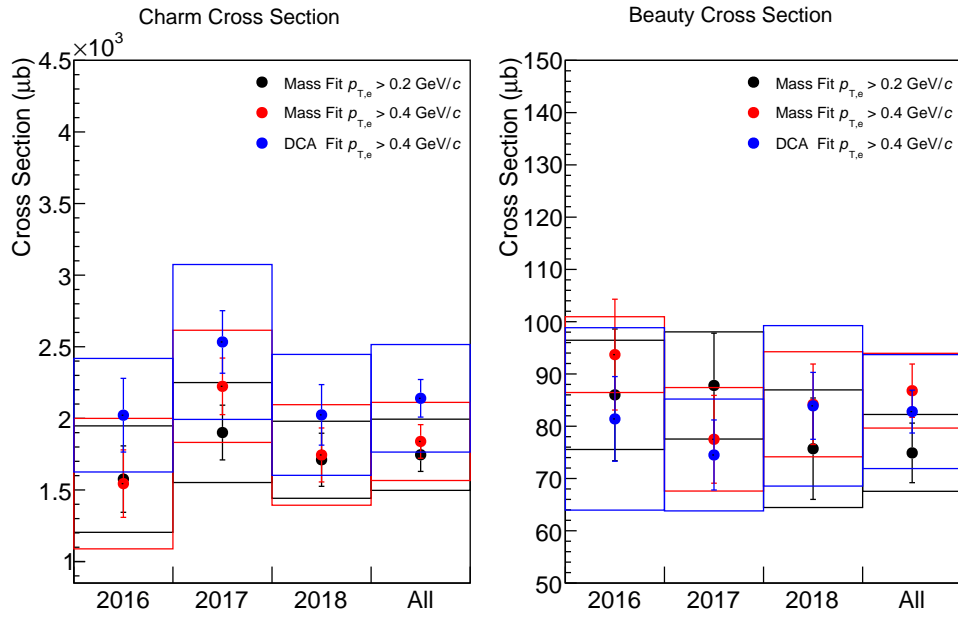


Figure 6.38: Heavy-flavour cross sections extracted through the  $m_{ee}$  and  $DCA_{xy}^{ee}$  fits as a function of the year and minimum  $p_{T,e}$  cut using PYTHIA cocktail. The  $m_{ee}$  results using a minimum  $p_{T,e}$  cut of 0.2 GeV/ $c$  are shown in black, in red for minimum  $p_{T,e}$  cut of 0.4 GeV/ $c$  and in blue for the  $DCA_{xy}^{ee}$  results. The vertical bars and boxes are the statistical and systematic uncertainties.

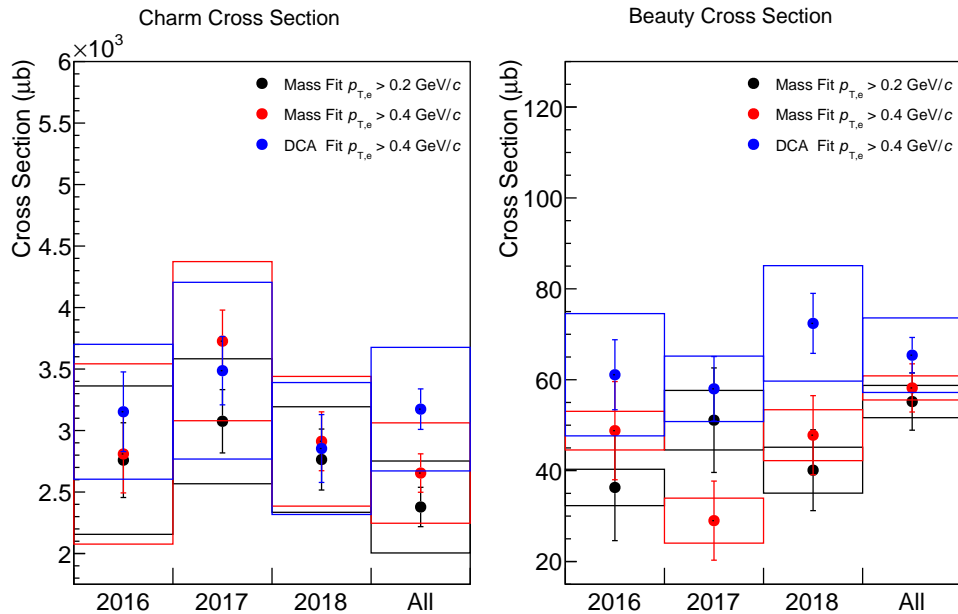


Figure 6.39: Heavy-flavour cross sections extracted through the  $m_{ee}$  and  $DCA_{xy}^{ee}$  fits as a function of the year and minimum  $p_{T,e}$  cut using POWHEG cocktail. The  $m_{ee}$  results using a minimum  $p_{T,e}$  cut of 0.2 GeV/ $c$  are shown in black, in red for minimum  $p_{T,e}$  cut of 0.4 GeV/ $c$  and in blue for the  $DCA_{xy}^{ee}$  results. The vertical bars and boxes are the statistical and systematic uncertainties.

## 6.3 Chapter Summary

The dielectron cross sections in pp collisions at  $\sqrt{s} = 13$  TeV as a function of the  $m_{ee}, p_{T,ee}$  and  $m_{ee}, DCA_{xy}^{ee}$  in the intermediate mass region were obtained for each of the 2016, 2017 and 2018 data-taking years, and for these merged years. In the case of the  $m_{ee}$ , the dielectron cross sections were obtained for both analyses with minimum  $p_{T,e}$  cut of 0.2 and 0.4 GeV/ $c^2$ . These measurements contain mainly heavy-flavour electron correlations, since the IMR is dominated by them.

The  $m_{ee}$  and  $DCA_{xy}^{ee}$  measurements as a function of the  $p_{T,ee}$  were compared to cocktail expectations of charm, beauty and  $J/\psi$  from both PYTHIA and POWHEG simulations. In the case of the  $DCA_{xy}^{ee}$ , the templates were obtained using pure MC sample calculations, determining the  $DCA_{xy}^{ee}$  by calculating the deviation of the electrons in the magnetic field of ALICE. This method was completely planned, developed, tested and performed in this thesis, with several validating tests and a final comparison between the cross section extracted by the  $DCA_{xy}^{ee}$  fits to the  $m_{ee}$  fits.

Starting with the  $m_{ee}$  analysis, it was found an agreement between the extracted cross sections and from previous ALICE measurements. These extracted cross sections are different for PYTHIA and POWHEG fits, due to differences in the acceptance of dielectrons between these generators and  $p_T$  distributions. There was an overall agreement within uncertainties between the analyses with different minimum  $p_{T,e}$  cut, allowing us to perform a comparison between  $DCA_{xy}^{ee}$  and  $m_{ee}$  without the expectation of further cut effects.

The heavy-flavour production cross section extracted from the  $DCA_{xy}^{ee}$  fits were completely compatible with those obtained with the  $m_{ee}$  analyses, within uncertainties. The data could be well described by the cocktail. The templates obtained by this method were found to be very satisfactory in the validation tests and very promising in the comparison between the cross-sections extraction from different observables. The summary of all of the charm and beauty cross section values for different years (2016, 2017, 2018 or merged), generator (PYTHIA or POWHEG) and measurements ( $m_{ee}$  or  $DCA_{xy}^{ee}$ ) can be found in Table 6.2.

As already mentioned, since our measurements are in complete agreement with the previous ALICE measurements, we reinforced the previous observation that the extracted charm cross section are above the upper uncertainty limit of the FONLL calculations (see Section 2.6 and Figure 2.12), with a higher precision. The beauty cross section, on the other hand, is well described by the FONLL calculations, as this work is in agreement with previous published results (Figure 2.12) and presents a better precision.



# 7 Heavy-Flavour Production Mechanisms

While the Chapter 6 focused in the determination of the charm and beauty production cross sections, this Chapter describes the study of the charm production mechanisms: flavour creating, flavour excitation and gluon splitting. To be able to disentangle the production mechanisms of heavy quarks, two different analyses were carried out: the first approach uses the angular correlations between heavy-flavour electrons ( $\Delta\varphi_{ee}$ ) (Section 7.1) while the second uses only the  $p_{T,ee}$  distribution (Section 7.2). A summary of the study of the production mechanisms of charm closes this Chapter at Section 7.3. The analyses will follow the same structure already seen in the study of  $m_{ee}$  and  $DCA_{xy}^{ee}$ , building the data signal in the IMR, the production of the templates, and the final comparison between the two of them, followed by a discussion of what could be extracted from such comparisons.

## 7.1 $\Delta\varphi$ Analysis

### 7.1.1 $\Delta\varphi$ Efficiency

The  $\Delta\varphi_{ee}$  efficiency was calculated using the process described in Section 5.2.6 for dielectrons from charm and beauty decays. In this case, the efficiencies are only calculated using the minimum  $p_{T,e}$  cut of 0.2 GeV/ $c$ . The efficiencies for all of the studied years are shown in Figure 7.1. For the  $\Delta\varphi_{ee}$ , the efficiencies are built as a 3D histogram of  $p_{T,ee}$ ,  $m_{ee}$  and  $\Delta\varphi_{ee}$ . The best signal over background ratio was found using a single bin in the  $m_{ee}$  (1.1 - 2.7 GeV/ $c^2$ ), as also done in the  $DCA_{xy}^{ee}$  analysis.

As already observed in the  $m_{ee}$  efficiencies, there is no difference in shape for all of the 3 years in all of the different  $p_{T,ee}$  intervals. Similarly, beauty electron pairs also present here an overall higher efficiency. Although it was not expected any correlation between the efficiency and the  $\Delta\varphi_{ee}$  parameter, it can be seen that each  $p_{T,ee}$  bin has its own  $\Delta\varphi_{ee}$  efficiencies behaviour. This must be due to the existent correlation between the  $\Delta\varphi_{ee}$  and the other parameters, such as  $p_{T,ee}$  and  $m_{ee}$ . Since we are using larger binning for a better signal over background ratio, the  $m_{ee}$  and  $p_{T,ee}$  interval efficiency gets mixed in the correlated  $\Delta\varphi_{ee}$  bins.

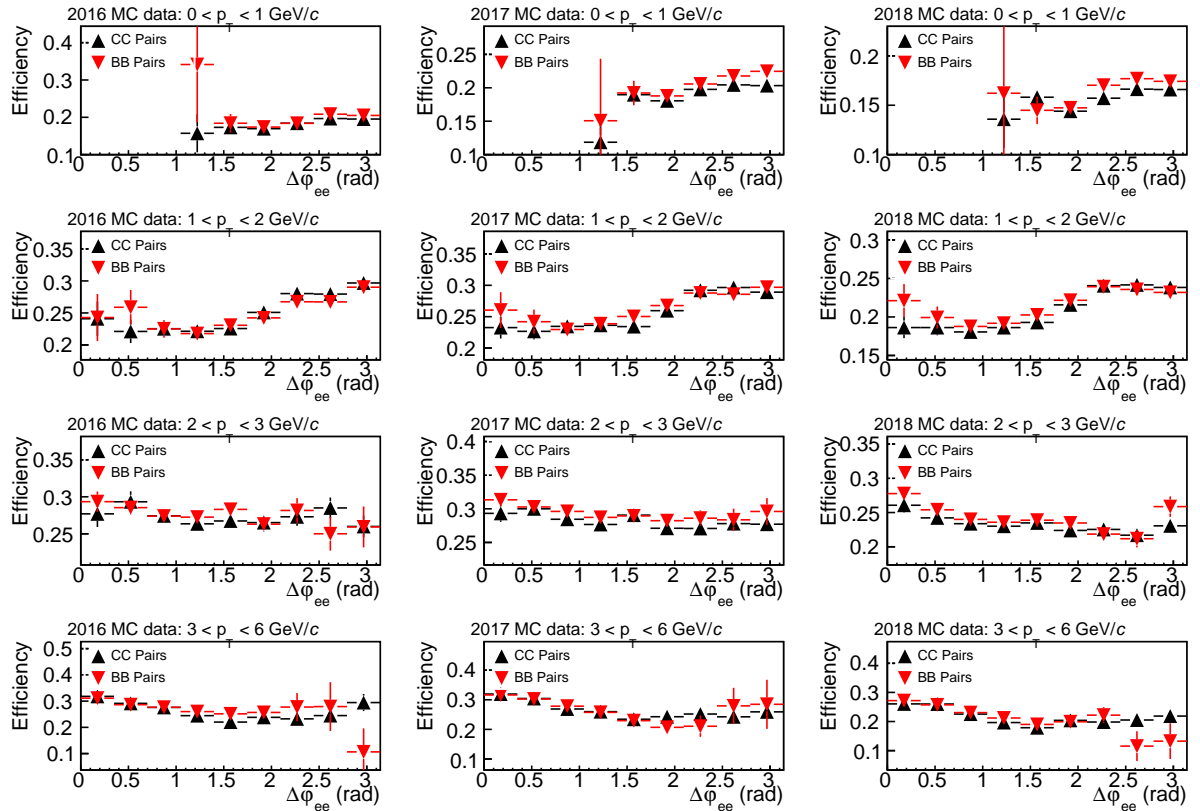


Figure 7.1:  $\Delta\varphi_{ee}$  efficiencies of heavy-flavour electron pairs using a minimum  $p_{T,e}$  cut of  $0.2 \text{ GeV}/c$ . On the left column of plots it is shown the efficiencies for the 2016 year, while in center for 2017 and on the right for 2018. In each line a different  $p_{T,ee}$  interval is presented, and can be directly compared with each of the neighbour columns.

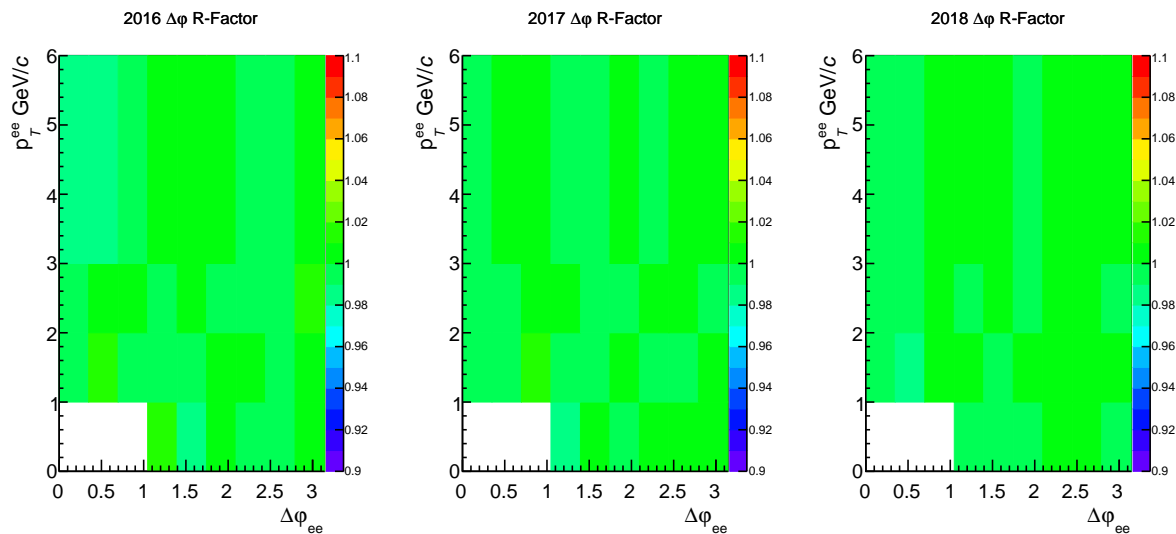


Figure 7.2: R-factor for each of the data taken years analyzed with minimum  $p_{T,e}$  of 0.2 GeV/ $c$ . From left to right: 2016, 2017 and 2018 data years.

### 7.1.2 Signal Extraction

The signal extraction of the  $\Delta\varphi_{ee}$  follows the procedure already described in Section 4.6 and previously applied to  $m_{ee}$  and  $DCA_{xy}^{ee}$ . The  $\Delta\varphi_{ee}$  extraction is one of the most complicated of the studied signals. Here it is used a 3D histogram of  $p_{T,ee}$ ,  $m_{ee}$  and  $\Delta\varphi_{ee}$ , corrected by a 3D-efficiency histogram with the exactly same binning, and finally it is projected into a 2D histogram of  $p_{T,ee}$  and  $\Delta\varphi_{ee}$ , only considering the contributions in the IMR of the  $m_{ee}$  axis. The R-factor is shown in Figure 7.2, and it shows that there are no differences in acceptance of different signed charged pairs. There are some empty bins for low  $p_{T,ee}$  and  $\Delta\varphi_{ee}$  because there is no contribution of dielectron pairs there, as it will be seen later.

In Figures 7.3 the ULS and LS signals for  $\Delta\varphi_{ee}$  are shown, while in Figure 7.4 the signal (ULS - LS) to background (LS) ratio is shown for the merged 2016, 2017 and 2018 data. There is an overall good signal to background ratio, although in the first  $p_{T,ee}$  interval there is an outlier with a high uncertainty. This happens because that specific  $\Delta\varphi_{ee}$  bin is in the limit between where we have and do not have a dielectron signal, so that bin presents both small contribution of ULS and LS pairs, leading to this high uncertainty by fluctuations. The signal for the different years were also extracted, but they are not shown here for simplicity.

### 7.1.3 Systematic Uncertainties

The systematic uncertainties of the  $\Delta\varphi_{ee}$  is determined using the procedure of cut variations described in Section 4.7. The comparison of all of the variations is shown in

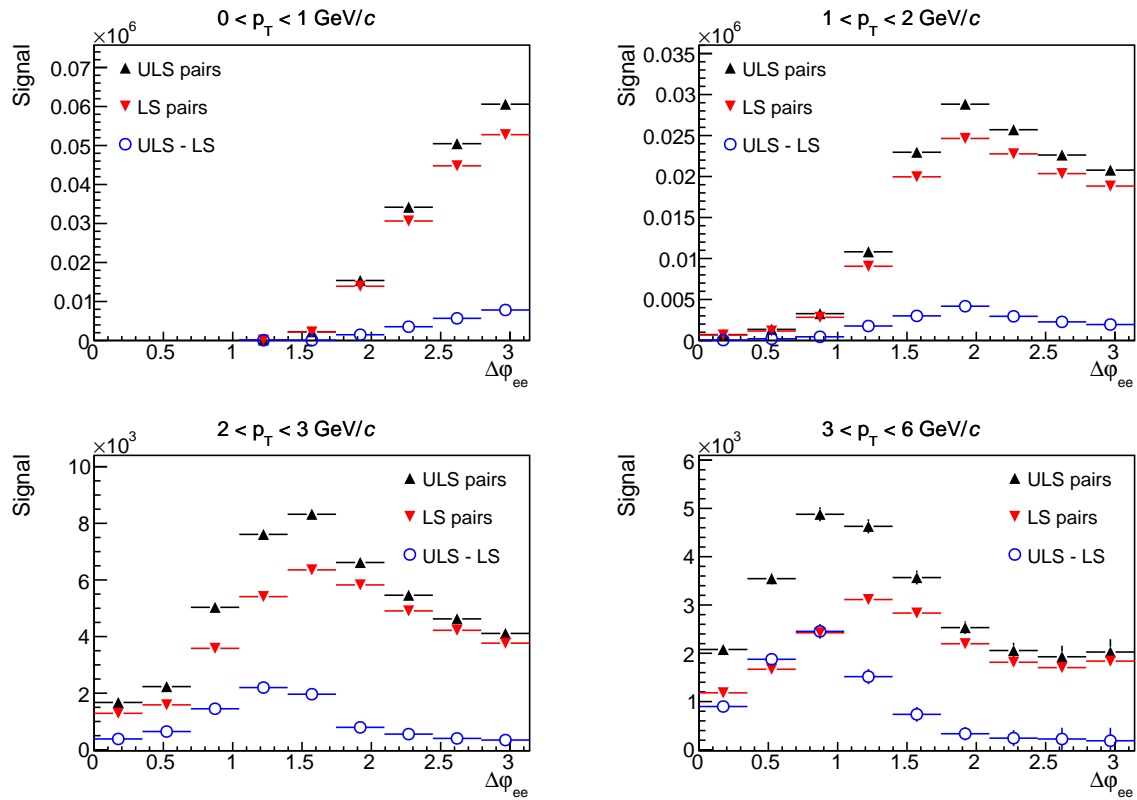


Figure 7.3: ULS and LS contributions for the  $\Delta\varphi_{ee}$  analysis as a function of the  $p_{T,ee}$ , using all of the data years (2016 + 2017 + 2018). The ULS is shown in black, the LS contribution in red and the ULS - LS subtraction in blue.

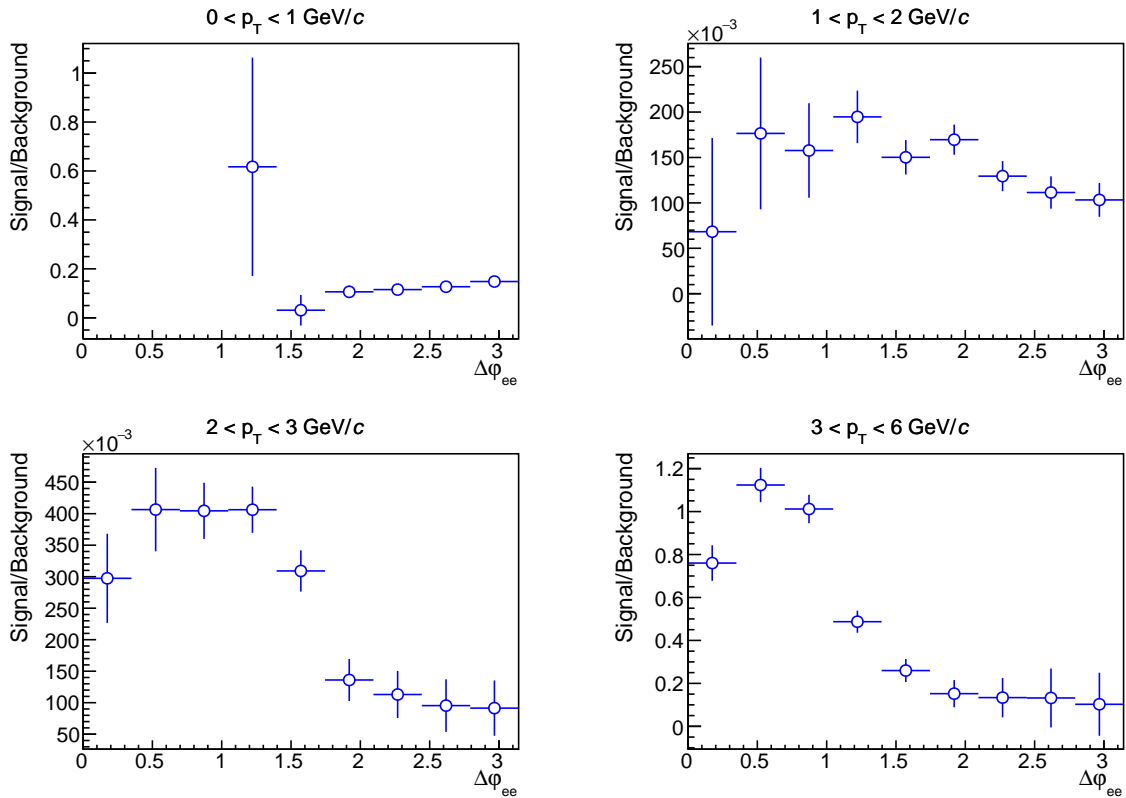


Figure 7.4: Signal over background ratio for the  $\Delta\varphi_{ee}$  analysis using all of the data years (2016 + 2017 + 2018).



Figure 7.5, while in the Figure 7.6 are shown the final systematic uncertainties determined by the variations. As in the other analyses, the same procedure was repeated for all of the years separately, but are not shown here for simplicity.

The uncertainties in each  $\Delta\varphi_{ee}$  bin depend on the  $p_{T,ee}$  interval. This happens because there is a strong dependence between the  $p_{T,ee}$  and the  $\Delta\varphi_{ee}$ . Most of the high uncertainties are placed in limited areas where the signal has poor statistics, and by changing the cuts we can increase/decrease the contribution of the signal in these areas. Outside of the statistically limited areas, the uncertainties stay at around 10 %, in all  $p_{T,ee}$  intervals. It is possible to see that, differently than what happened in the other analyses, although the track cuts still present the higher variations, the different eID by TPC and TOF plays a more important role here. In the second  $p_{T,ee}$  interval, there is a bin where the TOF eID is around 20 %, reinforcing the idea that we can have eID cuts that provide us more/less electrons, which can modify systematically the values, even though these signals are also corrected by their own efficiencies. By having a loose eID, for example, we also can have not only more electrons, but more misidentified hadrons which are not accountable in the efficiency.

The dielectron signal extracted using the procedure described in the last Sections as a function of the  $\Delta\varphi_{ee}$  in different  $p_{T,ee}$  intervals for the different data-taking years and for the merged years are shown in Figure 7.7. The signal for each given year was corrected by its own anchored efficiency, and the systematical uncertainties were evaluated separately for each year and for the case of the merged years in the process described in this Section.

## 7.1.4 Monte Carlo Templates

### $\Delta\varphi$ Inheritance

Since the main idea is to determine the  $\Delta\varphi$  of the  $c\bar{c}$  and  $b\bar{b}$  quarks through the  $\Delta\varphi$  of their decay electrons, it is investigated if this information is indeed inherited by the decay electrons - Figure 7.8. Since in the simulations it is not assumed the same difference of  $c$  and  $\bar{c}$  or ( $b$  and  $\bar{b}$ ) to their corresponding electrons ( $\Delta\varphi_{c\bar{c}}$  against  $\Delta\varphi_{e^+e^-}$  or  $\Delta\varphi_{e^-e^+}$ ), it would be observed both a symmetric and an anti-symmetric structure, due to the indistinguishability. If the information of  $\varphi_c - \varphi_{\bar{c}}$  were correlated as  $\varphi_{c\rightarrow e} - \varphi_{\bar{c}\rightarrow e}$  it will be observed the symmetric structure. On the other hand, in the case that the signal of  $\varphi_c - \varphi_{\bar{c}}$  is correlated as  $\varphi_{\bar{c}\rightarrow e} - \varphi_{c\rightarrow e}$  it will be seen the asymmetric structure. From these plots it can be determined that the HFe pair indeed inherits the important kinematic properties of the heavy quarks, within some resolution, which means that we can access the  $\Delta\varphi_{c\bar{c}}$  through its correlated decay electrons.

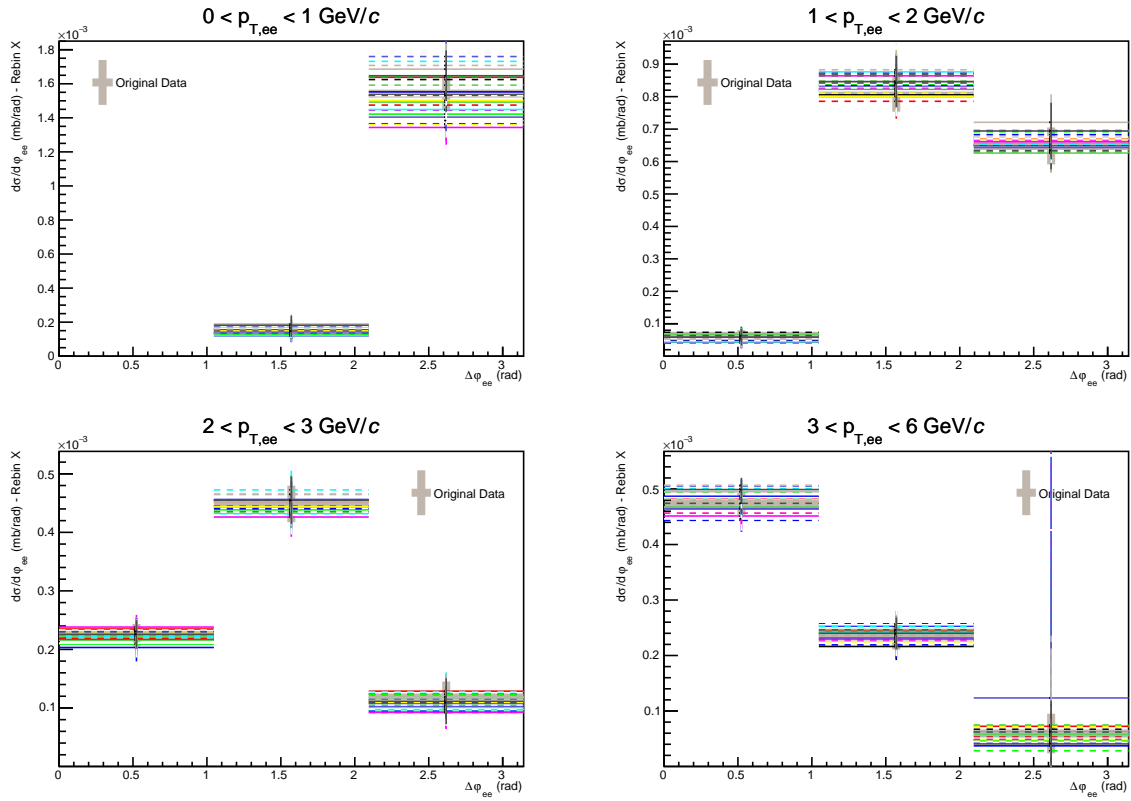


Figure 7.5: Comparison of the signal obtained using different sets of track and eID cuts for the  $\Delta\varphi_{ee}$  analysis as a function of the  $p_{T,ee}$ , using all of the data years (2016 + 2017 + 2018).

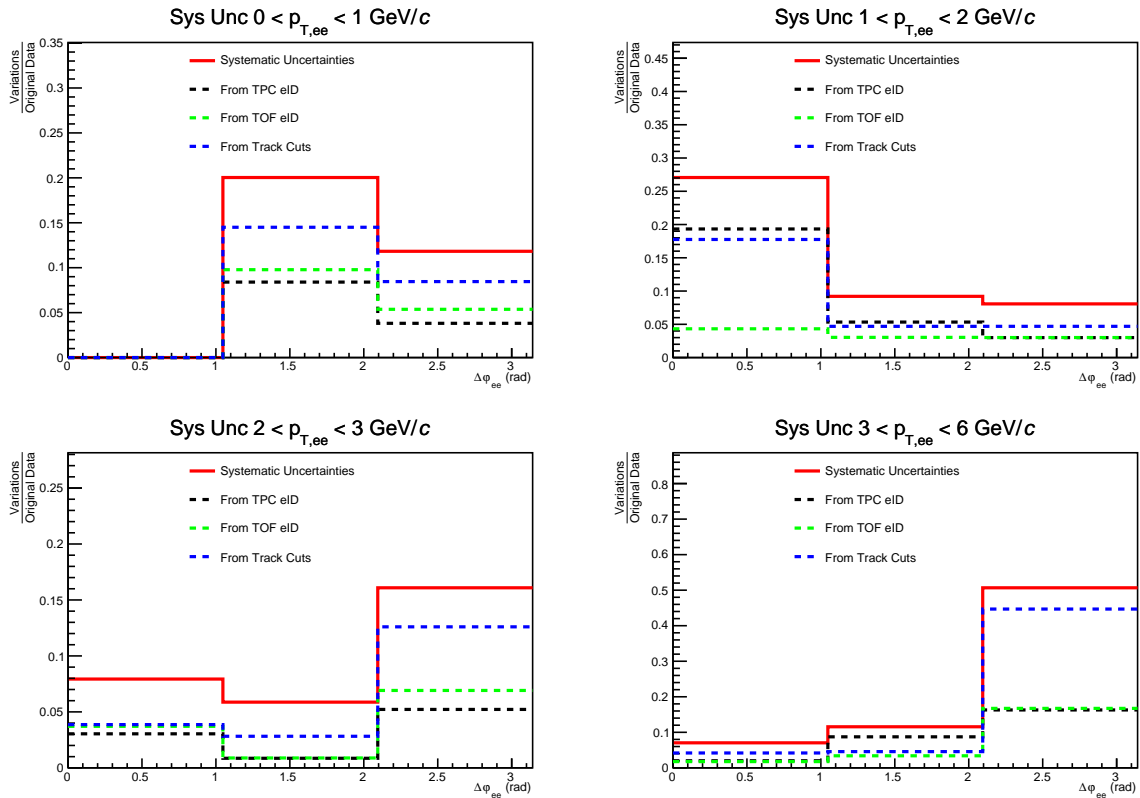


Figure 7.6: Systematic uncertainties of the  $\Delta\varphi_{ee}$  analysis as a function of the  $p_{T,ee}$ , using all of the data years (2016 + 2017 + 2018).

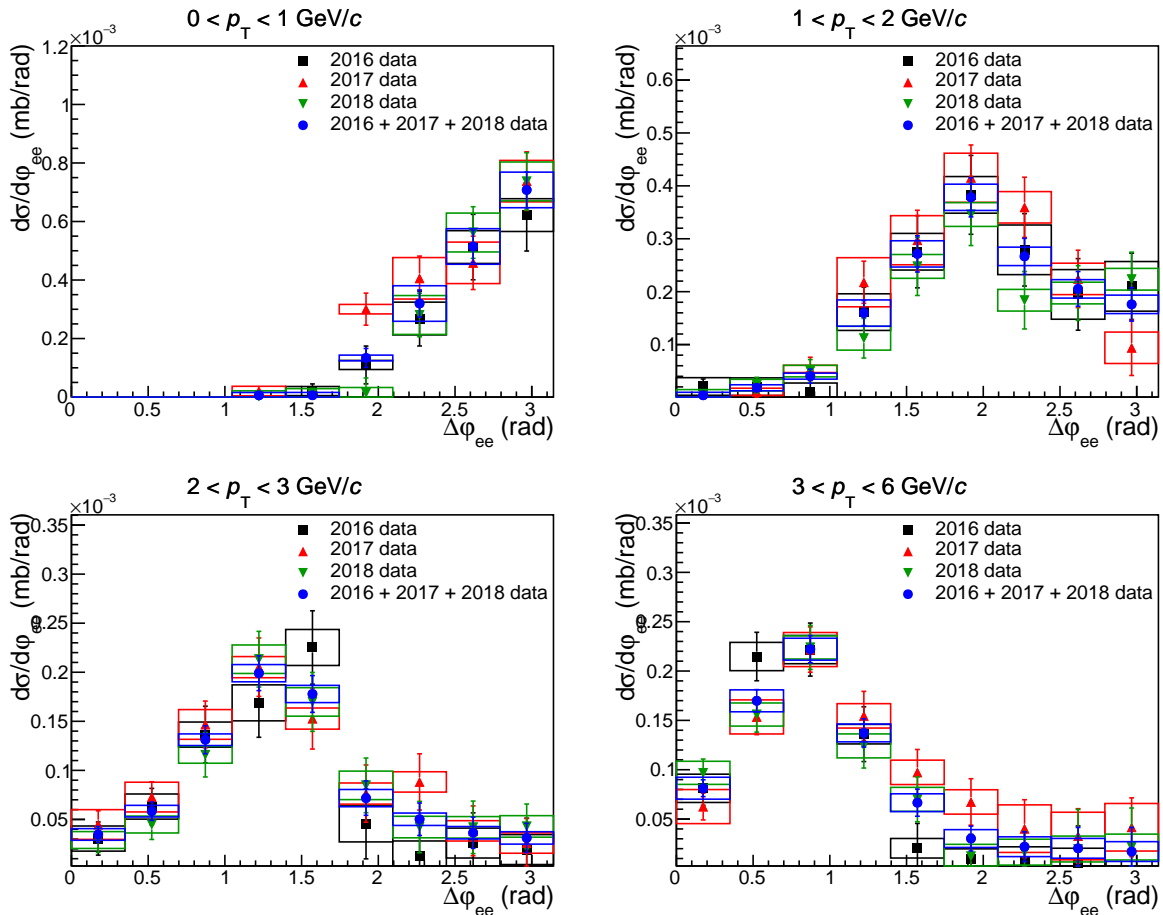


Figure 7.7: The dielectron cross section for the different data-taking years are shown as a function of the  $\Delta\varphi_{ee}$  in different pair momentum intervals for the analysis with  $p_{T,e} > 0.2 \text{ GeV}/c$ . The signal obtained using 2016 data is shown in black, 2017 in red, 2018 in green and in blue for the merged years. The bar and boxes represent the statistical and systematic uncertainties of the data.

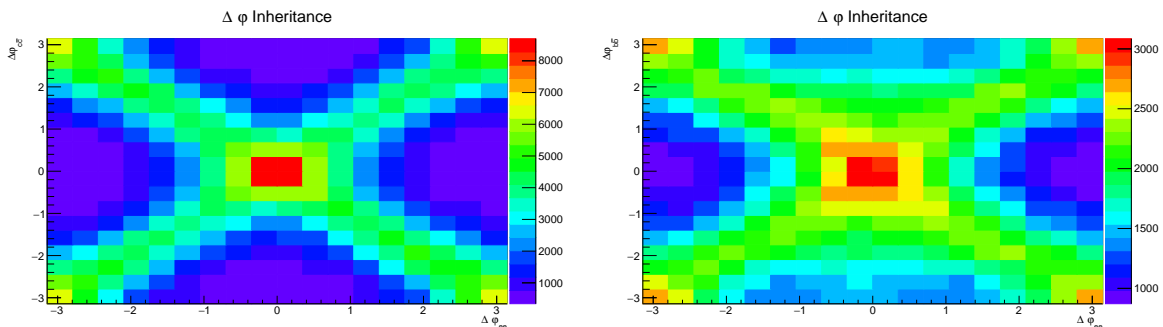


Figure 7.8: Histograms from PYTHIA of the inherited  $\Delta\varphi$  of heavy-quarks (y-axis) by the HFe pair (x-axis) for  $c\bar{c}$  (left) and  $b\bar{b}$  (right).

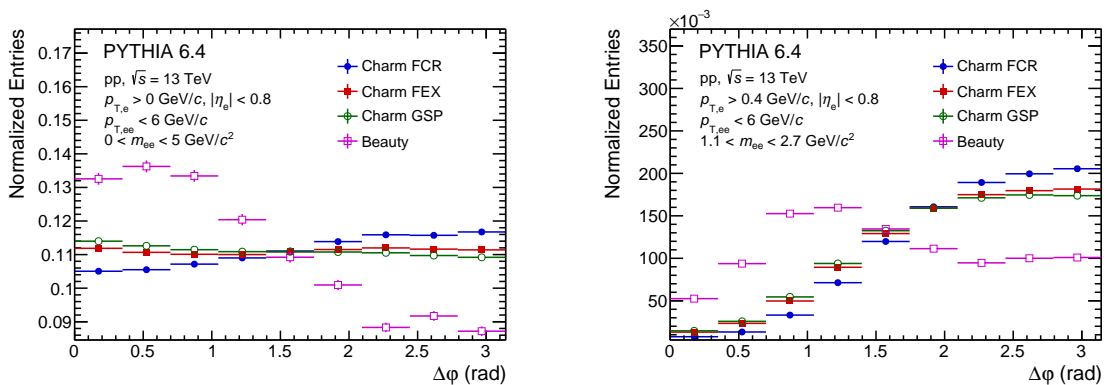


Figure 7.9: Angular correlation of each of the production mechanisms from charm and the beauty contribution for  $p_{T,ee}$  integrated. On the left: without  $p_{T,e}$  and  $m_{ee}$  cuts; on the right: with  $p_{T,e} > 0.4$  GeV/ $c$  and in the IMR of the  $m_{ee}$  distribution. All of the contributions are normalized to their integrals, in order to obtain a better visualization.

## Templates

The analysis over the PYTHIA and POWHEG saves all important pairing information between heavy-flavour electrons in different histograms for a post offline analysis. The results from the ISUB process 11 (pair creation) was merged with the process 53 (gluon fusion) as the flavour creation template. After the event selection described in Section 5.1.2, the fractions of all charm events analyzed by each production mechanism from PYTHIA are: 11% of events through Flavour Creation (FCR), 28% from Flavour Excitation (FEX) and 61% from Gluon Splitting (GSP). These are the predictions from the PYTHIA production. The angular correlations of each of these charm processes and for beauty are shown in Figure 7.9. On the left side of the Figure it is shown the angular distributions only applying the  $\eta$  cut, but the whole invariant mass yield was considered and also no  $p_{T,e}$  cut was applied. On the right plot, the distributions shown were obtained applying the  $p_{T,e}$  cut and also the invariant mass cut (dielectrons at the IMR). It is also important to note that each one of these contributions were normalized by their integrals in  $0 < p_{T,ee} < 6$  GeV/ $c$ - in this way the shapes can be easier compared at this stage. Since the  $\Delta\varphi_{ee}$  are symmetric around 0 - it does not matter if the  $\varphi$  of the electrons was subtracted from the  $\varphi$  of positrons or the other way around, the following results will be shown as a function of the absolute value of  $\Delta\varphi_{ee}$ .

Our first clue by looking at the left plot of Figure 7.10 would be that GSP has a higher contribution than the other process for small angles while the FCR has a higher contribution for back-to-back pairs, and the FEX stays in the middle of these two distributions, although presents some similarity to the GSP process (as it should since these processes present similarities - see Section 2.4). The second clue, now looking at the right side of the Figure would be to think that the necessary cuts needed for this analysis removes some of the particularities of each production mechanisms.

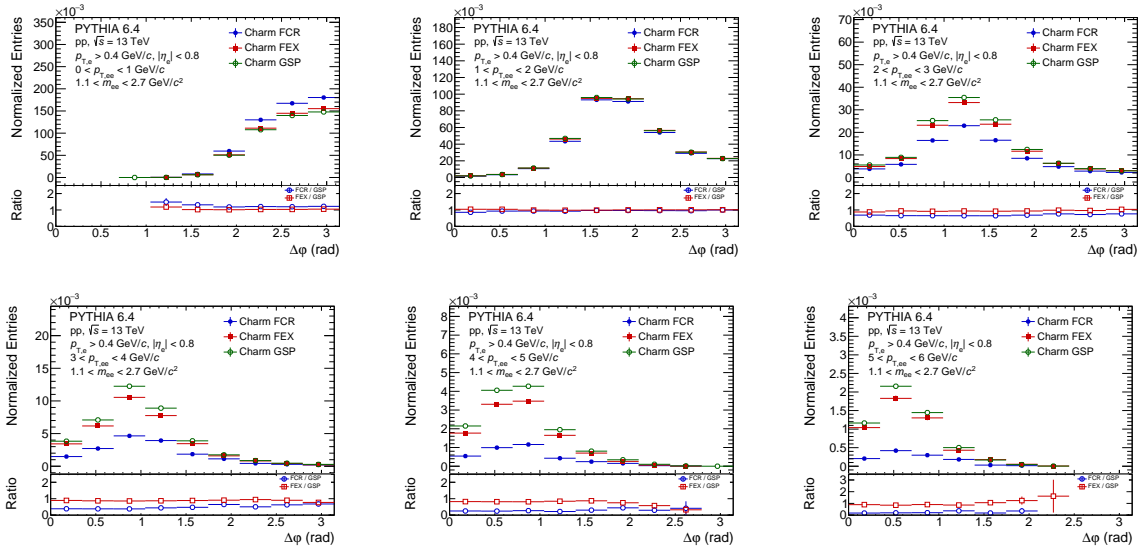


Figure 7.10: Angular correlation of each of the production mechanisms of charm in different  $p_{T,ee}$  intervals, with kinematics and  $m_{ee}$  cuts applied. The  $p_{T,ee}$  interval increases from left to right and from top to bottom, as shown in legends. The full 2D distributions were normalized by the integral over  $p_{T,ee}$  for a better visualization. In the bottom of each plot it is shown the ratio between the production mechanisms and the GSP process.

A good procedure to check if these ideas are correct would be to check the  $p_{T,ee}$  distributions along to the  $\Delta\varphi_{ee}$ , which is shown in Figure 7.10. In this Figure, it becomes clear that each of the production mechanisms presents similar distributions in each of the  $p_{T,ee}$  intervals, as seen by the ratios between the processes in the bottom of each  $p_{T,ee}$  intervals in the Figure.

What can be seen is an overall flat ratio between the production mechanisms in each of the  $p_{T,ee}$  intervals, which brings us to the conclusion that the production mechanisms do not present differences in shape of the  $\Delta\varphi_{ee}$  distribution in each of the  $p_{T,ee}$  intervals, only in the total integrated  $p_{T,ee}$ . This is actually expected (as already discussed before), since the angle between the decays of a particle decreases as we increase the pair momentum. So, it should be expected that different  $p_{T,ee}$  distributions will present different  $\Delta\varphi_{ee}$  distributions. Since the mother particles are always the same, independent of the production mechanisms, all of the production process should not present any differences in shape of the angles in each of the  $p_{T,ee}$  intervals. The differences in the angular distribution for the  $p_{T,ee}$  integrated happen because each one of the processes has a different  $p_{T,ee}$  distribution, so the GSP process, that has a greater contribution for higher  $p_{T,ee}$ , will also have a greater contribution than the other processes for small angles. The FCR process, that has a greater contribution for low  $p_{T,ee}$ , will have a greater contribution in the  $\Delta\varphi_{ee}$  for higher angles. So the difference in the angle is directly correlated to the differences in the  $p_{T,ee}$  distribution of each process, and the other way around. This conclusion tells us that there is a strong correlation between the  $\Delta\varphi_{ee}$  and the  $p_{T,ee}$ , and that the different

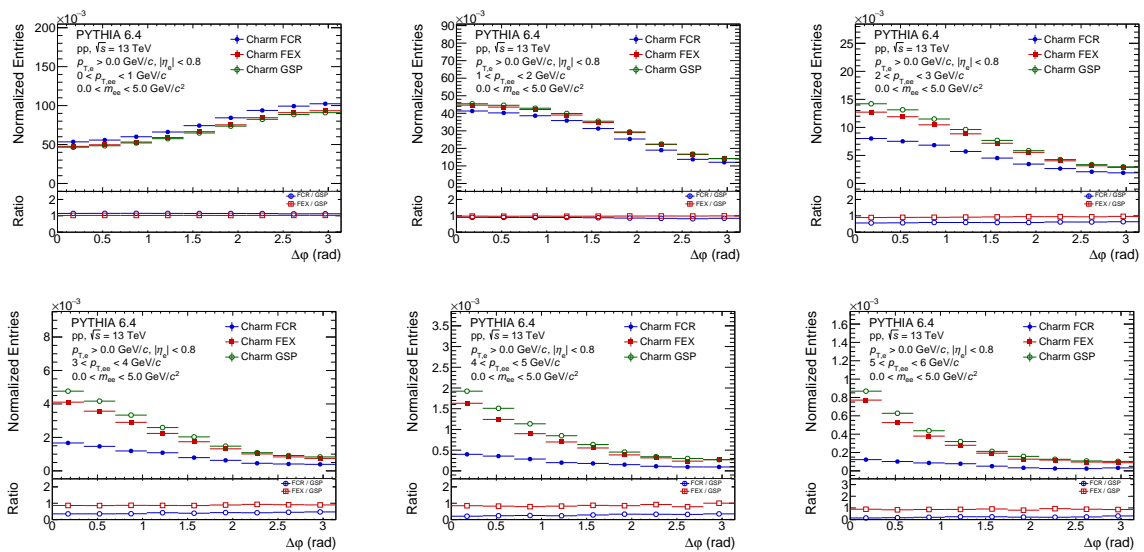


Figure 7.11: Angular correlation of each of the production mechanisms of charm in different  $p_{T,ee}$  intervals, without  $p_{T,e}$  and  $m_{ee}$  cuts. The  $p_{T,ee}$  interval increases from left to right and from top to bottom, as shown in legends. The full 2D distributions were normalized by the integral over  $p_{T,ee}$  for a better visualization. In the bottom of each plot it is shown the ratio between the production mechanisms and the GSP process.

$\Delta\varphi_{ee}$  distributions are completely correlated to the  $p_{T,ee}$  distributions.

One could argue that the  $\Delta\varphi_{ee}$  is only similar in each  $p_{T,ee}$  interval because of the invariant mass and kinematic cuts applied, and that these cuts modified the distributions, based on the Figure 7.9. To check whether this argument proceeds, we made the very same plots without any of these cuts, which can be seen in Figure 7.11. What can be observed is that, again, there is no difference in the  $\Delta\varphi_{ee}$  distributions in each of the  $p_{T,ee}$  intervals since the ratios are flat, and what only matters, again, is the  $p_{T,ee}$  distribution of the pair. It seems that the  $\Delta\varphi_{ee}$  is limited by the  $p_{T,ee}$  distributions, or the other way around, since these informations are totally correlated to the kinematic decay constrain, already discussed in the Equation 4.11.

The last question that arises is, what if the the electrons are too smeared from its production that the distributions gets somehow completely messed up? To answer this question, one can look at the  $\Delta\varphi$  distributions of  $D\bar{D}$  (Figure 7.12) and  $c\bar{c}$  (Figure 7.13) pairs, to check if the same thing happens there or if that is just a matter of smearing and the shape of the distributions in each  $p_{T,ee}$  are different. What is observed in these Figures is that, again, there is no difference in the  $\Delta\varphi$  distribution shapes in each of the  $p_T$  intervals since the ratios are constantly flat, presenting only a pair  $p_T$  dependence. Note that a direct comparison between the  $\Delta\varphi$  shape of electrons in each of the  $p_{T,ee}$  can not be directly made to  $D\bar{D}$  or  $c\bar{c}$  shapes in same pair  $p_T$ , since the electrons would not have inherited all of the  $p_T$  of the heavy hadrons and charms due to several decay channels and particles produced, carrying only a fraction of the charm and charmed hadron  $p_T$ .

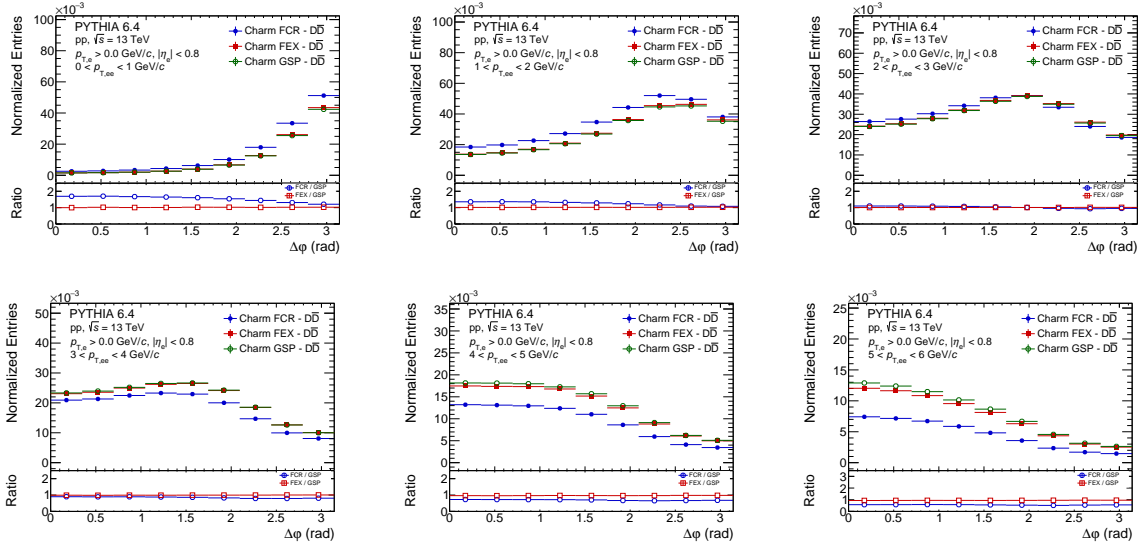


Figure 7.12: Angular correlation of each of the production mechanisms of charm in different  $p_{T,ee}$  intervals, without  $p_{T,e}$  and  $m_{ee}$  cuts for the  $D\bar{D}$  case. The full 2D distributions were normalized by the integral over  $p_{T,ee}$  for a better visualization. In the bottom of each plot it is shown the ratio between the production mechanisms and the GSP process.

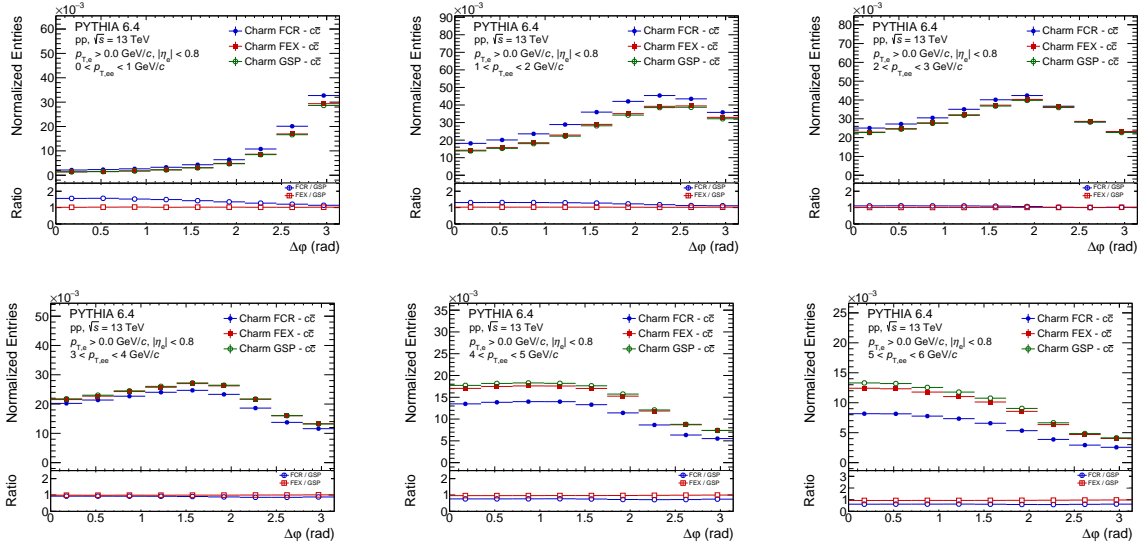


Figure 7.13: Angular correlation of each of the production mechanisms of charm in different  $p_{T,ee}$  intervals, without  $p_{T,e}$  and  $m_{ee}$  cuts, for the  $c\bar{c}$  case. The full 2D-distributions were normalized by the integral over the integrated  $p_{T,ee}$  for a better visualization. In the bottom of each plot it is shown the ratio between the production mechanisms and the GSP process.

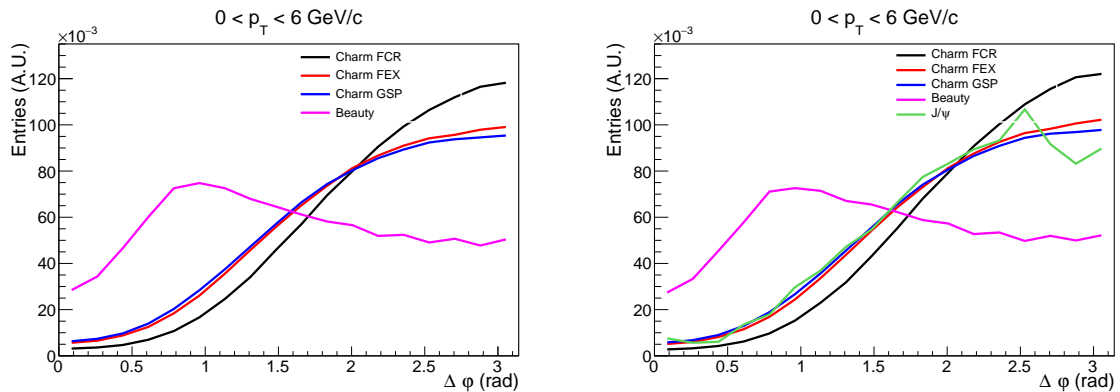


Figure 7.14: Comparison between charm, beauty and  $J/\psi$  templates using PYTHIA pure MC samples, without (left) and with  $p_T$ ,  $\eta$  and  $\varphi$  smearing (right). The templates were normalized by their integrals for a better comparison.

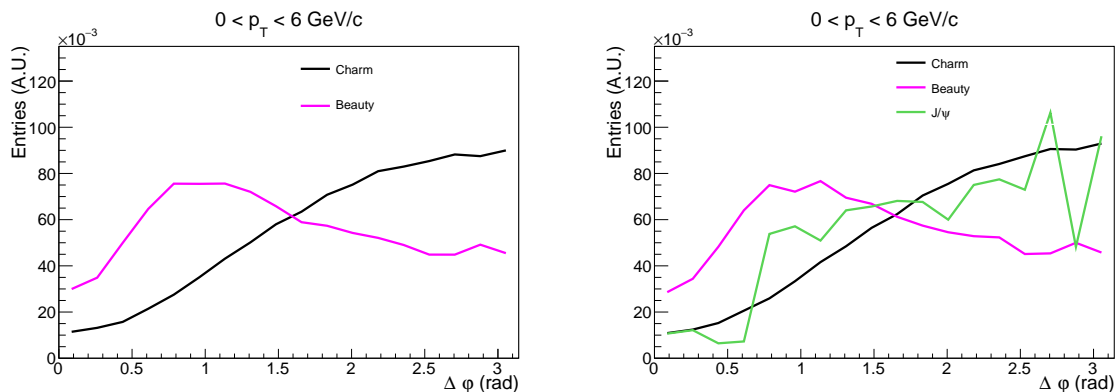


Figure 7.15: Comparison between charm, beauty and  $J/\psi$  templates using POWHEG pure MC samples, without (left) and with  $p_T$ ,  $\eta$  and  $\varphi$  smearing (right). The templates were normalized by their integrals for a better comparison.

From all of these checks of the templates it seems that when looking at both  $p_{T,ee}$  and  $\Delta\varphi_{ee}$ , the parameter with higher discrimination power between different production mechanisms is actually the  $p_{T,ee}$  of the pair, instead of the  $\Delta\varphi_{ee}$ . For this reason, our analysis will start with simultaneous fits on  $p_{T,ee}$  and  $\Delta\varphi_{ee}$  to be able to distinguish between the production mechanisms in a more reliable way, followed by analyses taking into account only the  $\Delta\varphi_{ee}$  or  $p_{T,ee}$  alone. A final comparison between the templates from PYTHIA and POWHEG can be seen in Figures 7.14 and 7.15, respectively, with (right plot) and without (left plot) the  $p_T$ ,  $\eta$  and  $\varphi$  smearing. The smearing has a very small effect on the  $\Delta\varphi_{ee}$  parameter, specially compared to the other observables, as  $m_{ee}$ . In POWHEG templates we can see that the charm template follows the shape of FEX and GSP on PYTHIA simulations, which makes sense since they have the higher contribution fractions to the total charm template when taking into account the prediction from PYTHIA (only  $\approx 11\%$  of FCR).



### 7.1.5 Results

#### 2D analysis

The dielectron spectrum is shown as a function of the  $p_{T,ee}$  and  $\Delta\varphi_{ee}$  in Figures 7.16 and 7.17 and compared to the expectation from the hadronic decay cocktail using PYTHIA and POWHEG simulations, respectively, with minimum  $p_{T,e}$  cut of 0.2 GeV/ $c$ . This is the first measurement of the angular correlations between heavy-flavour electrons -  $\Delta\varphi_{HF_e-HF_e}$ . The data followed what was already seen in the simulations, that the  $\Delta\varphi_{ee}$  decreases as the pair momentum increases. In these comparisons it seems clear that the fit under predicts the data in a specific region for higher  $p_{T,ee}$  intervals, around 0.75 - 1.75 rad. This region can be better described when including a  $J/\psi$  contribution to the fits, as seen in Figures 7.18 and 7.19, for PYTHIA and POWHEG simulations. The reduced  $\chi^2$  drops by  $\approx 35\%$  when the  $J/\psi$  contribution is included for PYTHIA, and it has a clear contribution in that region of the  $\Delta\varphi_{ee}$ . The  $\Delta\varphi_{ee}$  data is reasonably well described by the cocktail in all of the  $p_{T,ee}$  intervals.

In the PYTHIA plots it is also shown the three different production mechanisms of charm by its prediction: flavour creation (FCR), flavour excitation (FEX) and gluon splitting (GSP). The fractions of these contributions are the ones directly produced by PYTHIA, being  $\approx 11.2\%$  for FCR,  $\approx 27.7\%$  for FEX and  $\approx 61.0\%$  for GSP. The sum of these contributions produces the total charm contribution. The cross sections obtained through the  $\Delta\varphi_{ee}$  fits are compatible within uncertainties with the ones obtained by  $m_{ee}$  and  $DCA_{xy}^{ee}$  fits.

The second approach is to try to fit the three production mechanisms to check if we find a better description of the data, and that the fractions of the production mechanisms are different than the ones predicted by PYTHIA. What is seen, Figure 7.20, is that since the production mechanisms are similar between themselves, except by the  $p_{T,ee}$  distribution, the uncertainties of the fit are too high, making it harder to explore the result: 27 % FCR, 0 % FEX and 73 % GSP, but 60 - 150 % of uncertainties would allow them to be anything. A better  $\chi^2$  was achieved by letting the production mechanisms free but a worst reduced  $\chi^2$  due to the increase of the free parameters. To check the reality of the fit uncertainties, a fit was performed in the separated years, found in the Appendix F.

The fits over different years showed the high volatility of the parameters: while for 2016 data it seems to follow a similar behaviour than to the merged years, 13 % for FCR and 87 % for GSP, for 2017 it found better to use 100 % of GSP alone and for 2018 100 % of FCR alone. This behaviour could be suppressed by fixing the beauty contribution by the cross section extracted using the  $m_{ee}$  fits (smallest uncertainty): 74.9  $\mu b$  (Figure 7.21). The result of the fit predicts a higher GSP contribution, 94 %, and a smaller FCR contribution, 6 %. The uncertainties were also too high to explore a quantitative behaviour. The increase of the GSP when fixing the beauty contribution also makes sense

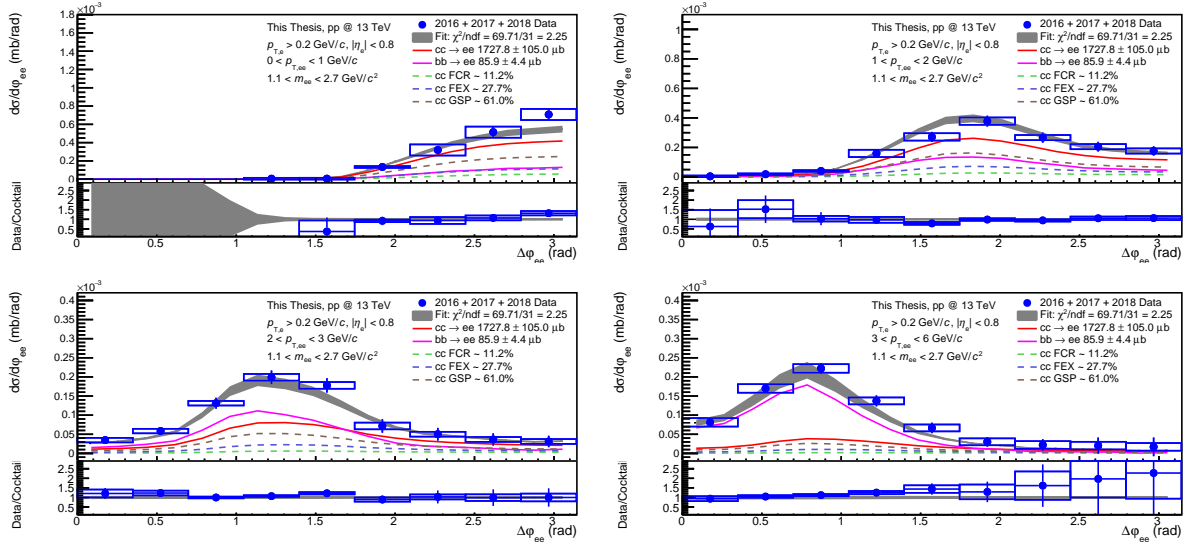


Figure 7.16: The dielectron cross section in pp collisions at 13 TeV as a function of  $\Delta\varphi$  in different pair momentum intervals is shown in blue circles for the analysis using the minimum  $p_{T,e}$  cut of 0.2 GeV/c, and the PYTHIA cocktail is shown in red and purple lines for charm and beauty, respectively, and dashed lines for the different charm production mechanisms. The bar and boxes represent the statistical and systematic uncertainties of the data, while the final cocktail is shown in a grey band. On the bottom of each pair momentum interval plot it is shown the data-to-cocktail ratio.

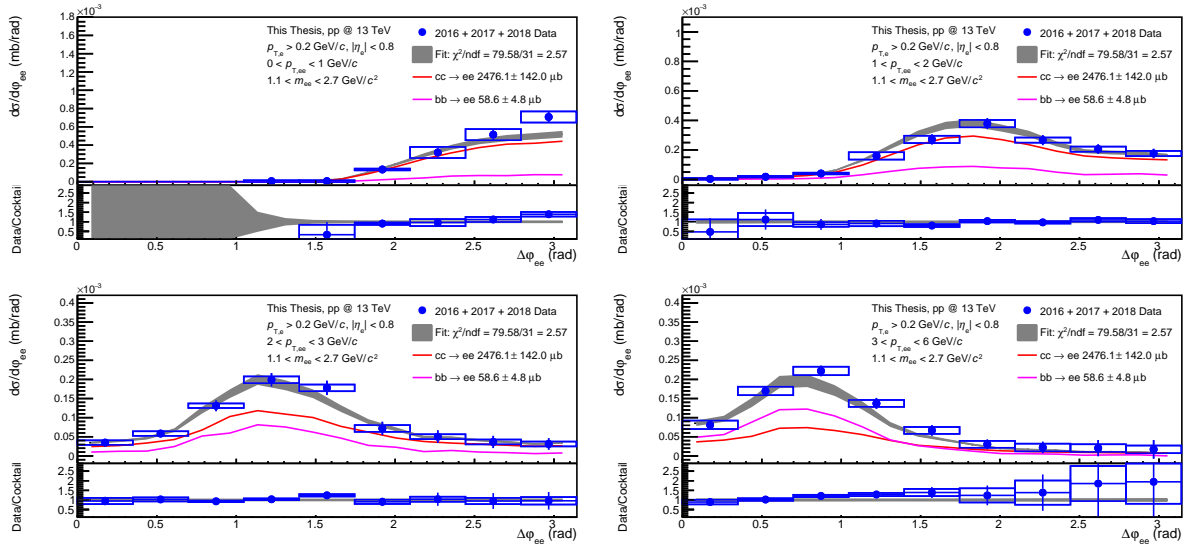


Figure 7.17: The dielectron cross section in pp collisions at 13 TeV as a function of  $\Delta\varphi$  in different pair momentum intervals is shown in blue circles for the analysis using the minimum  $p_{T,e}$  cut of 0.2 GeV/c, and the POWHEG cocktail is shown in red and purple lines for charm and beauty, respectively. The bar and boxes represent the statistical and systematic uncertainties of the data, while the final cocktail is shown in a grey band. On the bottom of each pair momentum interval plot it is shown the data-to-cocktail ratio.

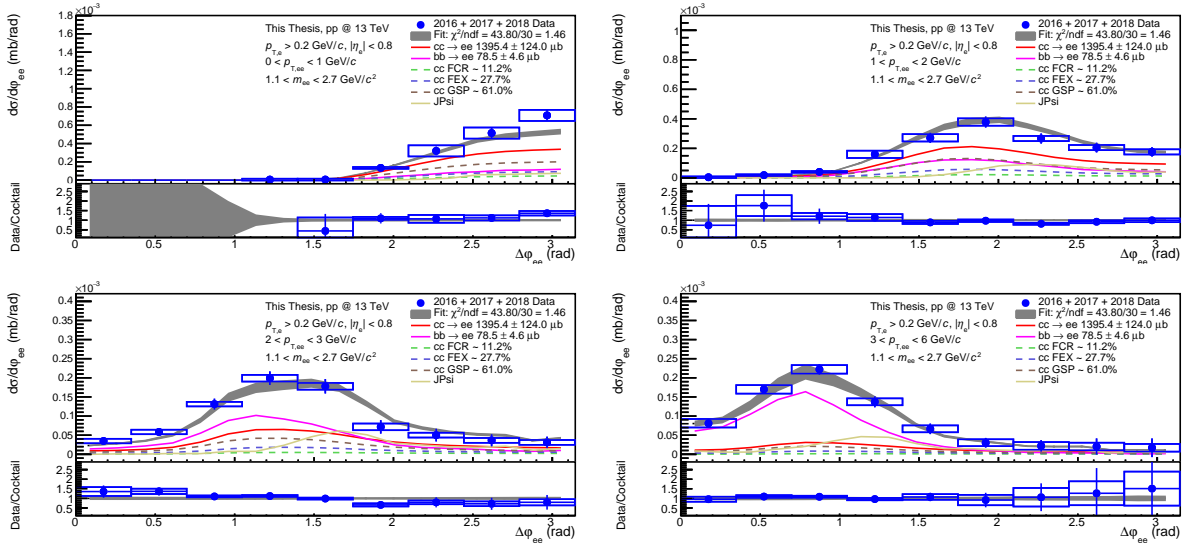


Figure 7.18: The dielectron cross section in pp collisions at 13 TeV as a function of  $\Delta\varphi$  in different pair momentum intervals is shown in blue circles for the analysis using the minimum  $p_{T,e}$  cut of 0.2 GeV/c, and the PYTHIA cocktail is shown in red, purple and brown lines for charm, beauty and  $J/\psi$ , respectively, and dashed lines for the different charm production mechanisms. The bar and boxes represent the statistical and systematic uncertainties of the data, while the final cocktail is shown in a grey band. On the bottom of each pair momentum interval plot it is shown the data-to-cocktail ratio.

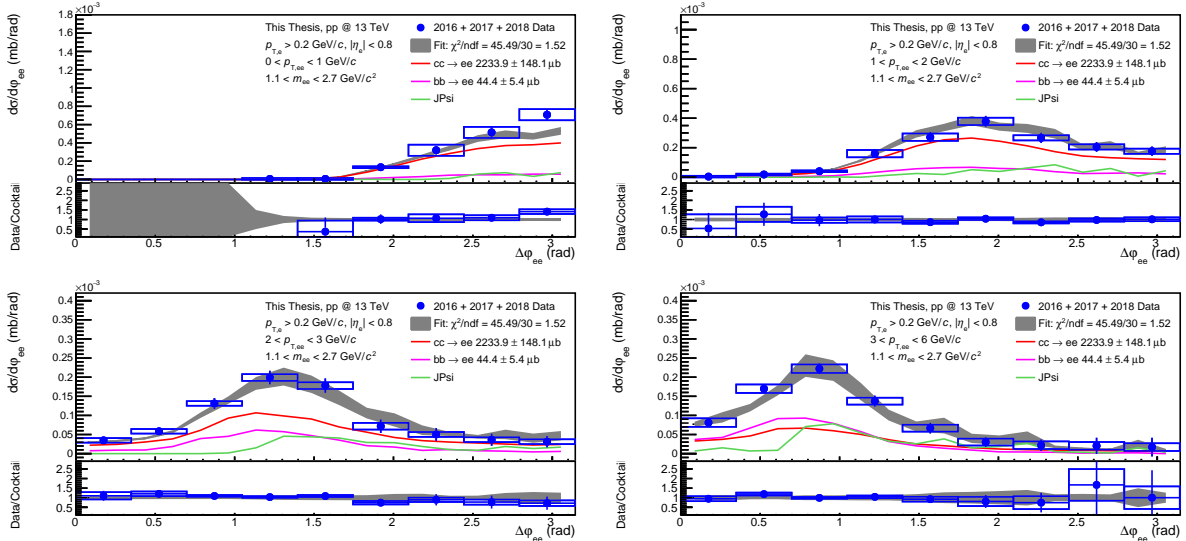


Figure 7.19: The dielectron cross section in pp collisions at 13 TeV as a function of  $\Delta\varphi$  in different pair momentum intervals is shown in blue circles for the analysis using the minimum  $p_{T,e}$  cut of 0.2 GeV/c, and the PYTHIA cocktail in red, purple and green lines for charm, beauty and  $J/\psi$  contributions, respectively. The bar and boxes represent the statistical and systematic uncertainties of the data, while the final cocktail is shown in a grey band. On the bottom of each pair momentum interval plot it is shown the data-to-cocktail ratio.

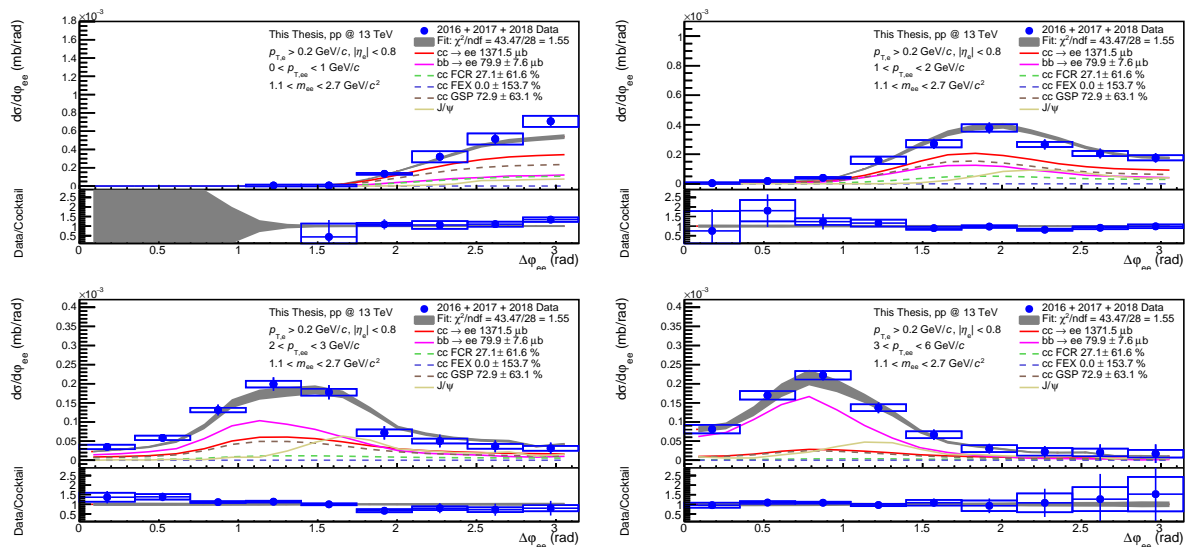


Figure 7.20: The dielectron cross section in pp collisions at 13 TeV as a function of  $\Delta\varphi$  in different pair momentum intervals is shown in blue circles for the analysis using the minimum  $p_{T,e}$  cut of 0.2 GeV/c, and the PYTHIA cocktail in red, purple and brown lines for charm, beauty and  $J/\psi$  contributions, respectively, and dashed lines for the different charm production mechanisms fit. The bar and boxes represent the statistical and systematic uncertainties of the data, while the final cocktail is shown in a grey band. On the bottom of each pair momentum interval plot it is shown the data-to-cocktail ratio.

when thinking of the  $p_{T,ee}$  distribution. The GSP has a higher contribution to higher  $p_{T,ee}$ , so if the beauty was reduced when fixing its contribution (from 79.9  $\mu b$  free to 74.9  $\mu b$  fixed), the fit preferred more GSP to balance the reduction of the beauty contribution in higher  $p_{T,ee}$ . This could be a hint for a preferable higher GSP/FEX contribution and a smaller FCR contribution, but the uncertainties do not allow us to extract a reliable information. The 2D fits take into account the informations of both  $\Delta\varphi_{ee}$  and  $p_{T,ee}$ , but since they are complementary, i.e., a higher  $p_{T,ee}$  means a small  $\Delta\varphi_{ee}$  and the other way around, we can try to explore the 1D distributions of  $\Delta\varphi_{ee}$  and/or  $p_{T,ee}$  to try to check if the uncertainties can be reduced.

The conclusion of these 2D-fit plots is that the balance of the fit is always performed by the  $p_{T,ee}$  distribution, since the  $\Delta\varphi_{ee}$  distribution over the production mechanisms are similar within the same  $p_{T,ee}$  interval, as discussed in Section 7.1.4. Although the correlated informations could allow us to extract more reliable parameters, the uncertainties when dealing with both informations at the same time made the uncertainties be unphysical, rising the hint to explore the 1D fits of  $\Delta\varphi_{ee}$  or  $p_{T,ee}$  alone. The PYTHIA and POWHEG could well describe the data in all of the  $p_{T,ee}$  intervals, but the production mechanisms could not be extracted from PYTHIA fits since the uncertainties were too high to be able to extract any information, something that had already been seen in  $m_{ee}$  analyses [47], and the data could be very well described by letting the production mechanisms free of fixed. The  $J/\psi$  templates were found to play an important role in a given region of the

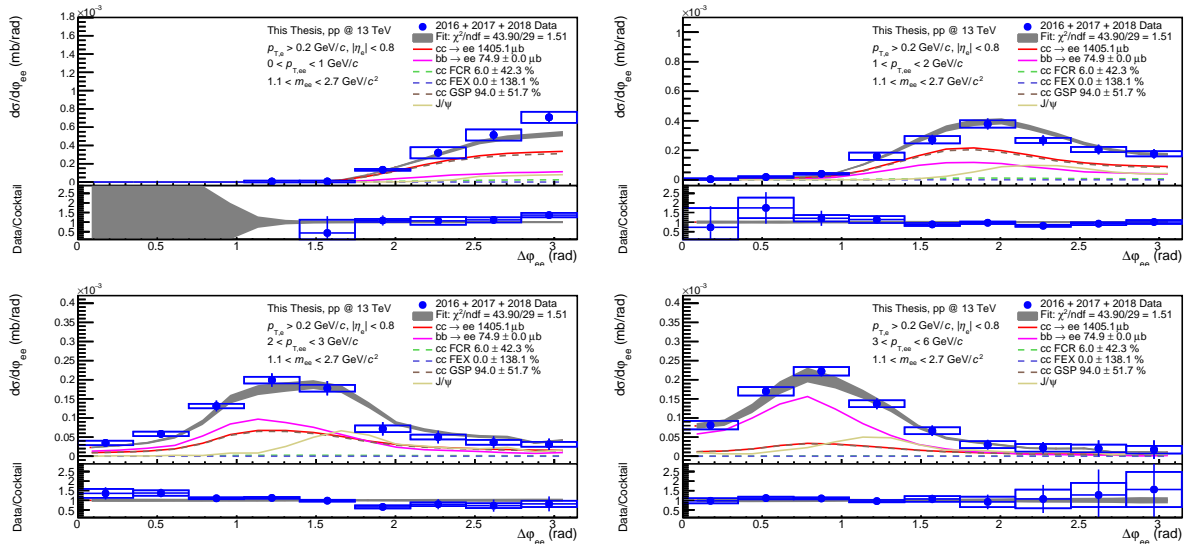


Figure 7.21: The dielectron cross section in pp collisions at 13 TeV as a function of  $\Delta\varphi$  in different pair momentum intervals is shown in blue circles for the analysis using the minimum  $p_{T,e}$  cut of 0.2 GeV/c, and the PYTHIA cocktail in red, purple and brown lines for charm, beauty and  $J/\psi$  contributions, respectively, and dashed lines for the different charm production mechanisms fit. The beauty contribution was kept fixed by the cross section extracted from the  $m_{ee}$  fits for the merged years. The bar and boxes represent the statistical and systematic uncertainties of the data, while the final cocktail is shown in a grey band. On the bottom of each pair momentum interval plot it is shown the data-to-cocktail ratio.

$\Delta\varphi_{ee}$  distribution, specially for higher  $p_{T,ee}$  intervals.

## 1D analysis

The dielectron cross section as a function of the angular correlations is shown in Figure 7.22. On the left plot the three mechanisms were fitted while on the right plot the FEX and GSP were merged. What is observed is that merging FEX and GSP did not modify the results and the uncertainties of the FEX vanishes. As seen in these plots, the uncertainties were drastically reduced when dealing only with one measurement ( $\Delta\varphi_{ee}$ ). The beauty is the most important contributor for smaller angles while charm to the higher angles. The GSP helps to balance both small and high angles, although it contributes more to higher angles.

The  $J/\psi$  did not play a role in the fits so it was kept out. The fractions of charm were not affected by the inclusion or removal of the  $J/\psi$ , and also the total cross section of beauty. The addition of the  $J/\psi$  templates only makes the total charm cross section to be smaller, but still maintaining the same fractions and this is why it was maintained out of the fit. The fit preferred a greater contribution from FCR ( $53 \pm 23\%$ ) than from FEX+GSP ( $47 \pm 26\%$ ) than predicted by PYTHIA, but also preferred a greater beauty contribution ( $86.0 \pm 7.8 \mu\text{b}$ ) than what was observed in the 2D fits and in the extracted

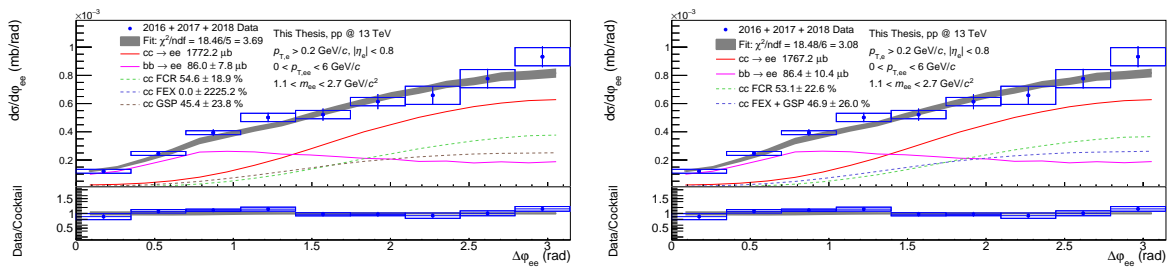


Figure 7.22: The dielectron cross section in pp collisions at 13 TeV as a function of the angular correlation is shown in blue circles for the analysis using the minimum  $p_{T,e}$  cut of 0.2 GeV/ $c$ , and the PYTHIA cocktail is shown in red and purple lines for charm and beauty, respectively, and dashed lines for the different charm production mechanisms that are kept as predicted by PYTHIA. The bar and boxes represent the statistical and systematic uncertainties of the data, while the final cocktail is shown in a grey band. On the bottom of each plot it is shown the data-to-cocktail ratio. On the left plot the 3 mechanisms were used to perform the fit while on the right the FEX and GSP were merged into a single mechanism.

cross sections. That is exactly the reason why we decided to try to fit both distributions at the same time,  $\Delta\varphi_{ee}$  and  $p_{T,ee}$ , so the  $p_{T,ee}$  distributions are also taken into account. To follow the same procedure already used and in an attempt to get results based and in agreement between measurements, the beauty contribution was fixed in Figure 7.23. Again, on the left plot the three mechanisms were fitted while on the right plot the FEX and GSP were merged. Again, merging the FEX and GSP has a small impact in the fraction but the uncertainties of the FEX vanishes. Fixing the beauty contribution to a smaller value than when it was free made the FEX and GSP obtain a higher fraction to balance the fit in small angles. The final extracted values for the fractions are:  $16 \pm 11$  (stat)  $\pm 15$  (sys) % for FCR and  $84 \pm 10$  (stat)  $\pm 15$  (sys) % for the merged FEX and GSP processes.

The central value measurements are in agreement with the values already predicted by PYTHIA with a  $\approx 10$  % statistical uncertainty, and a  $\approx 15$  % systematic uncertainty. The uncertainties of the measurement were drastically reduced but they are still greater than desired for a more precise measurement. The last check for this measurement is explore what can be observed from the  $p_{T,ee}$  distributions.

## 7.2 $p_T$ Analysis

### 7.2.1 $p_T$ Efficiency

The  $p_{T,ee}$  efficiency was calculated as in all of the other analyses, for charm and beauty electron pairs, using the minimum  $p_{T,e}$  cut of 0.2 GeV/ $c$ . Beauty electron pairs present a higher efficiency in the very beginning of the  $p_{T,ee}$  distribution and for higher values of

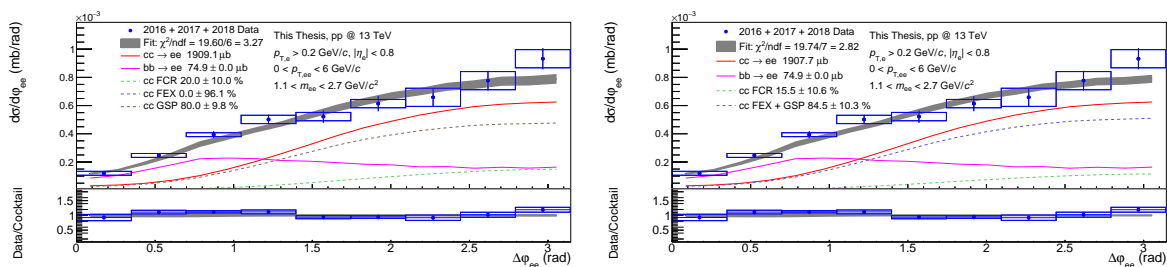


Figure 7.23: The dielectron cross section in pp collisions at 13 TeV as a function of the angular correlation is shown in blue circles for the analysis using the minimum  $p_{T,e}$  cut of 0.2 GeV/c, and the PYTHIA cocktail is shown in red and purple lines for charm and beauty, respectively, and dashed lines for the different charm production mechanisms that are kept as predicted by PYTHIA. The bar and boxes represent the statistical and systematic uncertainties of the data, while the final cocktail is shown in a grey band. On the bottom of each plot it is shown the data-to-cocktail ratio. On the left plot the 3 mechanisms were used to perform the fit while on the right the FEX and GSP were merged into a single mechanism, maintaining the beauty contribution fixed.

$p_{T,ee}$ , while for intermediate momentum the charm and beauty pair efficiencies are similar, as shown in Figure 7.24. The shapes of the efficiencies are again completely consistent along the 3 different years. What becomes even more clear and visible through these plots than in the other analyses is the fact that 2017 has the highest efficiency, while 2018 has the smallest efficiency. As already mentioned, differences in the efficiencies by different years are expected to happen depending on calibrations and detector fixes and also from ageing factors, and these effects should not modify the shape of the pair efficiencies, only a scaling factor. Of course, statistical uncertainties should be taken into account when analyzing such results.

## 7.2.2 Signal Extraction

The signal extraction of the  $p_{T,ee}$  follows the procedure already described in Section 4.6 and applied to  $m_{ee}$ ,  $DCA_{xy}^{ee}$  and  $\Delta\varphi_{ee}$  analysis. In this case, a 2D-histogram of the  $p_{T,ee}$  and  $m_{ee}$  is corrected by a 2D-efficiency histogram of  $m_{ee}$  and  $p_{T,ee}$ , and then it is projected only to the  $p_{T,ee}$  axis removing the contributions outside of the IMR. The R-factor is shown in Figure 7.25, and it shows that there are no differences in acceptance of different signed charged pairs.

In Figure 7.26 the ULS and LS signals for  $p_{T,ee}$  is shown on the left, while the signal (ULS - LS) to background (LS) ratio is shown on the right for the merged 2016, 2017 and 2018 data. The signal to background ratio gets better as we increase the  $p_{T,ee}$ , and this is due to the abundant background for smaller  $p_{T,ee}$ , which is drastically removed as we move to higher  $p_{T,ee}$ .

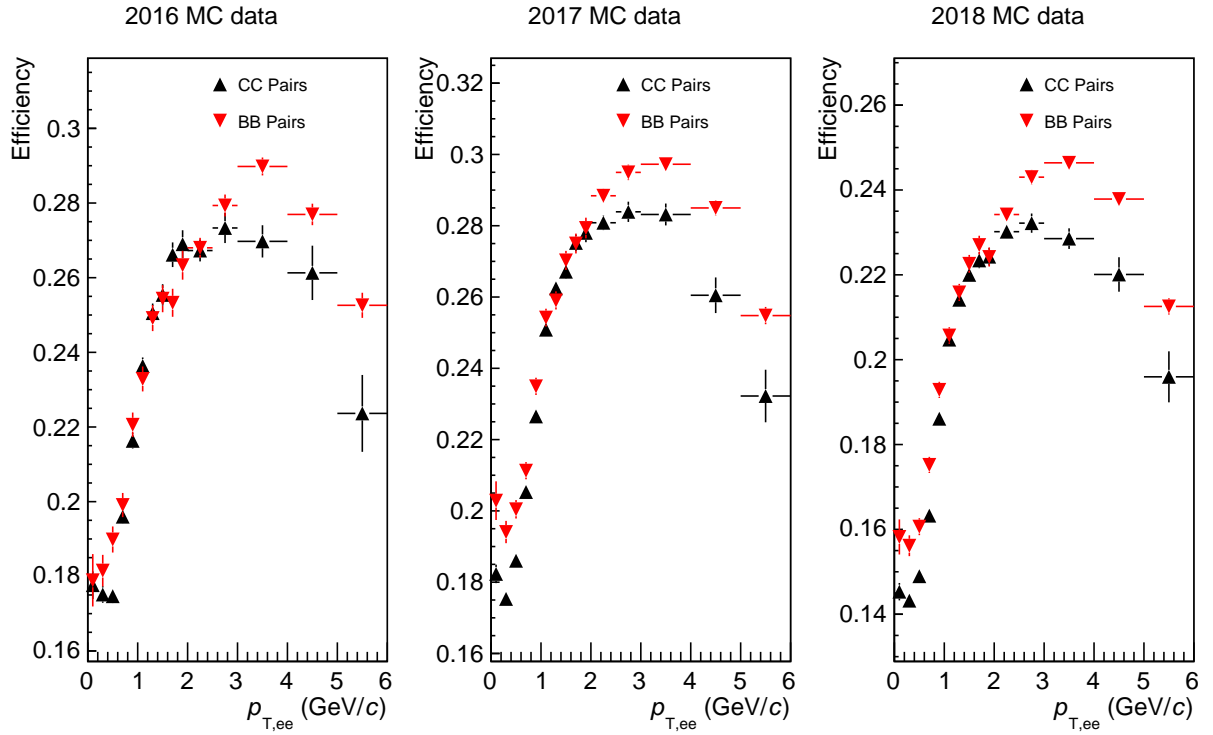


Figure 7.24: Transverse momentum efficiencies of heavy-flavour electron pairs using a minimum  $p_{T,e}$  cut of 0.2 GeV/c. On the left it is shown the efficiency for the 2016 year, in center for 2017 and on the right for 2018.

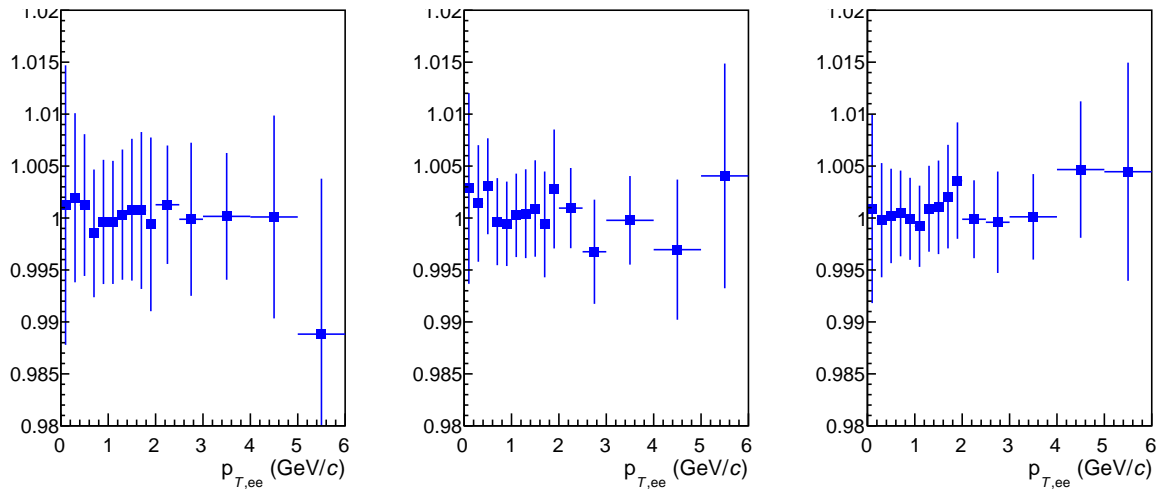


Figure 7.25: R-factor for each of the data taken years analyzed with minimum  $p_{T,e}$  of 0.2 GeV/c. From left to right: 2016, 2017 and 2018 data years.



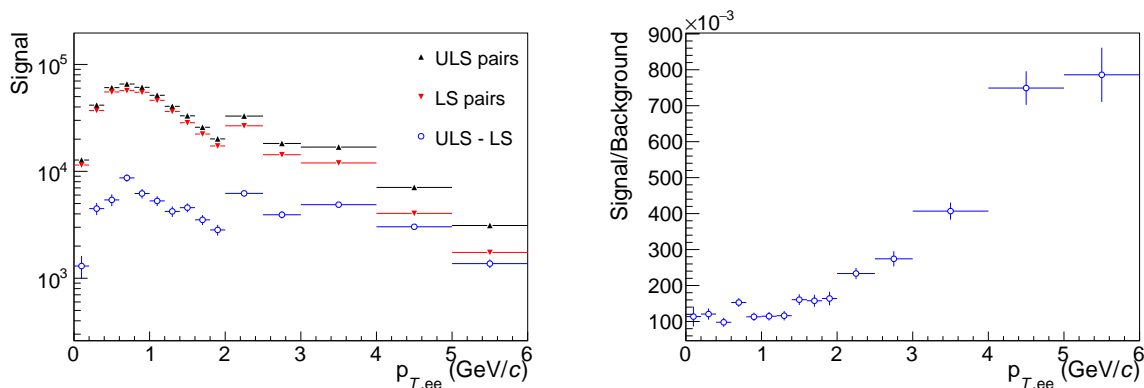


Figure 7.26: On the left: ULS and LS contributions for the  $p_{T,ee}$  analysis with minimum  $p_{T,e}$  of 0.2 GeV/c as a function of the  $p_{T,ee}$ , using all of the data years (2016 + 2017 + 2018). The ULS is shown in black, the LS contribution in red and the ULS - LS subtraction in blue. On the right: Signal over background ratio of the same analysis, using all of the data years (2016 + 2017 + 2018).

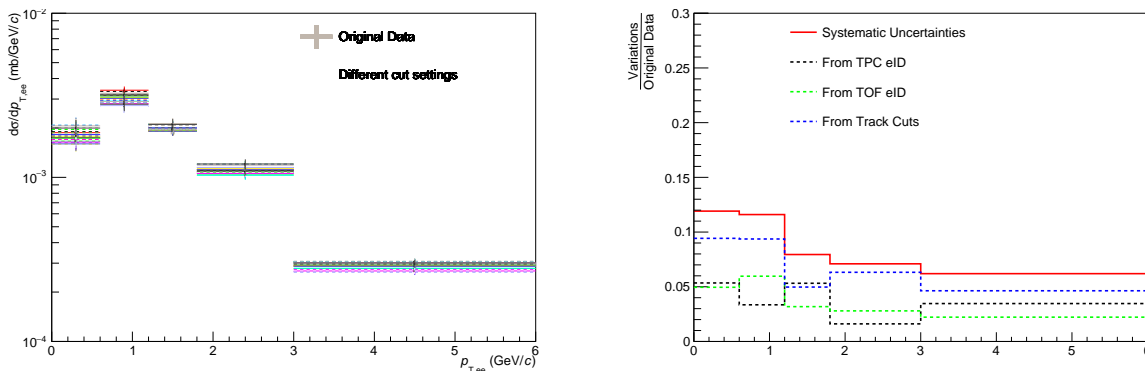


Figure 7.27: On the left: Comparison of the signals obtained using different sets of track and eID cuts. On the right: Systematic uncertainties. In both cases it was used the minimum  $p_{T,e}$  of 0.2 GeV/c, and all of the data years (2016 + 2017 + 2018).

### 7.2.3 Systematic Uncertainties

The systematic uncertainties of the  $p_{T,ee}$  were determined using the procedure of cut variations described in Section 4.7. The comparison of all of the variations and the final systematic uncertainties determined by the variations are shown in Figure 7.27. As in the other analyses case, the same procedure was repeated for all of the years separately, but are not shown here for simplicity. The uncertainties in  $p_{T,ee}$  stay stable at around 10 %, but has a clear decreasing tendency. The eID cuts show uncertainties at around 5 %, as already seen in previous systematics uncertainties evaluation in the other analyses.

The dielectron signal extracted using the procedure described in the last Sections as a function of the  $p_{T,ee}$  for the different data-taking years and for the merged years are shown in Figure 7.28. The signal for each given year was corrected by its own anchored

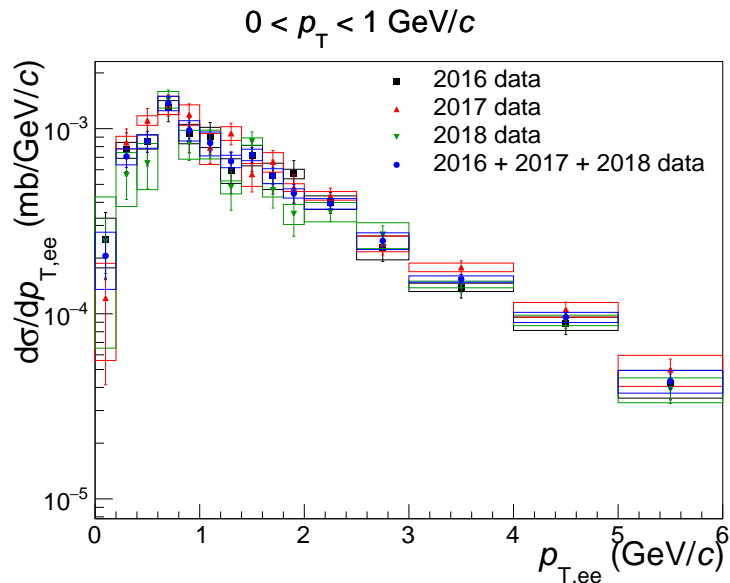


Figure 7.28: The dielectron cross section for the different data-taking years are shown as a function of the  $p_{T,ee}$  for the analysis with  $p_{T,e} > 0.2$  GeV/ $c$ . The signal obtained using 2016 data is shown in black, 2017 in red, 2018 in green and in blue for the merged years. The bar and boxes represent the statistical and systematic uncertainties of the data.

efficiency, and the systematical uncertainties were evaluated separately for each year and for the case of the merged years in the process described in this Section.

## 7.2.4 Monte Carlo Templates

The templates obtained by PYTHIA and POWHEG simulations are shown in Figures 7.29 and 7.30, respectively. Again, on the left plot of these Figures the templates without using  $p_T$ ,  $\eta$  and  $\varphi$  smearing are presented while of the right side the smeared ones. Although the differences are small, the smearing shift the  $p_{T,ee}$  distribution to smaller values, as the  $p_{T,e}$  smeared will be dominantly smaller than the generated. The templates there are normalized by their own integrals for a better visualization, and there are an overall agreement between PYTHIA and POWHEG templates, although POWHEG templates seem to observe a higher charm contribution than PYTHIA for higher  $p_{T,ee}$ , as POWHEG presents harder  $p_T$ . In PYTHIA templates it can be seen a very similar shape between FEX and GSP, which may make it hard to differentiate these two processes when trying to fitting them, as already seen in the  $\Delta\varphi_{ee}$  analysis.

## 7.2.5 Results

The dielectron cross section is shown as a function of the  $p_{T,ee}$  in Figures 7.31 and 7.32 and compared to the expectation from the hadronic decay cocktail using PYTHIA and POWHEG simulations, respectively, with minimum  $p_{T,e}$  cut of 0.2 GeV/ $c$ . The cross sections fitted using the  $p_{T,ee}$  are in the upper limits of the charm and beauty cross sections

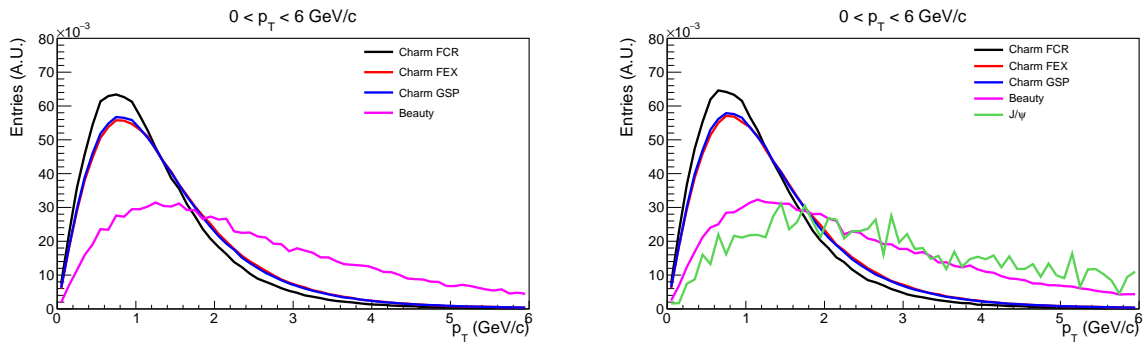


Figure 7.29: Comparison between charm, beauty and  $J/\psi$  templates using PYTHIA pure MC samples, without (left) and with  $p_T$ ,  $\eta$  and  $\varphi$  smearing (right). The templates were normalized by their integrals for a better comparison.

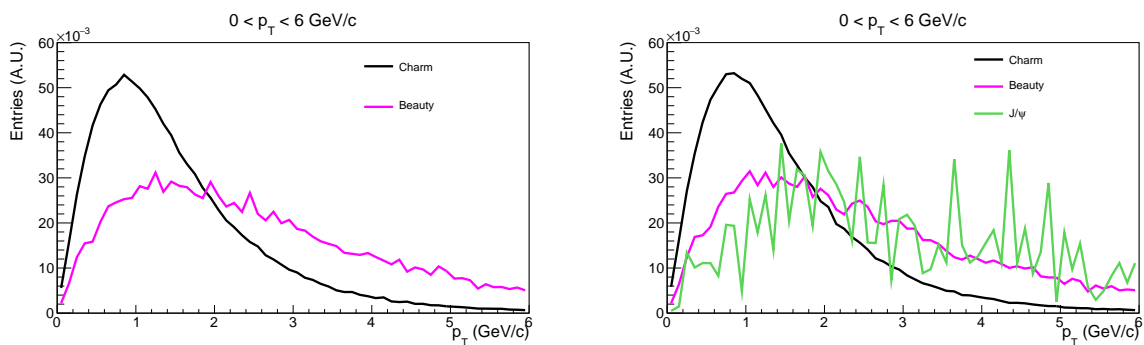


Figure 7.30: Comparison between charm, beauty and  $J/\psi$  templates using POWHEG pure MC samples, without (left) and with  $p_T$ ,  $\eta$  and  $\varphi$  smearing (right). The templates were normalized by their integrals for a better comparison.

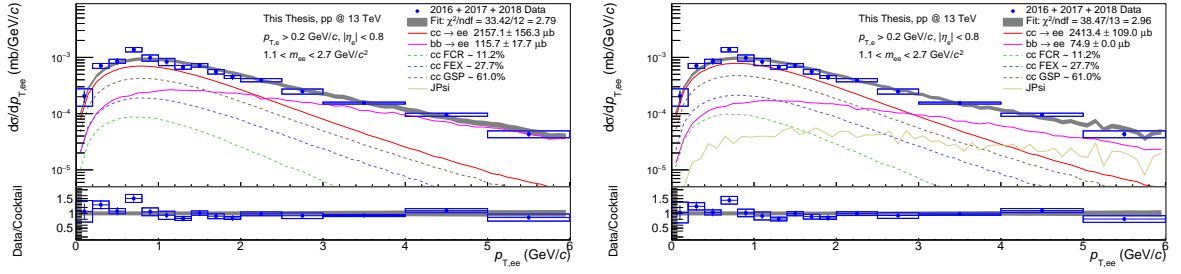


Figure 7.31: The dielectron cross section in pp collisions at 13 TeV as a function of the pair momentum is shown in blue circles for the analysis using the minimum  $p_{T,e}$  cut of 0.2 GeV/c, and the PYTHIA cocktail is shown in red, purple and brown lines for charm, beauty and  $J/\psi$ , respectively, and dashed lines for the different charm production mechanisms that are kept as predicted by PYTHIA. The bar and boxes represent the statistical and systematic uncertainties of the data, while the final cocktail is shown in a grey band. On the bottom of each pair momentum interval plot it is shown the data-to-cocktail ratio.

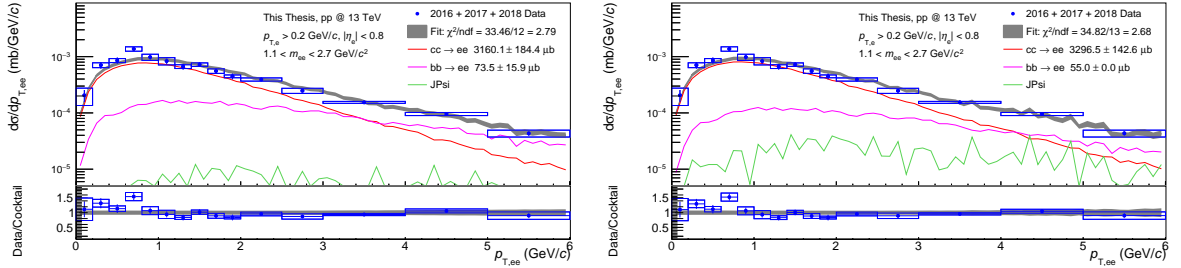


Figure 7.32: The dielectron cross section in pp collisions at 13 TeV as a function of the pair momentum is shown in blue circles for the analysis using the minimum  $p_{T,e}$  cut of 0.2 GeV/c, and the POWHEG cocktail is shown in red, purple and green lines for charm, beauty and  $J/\psi$ , respectively. The bar and boxes represent the statistical and systematic uncertainties of the data, while the final cocktail is shown in a grey band. On the bottom of each pair momentum interval plot it is shown the data-to-cocktail ratio. On the left plot the beauty was also fitted while in the right plot it was kept fixed.

seen in  $m_{ee}$  and  $DCA_{xy}^{ee}$  fits for both PYTHIA and POWHEG. In PYTHIA case, the beauty is even outside the extracted cross sections, which made it necessary to fix the beauty contribution even from the initial exploratory fits.

The next step is to let the production mechanisms of charm free to be fitted. For this purpose, the FEX and GSP were grouped into a single contribution due to their similarity, and the fit can be found in Figure 7.33. The systematic uncertainties of the fit parameters were also determined by moving the data by  $\pm\sigma$  of the systematic uncertainties of the data and they were found to be very stable.

The fractions found were  $4 \pm 24$  (stat)  $\pm \frac{20}{4}$  (sys) % for FCR and  $96 \pm 12$  (stat)  $\pm \frac{4}{20}$  (sys) % for the merged FEX and GSP processes. The central values present higher FEX+GSP and smaller FCR process than predicted by PYTHIA, but they all agree within the uncertainties of our measurements. They are also in agreement to the 1D  $\Delta\varphi_{ee}$  extracted parameters. The systematical uncertainties in the  $p_{T,ee}$  distribution is much

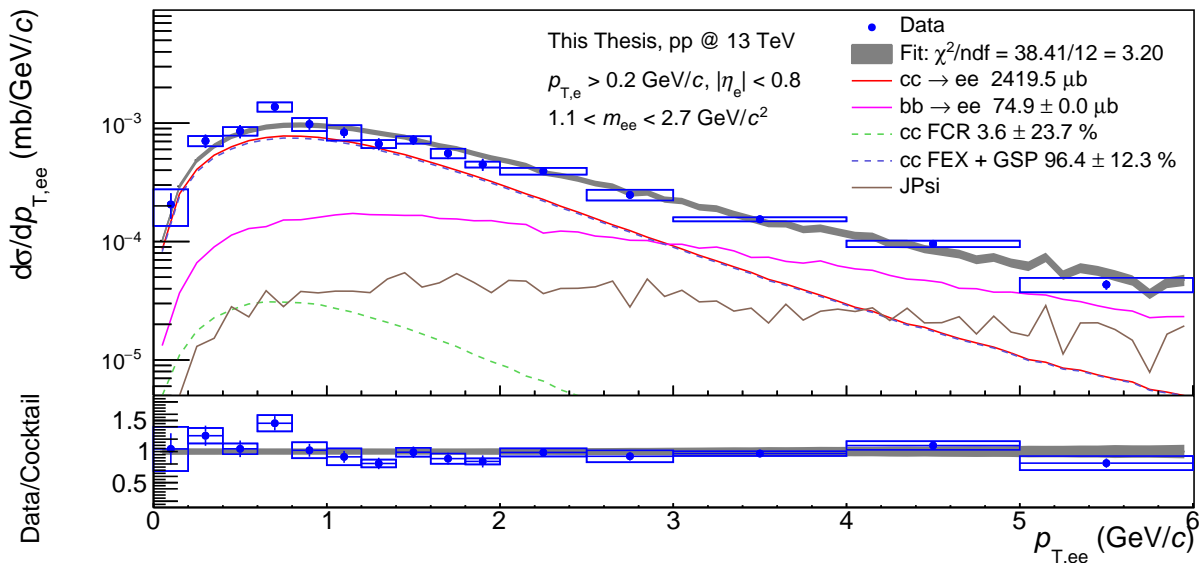


Figure 7.33: The dielectron cross section in pp collisions at 13 TeV as a function of the pair momentum is shown in blue circles for the analysis using the minimum  $p_{T,e}$  cut of 0.2  $\text{GeV}/c$ , and the PYTHIA cocktail is shown in red, purple and brown lines for charm, beauty and  $J/\psi$ , respectively, and dashed lines for the different charm production mechanisms fitted. The bar and boxes represent the statistical and systematic uncertainties of the data, while the final cocktail is shown in a grey band. On the bottom of each pair momentum interval plot it is shown the data-to-cocktail ratio. On the left plot the beauty was also fitted while in the right plot it was kept fixed.

smaller than in the  $\Delta\varphi_{ee}$  analysis, but a greater statistical uncertainty was found. These results are also strictly dependent on the fixed beauty cross section. If we move the beauty cross section to its lower statistical uncertainty ( $\approx 69.2 \mu\text{b}$ ) we obtain a 100 % FEX+GSP to balance the reduction of the beauty contribution to higher  $p_{T,ee}$ . On the other hand, if we fix the beauty cross section to its upper statistical uncertainty limit ( $\approx 80.8 \mu\text{b}$ ), we obtain a smaller FEX+GSP contribution to reduce the charm contribution to higher  $p_{T,ee}$ :  $11 \pm 13 \%$  for FCR and  $89 \pm 13 \%$  for FEX+GSP. The latest central values using the upper statistical limit for beauty cross section are extremely similar to the ones already predicted by PYTHIA: 11.5 % for FCR and 88.5 % for FEX+GSP.

The fit with the production mechanisms free had a timid reduction of the total  $\chi^2$ , from 38.47 to 38.41, but increased the number of free parameters, also increasing the reduced  $\chi^2$ , which in principle would not justify the usage of more parameters.

For a better extraction of such parameters it would still be necessary to have more data available, to extract an even more precise beauty cross section, and using a method with higher discriminating power between charm and beauty, such as the  $\text{DCA}_{xy}^{ee}$  analysis. Our measurements from both  $p_{T,ee}$  and  $\Delta\varphi_{ee}$  with the current beauty cross section are in agreement between themselves and with what was predicted by PYTHIA, within uncertainties, using the beauty contribution fixed to our own measurements of the production cross section.

### 7.3 Chapter Summary

The dielectron cross sections in pp collisions at  $\sqrt{s} = 13$  TeV as a function of the  $\Delta\varphi_{ee}$  and  $p_{T,ee}$  in the intermediate mass region were obtained for each of the 2016, 2017 and 2018 data-taking years, and for these merged years.

The first part of the analysis involving the 2D simultaneous fit of  $\Delta\varphi_{ee}$  and  $p_{T,ee}$  showed a greater discrimination power of  $p_{T,ee}$ , since all of the production mechanisms were similar between themselves in the same  $p_{T,ee}$  intervals. Without fixing the beauty contribution by our own measurements from  $m_{ee}$ , the fit preferred a greater FCR fraction ( $> 50$  %) than expected ( $\approx 11$  %) and a smaller FEX+GSP ( $< 50$  %) than predicted by PYTHIA ( $\approx 89$  %) but with unreasonable uncertainties, and also preferred a greater beauty contribution ( $79.9 \pm 7.8 \mu\text{b}$ ) than what was extracted from  $m_{ee}$  fits ( $74.9 \mu\text{b}$ ), although still completely in agreement within the uncertainties of both measurements. When fixing the beauty contribution to what was extracted from  $m_{ee}$  fits we obtained values compatible with those predicted by PYTHIA, but still within large uncertainties. This shows that a small difference in the beauty production cross section (in this case around 6 %) moved the production mechanisms fraction from more than 50 % for FCR (and a bit smaller than 50 % for FEX+GSP) to values compatible to the ones predicted by PYTHIA, showing the importance of having and even more precise measurement of the heavy-flavour production cross sections to extract reliable information.

The same analysis was then carried out for the  $\Delta\varphi_{ee}$  signal alone, which then preferred even greater contributions from beauty alone ( $86.0 \pm 7.8 \mu\text{b}$ ) and also observed a greater FCR fraction ( $> 50$  %) and a smaller FEX+GSP ( $< 50$  %), in agreement to what was observed in the 2D fits with the beauty parameter free. When fixing the beauty contribution to its production cross section, the fit preferred again a similar fraction to what was expected by PYTHIA, being  $16 \pm 11$  (stat)  $\pm 15$  (sys) % for FCR and  $85 \pm 10$  (stat)  $\pm 15$  (sys) % for a mixed FEX+GSP, in agreement to the 2D fits but with smaller uncertainties.

The last comparison observable was the dielectron  $p_{T,ee}$  spectrum, which needed to have the beauty cross section fixed from the beginning of the studies, since the cross section parameter from the fit was too high. The fit with the beauty fixed also saw fraction values to the production mechanisms similar to those predicted by PYTHIA within uncertainties,  $4 \pm 24$  (stat)  $\pm \frac{20}{4}$  (sys) % for FCR and  $96 \pm 12$  (stat)  $\pm \frac{4}{20}$  (sys) % for FEX+GSP.

All of these fits presented a great dependence of the beauty production cross section, since the production mechanisms present different  $p_{T,ee}$  and  $\Delta\varphi_{ee}$  distributions, and the balance of the fit is always performed by increasing or decreasing the FEX+GSP fraction if the beauty contribution is smaller or greater, respectively. Still, the data could be well described by both PYTHIA or POWHEG generators in all of the  $p_{T,ee}$  intervals. Having more data available would help to obtain even more precise heavy-flavour production cross

section measurements and also reduce the data uncertainties. This could even allow us to include a third experimental parameter: the  $\Delta y$ . The  $\Delta y$  could help us to separate FEX and GSP, as the FEX is depleted for small  $\Delta y$  - discussed in Figure 2.5.

To reduce the similarity of the templates one could also use the full invariant mass spectrum, instead of only the IMR. This would include uncertainties due to the additional LF sources needed, which are dominant when looking at the full spectrum, but would not need the  $m_{ee}$  cuts.





## 8 Summary and Outlook

This thesis presented the measurements and extractions of the charm and beauty cross sections at midrapidity with almost 4x more statistics in proton-proton collisions at  $\sqrt{s} = 13$  TeV than before [19, 20] using two different data analysis:  $m_{ee}$  and  $DCA_{xy}^{ee}$ . The dielectron spectra could be well described by the expected hadronic contributions from heavy-flavour electrons and  $J/\psi$ , validating the calculations and assumptions made to create the cocktails.

The statistical uncertainties of the charm and beauty production cross sections were reduced by more than 50 % in both PYTHIA and POWHEG simulations when these measurements are compared to the previous published ones [19, 20], providing an even more precise measurement than previously available. The heavy-flavour cross sections are consistent between different data-taking years and using analyses with different minimum  $p_{T,e}$  cut, such as  $m_{ee}$  and  $DCA_{xy}^{ee}$ . These measurements are consistent with the result already published by ALICE using only 2016 data. The differences in the extracted cross sections of PYTHIA and POWHEG suggest different kinematic correlations of heavy-flavour pairs of these generators, and these results could provide constraints to MC generators to describe the heavy-flavour production.

The heavy-flavour production cross section extracted using pure  $DCA_{xy}^{ee}$  calculations agree within uncertainties with the analysis of the invariant mass, but showed a systematically higher charm cross section in PYTHIA than  $m_{ee}$ , while systematically higher beauty cross section in POWHEG simulations. This result is very promising since we could describe a pure reconstructed parameter ( $DCA_{xy}^{ee}$ ) by using only calculations and extrapolations in pure MC samples (with only pure generated parameters). This can make it easier to perform  $DCA_{xy}^{ee}$  analysis in the future without the need of the reconstructed MC samples, drastically reducing the size and time of simulations. The calculated templates could also describe well the  $DCA_{xy}^{ee}$  in a selected range of invariant mass related to the  $J/\psi$  peak, which is one of the most important validation tests of the method because of the specific shape of the prompt distribution.

This thesis also presented the first measurement of the dielectron spectrum at midrapidity in proton-proton collisions at  $\sqrt{s} = 13$  TeV as a function of the  $\Delta\varphi_{ee}$ , focusing in the IMR. The data could be well described by the hadronic cocktail of charm, beauty and  $J/\psi$ . It is also the first attempt to estimate the fractions of the different production

mechanisms of charm using the angular correlation distribution of dielectrons. The 2D fits of  $\Delta\varphi_{ee}$  and  $p_{T,ee}$  lead to unreasonable uncertainties trying to separate the processes. The fit was unstable due to the high similarity of the templates within the same  $p_{T,e}$  intervals, which was already seen while studying the templates alone. The performed 2D-fits ( $p_{T,ee}$ ,  $\Delta\varphi_{ee}$ ) showed a greater discrimination power of the  $p_{T,ee}$  than the  $\Delta\varphi_{ee}$  in that simultaneous case. What was found is that due to a decay constrain, all of the different production mechanism templates would follow the same distribution in the same  $p_{T,ee}$  interval, and that the final  $\Delta\varphi_{ee}$  distribution over integrated  $p_{T,ee}$  is only due to their own  $p_{T,ee}$  distributions, which made it necessary to analyze also the  $\Delta\varphi_{ee}$  and  $p_{T,ee}$  spectra alone.

The analysis of the dielectron cross sections at midrapidity in proton-proton collisions at  $\sqrt{s} = 13$  TeV as a function of the  $\Delta\varphi_{ee}$  showed an agreement between the production mechanism fractions from FCR and FEX+GSP and what was expected by PYTHIA, within uncertainties, but only when fixing the beauty contribution by its production cross section. This was also observed in the analysis over the dielectron cross sections as a function of the  $p_{T,ee}$ , where, although the center values preferred a smaller FCR contribution and greater FEX-GSP, it is all in agreement with PYTHIA within the uncertainties when fixing the beauty contribution. The extraction of the production mechanisms is highly dependent on the beauty production cross section used to fix the parameter, which makes it necessary to obtain an even more precise measurement of the beauty cross section to be able to extract more precise parameters.

The ALICE experiment has already been prepared for a huge update for the LHC Run-3 period (2021-2023) [87, 88, 89, 90, 91, 92, 93]. The new Inner Tracking System [91, 92, 93] for Run-3 is expected to greatly improve the  $DCA_{xy}$  resolution at low- $p_T$ , allowing to access electrons currently inaccessible due to the resolution, drastically improving the  $DCA_{xy}^{ee}$  analysis and its measurements. This would help to make more precise measurements of heavy-flavour cross sections using  $DCA_{xy}^{ee}$ , reducing the current uncertainties. Interaction ratios up to 50 kHz are expected in Run-3 and a continuous readout [89, 90], a gain of a factor  $\approx 50$  compared to Run-2. This will drastically increase the statistics that will be available in Run-3 when compared to Run-2, making it possible to extract precise measurements and to study the production mechanisms of heavy-flavour production in details.

The analyses performed in this thesis could be also carried out in p-Pb and Pb-Pb collisions to study the heavy-flavour production and modifications related to different collision systems. More interestingly, not only the total production but, also, if the fractions of the heavy-flavour production mechanisms could be affected depending on the collision system using Run-3 data.

# A Kinematic Variables

## A.1 Kinematics

### Transverse Momentum

The particles can be described by their 4-momentum vector:

$$p^\mu = \left( \frac{E}{c}, \vec{p} \right) \quad (\text{A.1})$$

where  $E$  is the energy of the particle and  $\vec{p} = (p_x, p_y, p_z)$  its 3 momentum. The axes  $x$ ,  $y$  and  $z$  are defined by the coordinate system (see A.2 for ALICE). A natural choice of such system is cylindrical coordinates, where the momentum  $\vec{p}$  can be projected along the  $z$  axis (beam direction) and a  $xy$ -plane transverse to the beam direction  $\vec{p}_T = (p_x, p_y)$ :

$$p_T = \sqrt{p_x^2 + p_y^2} = \sqrt{p^2 - p_z^2} \quad (\text{A.2})$$

Since the transverse momentum and transverse mass ( $m_T = \sqrt{m^2 + p_T^2}$ ) are Lorentz invariant under the longitudinal transformation along axis  $z$ , these variables are valuable to the studies of particle production in experiments such ALICE.

### Rapidity

The rapidity,  $y$ , of a particle is defined as:

$$y = \frac{1}{2} \ln \frac{E + p_z}{E - p_z} \quad (\text{A.3})$$

### Pseudorapidity

In experiments, however, a different variable is used which is called pseudorapidity,  $\eta$ . This variable is widely used because in its calculation it is only necessary to determine the particle's momentum and the polar angle  $\theta$  between the particle 3-momentum and the beam axis:

$$\eta = -\ln\left(\tan\frac{\theta}{2}\right) \quad (\text{A.4})$$

The pseudorapidity goes to zero when  $\theta = 90^\circ$  while it tends to infinity as we approach small angles.

### Pair Transverse Momentum

When we are dealing with 2-particle correlations, such as dielectron studies, there is an important variable which is the transverse momentum of the parent, or also called pair transverse momentum:

$$\vec{p}_{\text{T,parent}} = (p_{x,1} + p_{x,2}, p_{y,1} + p_{y,2}) \quad (\text{A.5})$$

$$p_{\text{T,parent}}^2 = (p_{x,1} + p_{x,2})^2 + (p_{y,1} + p_{y,2})^2 \quad (\text{A.6})$$

### Angular Correlation

The 2-particle angular correlation is simply calculated as the difference in the azimuth angle between the particles:

$$\Delta\varphi_{12} = \varphi_1 - \varphi_2 \quad (\text{A.7})$$

### Invariant Mass

Another important variable for 2-particle correlations is the invariant mass of the parent particle which decays into two daughter particles:

$$m_{\text{parent}}^2 = (E_1 + E_2)^2 - (\vec{p}_1 + \vec{p}_2)^2 = m_1^2 + m_2^2 + 2E_1E_2 - 2\vec{p}_1 \cdot \vec{p}_2 \quad (\text{A.8})$$

### Distance of Closest Approach

The impact parameter is defined as the distance of closest approach (DCA) or the extrapolated orbit trajectory to the primary vertex. It can be calculated as the distance between the radius of the particle's orbit to the primary vertex, subtracting the radius:

$$DCA = |\vec{P}\vec{V} - \vec{R}| - |\vec{R}| \quad (\text{A.9})$$

In 2-particle correlations we can take a single impact parameter value from the 2 particles as the following:

$$DCA_{12} = \sqrt{\frac{DCA_1^2}{2} + \frac{DCA_2^2}{2}} \quad (\text{A.10})$$

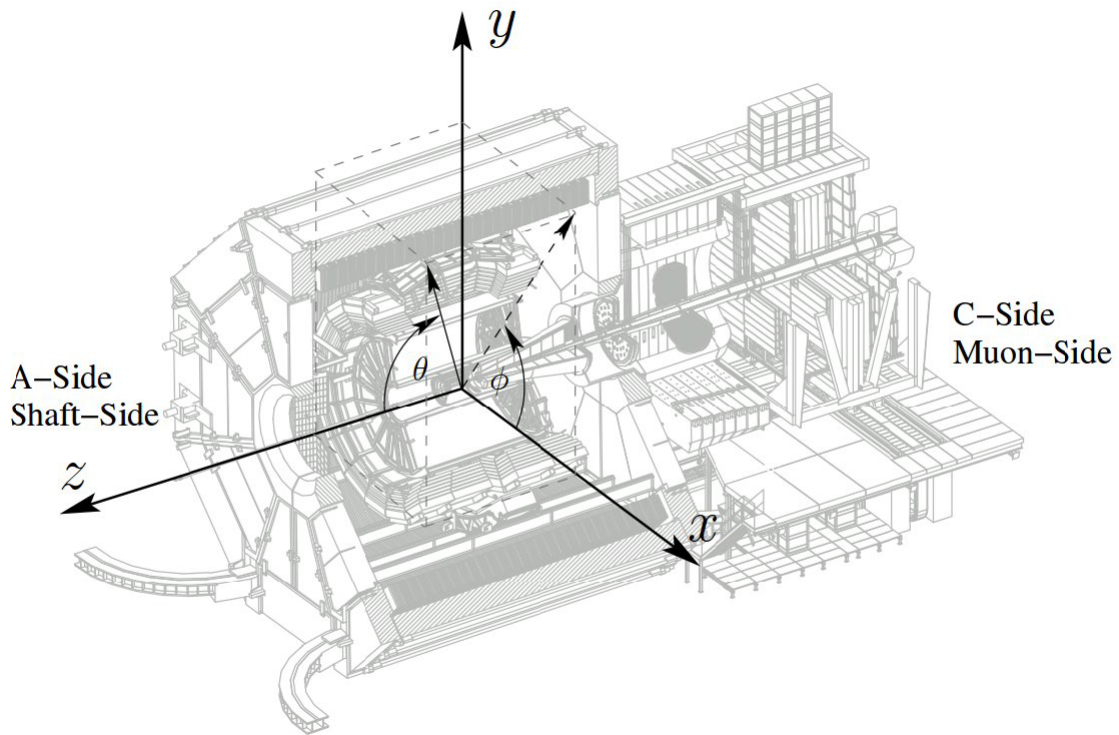


Figure A.1: Schematic view of the coordinate system within ALICE experiment. [94]

## A.2 ALICE Coordinates

Figure A.1 shows the schematic view of the ALICE experiment with respect to its coordinates. The  $z$  coordinate is the axis along the beam direction, and the  $x$ - and  $y$ - axis span the azimuthal plane to the beam-axis.



# B Data Sets

## B.1 2016 Data

### LHC16d

List of runs: 252235, 252248, 252271, 252310, 252317, 252319, 252322, 252325, 252326, 252330.

### LHC16e

List of runs: 253437, 253478, 253482, 253488, 253517, 253529, 253530, 253563, 253589, 253591.

### LHC16g

List of runs: 254128, 254147, 254149, 254174, 254175, 254178, 254193, 254199, 254204, 254205, 254293, 254302, 254304, 254330, 254331, 254332.

### LHC16h

List of runs: 254418, 254419, 254422, 254604, 254606, 254629, 254630, 254632, 254640, 254644, 254646, 254648, 254649, 254651, 254652, 254653, 254654, 255079, 255082, 255085, 255086, 255091, 255111, 255154, 255159, 255162, 255167, 255171, 255173, 255176, 255177, 255240, 255242, 255247, 255249, 255251, 255252, 255253, 255255, 255256, 255275, 255276, 255280, 255283, 255350, 255351, 255398, 255402, 255407, 255415, 255418, 255419, 255420, 255421, 255440, 255442, 255447, 255463, 255465, 255466, 255467.

### LHC16i

List of runs: 255539, 255540, 255541, 255542, 255543, 255577, 255582, 255583, 255591, 255614, 255615, 255616, 255617, 255618.

## **LHC16j**

List of runs: 256219, 256223, 256227, 256228, 256231, 256282, 256283, 256284, 256287, 256289, 256290, 256292, 256295, 256297, 256299, 256302, 256307, 256309, 256311, 256356, 256361, 256362, 256363, 256364, 256365, 256366, 256368, 256371, 256372, 256373, 256415, 256417, 256418.

## **LHC16k**

List of runs: 256504, 256506, 256510, 256512, 256552, 256554, 256556, 256557, 256560, 256562, 256564, 256565, 256567, 256589, 256591, 256592, 256619, 256620, 256658, 256676, 256677, 256681, 256684, 256691, 256692, 256695, 256697, 256941, 256942, 257012, 257021, 257026, 257028, 257077, 257080, 257082, 257084, 257086, 257092, 257095, 257100, 257136, 257137, 257139, 257141, 257204, 257206, 257209, 257224, 257322, 257330, 257358, 257364, 257433, 257457, 257468, 257474, 257487, 257488, 257490, 257491, 257492, 257530, 257531, 257539, 257540, 257541, 257560, 257561, 257562, 257566, 257587, 257588, 257590, 257592, 257594, 257605, 257630, 257632, 257635, 257636, 257642, 257644, 257682, 257684, 257685, 257687, 257688, 257689, 257692, 257694, 257697, 257724, 257725, 257727, 257733, 257734, 257735, 257737, 257754, 257757, 257765, 257773, 257797, 257798, 257799, 257800, 257803, 257804, 257850, 257851, 257853, 257936, 257937, 257939, 257957, 257960, 257979, 257986, 257989, 257992, 258008, 258012, 258014, 258017, 258019, 258039, 258041, 258042, 258045, 258049, 258053, 258059, 258060, 258062, 258063, 258107, 258108, 258109, 258113, 258114, 258117, 258178, 258197, 258198, 258202, 258203, 258204, 258256, 258257, 258258, 258270, 258271, 258273, 258274, 258278, 258299, 258301, 258302, 258303, 258306, 258307, 258332, 258336, 258359, 258387, 258391, 258393, 258426, 258452, 258454, 258456, 258477, 258499, 258537.

## **LHC16l**

List of runs: 258919, 258923, 258962, 258964, 259088, 259091, 259096, 259099, 259117, 259162, 259164, 259204, 259261, 259263, 259264, 259269, 259270, 259271, 259272, 259273, 259274, 259302, 259303, 259305, 259307, 259334, 259336, 259339, 259340, 259341, 259342, 259378, 259382, 259388, 259389, 259394, 259395, 259396, 259473, 259477, 259649, 259650, 259700, 259703, 259704, 259705, 259711, 259713, 259747, 259748, 259750, 259751, 259752, 259756, 259781, 259789, 259822, 259841, 259860, 259866, 259867, 259868.

## **LHC16o**

List of runs: 262424, 262425, 262426, 262428, 262705, 262706, 262708, 262713, 262717, 262719, 262723, 262725, 262727, 262768, 262776, 262777, 262778, 262841, 262842, 262847, 262849, 262853, 262855, 262858, 263331, 263487, 263490, 263496, 263497, 263529, 263682,



263690, 263691, 263737, 263739, 263741, 263743, 263744, 263784, 263785, 263786, 263787, 263790, 263792, 263793, 263803, 263810, 263863, 263866, 263905, 263916, 263920, 263923, 263977, 263978, 263984, 263985, 264033, 264035.

### LHC16p

List of runs: 264076, 264078, 264082, 264085, 264086, 264109, 264110, 264129, 264137, 264138, 264164, 264168, 264188, 264190, 264197, 264198, 264232, 264233, 264235, 264238, 264259, 264260, 264261, 264264, 264265, 264266, 264267, 264277, 264279, 264281, 264305, 264306, 264312, 264336, 264341, 264345, 264346, 264347.

## B.2 2017 Data

### LHC17c

List of runs: 270667, 270665, 270663, 270661, 270581.

### LHC17e

List of runs: 270830, 270828, 270827, 270824, 270822.

### LHC17f

List of runs: 270865, 270861, 270856, 270855, 270854.

### LHC17h

List of runs: 273103, 273100, 273099, 273077, 273010, 273009, 272985, 272983, 272976, 272949, 272947, 272939, 272935, 272934, 272933, 272932, 272905, 272903, 272880, 272873, 272871, 272870, 272836, 272834, 272833, 272829, 272828, 272784, 272783, 272782, 272764, 272763, 272760, 272749, 272747, 272712, 272691, 272690, 272620, 272610, 272608, 272607, 272585, 272577, 272575, 272574, 272521, 272468, 272466, 272463, 272462, 272461, 272413, 272411, 272400, 272399, 272395, 272394, 272389, 272388, 272360, 272359, 272340, 272335, 272194, 272156, 272155, 272154, 272153, 272152, 272151, 272123, 272101, 272100, 272076, 272042, 272040, 272039, 272038, 272036, 272020, 272018, 271886, 271880, 271874, 271873, 271871, 271870.

### LHC17i

List of runs: 274442, 274390, 274389, 274388, 274387, 274386, 274385, 274364, 274363, 274360, 274352, 274329, 274283, 274281, 274280, 274278, 274276, 274271, 274270, 274269,

274268, 274266, 274264, 274263, 274259, 274258, 274232, 274212, 274174, 274148, 274147, 274125, 274094, 274092, 274058, 273986, 273985, 273946, 273943, 273942, 273918, 273889, 273887, 273886, 273885, 273825, 273824, 273654, 273653, 273593, 273592, 273591.

## **LHC17j**

List of runs: 274671, 274669, 274667, 274657, 274653, 274601, 274596, 274595, 274594, 274593.

## **LHC17k**

List of runs: 276508, 276507, 276506, 276462, 276439, 276438, 276437, 276435, 276351, 276348, 276302, 276297, 276294, 276292, 276290, 276259, 276257, 276230, 276205, 276178, 276177, 276170, 276169, 276166, 276145, 276140, 276135, 276104, 276102, 276099, 276098, 276097, 275847, 275664, 275661, 275650, 275648, 275647, 275624, 275623, 275622, 275621, 275617, 275612, 275559, 275558, 275515, 275472, 275471, 275467, 275459, 275457, 275456, 275453, 275452, 275448, 275443, 275406, 275404, 275401, 275372, 275369, 275361, 275360, 275333, 275332, 275328, 275326, 275324, 275322, 275314, 275283, 275247, 275246, 275245, 275239, 275188, 275184, 275180, 275177, 275174, 275173, 275151, 275150, 275149, 275076, 275075, 275073, 275068, 275067, 274979, 274978, 274886, 274882, 274878, 274877, 274822, 274821, 274815, 274806, 274803, 274802, 274801, 274708, 274690.

## **LHC17l**

List of runs: 278216, 278215, 278191, 278189, 278167, 278166, 278165, 278164, 278158, 278127, 278126, 278123, 278122, 278121, 277996, 277991, 277989, 277987, 277952, 277930, 277907, 277904, 277903, 277900, 277899, 277898, 277897, 277876, 277870, 277848, 277847, 277845, 277842, 277841, 277836, 277834, 277805, 277802, 277801, 277800, 277799, 277795, 277794, 277749, 277747, 277746, 277745, 277725, 277723, 277722, 277721, 277577, 277576, 277575, 277574, 277537, 277536, 277534, 277531, 277530, 277479, 277478, 277477, 277476, 277473, 277472, 277418, 277417, 277416, 277389, 277386, 277385, 277384, 277383, 277360, 277314, 277312, 277310, 277293, 277262, 277257, 277256, 277197, 277196, 277194, 277193, 277189, 277188, 277184, 277183, 277182, 277181, 277180, 277155, 277121, 277117, 277091, 277087, 277082, 277079, 277076, 277073, 277037, 277017, 277016, 277015, 276972, 276971, 276970, 276969, 276967, 276920, 276917, 276916, 276762, 276675, 276674, 276672, 276671, 276670, 276644, 276608, 276557, 276556, 276553, 276552, 276551.

## **LHC17m**

List of runs: 280140, 280135, 280134, 280131, 280126, 280118, 280114, 280111, 280108, 280107, 280066, 280052, 280051, 279879, 279855, 279854, 279853, 279830, 279827, 279826,

279773, 279749, 279747, 279719, 279718, 279715, 279689, 279688, 279687, 279684, 279683, 279682, 279679, 279677, 279676, 279642, 279641, 279632, 279630, 279559, 279550, 279491, 279488, 279487, 279483, 279441, 279439, 279435, 279410, 279391, 279355, 279354, 279349, 279348, 279344, 279342, 279312, 279310, 279309, 279274, 279273, 279270, 279268, 279267, 279265, 279264, 279242, 279238, 279235, 279234, 279232, 279208, 279207, 279201, 279199, 279157, 279155, 279130, 279123, 279122, 279118, 279117, 279107, 279106, 279075, 279074, 279073, 279069, 279068, 279044, 279043, 279041, 279036, 279035, 279008, 279007, 279005, 279000, 278999, 278964, 278963, 278960, 278959, 278941, 278939, 278936, 278915, 278914.

### LHC17o

List of runs: 281961, 281956, 281953, 281940, 281939, 281932, 281931, 281928, 281920, 281918, 281916, 281915, 281895, 281894, 281893, 281892, 281633, 281592, 281583, 281574, 281569, 281568, 281563, 281562, 281557, 281511, 281509, 281477, 281475, 281450, 281449, 281446, 281444, 281443, 281441, 281415, 281321, 281301, 281277, 281275, 281273, 281271, 281244, 281243, 281242, 281241, 281240, 281213, 281212, 281191, 281190, 281189, 281181, 281180, 281179, 281081, 281080, 281062, 281061, 281060, 281036, 281035, 281033, 281032, 280999, 280998, 280997, 280996, 280994, 280990, 280947, 280943, 280940, 280936, 280897, 280880, 280856, 280854, 280849, 280848, 280847, 280844, 280842, 280793, 280792, 280787, 280786, 280768, 280767, 280766, 280765, 280764, 280763, 280762, 280761, 280757, 280756, 280755, 280754, 280753, 280729, 280706, 280705, 280681, 280679, 280671, 280647, 280645, 280639, 280637, 280636, 280634, 280613, 280583, 280581, 280574, 280551, 280550, 280547, 280546, 280519, 280518, 280499, 280490, 280448, 280447, 280446, 280445, 280443, 280419, 280415, 280412, 280406, 280405, 280403, 280375, 280374, 280351, 280350, 280349, 280348, 280312, 280310, 280290, 280286, 280285, 280284, 280282.

### LHC17r

List of runs: 282704, 282703, 282702, 282700, 282677, 282676, 282673, 282671, 282670, 282667, 282666, 282651, 282629, 282622, 282620, 282618, 282609, 282608, 282607, 282606, 282580, 282579, 282575, 282573, 282546, 282545, 282544, 282528.

## B.3 2018 Data

### LHC18b

List of runs: 285396, 285365, 285364, 285347, 285328, 285327, 285224, 285222, 285203, 285202, 285200, 285165, 285127, 285125, 285108, 285106, 285066, 285065, 285064, 285015, 285014, 285013, 285012, 285011, 285009.

## **LHC18c**

List of runs: 285958, 285957, 285946, 285917, 285893, 285892, 285869, 285851, 285830, 285812, 285811, 285810, 285806, 285805, 285804, 285781, 285778, 285777, 285756, 285755, 285753, 285722, 285698, 285666, 285664, 285663, 285662, 285643, 285642, 285641, 285640, 285639, 285603, 285602, 285601, 285599, 285578, 285577, 285576, 285575, 285557, 285550, 285545, 285516, 285515, 285497, 285496, 285481, 285471.

## **LHC18d**

List of runs: 286350, 286349, 286348, 286345, 286341, 286340, 286337, 286336, 286314, 286313, 286312, 286311, 286310, 286309, 286308, 286289, 286288, 286287, 286284, 286282, 286263, 286261, 286258, 286257, 286254, 286231, 286230, 286229, 286203, 286202, 286201, 286199, 286198, 286159, 286130, 286129, 286127, 286124, 286064, 286025, 286014, 285980, 285979, 285978.

## **LHC18e**

List of runs: 286937, 286936, 286933, 286932, 286931, 286930, 286911, 286910, 286907, 286877, 286876, 286874, 286852, 286850, 286846, 286809, 286805, 286801, 286799, 286731, 286695, 286661, 286653, 286633, 286592, 286591, 286569, 286568, 286567, 286566, 286511, 286509, 286508, 286502, 286482, 286455, 286454, 286428, 286427, 286426, 286380.

## **LHC18f**

List of runs: 287658, 287657, 287656, 287654, 287578, 287575, 287524, 287521, 287518, 287517, 287516, 287513, 287486, 287484, 287481, 287480, 287451, 287413, 287389, 287388, 287387, 287385, 287381, 287380, 287360, 287356, 287355, 287353, 287349, 287347, 287346, 287344, 287343, 287325, 287324, 287323, 287283, 287254, 287251, 287250, 287249, 287248, 287209, 287208, 287204, 287203, 287202, 287201, 287185, 287155, 287137, 287077, 287072, 287071, 287066, 287064, 287063, 287021, 287000.

## **LHC18g**

List of runs: 288750, 288748, 288743, 288690, 288689, 288687, 288650, 288644, 288642, 288640, 288619.

## **LHC18h**

List of runs: 288806, 288804.

## LHC18i

List of runs: 288909, 288908, 288903, 288902, 288868, 288864, 288863, 288862, 288861.

## LHC18j

List of runs: 288943.

## LHC18k

List of runs: 289201, 289200, 289199, 289198, 289177, 289176, 289175, 289172, 289169, 289167, 289166, 289165.

## LHC18l

List of runs: 289971, 289966, 289965, 289943, 289941, 289940, 289935, 289931, 289928, 289884, 289880, 289879, 289857, 289856, 289855, 289854, 289852, 289849, 289830, 289818, 289817, 289816, 289815, 289814, 289811, 289808, 289775, 289757, 289732, 289731, 289729, 289724, 289723, 289721, 289547, 289521, 289494, 289493, 289468, 289466, 289465, 289463, 289462, 289444, 289426, 289374, 289373, 289370, 289369, 289368, 289367, 289366, 289365, 289356, 289355, 289354, 289353, 289309, 289308, 289306, 289303, 289300, 289281, 289280, 289278, 289277, 289276, 289275, 289254, 289253, 289249, 289247, 289243, 289242, 289241, 289240.

## LHC18m

List of runs: 292839, 292836, 292834, 292832, 292831, 292811, 292810, 292809, 292804, 292803, 292752, 292750, 292748, 292747, 292744, 292739, 292737, 292704, 292701, 292698, 292696, 292695, 292693, 292586, 292584, 292563, 292560, 292559, 292557, 292554, 292553, 292526, 292524, 292523, 292521, 292500, 292497, 292496, 292495, 292461, 292460, 292457, 292456, 292434, 292432, 292430, 292429, 292428, 292406, 292405, 292398, 292397, 292298, 292273, 292265, 292242, 292241, 292240, 292218, 292192, 292168, 292167, 292166, 292164, 292163, 292162, 292161, 292160, 292140, 292115, 292114, 292109, 292108, 292107, 292106, 292081, 292080, 292077, 292075, 292067, 292062, 292061, 292060, 292040, 292012, 291982, 291977, 291976, 291953, 291948, 291946, 291945, 291944, 291943, 291942, 291803, 291796, 291795, 291769, 291768, 291766, 291762, 291760, 291756, 291755, 291729, 291706, 291698, 291697, 291690, 291665, 291661, 291657, 291626, 291624, 291622, 291618, 291615, 291614, 291590, 291485, 291484, 291482, 291481, 291457, 291456, 291453, 291451, 291447, 291424, 291420, 291417, 291416, 291402, 291400, 291399, 291397, 291377, 291375, 291363, 291362, 291361, 291360, 291286, 291285, 291284, 291282, 291266, 291265, 291263, 291262, 291257, 291240, 291209, 291188, 291143, 291116, 291111, 291110, 291101, 291100, 291093, 291069,

291066, 291065, 291041, 291037, 291035, 291006, 291005, 291004, 291003, 291002, 290980, 290979, 290976, 290975, 290974, 290948, 290944, 290943, 290941, 290935, 290932, 290895, 290894, 290888, 290887, 290886, 290862, 290860, 290853, 290848, 290846, 290843, 290841, 290790, 290787, 290766, 290689, 290687, 290665, 290660, 290645, 290632, 290627, 290615, 290614, 290613, 290612, 290590, 290588, 290553, 290550, 290549, 290544, 290540, 290539, 290538, 290501, 290500, 290499, 290469, 290467, 290459, 290458, 290456, 290427, 290426, 290425, 290423, 290412, 290411, 290404, 290401, 290399, 290376, 290375, 290374, 290350, 290327, 290323.

### **LHC18n**

List of runs: 293359, 293357.

### **LHC18o**

List of runs: 293898, 293896, 293893, 293891, 293886, 293856, 293831, 293830, 293829, 293809, 293807, 293806, 293805, 293802, 293776, 293774, 293773, 293770, 293741, 293740, 293698, 293696, 293695, 293692, 293691, 293690, 293689, 293686, 293588, 293587, 293583, 293582, 293579, 293578, 293573, 293571, 293570, 293475.

### **LHC18p**

List of runs: 294925, 294916, 294884, 294883, 294880, 294875, 294852, 294818, 294817, 294816, 294815, 294813, 294809, 294805, 294775, 294774, 294772, 294769, 294749, 294747, 294746, 294745, 294744, 294742, 294741, 294722, 294718, 294715, 294710, 294703, 294653, 294636, 294633, 294632, 294593, 294591, 294590, 294587, 294586, 294563, 294562, 294558, 294556, 294553, 294531, 294530, 294529, 294527, 294526, 294525, 294524, 294310, 294308, 294307, 294242, 294241, 294212, 294210, 294208, 294205, 294201, 294200, 294199, 294156, 294155, 294154, 294152, 294131, 294013, 294012, 294011, 294010, 294009.

# C TPC and TOF Post-Calibration

The re-calibration maps obtained for Data C.1 and Monte Carlo C.2 are show in this Appendix, as described in Sections 4.5 and 5.2.3, respectively.

## C.1 Data

The mean re-calibration maps for TPC are shown in the Figures C.1, C.2 and C.3, for 2016, 2017 and 2018 data, respectively, while the width re-calibration maps for TPC are show in Figures C.4, C.5, C.6. The same re-calibration maps are shown for TOF detector in Figures C.7, C.8 and C.9 for 2016, 2017 and 2018 mean and in Figures C.10, C.11 and C.12 for the width. To avoid statistical fluctuations these maps are also smoothed for momentum above 1 GeV/ $c$ , and the results showed there are already smoothed. For 2018 data the momentum range studied was different because there are periods without TPC splines available<sup>1</sup>, making it necessary to check the electron distribution also for higher momentum ranges (which is not needed when there are TPC Splines available). The TPC splines are available for all 2016 and 2017 data analyzed and also for 2018 periods b, d, e, i and m.

The 2016, 2017 and 2018 (with splines) re-calibration maps are extremely similar, presenting differences only for periods with really small statistics (and so, unreliable differences). As expected, there are no differences in TOF recalibration maps depending on the TPC splines availability, while in TPC maps the differences are clear.

Since the fits are not too reliable for low statistics and all of the periods in the same year present really similar behaviours, it was decided to use the maps obtained using all periods of the respecting year of data-taking. In summary, periods will use the re-calibration maps obtained by using all the periods of the year. For 2018 the periods were grouped by having or not TPC splines available, and the maps obtained by using all maps with/without TPC splines were used in each case. The spectra of the re-calibrated PID after this corrections is shown in Figures C.13, C.14 and C.15.

---

<sup>1</sup><https://twiki.cern.ch/twiki/bin/view/ALICE/TPCSplines>

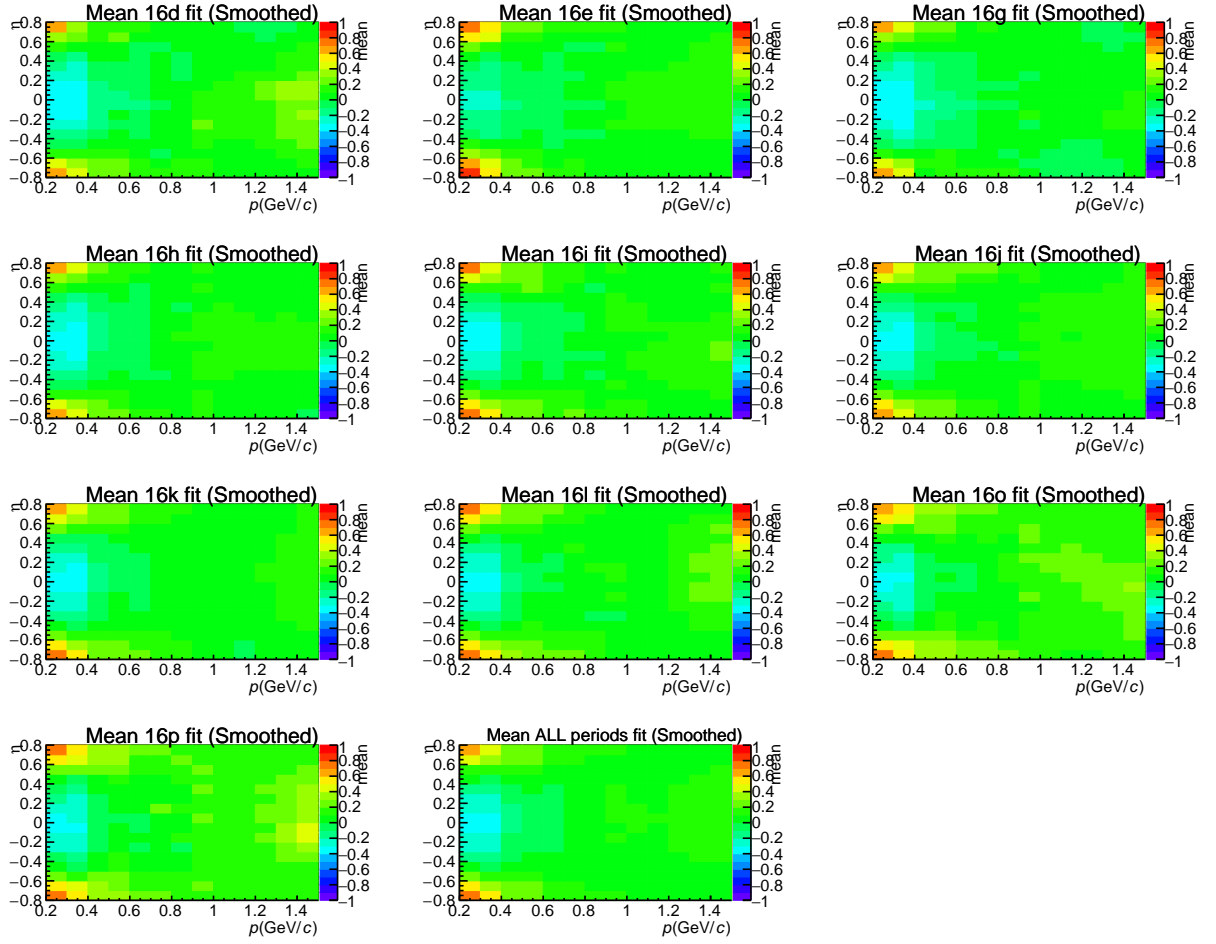


Figure C.1: TPC mean re-calibration maps obtained for 2016 periods: d, e, g, h, i, j, k, l, o, p and the last one is the same analysis over all 2016 periods.

## C.2 Monte Carlo

The mean and width maps for TPC electron distribution before the correction is shown in Figures C.16, C.17, C.18 for 2016, 2017, and 2018 data, respectively. The recalibrated mean and width maps for TPC electron distribution is shown in Figures C.19, C.20, C.21 for 2016, 2017, and 2018 data, respectively. Even though the TPC electron distribution maps before the re-calibration are already close to perfection (note the scale in the plots), it is possible to observe a small improvement by using the offline correction maps.



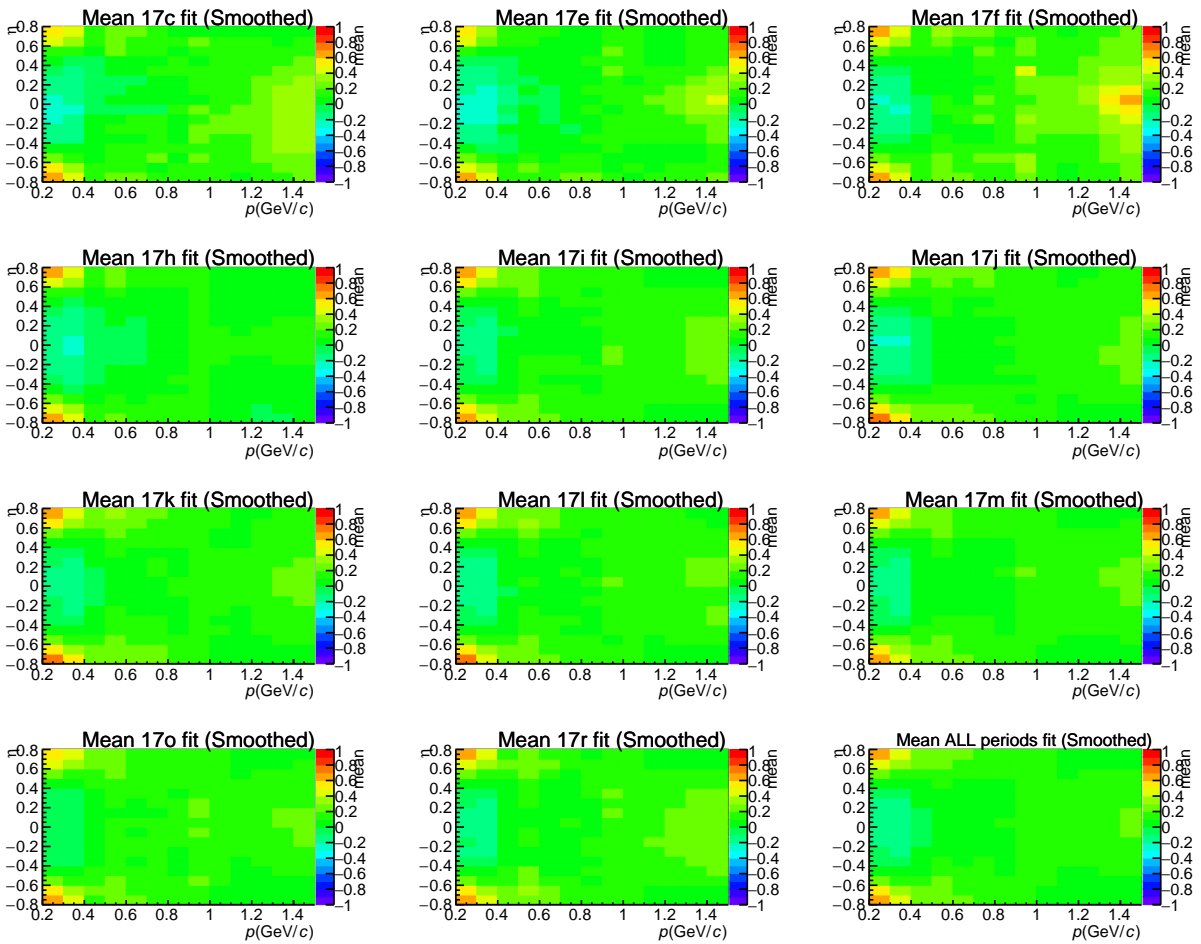


Figure C.2: TPC mean re-calibration maps obtained for 2017 periods: c, e, f, h, i, j, k, l, m, o, r, and the last one is the same analysis over all 2017.

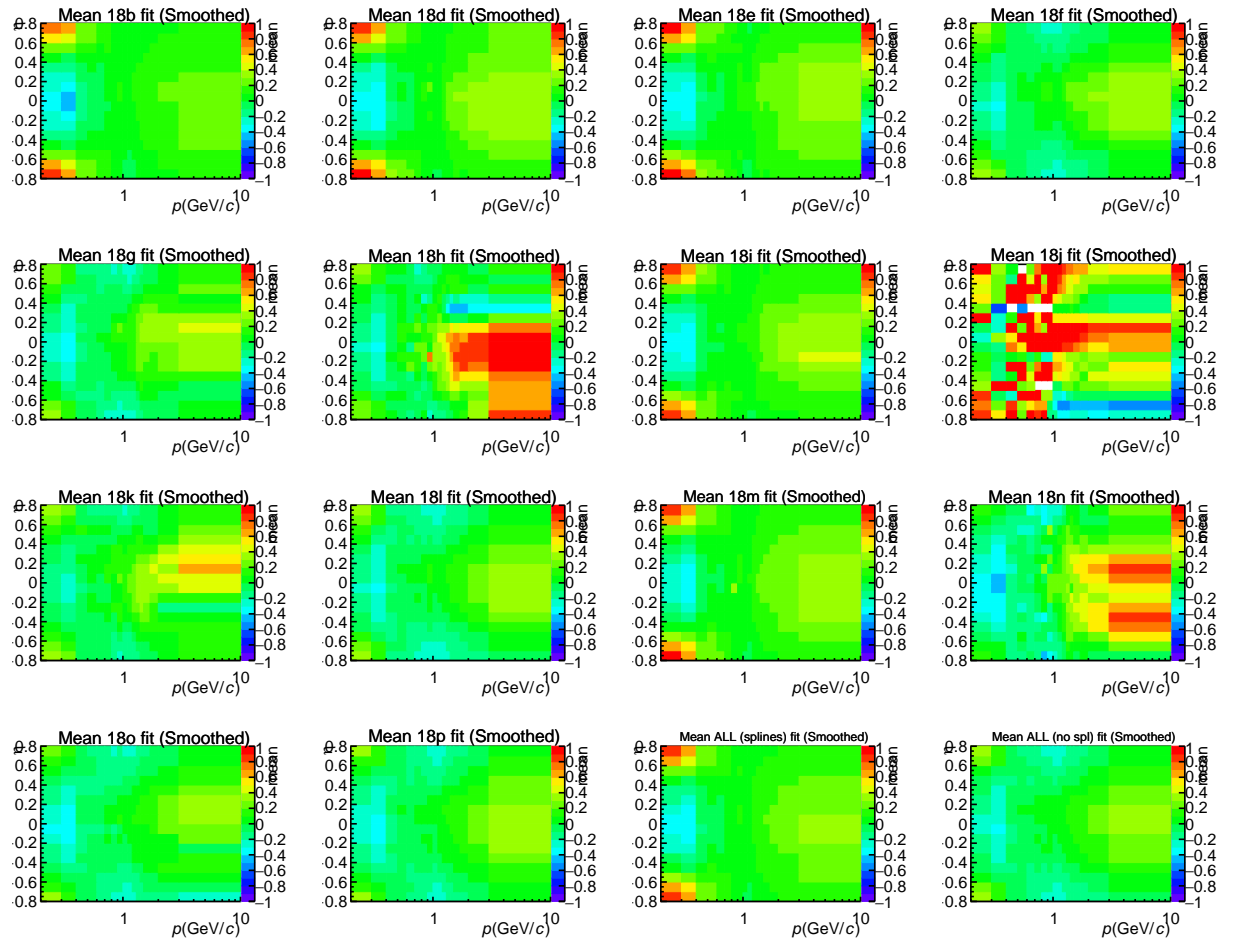


Figure C.3: TPC mean re-calibration maps obtained for 2018 periods: b, d, e, f, h, i, j, k, l, m, n, o, p, and the two last ones are the same analysis over all 2018 data with and without splines available.

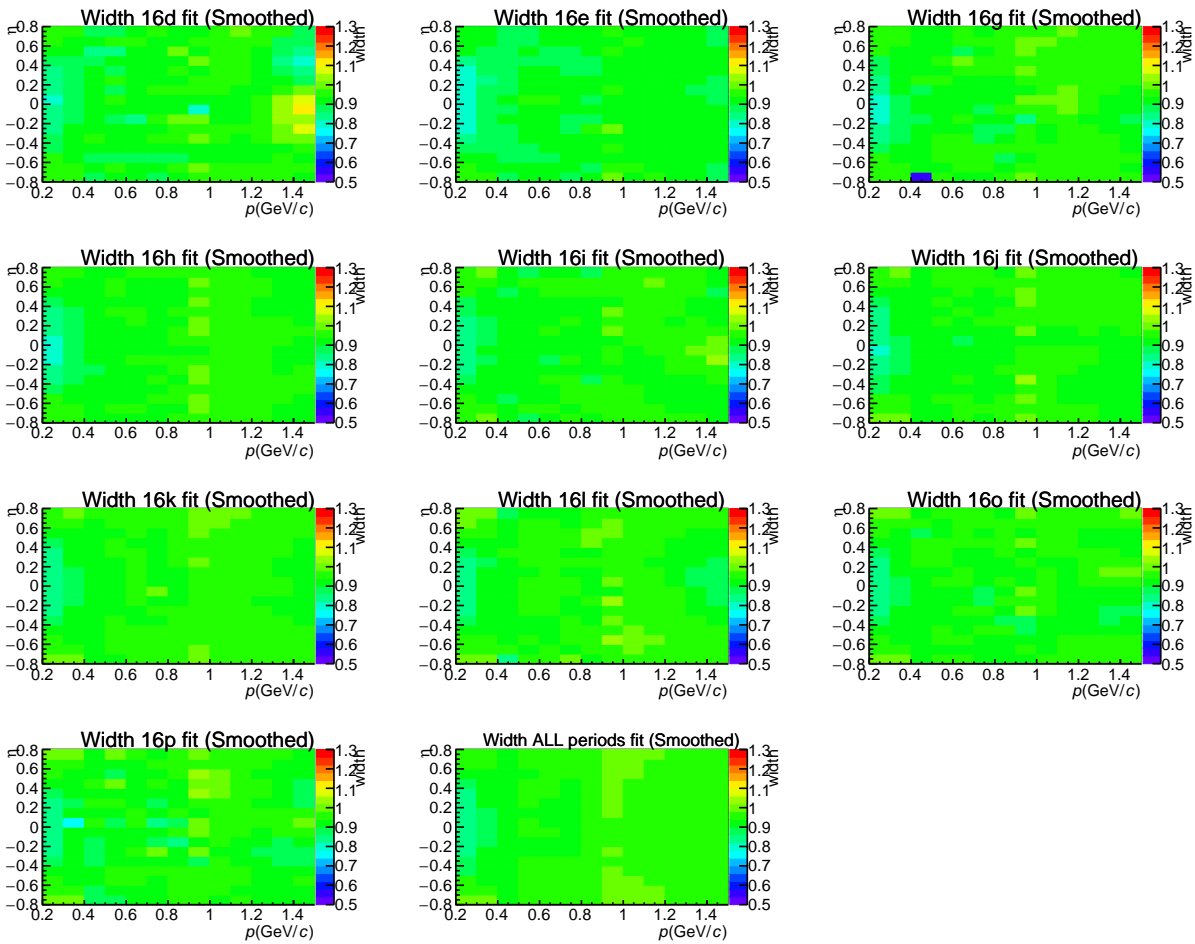


Figure C.4: TPC width re-calibration maps obtained for 2016 periods: d, e, g, h, i, j, k, l, o, p and the last one is the same analysis over all 2016 periods.

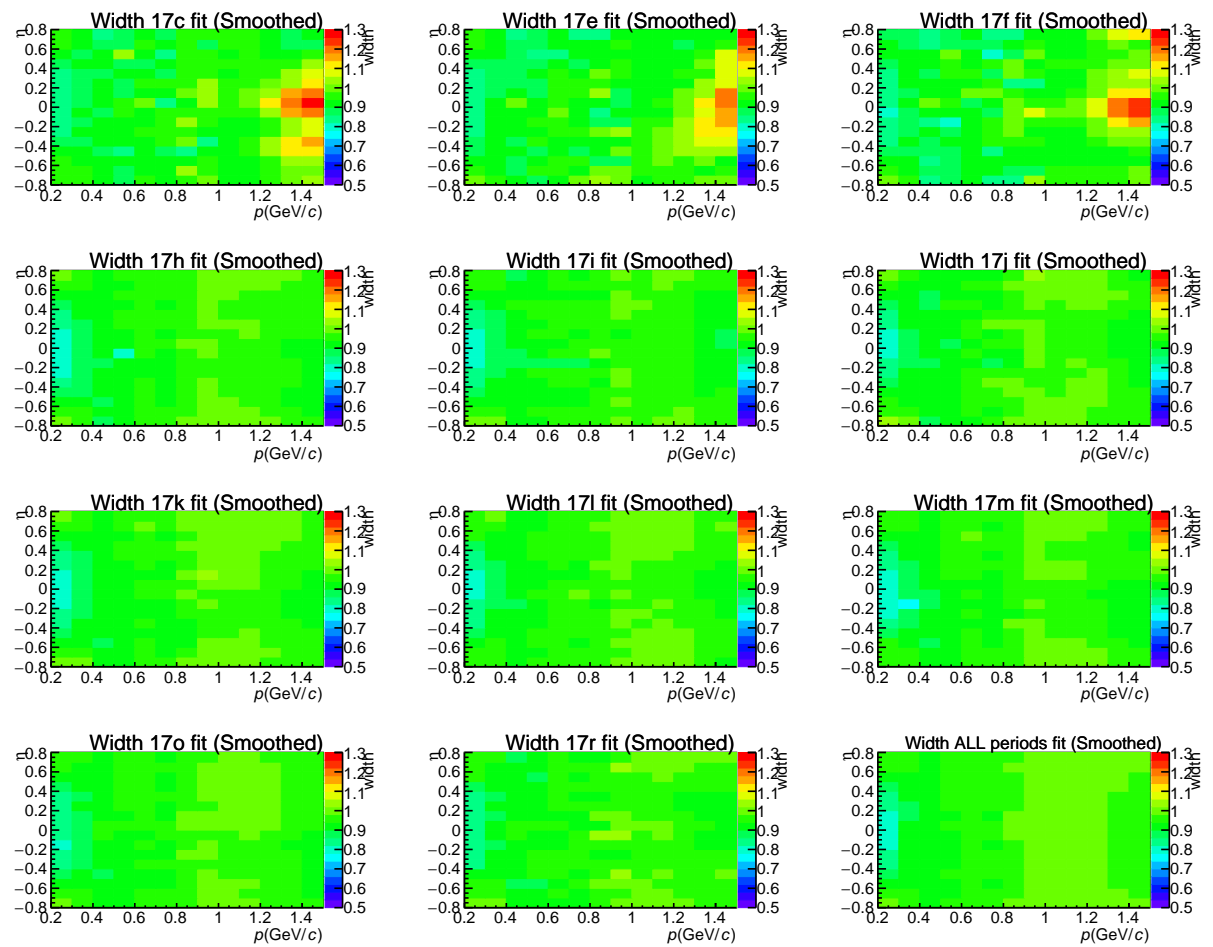


Figure C.5: TPC width re-calibration maps obtained for 2017 periods: c, e, f, h, i, j, l, m, o, r, and the last one is the same analysis over all 2017 periods.

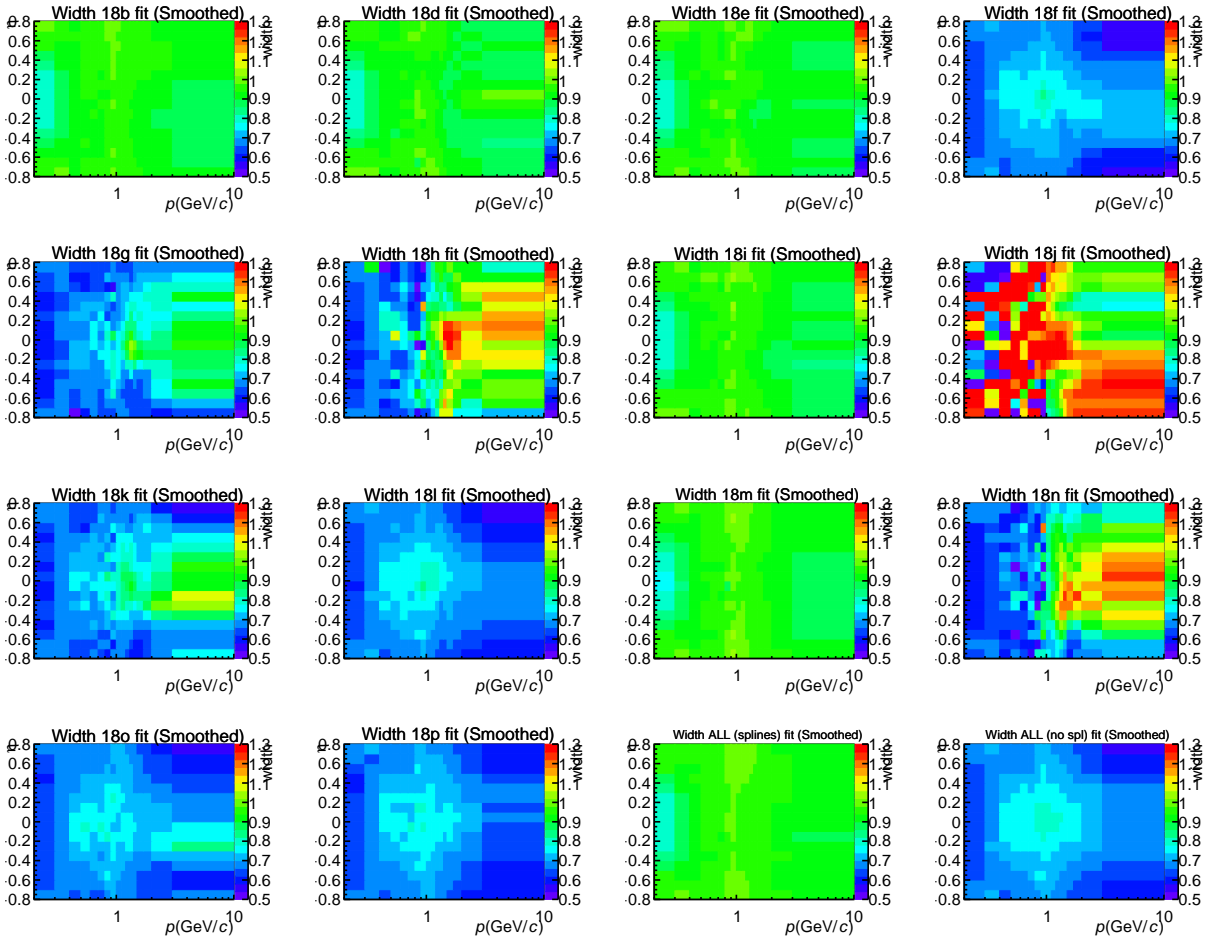


Figure C.6: TPC width re-calibration maps obtained for 2018 periods: b, d, e, f, h, i, j, k, l, m, n, o, p, and the two last ones are the same analysis over all 2018 data with and without splines available.

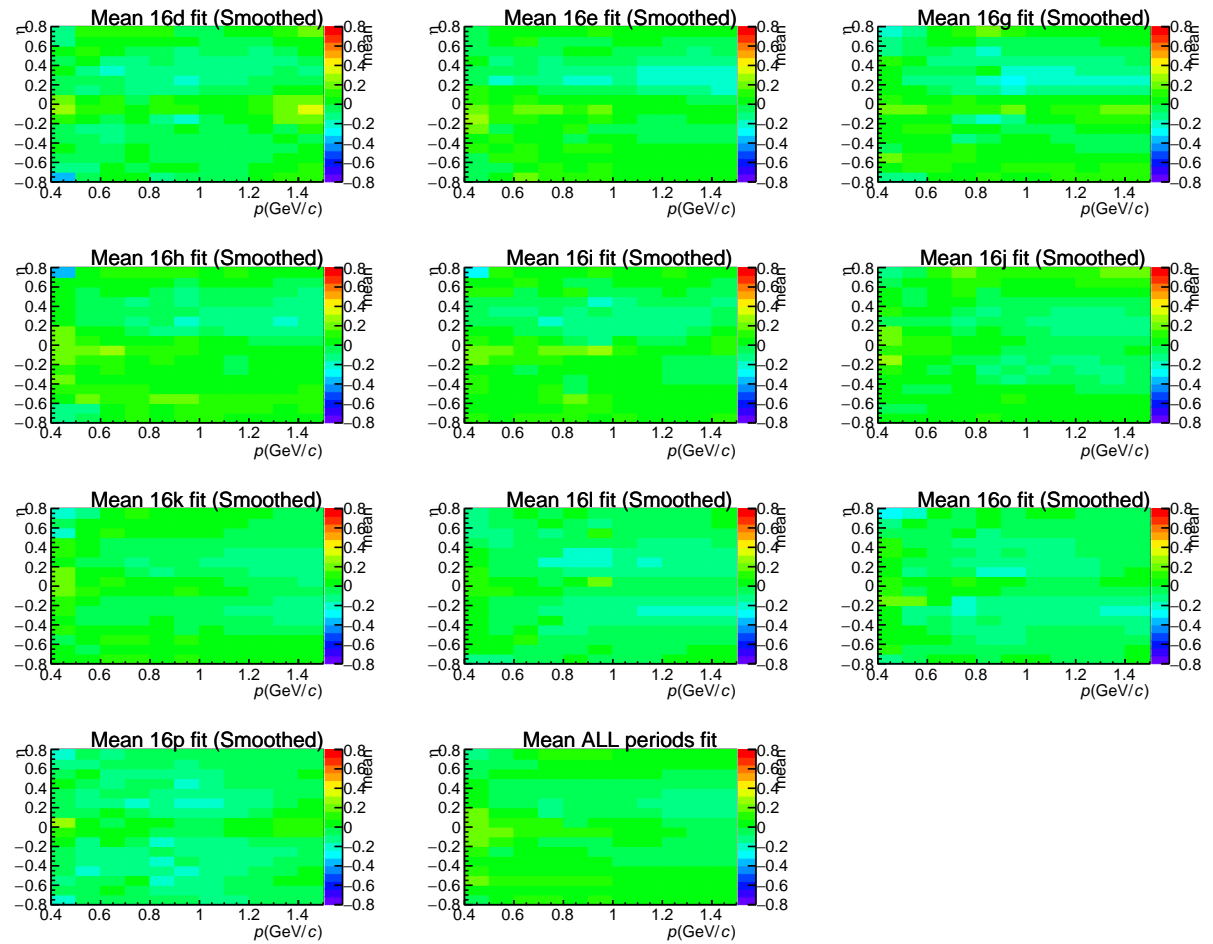


Figure C.7: TOF mean re-calibration maps obtained for 2016 periods: d, e, g, h, i, j, k, l, o, p and the last one is the same analysis over all 2016 periods.

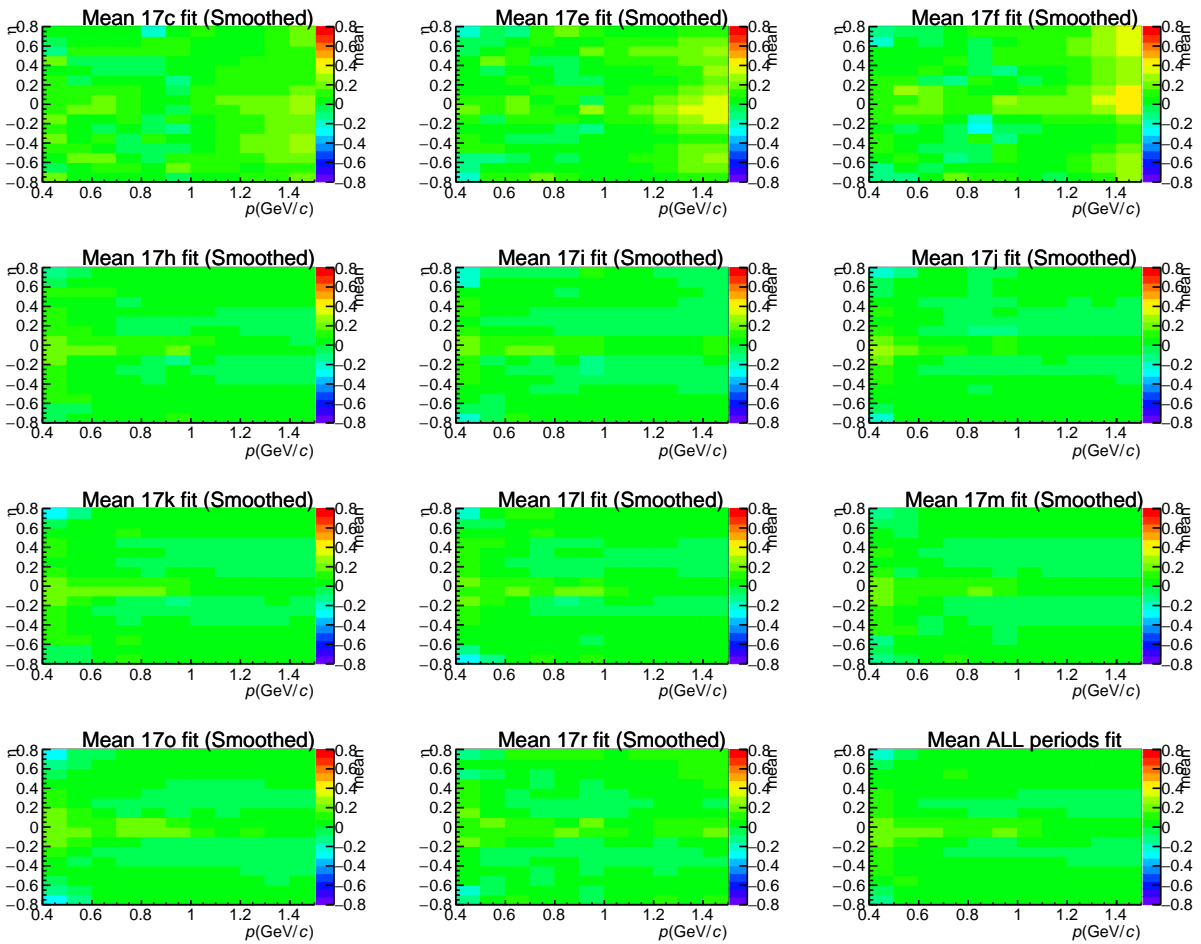


Figure C.8: TOF mean re-calibration maps obtained for 2017 periods: c, e, f, h, i, j, l, m, o, r, and the last one is the same analysis over all 2017 periods.

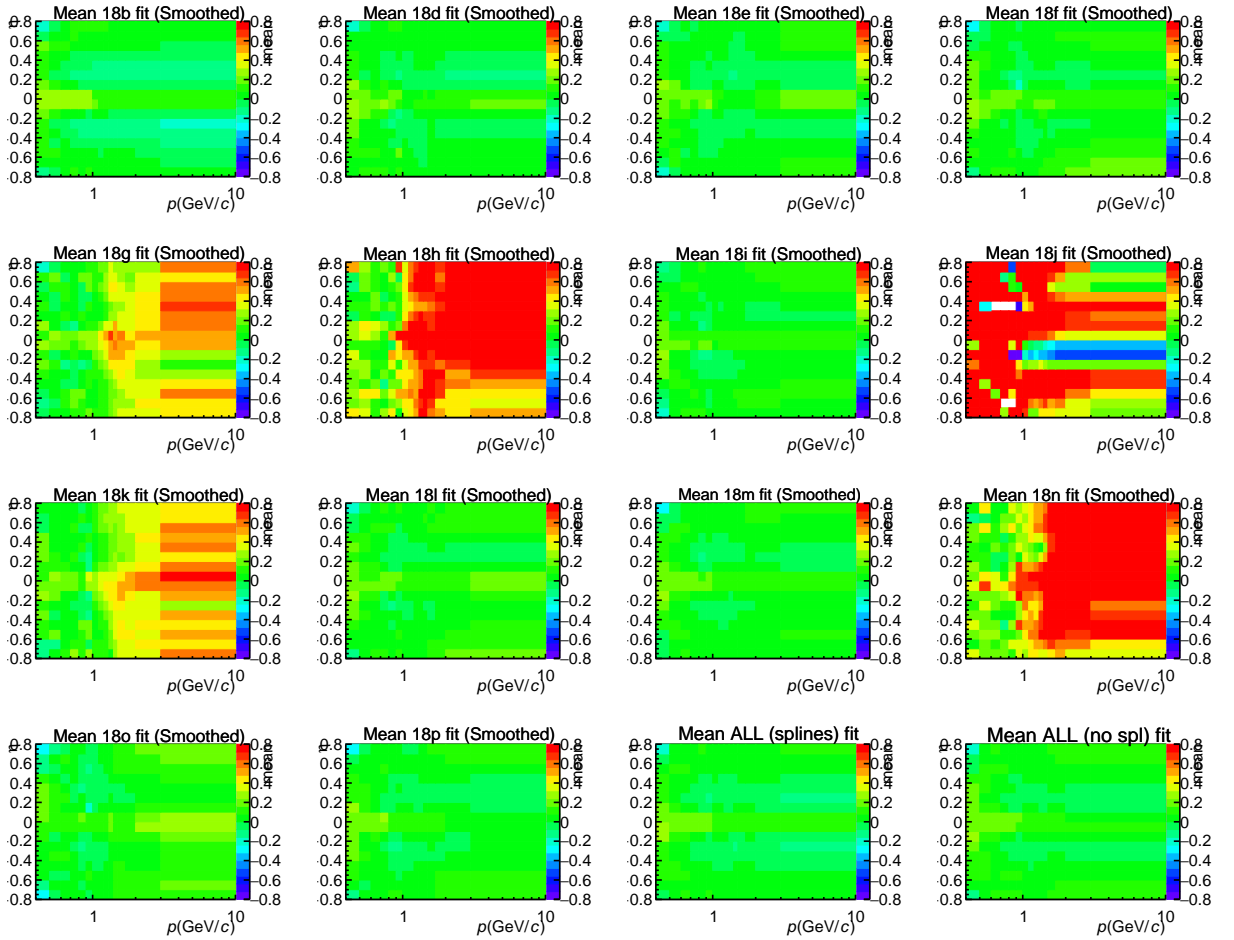


Figure C.9: TOF mean re-calibration maps obtained for 2018 periods: b, d, e, f, h, i, j, k, l, m, n, o, p, and the two last ones are the same analysis over all 2018 data with and without splines available.



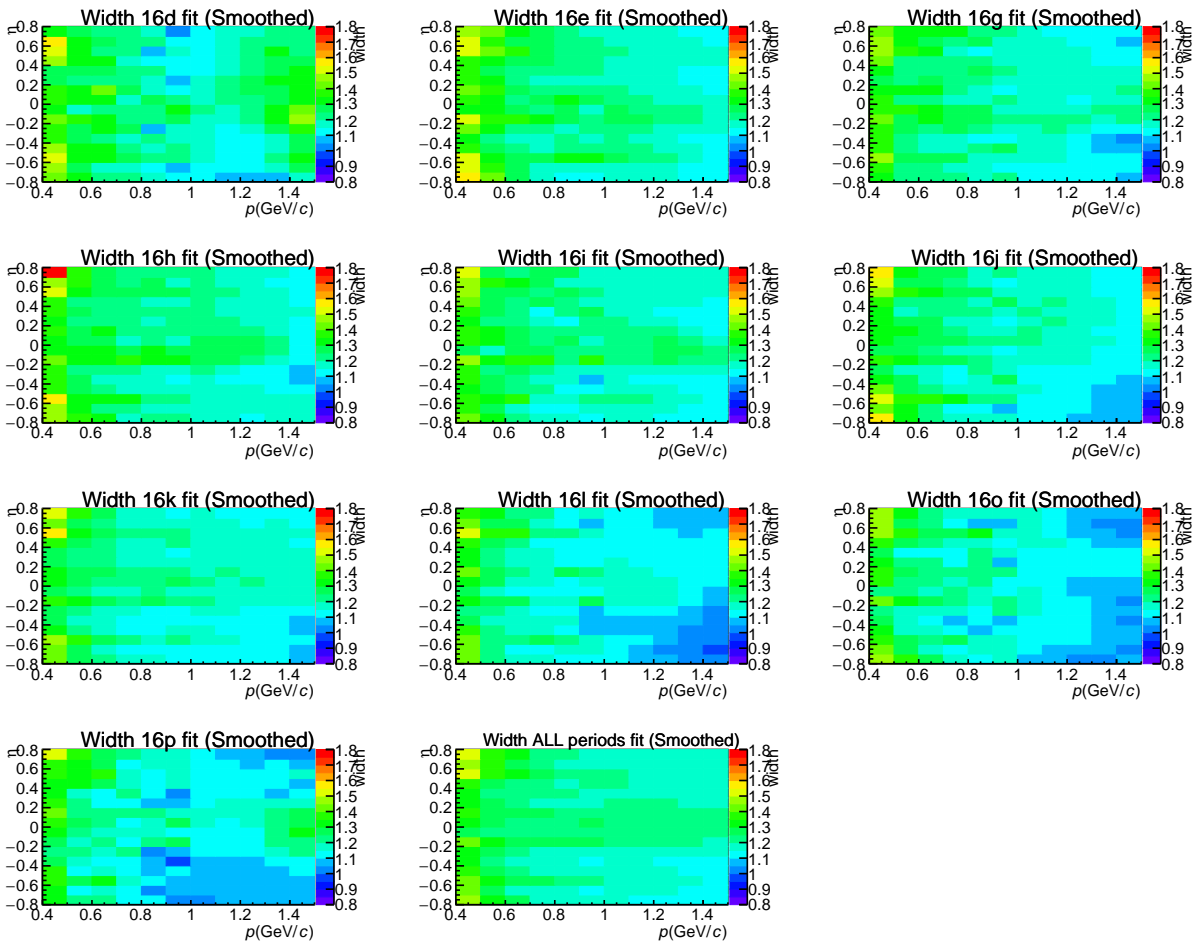


Figure C.10: TOF width re-calibration maps obtained for 2016 periods: d, e, g, h, i, j, k, l, o, p and the last one is the same analysis over all 2016 periods.

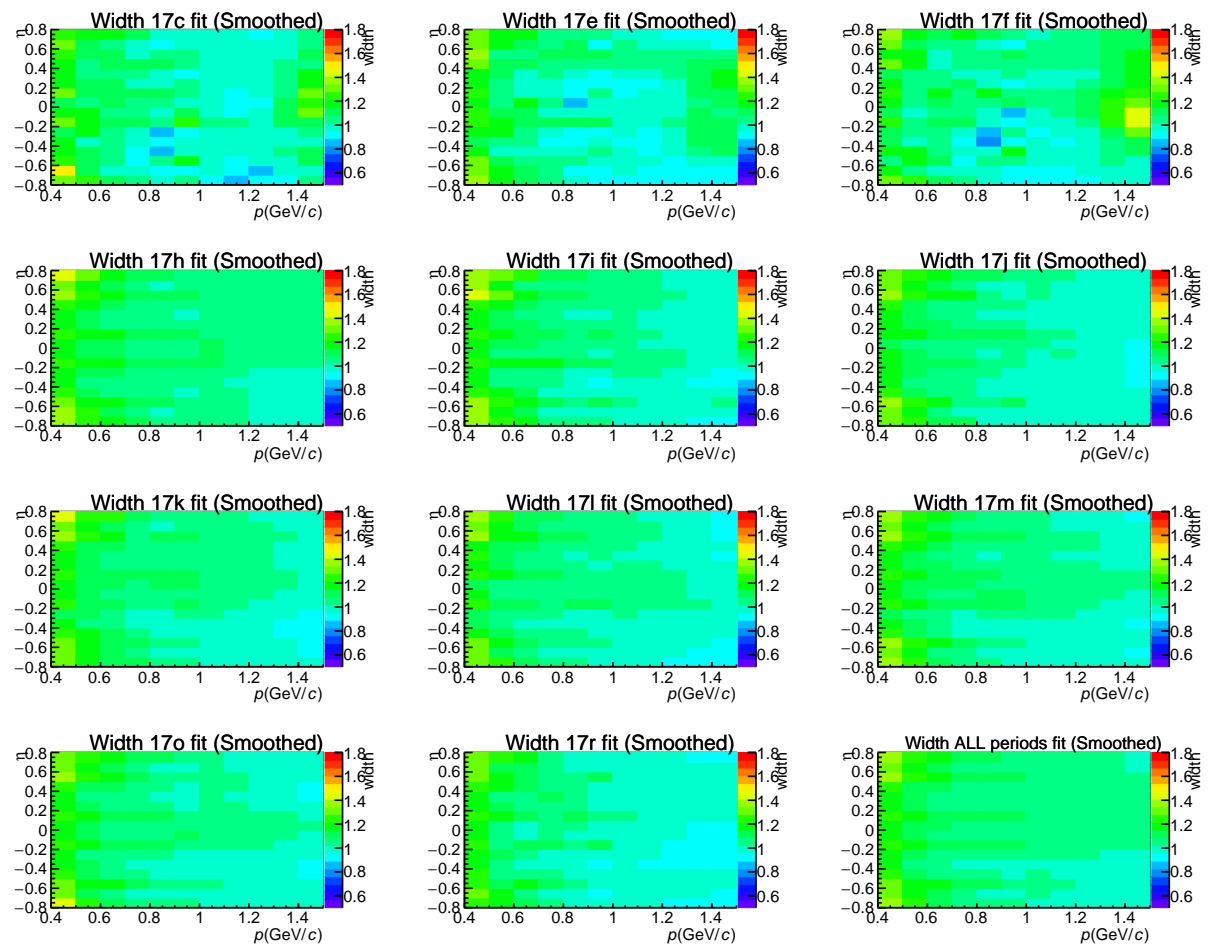


Figure C.11: TOF width re-calibration maps obtained for 2017 periods: c, e, f, h, i, j, l, m, o, r, and the last one is the same analysis over all 2017 periods.

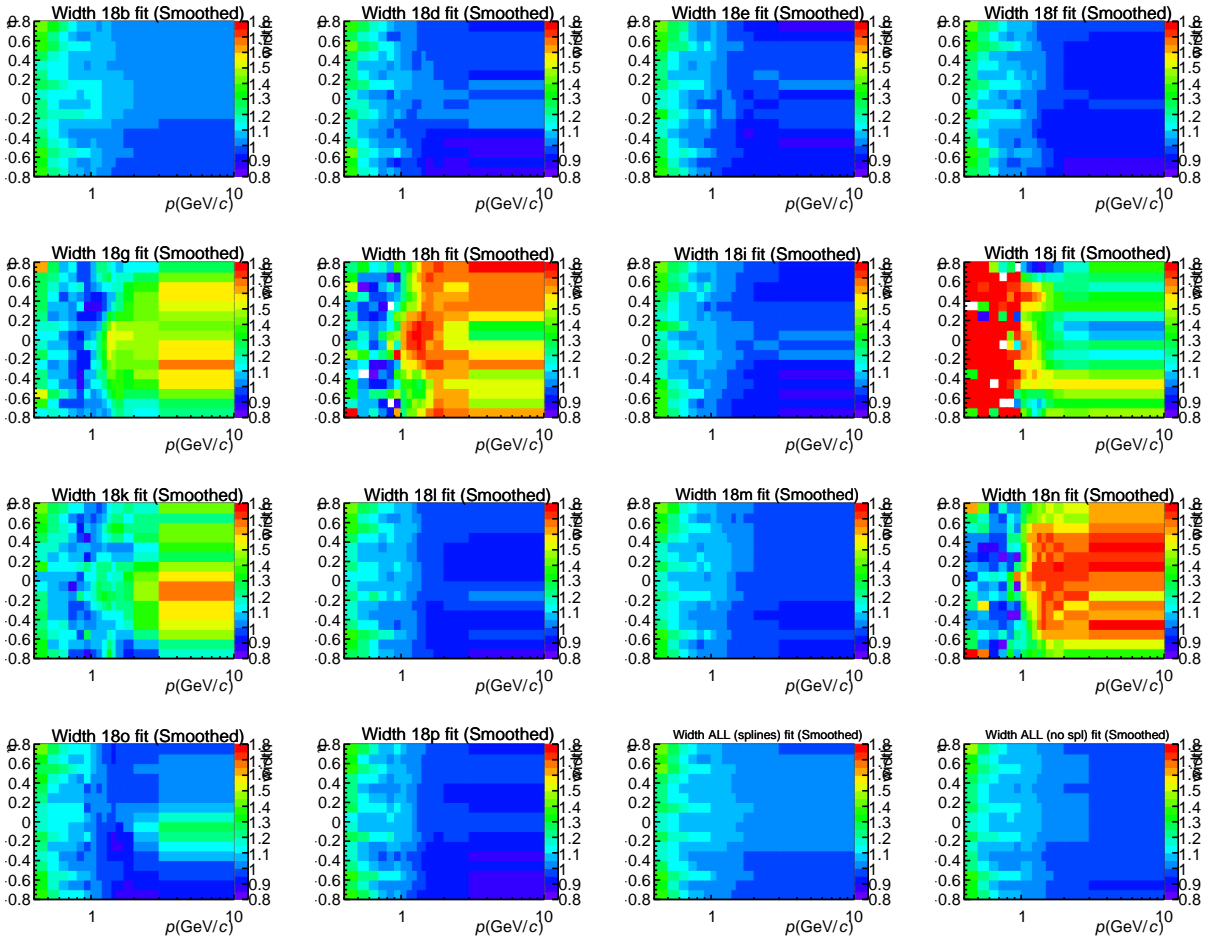


Figure C.12: TOF width re-calibration maps obtained for 2018 periods: b, d, e, f, h, i, j, k, l, m, n, o, p, and the two last ones are the same analysis over all 2018 data with and without splines available.

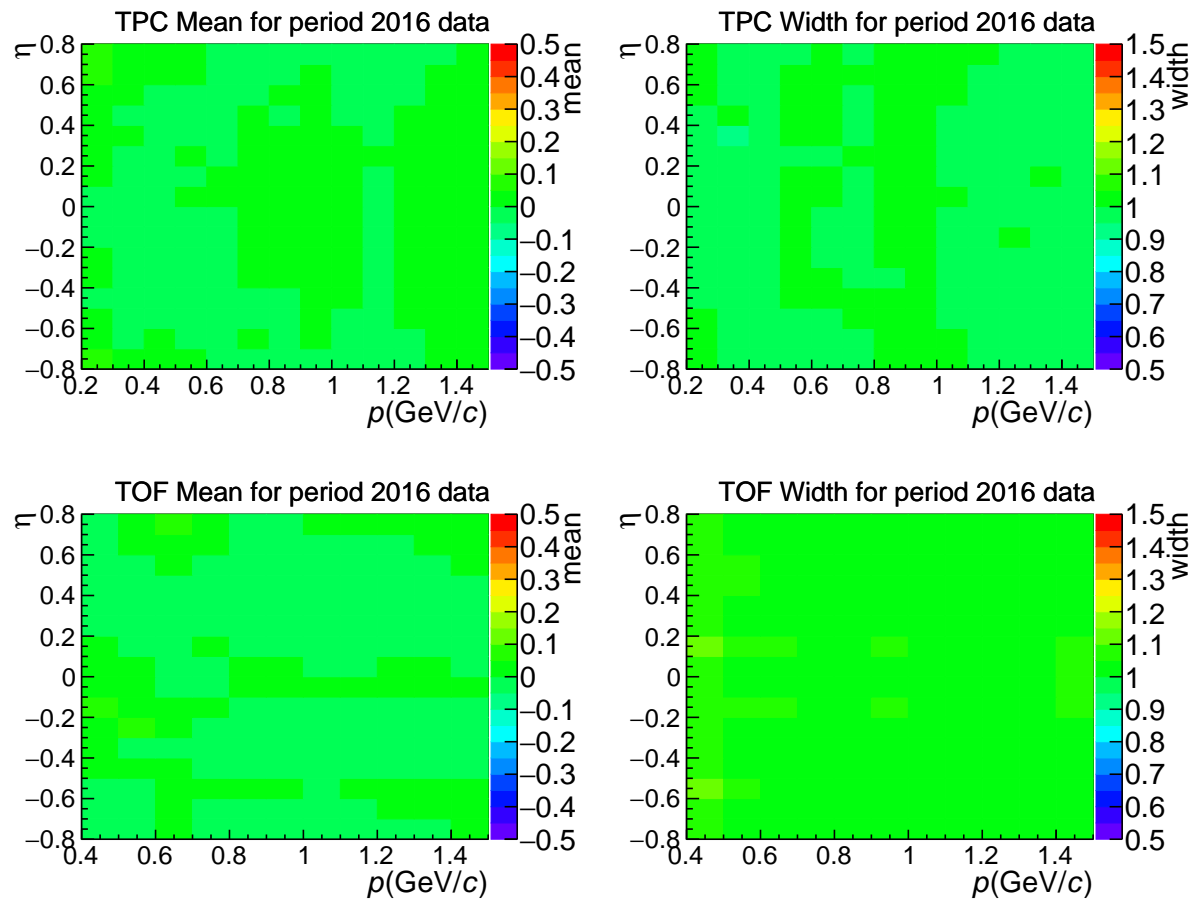


Figure C.13: TPC and TOF electron spectra for 2016 periods after using the re-calibration maps to correct the PID.

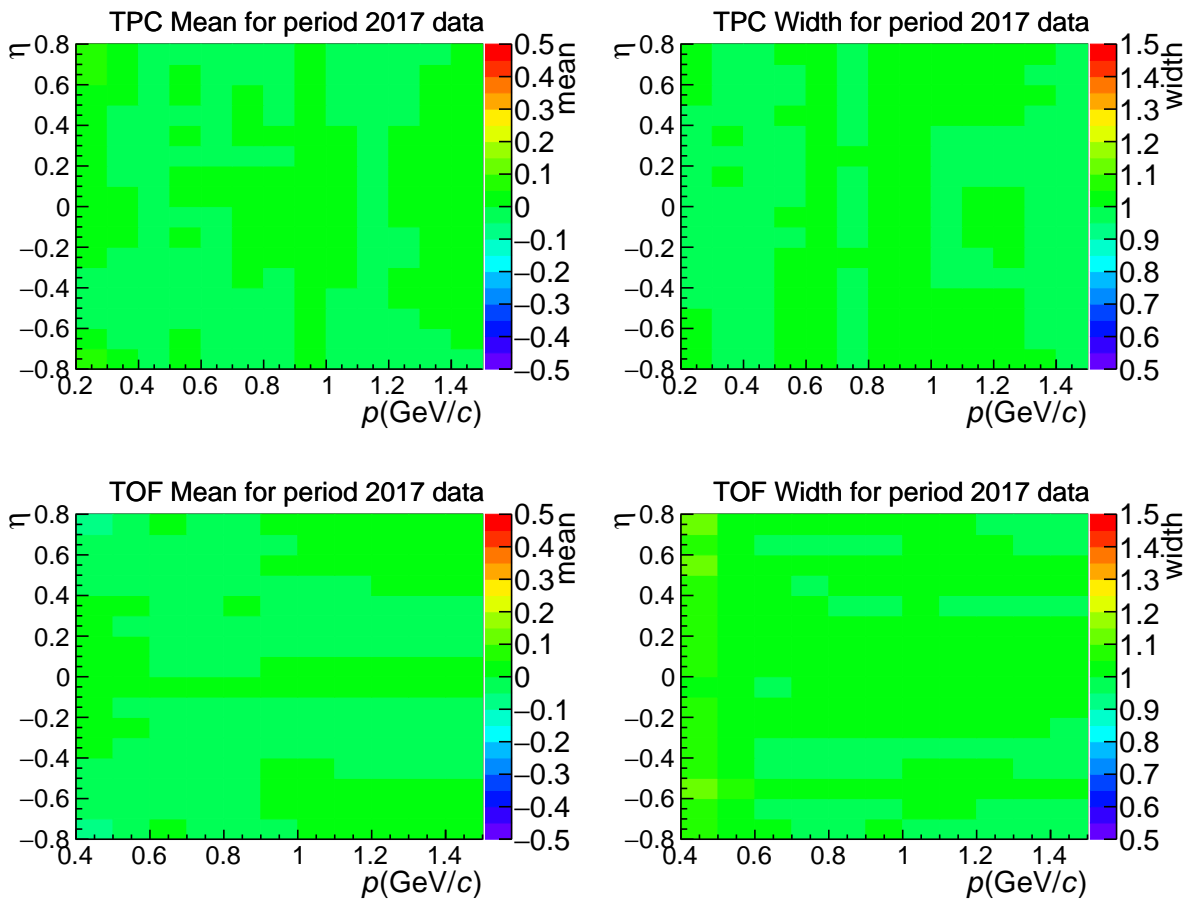


Figure C.14: TPC and TOF electron spectra for 2017 periods after using the re-calibration maps to correct the PID.

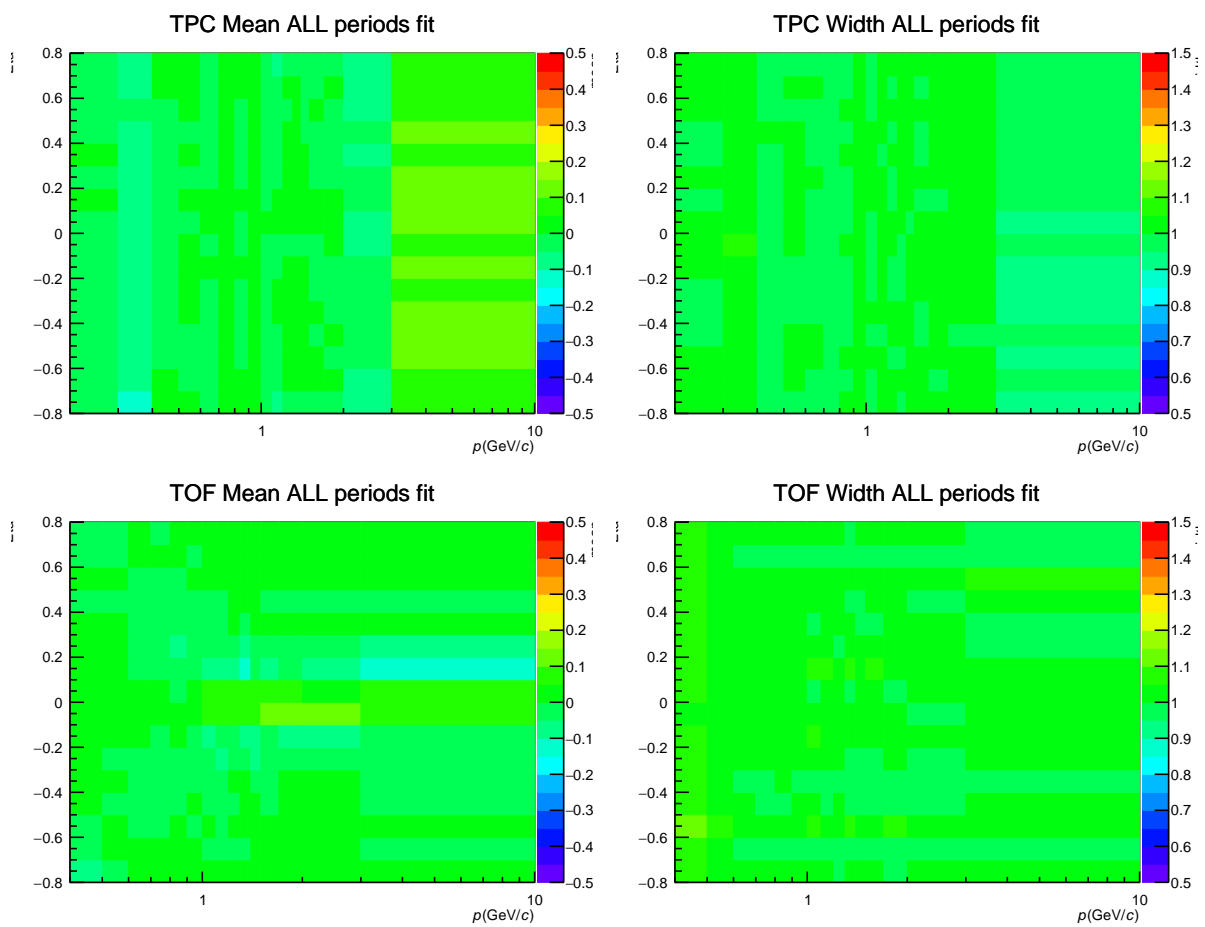


Figure C.15: TPC and TOF electron spectra for 2018 data after using the re-calibration maps to correct the PID.

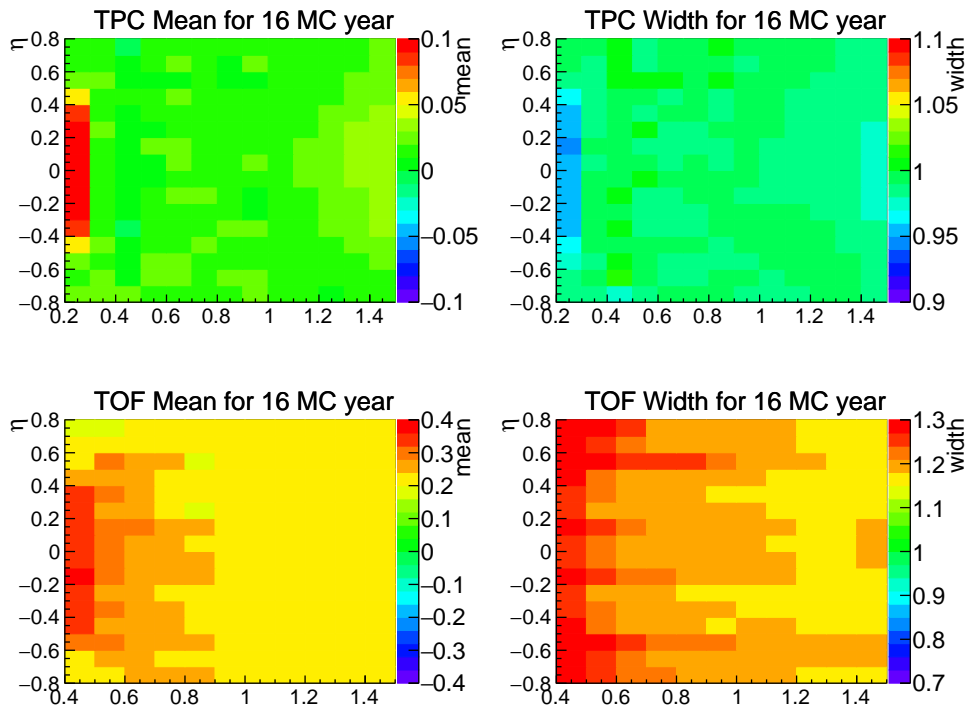


Figure C.16: TPC (top) and TOF (bottom) re-calibration maps for 2016 reconstructed MC data.

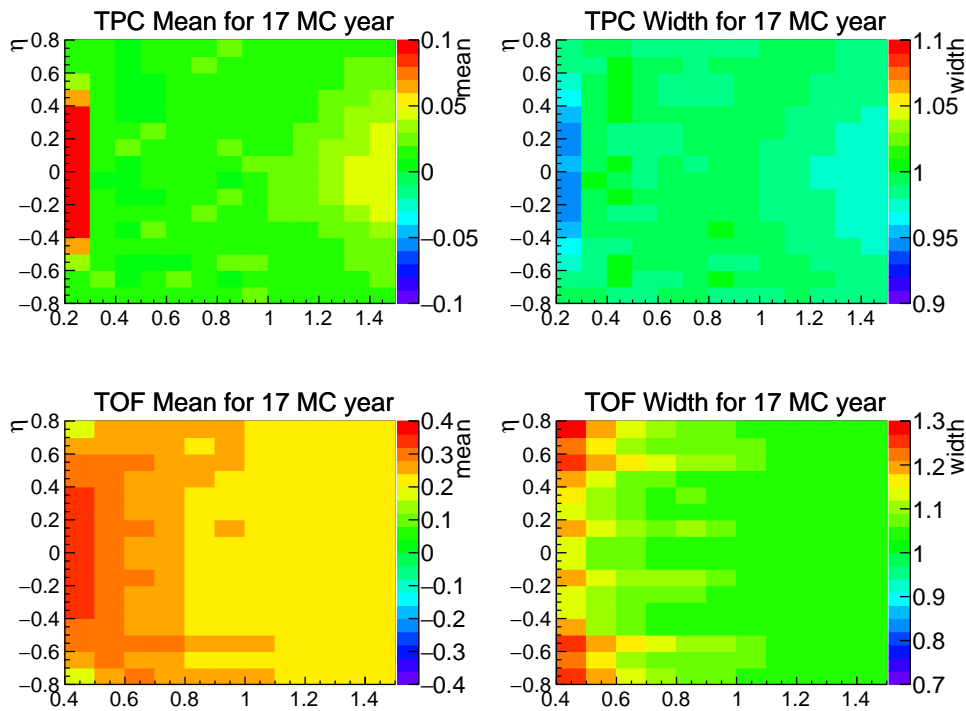


Figure C.17: TPC (top) and TOF (bottom) re-calibration maps for 2017 reconstructed MC data.

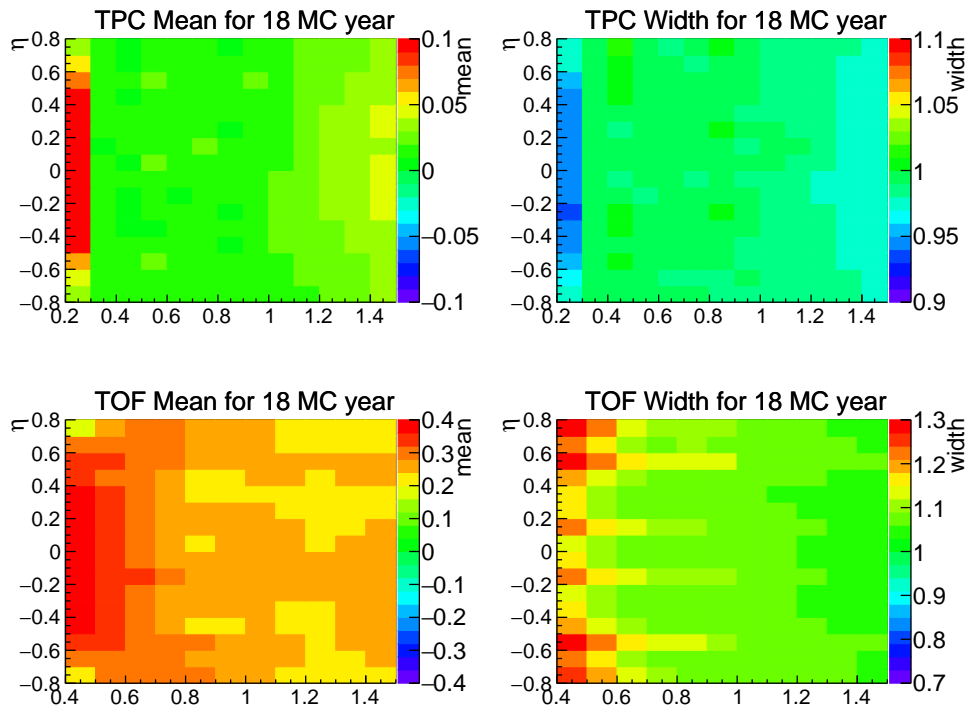


Figure C.18: TPC (top) and TOF (bottom) re-calibration maps for 2018 reconstructed MC data.

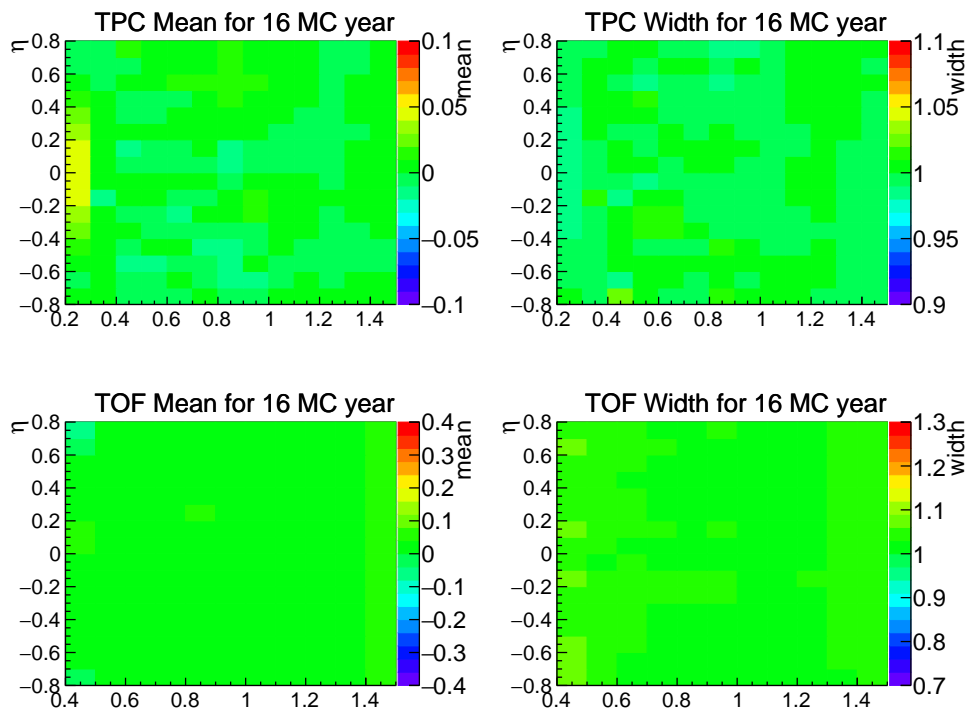


Figure C.19: TPC (top) and TOF (bottom) mean and sigma after PID re-calibration (2016 MC data).



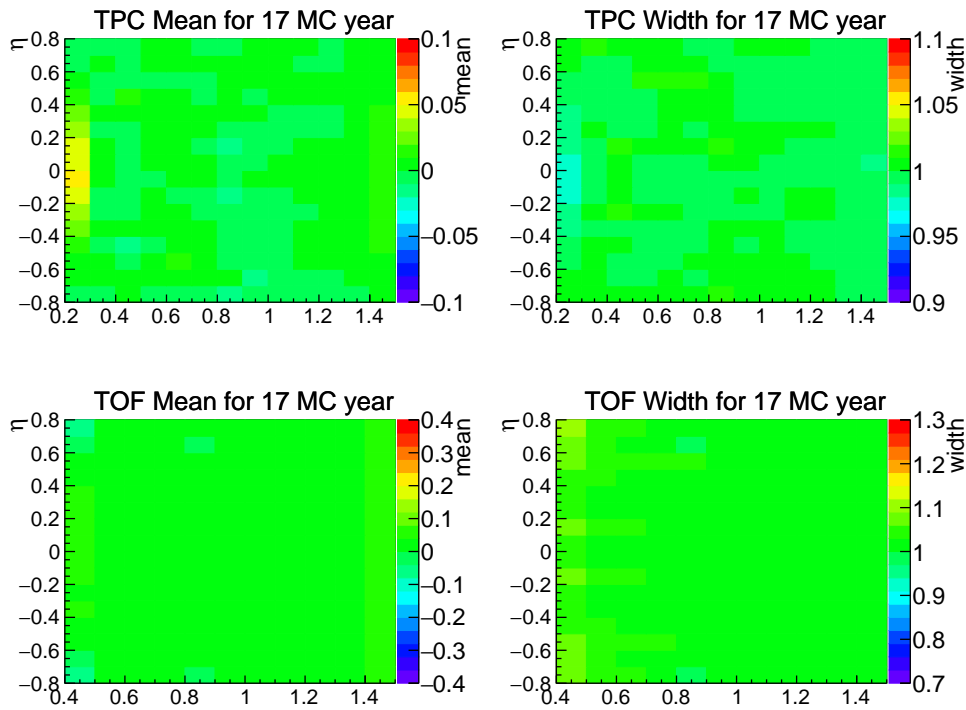


Figure C.20: TPC (top) and TOF (bottom) mean and sigma after PID re-calibration (2017 MC data).

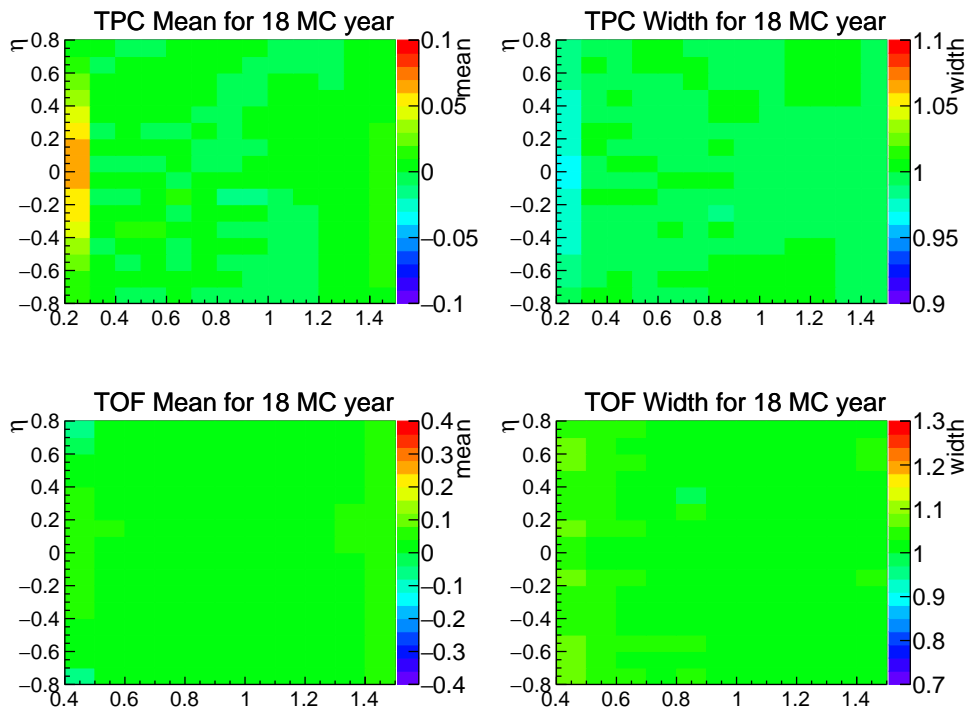


Figure C.21: TPC (top) and TOF (bottom) mean and sigma after PID re-calibration (2018 MC data).



## D $m_{ee}$ Additional Fits

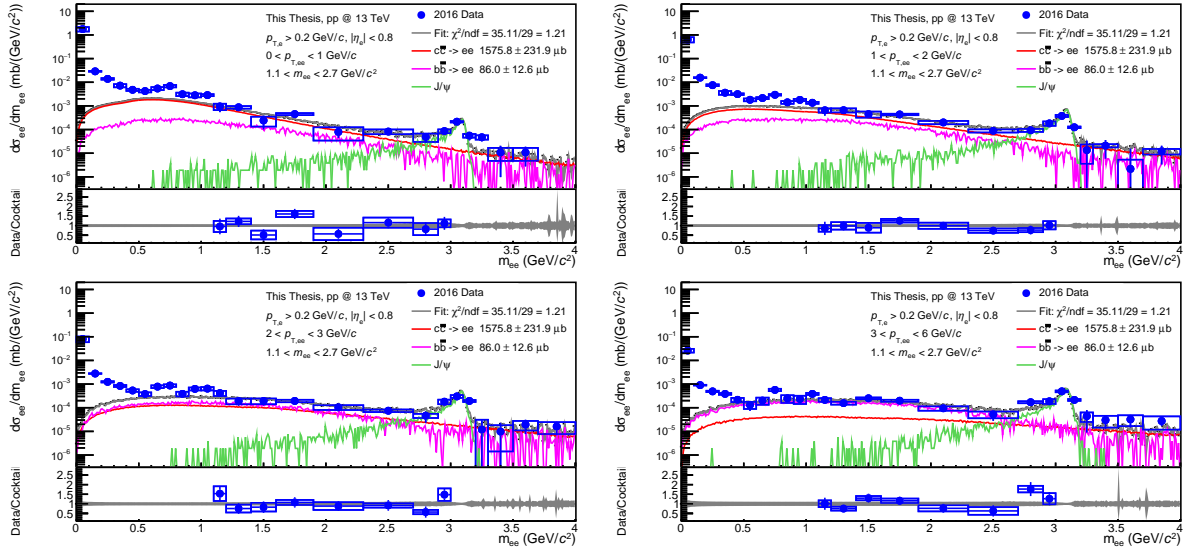


Figure D.1: The dielectron cross section in pp collisions at 13 TeV as a function of invariant mass in different pair momentum intervals is shown in blue circles for the analysis using the minimum  $p_{T,e}$  cut of 0.2 GeV/ $c$ , using 2016 data alone, and the PYTHIA cocktail is shown in red, purple and green for charm, beauty and  $J/\psi$  contributions, respectively. The bar and boxes represent the statistical and systematic uncertainties of the data, while the final cocktail is shown in a grey band. On the bottom of each pair momentum interval plot it is shown the data-to-cocktail ratio.

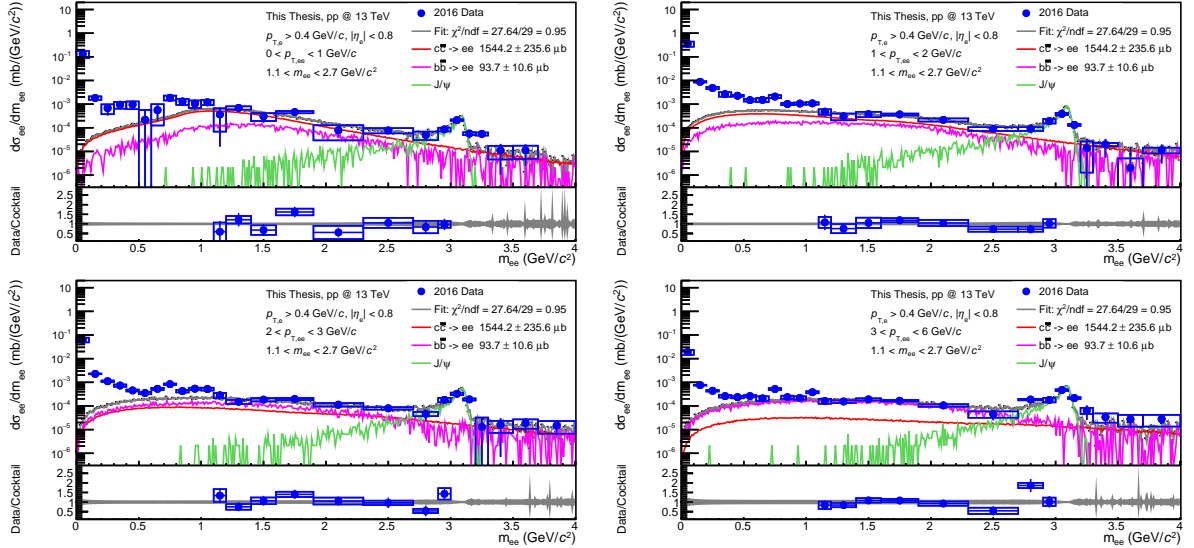


Figure D.2: The dielectron cross section in pp collisions at 13 TeV as a function of invariant mass in different pair momentum intervals is shown in blue circles for the analysis using the minimum  $p_{T,e}$  cut of 0.4 GeV/ $c$ , using 2016 data alone, and the PYTHIA cocktail is shown in red, purple and green for charm, beauty and  $J/\psi$  contributions, respectively. The bar and boxes represent the statistical and systematic uncertainties of the data, while the final cocktail is shown in a grey band. On the bottom of each pair momentum interval plot it is shown the data-to-cocktail ratio.

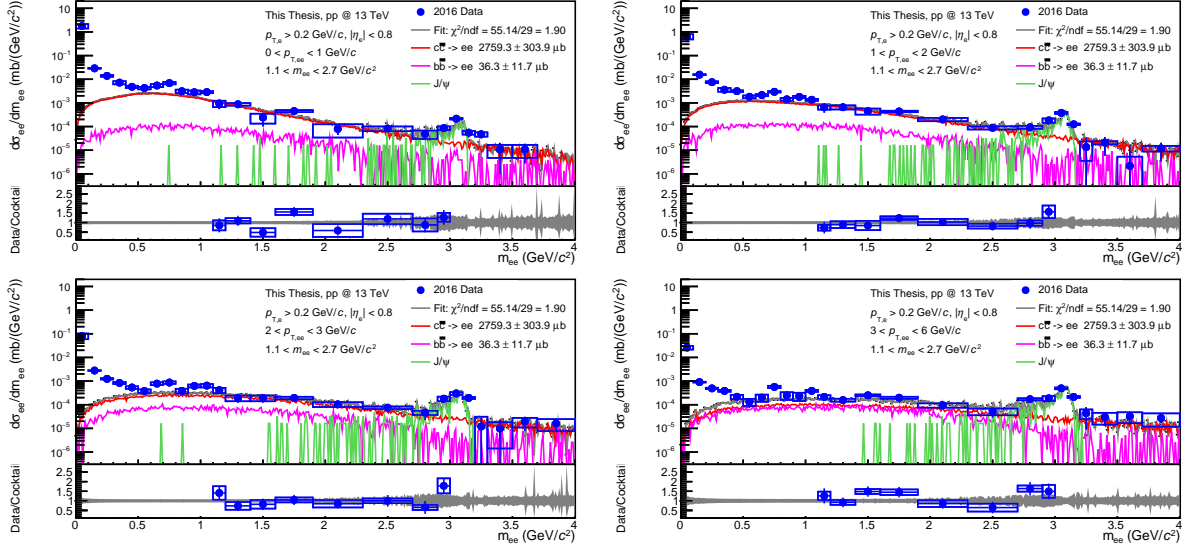


Figure D.3: The dielectron cross section in pp collisions at 13 TeV as a function of invariant mass in different pair momentum intervals is shown in blue circles for the analysis using the minimum  $p_{T,e}$  cut of 0.2 GeV/c, using 2016 data alone, and the POWHEG cocktail is shown in red, purple and green for charm, beauty and  $J/\psi$  contributions, respectively. The bar and boxes represent the statistical and systematic uncertainties of the data, while the final cocktail is shown in a grey band. On the bottom of each pair momentum interval plot it is shown the data-to-cocktail ratio.

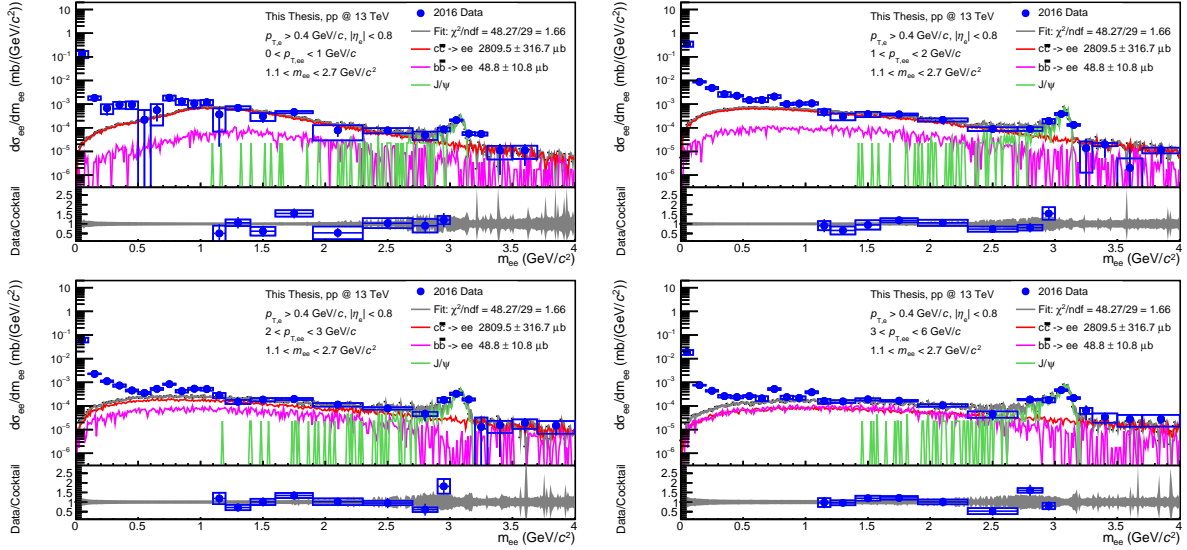


Figure D.4: The dielectron cross section in pp collisions at 13 TeV as a function of invariant mass in different pair momentum intervals is shown in blue circles for the analysis using the minimum  $p_{T,e}$  cut of 0.4 GeV/c, using 2016 data alone, and the POWHEG cocktail is shown in red, purple and green for charm, beauty and  $J/\psi$  contributions, respectively. The bar and boxes represent the statistical and systematic uncertainties of the data, while the final cocktail is shown in a grey band. On the bottom of each pair momentum interval plot it is shown the data-to-cocktail ratio.

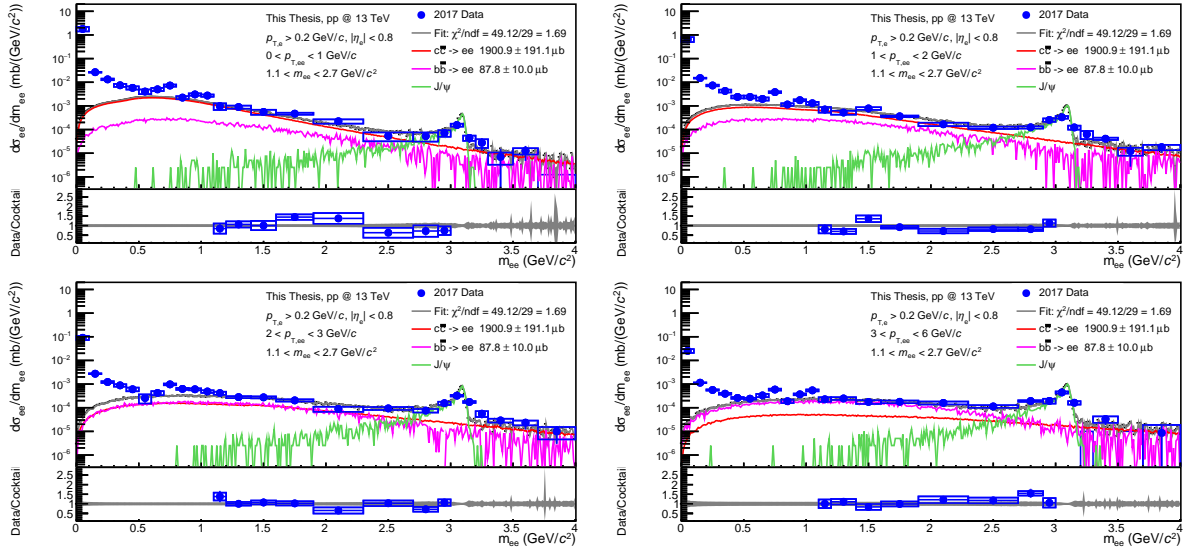


Figure D.5: The dielectron cross section in pp collisions at 13 TeV as a function of invariant mass in different pair momentum intervals is shown in blue circles for the analysis using the minimum  $p_{T,e}$  cut of 0.2 GeV/ $c$ , using 2017 data alone, and the PYTHIA cocktail is shown in red, purple and green for charm, beauty and  $J/\psi$  contributions, respectively. The bar and boxes represent the statistical and systematic uncertainties of the data, while the final cocktail is shown in a grey band. On the bottom of each pair momentum interval plot it is shown the data-to-cocktail ratio.

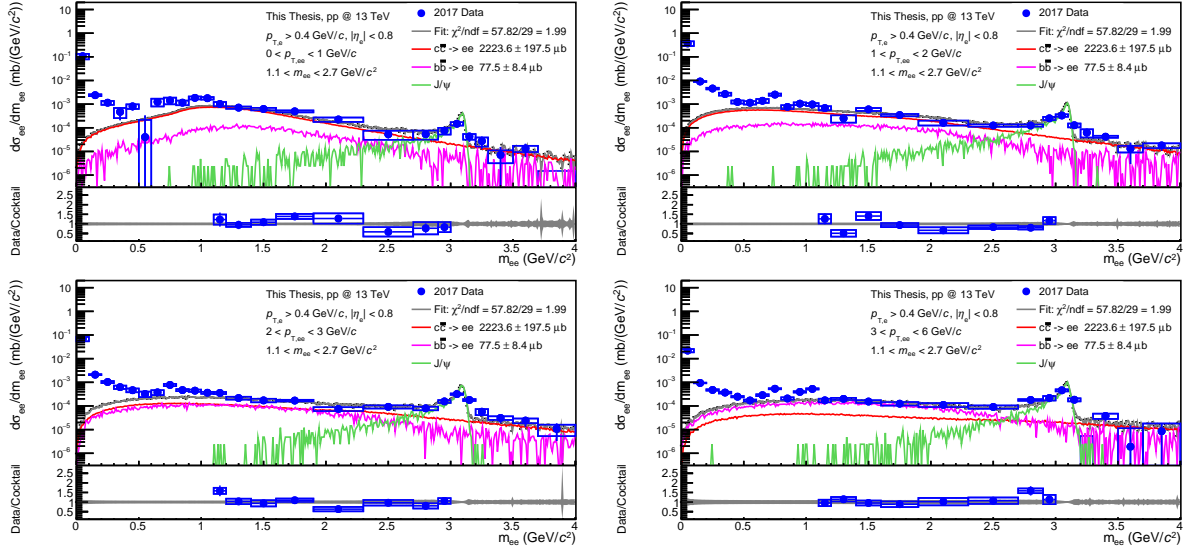


Figure D.6: The dielectron cross section in pp collisions at 13 TeV as a function of invariant mass in different pair momentum intervals is shown in blue circles for the analysis using the minimum  $p_{T,e}$  cut of 0.4 GeV/ $c$ , using 2017 data alone, and the PYTHIA cocktail is shown in red, purple and green for charm, beauty and  $J/\psi$  contributions, respectively. The bar and boxes represent the statistical and systematic uncertainties of the data, while the final cocktail is shown in a grey band. On the bottom of each pair momentum interval plot it is shown the data-to-cocktail ratio.

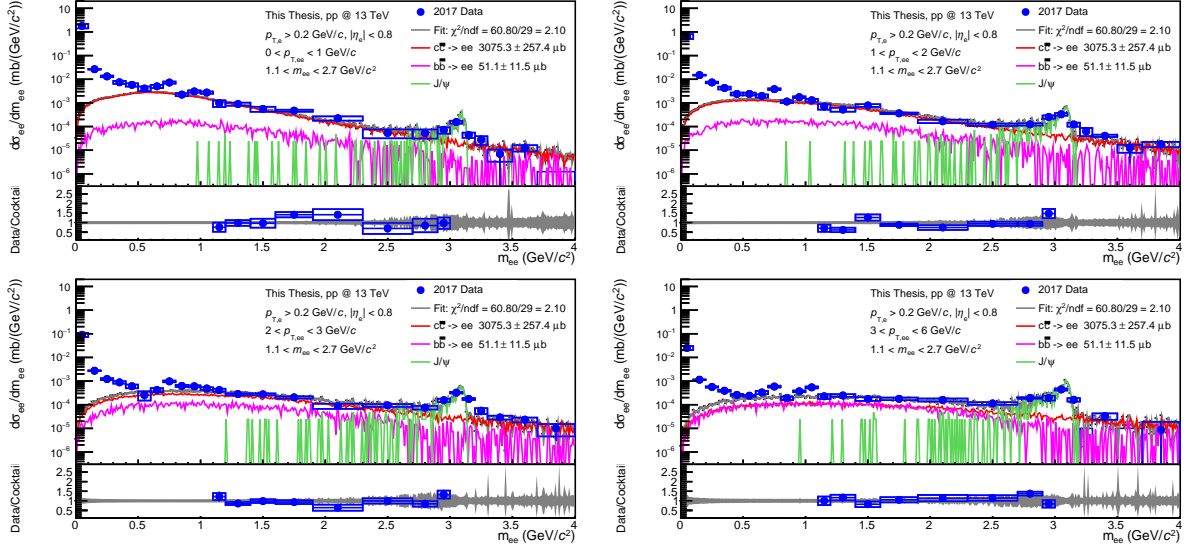


Figure D.7: The dielectron cross section in pp collisions at 13 TeV as a function of invariant mass in different pair momentum intervals is shown in blue circles for the analysis using the minimum  $p_{T,e}$  cut of 0.2 GeV/c, using 2017 data alone, and the POWHEG cocktail is shown in red, purple and green for charm, beauty and  $J/\psi$  contributions, respectively. The bar and boxes represent the statistical and systematic uncertainties of the data, while the final cocktail is shown in a grey band. On the bottom of each pair momentum interval plot it is shown the data-to-cocktail ratio.

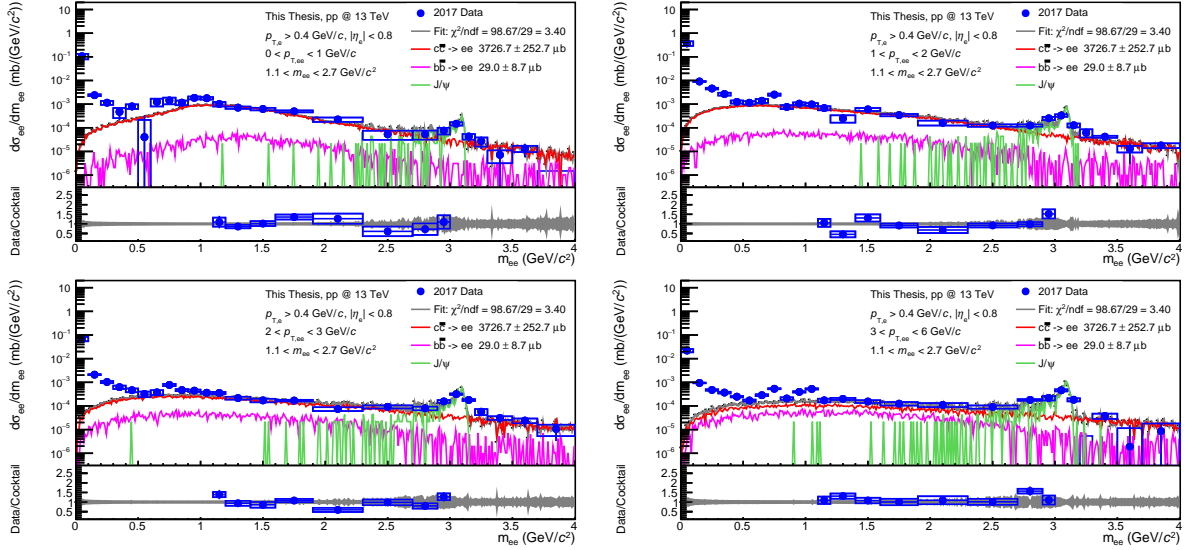


Figure D.8: The dielectron cross section in pp collisions at 13 TeV as a function of invariant mass in different pair momentum intervals is shown in blue circles for the analysis using the minimum  $p_{T,e}$  cut of 0.4 GeV/c, using 2017 data alone, and the POWHEG cocktail is shown in red, purple and green for charm, beauty and  $J/\psi$  contributions, respectively. The bar and boxes represent the statistical and systematic uncertainties of the data, while the final cocktail is shown in a grey band. On the bottom of each pair momentum interval plot it is shown the data-to-cocktail ratio.

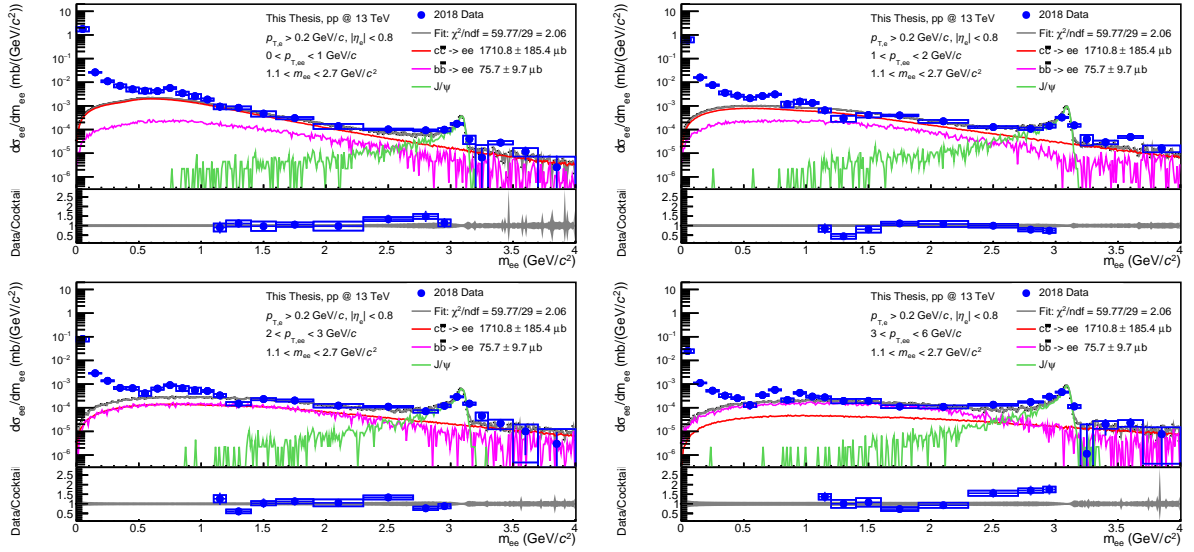


Figure D.9: The dielectron cross section in pp collisions at 13 TeV as a function of invariant mass in different pair momentum intervals is shown in blue circles for the analysis using the minimum  $p_{T,e}$  cut of 0.2 GeV/ $c$ , using 2018 data alone, and the PYTHIA cocktail is shown in red, purple and green for charm, beauty and  $J/\psi$  contributions, respectively. The bar and boxes represent the statistical and systematic uncertainties of the data, while the final cocktail is shown in a grey band. On the bottom of each pair momentum interval plot it is shown the data-to-cocktail ratio.

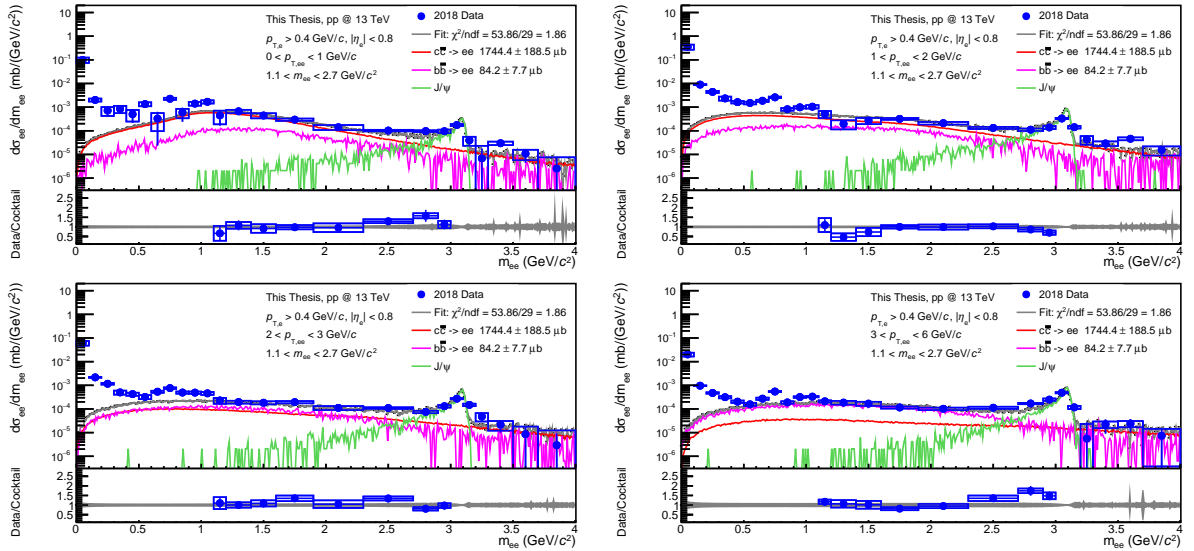


Figure D.10: The dielectron cross section in pp collisions at 13 TeV as a function of invariant mass in different pair momentum intervals is shown in blue circles for the analysis using the minimum  $p_{T,e}$  cut of 0.4 GeV/ $c$ , using 2018 data alone, and the PYTHIA cocktail is shown in red, purple and green for charm, beauty and  $J/\psi$  contributions, respectively. The bar and boxes represent the statistical and systematic uncertainties of the data, while the final cocktail is shown in a grey band. On the bottom of each pair momentum interval plot it is shown the data-to-cocktail ratio.



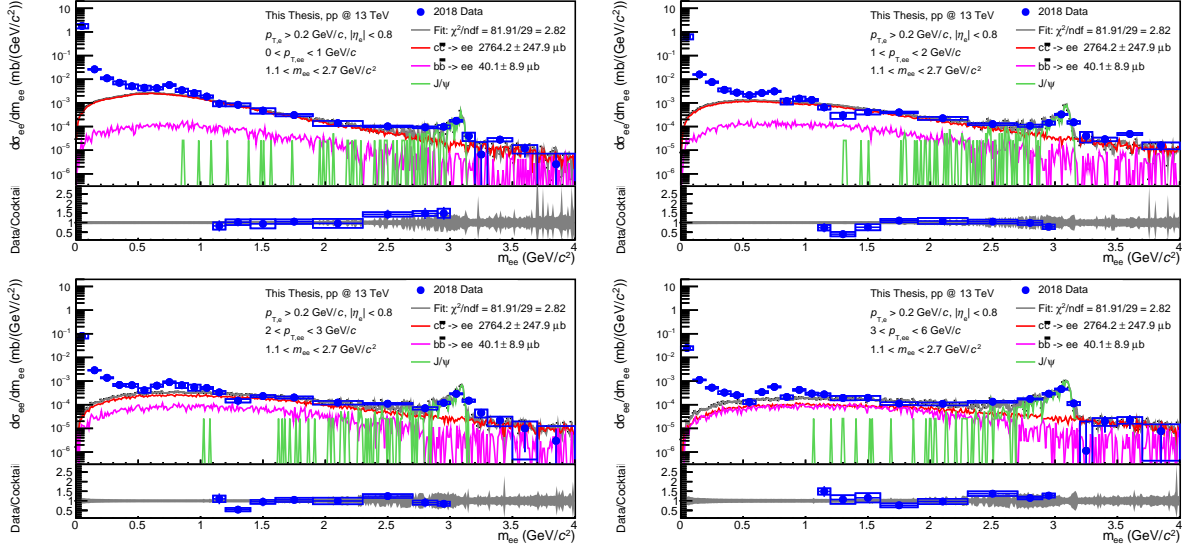


Figure D.11: The dielectron cross section in pp collisions at 13 TeV as a function of invariant mass in different pair momentum intervals is shown in blue circles for the analysis using the minimum  $p_{T,e}$  cut of 0.2 GeV/c, using 2018 data alone, and the POWHEG cocktail is shown in red, purple and green for charm, beauty and  $J/\psi$  contributions, respectively. The bar and boxes represent the statistical and systematic uncertainties of the data, while the final cocktail is shown in a grey band. On the bottom of each pair momentum interval plot it is shown the data-to-cocktail ratio.

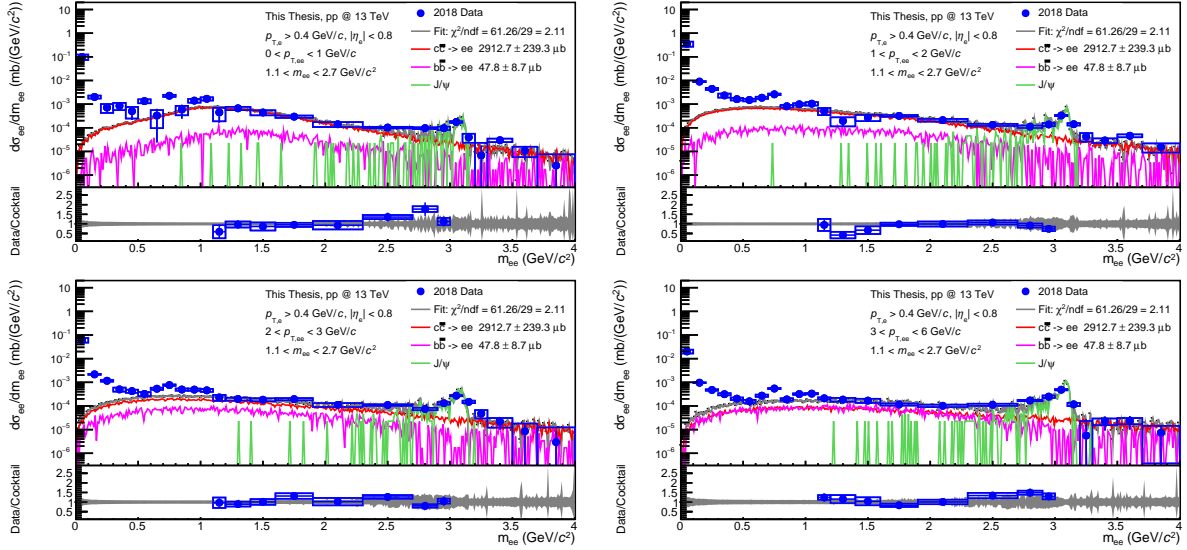


Figure D.12: The dielectron cross section in pp collisions at 13 TeV as a function of invariant mass in different pair momentum intervals is shown in blue circles for the analysis using the minimum  $p_{T,e}$  cut of 0.4 GeV/c, using 2018 data alone, and the POWHEG cocktail is shown in red, purple and green for charm, beauty and  $J/\psi$  contributions, respectively. The bar and boxes represent the statistical and systematic uncertainties of the data, while the final cocktail is shown in a grey band. On the bottom of each pair momentum interval plot it is shown the data-to-cocktail ratio.



## E $DCA_{xy}^{ee}$ Additional Fits

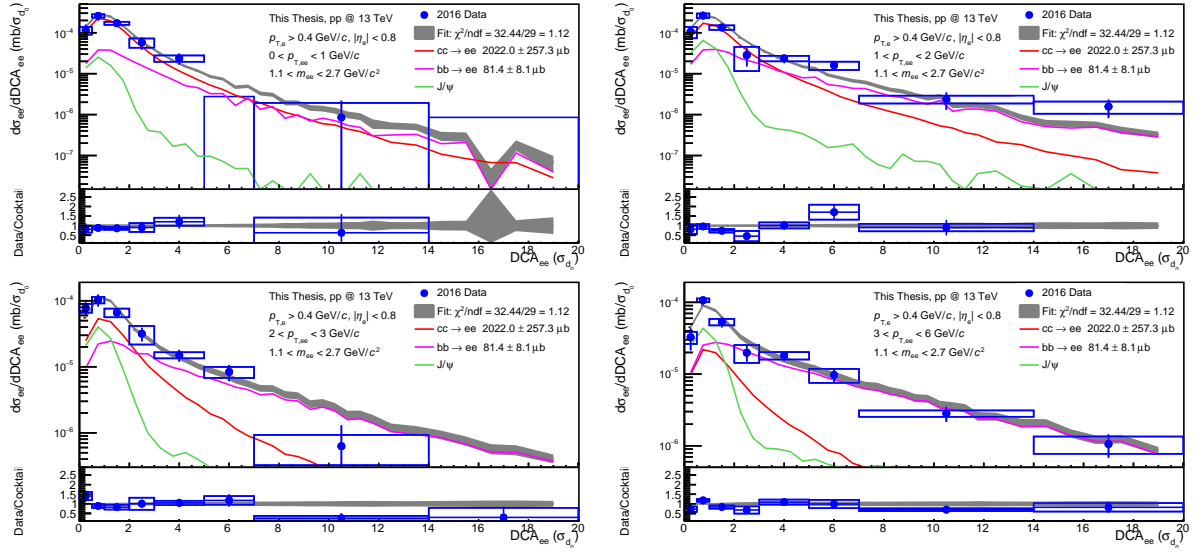


Figure E.1: The dielectron cross section in pp collisions at 13 TeV as a function of impact parameter in different pair momentum intervals is shown in blue circles for the analysis using the minimum  $p_{T,e}$  cut of 0.4 GeV/c, using 2016 data alone, and the PYTHIA cocktail is shown in red, purple and green for charm, beauty and  $J/\psi$  contributions, respectively. The bar and boxes represent the statistical and systematic uncertainties of the data, while the final cocktail is shown in a grey band. On the bottom of each pair momentum interval plot it is shown the data-to-cocktail ratio.

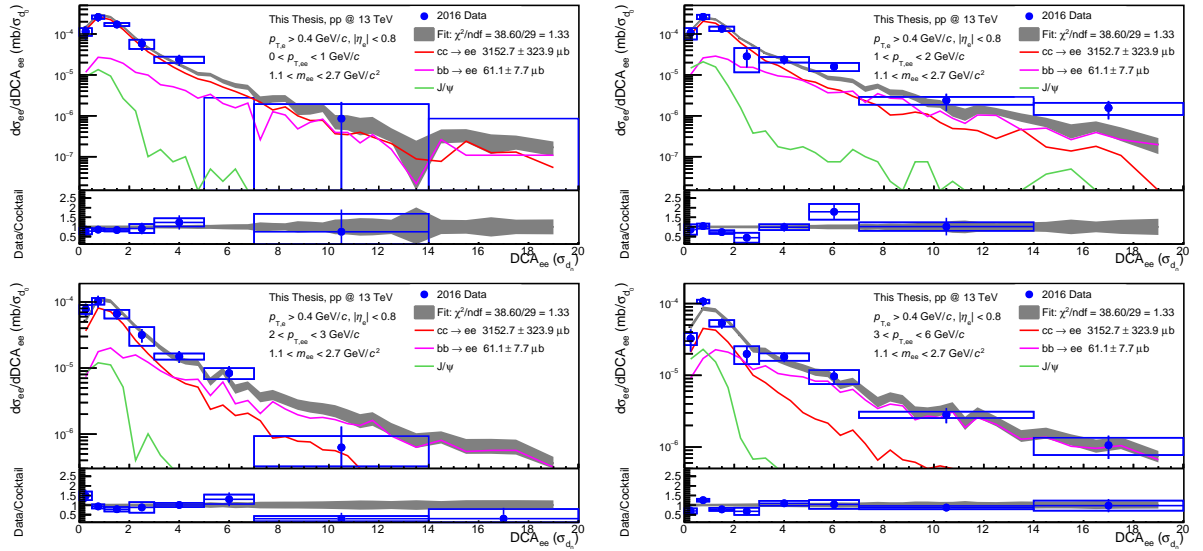


Figure E.2: The dielectron cross section in pp collisions at 13 TeV as a function of impact parameter in different pair momentum intervals is shown in blue circles for the analysis using the minimum  $p_{T,e}$  cut of 0.4 GeV/c, using 2016 data alone, and the POWHEG cocktail is shown in red, purple and green for charm, beauty and  $J/\psi$  contributions, respectively. The bar and boxes represent the statistical and systematic uncertainties of the data, while the final cocktail is shown in a grey band. On the bottom of each pair momentum interval plot it is shown the data-to-cocktail ratio.

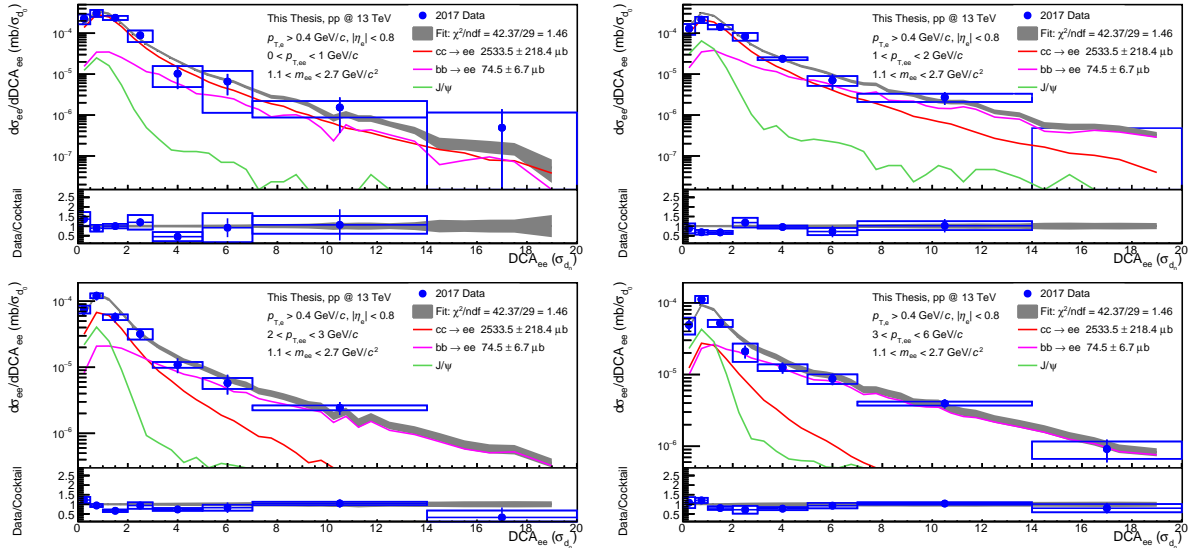


Figure E.3: The dielectron cross section in pp collisions at 13 TeV as a function of impact parameter in different pair momentum intervals is shown in blue circles for the analysis using the minimum  $p_{T,e}$  cut of  $0.4 \text{ GeV}/c$ , using 2017 data alone, and the PYTHIA cocktail is shown in red, purple and green for charm, beauty and  $J/\psi$  contributions, respectively. The bar and boxes represent the statistical and systematic uncertainties of the data, while the final cocktail is shown in a grey band. On the bottom of each pair momentum interval plot it is shown the data-to-cocktail ratio.

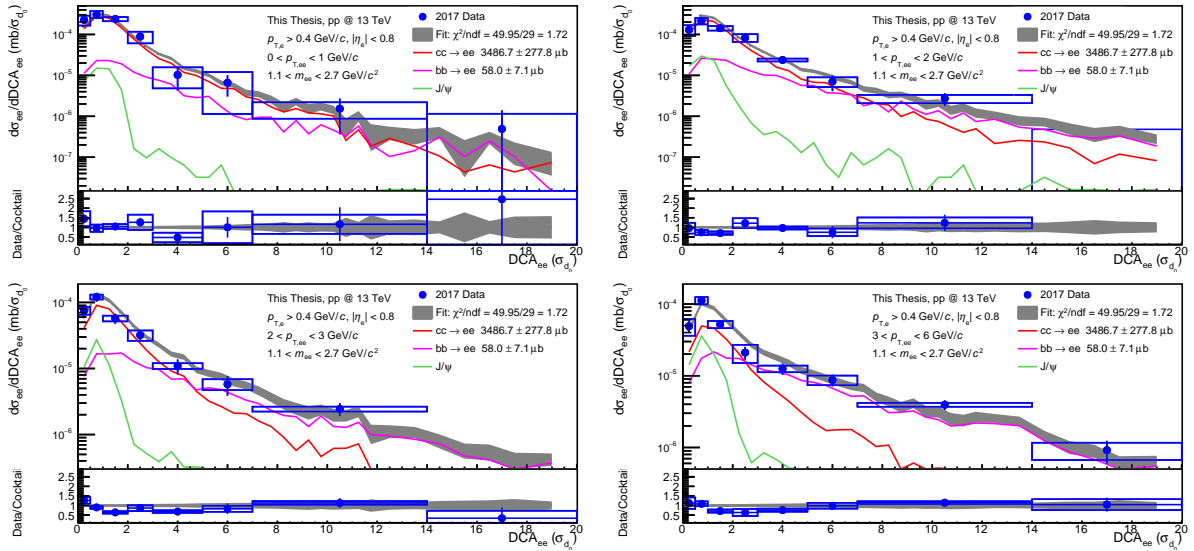


Figure E.4: The dielectron cross section in pp collisions at 13 TeV as a function of impact parameter in different pair momentum intervals is shown in blue circles for the analysis using the minimum  $p_{T,e}$  cut of  $0.4 \text{ GeV}/c$ , using 2017 data alone, and the POWHEG cocktail is shown in red, purple and green for charm, beauty and  $J/\psi$  contributions, respectively. The bar and boxes represent the statistical and systematic uncertainties of the data, while the final cocktail is shown in a grey band. On the bottom of each pair momentum interval plot it is shown the data-to-cocktail ratio.

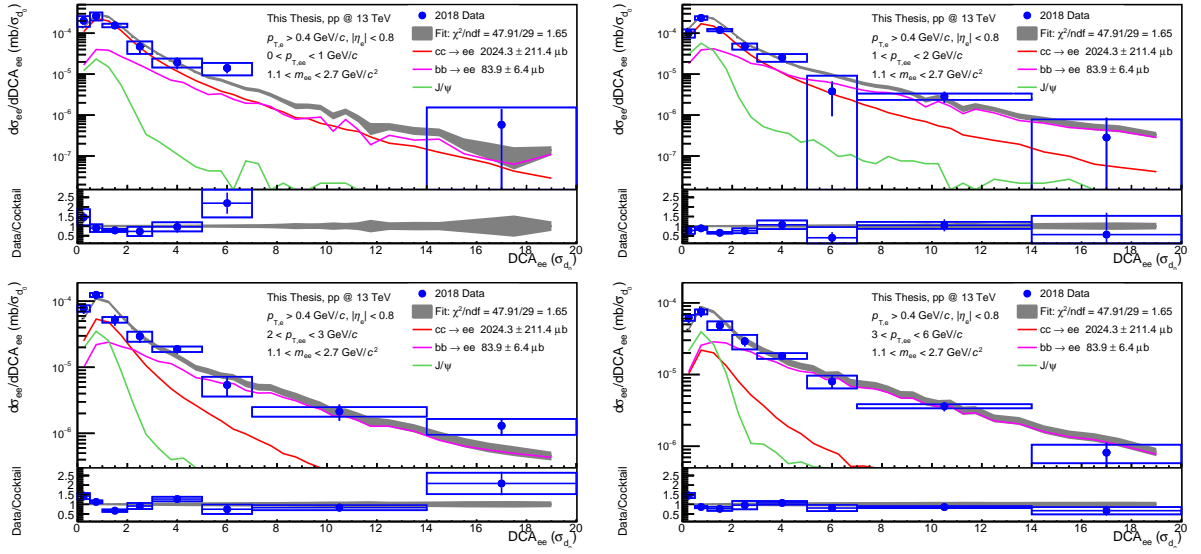


Figure E.5: The dielectron cross section in pp collisions at 13 TeV as a function of impact parameter in different pair momentum intervals is shown in blue circles for the analysis using the minimum  $p_{T,e}$  cut of 0.4 GeV/c, using 2018 data alone, and the PYTHIA cocktail is shown in red, purple and green for charm, beauty and  $J/\psi$  contributions, respectively. The bar and boxes represent the statistical and systematic uncertainties of the data, while the final cocktail is shown in a grey band. On the bottom of each pair momentum interval plot it is shown the data-to-cocktail ratio.

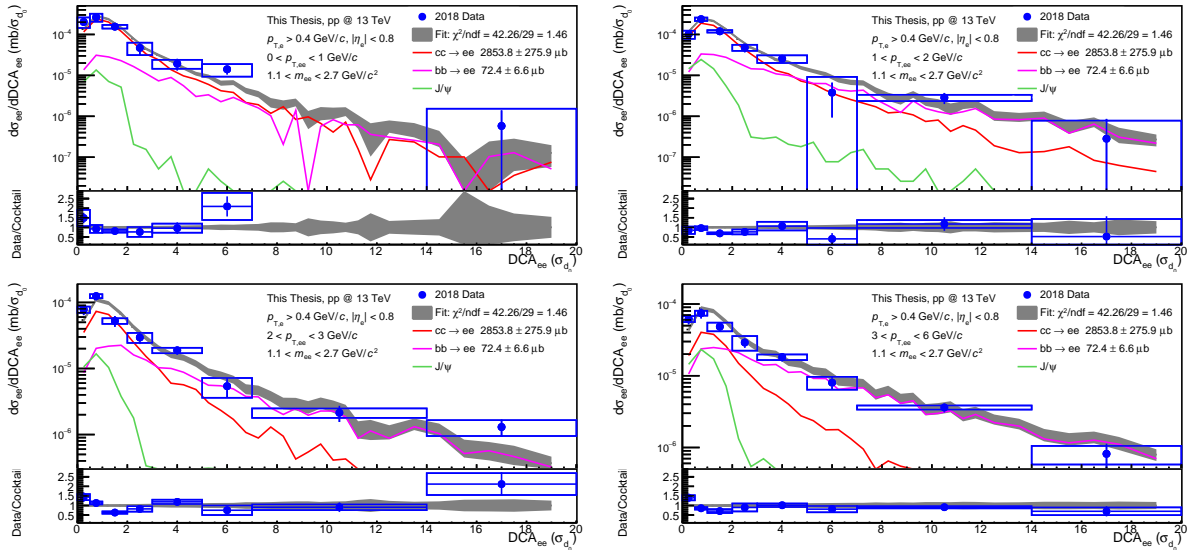


Figure E.6: The dielectron cross section in pp collisions at 13 TeV as a function of impact parameter in different pair momentum intervals is shown in blue circles for the analysis using the minimum  $p_{T,e}$  cut of 0.4 GeV/c, using 2018 data alone, and the POWHEG cocktail is shown in red, purple and green for charm, beauty and  $J/\psi$  contributions, respectively. The bar and boxes represent the statistical and systematic uncertainties of the data, while the final cocktail is shown in a grey band. On the bottom of each pair momentum interval plot it is shown the data-to-cocktail ratio.

## F $\Delta\varphi_{ee}$ Additional Fits

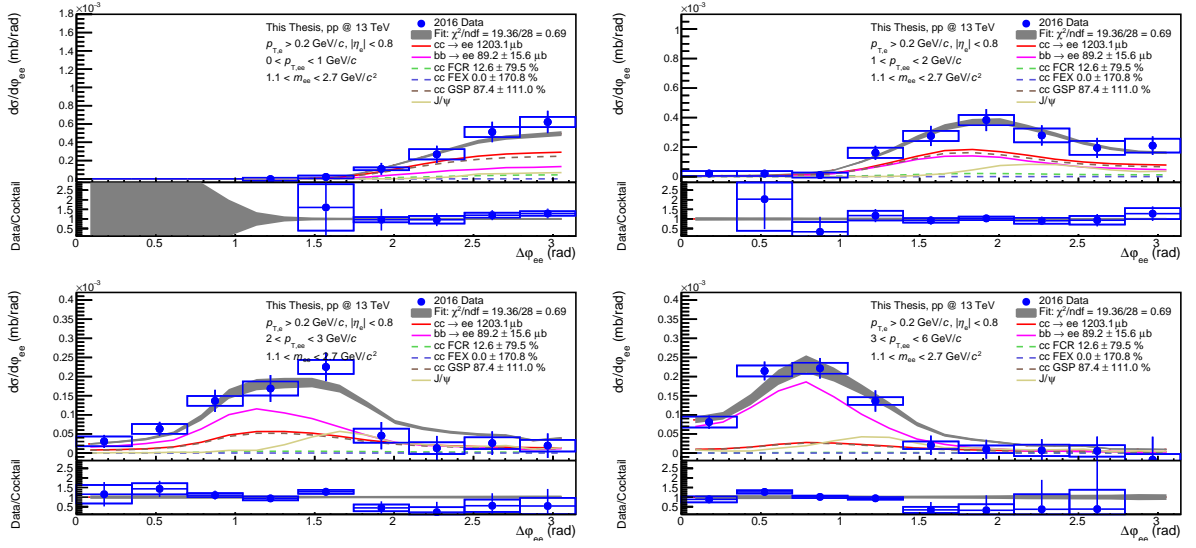


Figure F.1: The dielectron cross section in pp collisions at 13 TeV as a function of  $\Delta\varphi$  in different pair momentum intervals is shown in blue circles for the analysis using the minimum  $p_{T,e}$  cut of 0.2 GeV/c and using 2016 data alone, and the PYTHIA cocktail in red, purple and brown lines for charm, beauty and  $J/\psi$  contributions, respectively, and dashed lines for the different charm production mechanisms fit. The bar and boxes represent the statistical and systematic uncertainties of the data, while the final cocktail is shown in a grey band. On the bottom of each pair momentum interval plot it is shown the data-to-cocktail ratio.

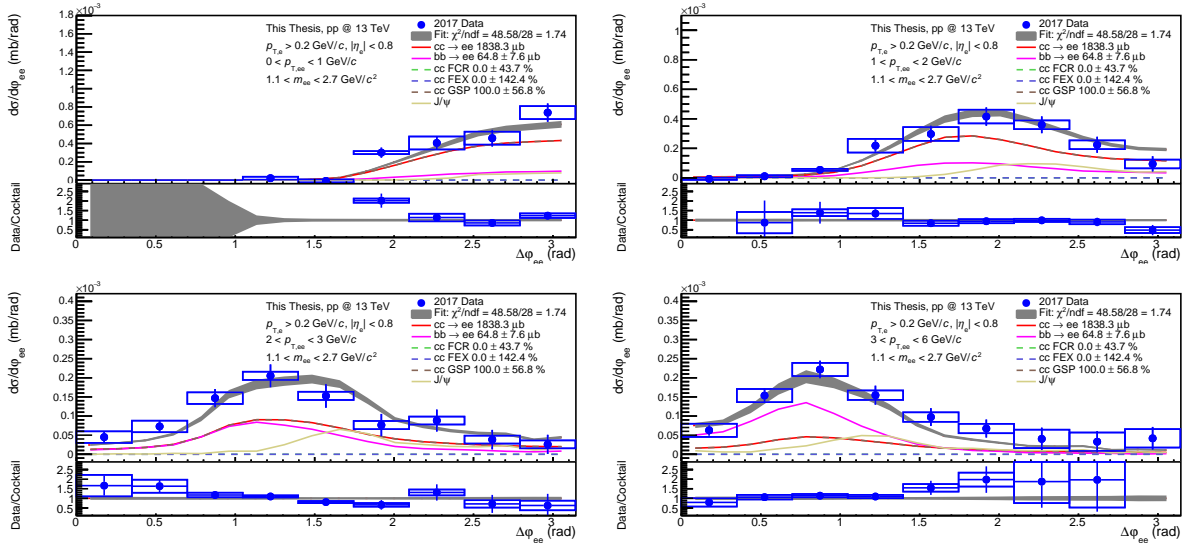


Figure F.2: The dielectron cross section in pp collisions at 13 TeV as a function of  $\Delta\varphi$  in different pair momentum intervals is shown in blue circles for the analysis using the minimum  $p_{T,e}$  cut of 0.2 GeV/c and using 2017 data alone, and the PYTHIA cocktail in red, purple and brown lines for charm, beauty and  $J/\psi$  contributions, respectively, and dashed lines for the different charm production mechanisms fit. The bar and boxes represent the statistical and systematic uncertainties of the data, while the final cocktail is shown in a grey band. On the bottom of each pair momentum interval plot it is shown the data-to-cocktail ratio.



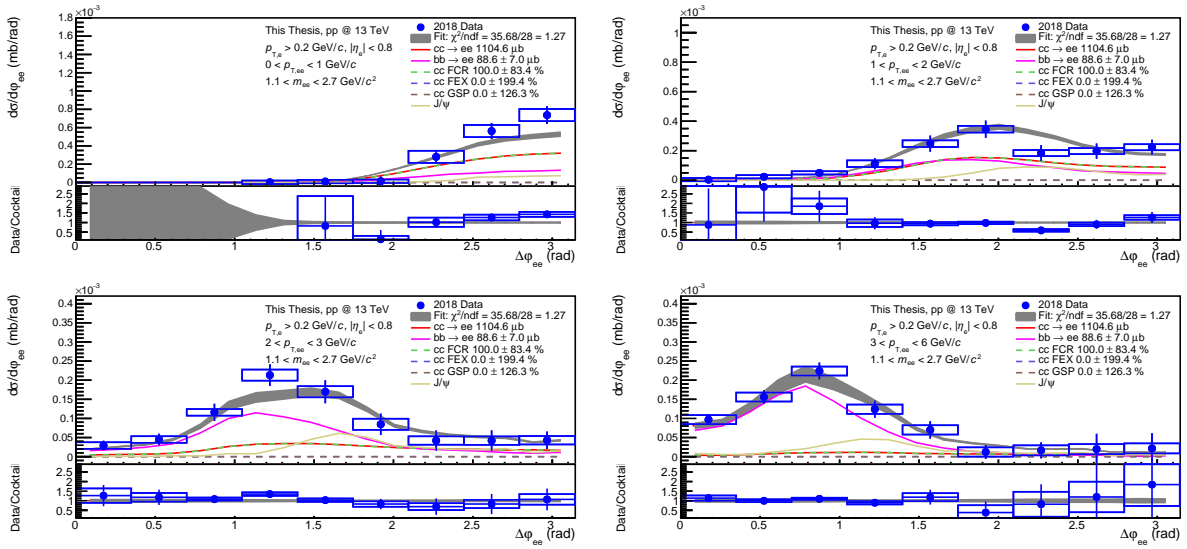


Figure F.3: The dielectron cross section in pp collisions at 13 TeV as a function of  $\Delta\varphi$  in different pair momentum intervals is shown in blue circles for the analysis using the minimum  $p_{T,e}$  cut of 0.2 GeV/c and using 2018 data alone, and the PYTHIA cocktail in red, purple and brown lines for charm, beauty and  $J/\psi$  contributions, respectively, and dashed lines for the different charm production mechanisms fit. The bar and boxes represent the statistical and systematic uncertainties of the data, while the final cocktail is shown in a grey band. On the bottom of each pair momentum interval plot it is shown the data-to-cocktail ratio.



# Bibliography

- [1] T. Muta, *Foundations Of Quantum Chromodynamics: An Introduction to Perturbative Methods in Gauge Theories*. World Scientific Lecture Notes in Physics, World Scientific Publishing Company, 3 ed., 2009.
- [2] M. E. Peskin and D. V. Schroeder, *An Introduction to Quantum Field Theory*. PERSEUS BOOKS, 1995.
- [3] M. Kaku, *Quantum Field Theory*. OXFORD UNIVERSITY PRESS, 1993.
- [4] S. Sarkar, H. Satz, and B. Sinha, *The Physics of the Quark-Gluon Plasma*. 2010.
- [5] G. Chapline and M. Nauenberg, “Asymptotic freedom and the baryon-quark phase transition,” *Physical Review D*, vol. 16, 1977.
- [6] J. C. Collins and M. J. Perry, “Superdense Matter: Neutrons or Asymptotically Free Quarks?,” *Physical Review Letters*, vol. 34, 1975.
- [7] T. D. Lee, “RHIC and QCD: an overview,” *Nuclear Physics A*, vol. 590, pp. 11 – 27, 1995.
- [8] N. P. Samios, “Conceptual design of the Relativistic Heavy Ion Collider: RHIC,” 1986.
- [9] L. Evans and P. Bryant, “LHC machine,” *Journal of Instrumentation*, vol. 3, 2008.
- [10] STAR Collaboration, “Conceptual design report for the Solenoidal Tracker at RHIC,” 1992.
- [11] ALICE Collaboration, “The ALICE experiment at the CERN LHC,” *Journal of Instrumentation*, vol. 3, 2008.
- [12] ALICE Collaboration, “Performance of the ALICE experiment at the CERN LHC,” *International Journal of Modern Physics A*, vol. 29, 2014.
- [13] ALICE Collaboration, “ALICE: Physics Performance Report, Volume I,” *Journal of Physics G*, vol. 30, 2004.
- [14] ALICE Collaboration, “ALICE: Physics Performance Report, Volume II,” *Journal of Physics G*, vol. 32, 2006.
- [15] C. Loizides, “Experimental overview on small collision systems at the lhc,” *Nuclear Physics A*, vol. 956, pp. 200–207, 2016. The XXV International Conference on Ultrarelativistic Nucleus-Nucleus Collisions: Quark Matter 2015.

- [16] The CMS Collaboration, “Evidence for collectivity in pp collisions at the lhc,” *Physics Letters B*, vol. 765, pp. 193–220, 2017.
- [17] J. L. Nagle and W. A. Zajc, “Small system collectivity in relativistic hadronic and nuclear collisions,” *Annual Review of Nuclear and Particle Science*, vol. 68, no. 1, pp. 211–235, 2018.
- [18] The ALICE collaboration, “Dielectron production in proton-proton collisions at  $\sqrt{s}=7$  TeV,” *Journal of High Energy Physics*, vol. 64, 2018.
- [19] ALICE Collaboration, “Dielectron and heavy-quark production in inelastic and high-multiplicity proton–proton collisions at  $\sqrt{s} = 13$  TeV,” *Physics Letters B*, vol. 788, pp. 505 – 518, 2019.
- [20] I. Vorobyev, *Low-mass dielectron production in proton–proton collisions at  $\sqrt{s} = 13$  TeV with ALICE*. PhD thesis, 2018.
- [21] STAR Collaboration, “Experimental and theoretical challenges in the search for the quark-gluon plasma: The STAR Collaboration’s critical assessment of the evidence from RHIC collisions,” *Nuclear Physics A*, vol. 757, pp. 102 – 183, 2005.
- [22] STAR Collaboration, “Disappearance of Back-To-Back High- $p_T$  Hadron Correlations in Central Au + Au Collisions at  $\sqrt{s_{NN}} = 200$  GeV,” *Physical Review Letters*, vol. 90, 2003.
- [23] STAR Collaboration, “Evidence from d + Au Measurements for Final-State Suppression of High- $p_T$  Hadrons in Au + Au Collisions at RHIC,” *Physical Review Letters*, vol. 90, 2003.
- [24] DELPHI Collaboration, “Two-Particle Angular Correlations in  $e^+e^-$  Interactions compared with QCD Predictions,” *Physics Letters B (CERN-EP/98/138)*, 1998.
- [25] B. Alver et al., “Cluster properties from two-particle angular correlations in p+p collisions at  $\sqrt{s} = 200$  and 410 GeV,” *Physical Review C* 75, 054913, 2007.
- [26] The CMS Collaboration, “Observation of long-range, near-side angular correlations in proton-proton collisions at the LHC,” *Journal of High Energy Physics*, 09 091, 2010.
- [27] B. Alver et al., “System size dependence of cluster properties from two-particle angular correlations in Cu + Cu and Au + Au collisions at  $\sqrt{s_{NN}} = 200$  GeV,” *Physical Review C* 81, 024904, 2010.
- [28] The ALICE Collaboration, “Harmonic decomposition of two particle angular correlations in Pb–Pb collisions at  $\sqrt{s_{NN}} = 2.76$  TeV,” *Physics Letters B* 708 249–264, 2012.
- [29] The CMS Collaboration, “Measurement of Long-Range Near-Side Two-Particle Angular Correlations in pp Collisions at  $\sqrt{s} = 13$  TeV,” *Physical Review Letters* 116, 172302, 2016.
- [30] X. Lin, *Non-Photonic Electron Angular Correlations with Charged Hadrons from the STAR Experiment: First Measurement of Bottom Contribution to Non-Photonic Electrons at RHIC*. PhD thesis, 2007.

- 
- [31] E. Filho, *Study of the angular correlation between heavy-flavour decay electrons and charged unidentified particles in pp and p-Pb collisions with ALICE*. PhD thesis, 2014.
- [32] D. Thomas, *Jet-like heavy-flavour particle correlations in proton-proton and lead-lead collisions in ALICE*. PhD thesis, 2014.
- [33] H. Zanolì, *Azimuthal anisotropy of electrons from heavy quarks in p-Pb collisions with ALICE*. PhD thesis, 2018.
- [34] Sandro Bjelogrić (for the ALICE Collaboration), “Heavy-flavour correlations in pp, p–Pb and Pb–Pb collisions,” *Nuclear Physics A*, vol. 931, p. 563–568, 2014.
- [35] K. GOTTFRIED and J. D. JACKSON, “On the Connection between Production Mechanism and Decay of Resonances at High Energies,” *IL NUOVO CIMENTO*, 1964.
- [36] R. BLUTNER et al., “Inclusive two-particle correlations in 40 GeV/c n-p collisions and particle production mechanisms,” *Nuclear Physics B*, 78 333–344, 1974.
- [37] Y. Miake et al., “Production mechanism of backward energetic protons studied from two-particle correlations in 800 MeV proton-nucleus collisions,” *Physical Review C*, 31, 6, 1985.
- [38] M. A. Janik, “Studying the mechanisms of particle production using the angular correlations,” *Proc. of SPIE Vol. 10031*, 2016.
- [39] The ALICE Collaboration, “Insight into particle production mechanisms via angular correlations of identified particles in pp collisions at  $\sqrt{s} = 7$  TeV,” *European Physical Journal C* 77, 569, 2017.
- [40] M. A. Janik, “Exploration of particle production mechanisms via angular correlations of  $\pi$ , K, p,  $\Lambda$  with ALICE in pp collisions at  $\sqrt{s} = 7$  TeV,” *EPJ Web of Conferences* 171, 19003, 2018.
- [41] M. A. Janik, “Studying baryon production using two-particle angular correlations,” *EPJ Web of Conferences* 235, 01004, 2020.
- [42] B.Andersson, H.U.Bengtsson, G.Gustafson, “Charm Production and the Confining Force Field,” *LU TP 83-4*, 1983.
- [43] B.Andersson, H.U.Bengtsson, G.Gustafson, “Asymmetries between the production of  $D^+$  and  $D^-$  mesons from 500 GeV/c  $\pi^-$ -nucleus interactions as a function of  $X_F$  and  $p_t^2$ ,” *Physics Letters B* 371 157–162, 1996.
- [44] E. Norrbin, T. Sjostrand, “Production mechanisms of charm hadrons in the string model,” *Physics Letters B* 442, 407–416, 1998.
- [45] E. Norrbin, T. Sjostrand, “Production and hadronization of heavy quarks,” *European Physical Journal C* 17, 137–161, 2000.
- [46] DØ Collaboration, “The  $b\bar{b}$  production cross section and angular correlations in  $p\bar{p}$  collisions at  $\sqrt{s} = 1.8$  TeV,” *Physics Letters B* 487, 264–272, 2000.

- [47] A. Dashi, “Constraining heavy flavour production with dielectrons in pp collisions at  $\sqrt{s} = 13$  TeV,” Master’s thesis, April, 2018.
- [48] K. Garner, “Separation of Heavy-Flavour Production Mechanisms via Two-Particle Angular Correlations in pp Collisions at  $\sqrt{s} = 2.76$  TeV,” Master’s thesis, 2017.
- [49] F. Halzen and A. D. Martin, *Quarks and Leptons: An Introductory Course in Modern Particle Physics*. John Wiley & Sons, 1984.
- [50] D. Griffiths, *Introduction to Elementary Particles*. John Wiley & Sons, 1987.
- [51] A. Chodos, R. L. Jaffe, K. Johnson, and C. B. Thorn, “Baryon structure in the bag theory,” *Physical Review D*, vol. 10, pp. 2599–2604, Oct 1974.
- [52] A. Chodos, R. L. Jaffe, K. Johnson, C. B. Thorn, and V. F. Weisskopf, “New extended model of hadrons,” *Physical Review D*, vol. 9, pp. 3471–3495, Jun 1974.
- [53] A. Bazavov, T. Bhattacharya, C. DeTar, *et al.*, “Equation of state in (2 + 1)-flavor QCD,” *Physical Review D*, vol. 90, Nov 2014.
- [54] B. S. Sourav Sarkar, Helmut Satz, *The Physics of the Quark-Gluon Plasma*. Lecture Notes in Physics 785, 2010.
- [55] A. Dainese, “Lectures on Heavy Ions,” *CERN-Fermilab HCP Summer School (2013) Part 1/3*: <http://indico.cern.ch/event/226365/contribution/23/material/slides/0.pdf>  
*Part 2/3*: <http://indico.cern.ch/event/226365/contribution/24/material/slides/0.pdf>  
*Part 3/3*: <http://indico.cern.ch/event/226365/contribution/25/material/slides/0.pdf>
- [56] F. Gelis, E. Iancu, J. Jalilian-Marian, and R. Venugopalan, “The Color Glass Condensate,” *Annual Review of Nuclear and Particle Science*, volume 60, 2010.
- [57] A. Dainese, *Charm production and in-medium QCD energy loss in nucleus-nucleus collisions with ALICE. A performance study*. PhD thesis, 2003.
- [58] M. Cacciari, M. Greco, and P. Nason, “The  $p_T$  spectrum in heavy-flavour hadroproduction,” *Journal of High Energy Physics*, vol. 1998, no. 05, p. 007, 1998.
- [59] M. Cacciari, S. Frixione, N. Houdeau, *et al.*, “Theoretical predictions for charm and bottom production at the LHC,” *Journal of High Energy Physics*, vol. 10, p. 137, 2012, 1205.6344.
- [60] J. J. Aubert *et al.*, “Experimental Observation of a Heavy Particle J,” *Physical Review Letters* 33, 1404, 1974.
- [61] J. E. Augustin *et al.*, “Discovery of a Narrow Resonance in  $e^+e^-$  Annihilation,” *Physical Review Letters* 33, 1406, 1974.
- [62] G. S. Abrams *et al.*, “Discovery of a Second Narrow Resonance in  $e^+e^-$  Annihilation,” *Physical Review Letters* 33, 1453, 1974.
- [63] S. W. Herb *et al.*, “Observation of a dimuon resonance at 9.5-GeV in 400-GeV proton-nucleus collisions,” *Physical Review Letters* 39, 252, 1977.

- 
- [64] S. P. K. Tavernier, “Charmed and bottom flavoured particle production in hadronic interactions,” *Reports on Progress in Physics*, Vol 50, 1439, 1987.
- [65] The ALICE Collaboration, “Measurement of D-meson production at mid-rapidity in pp collisions at  $\sqrt{s} = 7$  TeV,” *The European Physical Journal C*, volume 77, 2017.
- [66] ALICE, “Charm-quark fragmentation fractions and production cross section at midrapidity in pp collisions at the LHC,” 2021, arXiv:2105.06335.
- [67] C. Amsler et al, “Review of Particle Physics,” *Physics Letters B*, vol. 667, pp. 1–6, 9 2008.
- [68] S. D. Drell and T.-M. Yan, “Massive Lepton Pair Production in Hadron-Hadron Collisions at High-Energies,” *Physical Review Letters*, 25, 1970.
- [69] CMS Collaboration, “Measurement of the Drell-Yan Cross Section in pp Collisions at  $\sqrt{s} = 7$  TeV,” *Journal of High Energy Physics*, 10, 2011.
- [70] CMS Collaboration, “Measurements of differential and double-differential Drell-Yan cross sections in proton-proton collisions at 8 TeV,” *European Physical Journal C*, 75, 2015.
- [71] The ALICE collaboration, “Dielectron production in proton-proton and proton-lead collisions at  $\sqrt{s_{NN}} = 5.02$  TeV,” *Physical Review C* 102, 055204, 2020.
- [72] R. Voss and A. Breskin, eds., *The CERN Large Hadron Collider, accelerator and experiments*, vol. 1. 2009.
- [73] R. Voss and A. Breskin, eds., *The CERN Large Hadron Collider, accelerator and experiments*, vol. 2. 2009.
- [74] ALICE Collaboration, “The Current Inner Tracking System of ALICE.” [http://alicematters.web.cern.ch/?q=ALICE\\_currentITS](http://alicematters.web.cern.ch/?q=ALICE_currentITS).
- [75] C. Grupen and B. Shwartz, *Particle Detectors*. Cambridge University Press, 2 ed., 2008.
- [76] G. F. Knoll, *Radiation Detection and Measurement*. John Wiley & Sons, Inc, 3 ed., 2009.
- [77] W. R. Leo, *Techniques for Nuclear and Particle Physics Experiments*. Springer-Verlag, 1987.
- [78] W. R. W. Blum and L. Rolandi, *Particle Detection with Drift Chambers*. Springer-Verlag, 2008.
- [79] B. A. Heß, *Particle Identification in Jets and High-Multiplicity pp Events with the ALICE TPC*. PhD thesis, 2015.
- [80] B. Lasiuk and T. Ullrich, “Star C++ Class Library - User Guide and Reference Manual,” 2001.
- [81] T. Sjöstrand, S. Mrenna and P. Skands, “PYTHIA 6.4 Physics and Manual,” *Journal of High Energy Physics*, 05, vol. 026, 2006.

- [82] S. Frixione, P. Nason and C. Oleari, “Matching NLO QCD computations with Parton Showers simulations: the POWHEG method,” *Journal of High Energy Physics*, vol. 0711, 2007.
- [83] J.-P. Guillaud, *PYTHIA miniguide*. Laboratoire d’Annecy-le-Vieux de Physique des Particules, 2000.
- [84] S. Scheid, “Separating prompt and non-prompt dielectrons in pp collisions at  $\sqrt{s} = 7$  TeV with ALICE at the LHC,” Master’s thesis, 2016.
- [85] L. Layer, “Development of a fast simulation tool for vertexing studies in ALICE,” 2015.
- [86] P.A. Zyla et al. (Particle Data Group) *Prog. Theor. Exp. Phys.* 2020, 083C01, 2020.
- [87] B. Abelev, N. Arbor, G. Balbastre, *et al.*, “Upgrade of the ALICE Experiment: Letter Of Intent,” 01 2014.
- [88] W. H. Trzaska, “New ALICE detectors for Run 3 and 4 at the CERN LHC,” *Nuclear Instruments and Methods in Physics Research A*, vol. 958, p. 162116, 2020. Proceedings of the Vienna Conference on Instrumentation 2019.
- [89] C. Lippmann, “Upgrade of the ALICE Time Projection Chamber,” 3 2014.
- [90] J. Adolfsson *et al.*, “The upgrade of the ALICE TPC with GEMs and continuous readout,” *Journal of Instrumentation*, vol. 16, no. 03, p. P03022, 2021, 2012.09518.
- [91] L. Musa, “Conceptual Design Report for the Upgrade of the ALICE ITS,” *Tech. Rep. CERN-LHCC-2012-013. LHCC-P-005, CERN*. <https://cds.cern.ch/record/1475244>, 2012.
- [92] Svetlana Kushpil and for the ALICE Collaboration, “Upgrading the Inner Tracking System and the Time Projection Chamber of ALICE,” *J. Phys.: Conf. Ser.* 675 012038, 2016.
- [93] The ALICE Collaboration, “Upgrading the Inner Tracking System and the Time Projection Chamber of ALICE,” *Nuclear Physics A* 1005, 121793, 2021.
- [94] J. Wiechula, *Commissioning and Calibration of the ALICE-TPC*. PhD thesis, 2008.